Joint Trajectory and Resource Allocation Design for UAV Communication Systems

Yuanxin Cai

A thesis submitted to the Graduate Research School of
The University of New South Wales
in partial fulfillment of the requirements for the degree of

Doctor of Philosophy

School of Electrical Engineering and Telecommunications
Faculty of Engineering
The University of New South Wales

June 2021

Copyright Statement

Signature

Date 17/06/2021

Authenticity Statement

Signature

Date 17/06/2021

Thesis submission for the degree of Doctor of Philosophy

Thesis Title and Abstract | Declarations | Inclusion of Publications Statement | Corrected Thesis and Responses

ORIGINALITY STATEMENT

☑ I hereby declare that this submission is my own work and to the best of my knowledge it contains no materials previously published or written by another person, or substantial proportions of material which have been accepted for the award of any other degree or diploma at UNSW or any other educational institution, except where due acknowledgement is made in the thesis. Any contribution made to the research by others, with whom I have worked at UNSW or elsewhere, is explicitly acknowledged in the thesis. I also declare that the intellectual content of this thesis is the product of my own work, except to the extent that assistance from others in the project's design and conception or in style, presentation and linguistic expression is acknowledged.

COPYRIGHT STATEMENT

☑ I hereby grant the University of New South Wales or its agents a non-exclusive licence to archive and to make available (including to members of the public) my thesis or dissertation in whole or part in the University libraries in all forms of media, now or here after known. I acknowledge that I retain all intellectual property rights which subsist in my thesis or dissertation, such as copyright and patent rights, subject to applicable law. I also retain the right to use all or part of my thesis or dissertation in future works (such as articles or books).

For any substantial portions of copyright material used in this thesis, written permission for use has been obtained, or the copyright material is removed from the final public version of the thesis.

AUTHENTICITY STATEMENT

☑ I certify that the Library deposit digital copy is a direct equivalent of the final officially approved version of my thesis.

Thesis submission for the degree of Doctor of Philosophy

Thesis Title and Abstract | Declarations | Inclusion of Publications Statement | Corrected Thesis and Responses

UNSW is supportive of candidates publishing their research results during their candidature as detailed in the UNSW Thesis Examination Procedure.

Publications can be used in the candidate's thesis in lieu of a Chapter provided:

- The candidate contributed **greater than 50%** of the content in the publication and are the "primary author", i.e. they were responsible primarily for the planning, execution and preparation of the work for publication.
- The candidate has obtained approval to include the publication in their thesis in lieu of a Chapter from their Supervisor and Postgraduate Coordinator.
- The publication is not subject to any obligations or contractual agreements with a third party that would constrain its inclusion in the thesis.

☑ The candidate has declared that **some of the work described in their thesis has been published and has been documented in the relevant Chapters with acknowledgement**.

A short statement on where this work appears in the thesis and how this work is acknowledged within chapter/s:

Some fundamental information in Chapter 2 has been presented in the following publications:

Z. Wei, Y. Cai, J. Li, D. W. K. Ng, and J. Yuan, "Energy-efficient resource allocation design for NOMA systems," in Green Communications for Energy-Efficient Wireless Systems and Networks, H. A. Suraweera, J. Yang, A. Zappone, and J. Thompson, Eds. London: IET, 2020, ch. 13, pp. 363-399.

==========

Some introduction in Chapter 1 and the results in Chapter 3 have been presented in the following publications:

Y. Cai, Z. Wei, R. Li, D. W. K. Ng, and J. Yuan, "Energy-Efficient Resource Allocation for Secure UAV Communication Systems," in 2019 IEEE Wireless Commun. Netw. Conf. (WCNC), Apr. 2019, pp. 18.

Y. Cai, Z. Wei, R. Li, D. W. K. Ng, and J. Yuan, "Joint Trajectory and Resource Allocation Design for Energy-Efficient Secure UAV Communication Systems," IEEE Trans. Commun., vol. 68, no. 7, pp. 4536-4553, Mar. 2020.

==========

Some introduction in Chapter 1 and the results in Chapter 4 have been presented in the following publications:

Y. Cai, Z. Wei, S. Hu, D. W. K. Ng, and J. Yuan, "Resource Allocation for Power-Efficient IRS-Assisted UAV Communications," in Proc. IEEE Intern. Commun. Conf. Workshops (ICC Workshops), Jun. 2020, pp. 17.

==========

Some introduction in Chapter 1 and the results in Chapter 5 have been presented in the following publications:

Y. Cai, Z. Wei, S. Hu, C. Liu, D. W. K. Ng, and J. Yuan, "Resource Allocation and 3D Trajectory Design for Power-Efficient IRS-Assisted UAV-NOMA Communications," IEEE Trans. Commun., major revision, Apr. 2021.

==========

Candidate's Declaration

I declare that I have complied with the Thesis Examination Procedure.

Abstract

Recently, the rapid growth of expectations on future wireless networks poses enormous challenges to existing wireless communication systems deployed with fixed infrastructure. Fortunately, unmanned aerial vehicle (UAV)-assisted communication systems serve as a viable solution, which relaxes the limitation of traditional wireless communications on the physical layer. However, joint resource allocation and trajectory designs in terms of energy and spectral efficiency have not been fully studied and investigated in the literature. In this thesis, we aim to provide a thorough study on resource allocation and trajectory design for various practical communication systems employing UAVs.

We first study the trajectory and resource allocation design for downlink energy-efficient secure UAV communication systems, where an information UAV assisted by a multi-antenna jammer UAV serves multiple ground users in the existence of multiple ground eavesdroppers. The resource allocation strategy and the trajectory of the information UAV, and the jamming policy of the jammer UAV are jointly optimized for maximizing the system energy efficiency.

Then, we investigate a multi-antenna UAV-enabled time division multiple access (TDMA) wireless communication system with the assistance of an intelligent reflection surface (IRS). We aim to minimize the average total power consumption of the system by jointly optimizing the resource allocation strategy, UAVs trajectory and velocity, as well as phase control at the IRS. To this end, a non-convex optimization problem is formulated taking into account the individual minimum data rate requirement and the limited energy budget of the IRS.

Additionally, to accommodate more users and to improve the spectral efficiency, an IRS is introduced to assist a UAV communication system based on non-orthogonal multiple access (NOMA) for serving multiple ground users. We aim to minimize the average total system energy consumption by jointly designing the resource allocation strategy, the three-dimensional (3D) trajectory of the UAV, as well as the phase control at the IRS. The design is formulated as a non-convex optimization problem taking into account the maximum tolerable outage probability constraint and the individual minimum data rate requirement. To circumvent the problem intractability due to the altitude-dependent Rician fading in UAV-to-user links, we adopt the machine learning (ML) approach to accurately approximate the effective channel gains in the system.

List of Publications

The work in this thesis has been published or has been submitted for publication as journal papers. These papers are:

Journal Articles:

J1 **Y. Cai**, Z. Wei, S. Hu, C. Liu, D. W. K. Ng, and J. Yuan, "Resource Allocation and 3D Trajectory Design for Power-efficient IRS-Assisted UAV-NOMA Communications," IEEE Trans. Commun., major revision, Apr. 2021.

J2 **Y. Cai**, Z. Wei, R. Li, D. W. K. Ng, and J. Yuan, "Joint Trajectory and Resource Allocation Design for Energy-efficient Secure UAV Communication Systems," IEEE Trans. Commun., vol. 68, no. 7, pp. 4536-4553, Mar. 2020.

Conference Articles:

C1 **Y. Cai**, Z. Wei, S. Hu, D. W. K. Ng, and J. Yuan, "Resource Allocation for Power-efficient IRS-Assisted UAV Communications," in Proc. IEEE Intern. Commun. Conf. Workshops (ICC Workshops), Jun. 2020, pp. 1-7.

C2 **Y. Cai**, Z. Wei, R. Li, D. W. K. Ng, and J. Yuan, "Energy-efficient Resource Allocation for Secure UAV Communication Systems," in 2019 IEEE Wireless Commun. Netw. Conf. (WCNC), Apr. 2019, pp. 1-8.

The following publications are also the results from my Ph.D. study but not included in this thesis:

Journal Articles:

J1 Z. Wei, **Y. Cai**, J. Li, D. W. K. Ng, and J. Yuan, "Energy-efficient Resource Allocation Design for NOMA systems," IEEE Trans. Commun., vol. 20, no. 4, pp. 2530-2550, Apr. 2021.

Book Chapter:

BC1 Z. Wei, **Y. Cai**, J. Li, D. W. K. Ng, and J. Yuan, "Energy-efficient Resource Allocation Design for NOMA Systems," in *Green Communications for Energy-Efficient Wireless Systems and Networks*, H. A. Suraweera, J. Yang, A. Zappone, and J. Thompson, Eds. London: IET, 2020, ch. 13, pp. 363–399.

BC2 Z. Wei, **Y. Cai**, D. W. K. Ng, and J. Yuan, "Energy-efficient Radio Resource Management," in *Wiley 5G Ref: The Essential 5G Reference Online*, R. Tafazolli, P. Chatzimisios, and C.-L. Wang, Eds. Wiley Online Library, 2019, pp. 1–23.

Conference Articles:

C2 S. Hu, Z. Wei, **Y. Cai**, D. W. K. Ng and J. Yuan, "Sum-Rate Maximization for Multiuser MISO Downlink Systems with Self-sustainable IRS," in IEEE Global Commun. Conf., Dec. 2020, pp. 1-7.

Abbreviations

2D	Two-dimensional
3D	Three-dimensional
2G	Second-generation
3G	Third-generation
4G	Fourth-generation
5G	Fifth-generation
AO	Alternating optimization
AOA	Angle-of-arrival
AOD	Angle-of-departure
AWGN	Additive white Gaussian noise
B5G	Beyond fifth-generation
BS	Base station
CDF	Cumulative distribution function
CDMA	Code division multiple access
CSI	Channel state information
dB	Decibel
DC	Difference of convex
DD	Delay-Doppler
DNN	Deep neural network
DoF	Degrees of freedom
EM	Electromagnetic
eMBB	Enhanced mobile broadband
FDMA	Frequency division multiple access

GPRS	General packet radio service
GSM	Global system for mobile communication
GU	Ground user
i.i.d.	Independent and identically distributed
IoT	Internet-of-Things
IRS	Intelligent reflection surface
IS-95	Interim standard 95
ISI	Inter-symbol interference
KKT	Karush-Kuhn-Tucker
LDPC	Low-density parity-check
LMI	Linear matrix inequality
LoS	Line-of-sight
LTE	Long-term evolution
MAI	Multiple access interference
MEC	Mobile edge computing
MIMO	Multiple-input multiple-output
mMTC	Massive machine-type communications
MRT	Maximal-ratio transmission
MUD	Multi-user detection
NLoS	Non-line-of-sight
NMSE	Normalized mean squared error
NOMA	Non-orthogonal multiple access
OFDM	Orthogonal frequency division multiplexing
OFDMA	Orthogonal frequency division multiple access
OMA	Orthogonal multiple access
OTFS	Orthogonal time frequency space
QoS	Quality-of-service
RF	Radio frequency
ReLU	Rectified linear unit

SAA	Sense-and-avoid
SCA	Successive convex approximation
SDP	Semidefinite programming
SIC	Successive interference cancelation
SINR	Signal-to-interference-plus-noise ratio
SNR	Signal-to-noise ratio
SWaP	Size, weight, and power
TDMA	Time division multiple access
s.t.	Subject to
UAV	Unmanned arial vehicle
URLLC	Ultra reliable and low latency communications
WCDMA	Wideband code division multiple access
w.r.t.	With respect to

List of Notations

Scalars, vectors, and matrices are written in italic, boldface lower-case and upper-case letters, respectively, e.g., x, $\mathbf{x}$, and $\mathbf{X}$.

$\mathbf{X}^{\mathrm{T}}$	Transpose of $\mathbf{X}$
$\mathbf{X}^{\mathrm{H}}$	Hermitian transpose of $\mathbf{X}$
$\mathbf{X}^{-1}$	Inverse of $\mathbf{X}$
$\mathbf{X}_{i,j}$	The element in the row i and the column j of $\mathbf{X}$
$\det(\mathbf{X})$	Determinant of a square matrix $\mathbf{X}$
$\mathrm{Tr}(\mathbf{X})$	Trace of a square matrix $\mathbf{X}$
$\mathrm{Rank}(\mathbf{X})$	Rank of a matrix $\mathbf{X}$
$\mathbf{X} \otimes \mathbf{Y}$	The Kronecker product of two matrices $\mathbf{X}$ and $\mathbf{Y}$
$\lvert x \rvert$	Absolute value (modulus) of the complex scalar x
$\lVert \mathbf{x} \rVert$	The Euclidean norm of a vector $\mathbf{x}$
$\lVert \mathbf{X} \rVert_{\mathrm{F}}$	The Frobenius norm of a matrix $\mathbf{X}$
$[x]^+$	$\max(0, x)$
$\mathbb{R}^{M \times N}$	The space of all $M \times N$ matrices with real values
$\mathbb{C}^{M \times N}$	The space of all $M \times N$ matrices with complex values
$\mathbb{S}^{M \times N}$	The space of all $M \times N$ symmetric matrices
$\Pr\{E\}$	The probability of event E occurs
$x \sim p(x)$	x is distributed according to $p(x)$
$\mathbf{0}$	A vector or a matrix with all-zero entries
$\mathbf{I}_{\mathrm{N}}$	N dimension identity matrix
$\mathrm{E}\{\cdot\}$	Statistical expectation
$\mathcal{N}(\mu, \sigma^2)$	Real Gaussian random variable with mean μ and variance σ^2

$\mathcal{CN}(\mu, \sigma^2)$	Circularly symmetric complex Gaussian random variable: the real and imaginary parts are i.i.d. $\mathcal{N}(\mu/2, \sigma^2/2)$
$\ln(\cdot)$	Natural logarithm
$\log_a(\cdot)$	Logarithm in base a
$\text{diag}\{\boldsymbol{a}\}$	A diagonal matrix with the entries of $\boldsymbol{a}$ on its diagonal
$\max\{\cdot\}$	Return the maximum element of its input
$\min\{\cdot\}$	Return the minimum element of its input
$\frac{\partial f}{\partial x}$	A partial derivative of a function f w.r.t. variable x
$e^x, \exp(x)$	Natural exponential function
$\mathcal{O}(\cdot)$	The big-O notation

Contents

List of Figures

List of Tables

List of Algorithms

Chapter 1

Introduction

In this chapter, we first provide an overview on the fifth-generation (5G) wireless networks before introducing the motivations of our research for studying unmanned aerial vehicles (UAVs) communications in this thesis. Then, a thorough literature review on UAV communications and a brief introduction on the research challenges of UAV communications are presented. In addition, we also outline the main contributions of the thesis.

1.1 Overview of 5G

In recent years, the dramatic growth in the number of wireless devices and the associated demanding quality-of-services (QoS) have fueled the development of new technologies for 5G and beyond 5G (B5G) [7–9] wireless networks. Three main services with different requirements have been imposed which are expected to be supported by 5G wireless technology, which are enhanced mobile broadband (eMBB), massive machine-type communications (mMTCs), and ultra-reliable low-latency communications (URLLCs). These services lead to unprecedented demands for system resources. For example, eMBB requires

ultra-high data rates, i.e., $100 \sim 1,000$ times of the current fourth-generation (4G) technology while offering moderate rates of the cell-edge users; mMTC requires massive connectivity for a large number of the Internet-of-Things (IoT) devices; and URLLC requires lower latency, i.e., $10 \sim 20$ times shorter than that achieved by current 4G technology. Although several potential technologies, e.g., millimeter wave [10], energy harvesting communications [11–13], and massive multiple-input multiple-output (MIMO) [14–16], offer some promising solutions to guarantee ubiquitous and ultra-high data rate services, e.g., [17, 18], the system performance is still limited by some bottlenecks, such as overloaded traffic demand or shadowed communication links. On the other hand, due to the growing environmental concerns and the increasing requirements of energy consumption, energy-efficient communications have drawn significant attention from both academia and industry [10, 19–23]. In particular, to reduce the power consumption and relieve the problem of spectrum scarcity [24–27], the trade-off between energy efficiency and spectral efficiency of cellular networks is of fundamental importance for system design and optimization in 5G wireless networks. As such, there is an emerging call for a new paradigm for realizing energy-efficient wireless communication systems.

1.2 Motivations

In the past decades, the advancement of mechanical engineering has reduced the cost of the manufacturing of UAVs which triggers their wide applications in different research areas. In particular, the applications of UAVs to communication systems are promising which are summarized as follows. Due to the high flexibility, mobility, and lost-cost deployment of UAVs offered to wireless communication systems [28–30], several interesting applications of UAV have been

proposed, such as aerial mobile base stations (BS) [31, 32], aerial mobile relays [33–37], and aerial mobile data collections [38–40], etc. Specifically, the mobility of the UAV has significantly improve the system performance due to the higher degrees of freedom (DoF) offered by the UAV for effective resource allocation design. Moreover, the channel conditions of the air-to-ground links from the UAV are generally better than the traditional links between the terrestrial BS and ground terminals, since line-of-sight (LoS) paths usually dominate the air-to-ground channels when the flying altitude of the UAV is sufficiently high. In such cases, time-varying communication channels become more deterministic which facilitate the provisioning of stable communication services. However, there are various practical open problems that remain unsolved. For instance, although the air-to-ground channels become less uncertain with an increasing UAV's altitude, the associated path loss increases reducing the received signal strength. As a result, there is a non-trivial trade-off between designing UAV's three-dimensional (3D) trajectory and communication performance. Besides, to maintain both the stable flight and wireless transmission for UAV-based communications, the energy-efficiency has become an important figure of merit for the system design due to the limit total energy budget determined by the onboard battery capacity. Meanwhile, secure communications have become a major concern in UAV-based communications as these systems are susceptible to potential eavesdropping due to the dominated LoS paths. Thus, there is an emerging need for designing secure energy-efficient UAV-based communications. More background information of UAV-based communication will be provided in Chapter 2.

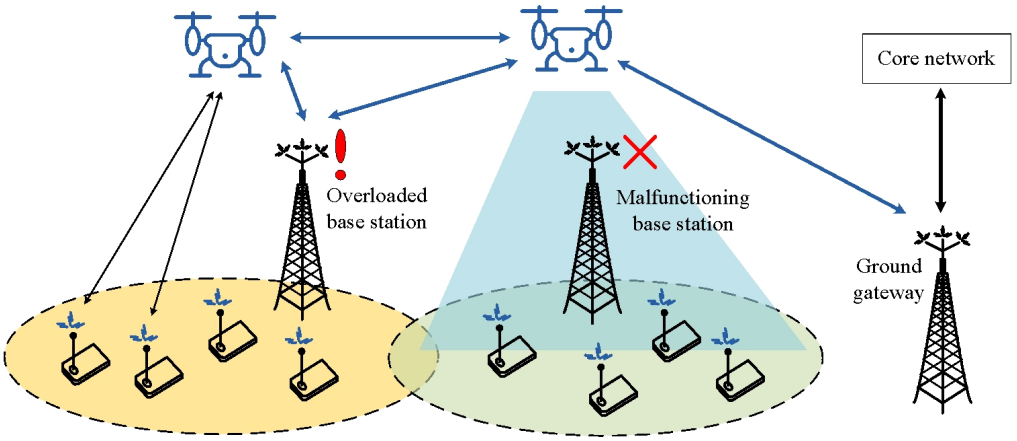

Figure 1.1: Typical use case of UAV-aided wireless communications: UAV-aided ubiquitous coverage.

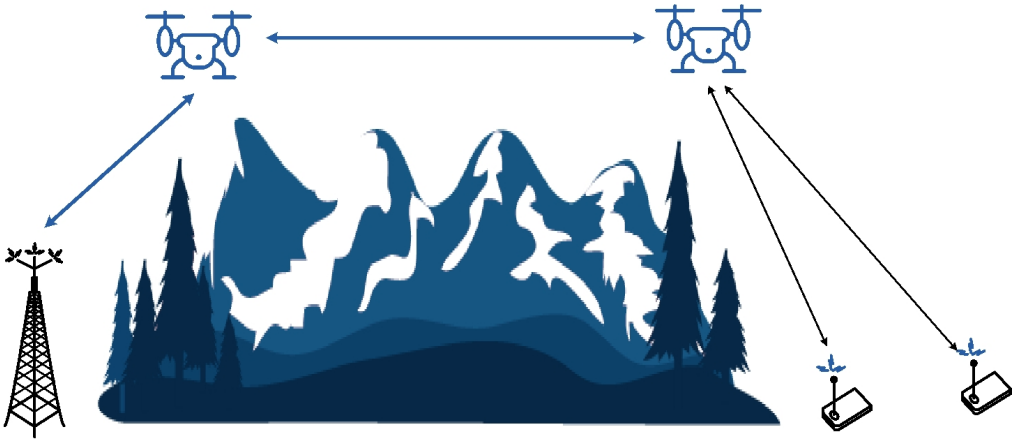

Figure 1.2: Typical use case of UAV-aided wireless communications: UAV-aided relaying.

1.3 Literature Review

In this section, the related topics of this thesis, e.g., UAV communications, UAV-intelligent reflection surface (IRS) communications, and UAV-non-orthogonal multiple access (NOMA) are discussed and reviewed.

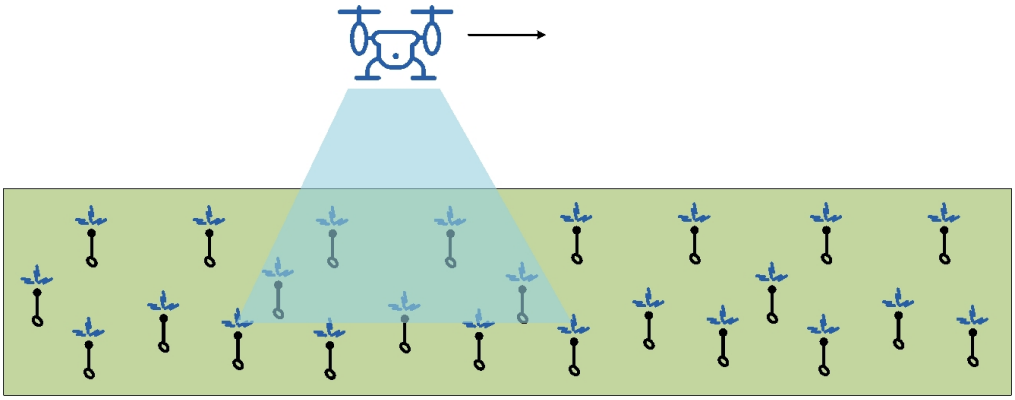

Figure 1.3: Typical use case of UAV-aided wireless communications: UAV-aided information dissemination and data collection.

1.3.1 UAV Communications

The rollout of numerous data-hungry wireless applications, e.g., video streaming and real-time gaming, have posed enormous challenges on future wireless networks, e.g., ultra-high data rates, low latency, and massive connectivity, etc., [7–9]. Despite various disruptive technologies have been adopted in practice, e.g., massive MIMO [10–18], providing high-data-rate communications in emergencies and important scenarios, such as natural disasters and overloaded traffic demand, remains challenging. Fortunately, UAV-enabled wireless communication systems provide a feasible solution [41–46] to address these problems, which address the limitation of traditional wireless communications on the physical layer. Due to the high flexibility, mobility, and lost-cost deployment of UAVs offered to wireless communication systems, several interesting applications of UAV have been proposed, such as mobile base stations, mobile relays, and mobile data collections, etc [41]. For example, in Figure 1.1, the UAV is served as a mobile aerial base station. It could transmit information to ground users where the traditional base station is overloaded or broken. This application is generally used in a critical situation or natural hazard. In case there are extra users than

expected or damaged base station. The case in Figure 1.2 treats the UAV as a relay in wireless communications. The UAV can serve establish end-to-end communication between two users in the existence of some ground obstacles. Figure 1.3 utilizes the UAV for information dissemination and data collection for a large number of ground users or sensor nodes in a large area. This could be wildly used in digital agriculture and the Internet-of-Things. In particular, there are two types of UAV who generally adopted in wireless communication system, e.g., fixed wing UAVs [1] and rotary wing UAVs [3]. Specifically, the rotary wing UAV is the main focus of this thesis since it can hover in the air and offer a higher flexibility for designing the UAV's trajectory than that of the fixed wing UAV for enhancing the performance of communication systems. To capture the impact of UAV on communication systems, the flight power consumption model for the rotary wing UAV and the related details will be discussed in Chapter 2.

In practice, by exploiting the high flexibility and mobility of UAVs, the performance of the communication systems can be improved by cruising UAVs close to the desired users. Besides, in practice, UAVs offer a higher probability to establish a strong LoS wireless channels between UAVs and ground terminals compared with conventional terrestrial communication systems. Therefore, in recent years, there are several exciting and practical applications of UAV proposed in academia and industry. For example, sensing for UAV and UAV for sensing are two typical applications [47]. In the general scenarios of sensing for UAV, two commonly adopted cases are sense-and-avoid (SAA) [48] as well as adversary UAV detection, tracking, and classification [49]. As for adopting a UAV for sensing, the UAV serves as an aerial node to support wireless sensing from the sky [49, 50]. Also, to enable computation offloading with UAV in mobile edge computing (MEC) of cellular networks, the UAV could act as an edge device or

an aerial user who executes the computation tasks by offloading to BSs and MEC servers on the ground [51], or carry a MEC server to support the computation implementation for the ground devices [52].

In the following parts, different aspects of UAV communications are presented, i.e., resource allocation and trajectory design, physical layer security, IRS assisted communications, and UAV communications with multiple access.

1.3.2 Resource Allocation and Trajectory Design for UAV

In practice, although UAV-based communications enjoy various promising advantages [31, 32, 41, 53], some technical problems need to be solved to unlock the promised performance gains. Firstly, stringent power limitation is one of the bottlenecks for enabling efficient UAV communications. In fact, the energy storage of onboard battery of a UAV is usually small due to the size and weight restrictions of the UAV. Besides, the power consumptions of flight and communication depends on the UAV's trajectory and velocity, as will be discussed in Chapter 2. As a result, energy-efficient UAV has drawn significant research interests in the literature. To fully unleash the performance of UAV communication systems, various studies have been conducted in the literature to improve the power efficiency. For instance, in [54], the authors studied the optimal deployment of multiple UAVs to minimize the total system transmit power satisfying the individual user data rate requirement simultaneously. Also, the authors in [38] studied the energy efficiency maximization for wireless sensor networks via jointly optimizing the weak up schedule of sensor nodes and UAV's trajectory. However, the flight power consumption of the UAV was ignored in these work which contributes a major proportion of the total system power consumption. Besides, the authors in [3] minimized the total power consumption

of both communication and flying via jointly optimizing UAV's trajectory and user scheduling for a rotary-wing UAV. Yet, pure LoS wireless channels between the UAV and ground users were assumed [3, 32, 53, 54], which are generally invalid in practice, particularly in urban environments. Also, a probabilistic LoS channel model for UAV-enabled data harvesting system was proposed in [55], which is suitable to a system with a relatively low flying altitude UAV when the shadowing effect dominates the system performance. Despite various attempts in the literature, the research in [3, 32, 53–55] only limited to two-dimensional (2D) trajectory planning. For a relatively high altitude UAV with a clear LoS, in [40], the UAV's 3D trajectory was optimized taking into account a practical model with an angle-dependent Rician fading channel to maximize the minimum average collected data rate. Therefore, UAV's 3D trajectory design and resource allocation with the angle-dependent Rician fading channel is practical interacts which will be addressed in Chapter 5.

1.3.3 Physical Layer Security UAV Communications

On the other hand, since the LoS dominated channels between a UAV and ground nodes are susceptible to potential eavesdropping [41, 56], guaranteeing communication security is a challenging task for UAV communication systems. Thus, there is an emerging need for designing secure UAV-based communication. For instance, the authors in [43] proposed a joint power allocation and trajectory design to maximize the secrecy rate in both uplink and downlink systems. Also, in [57], secure energy efficiency maximization for UAV-based relaying systems was studied. However, both works only considered the case of single-user and the proposed designs in [43, 57] are not applicable to the case of multiple users. Besides, the availability of the eavesdropper location was assumed in

[43, 57], which is generally over optimistic. Although [44] studied the resource allocation design for secure UAV systems by taking into account the imperfect channel state information (CSI) of an eavesdropper, the energy efficiency of such systems is still an unknown. Besides, a robust trajectory and resource allocation design for energy-efficient secure UAV communication systems considering the uncertainty of eavesdropper's location has not been investigated. Furthermore, although deploying a single UAV in the system was demonstrated to offer some advantages for wireless communications [35, 53], the performance of single UAV communication systems can be unsatisfactory due to the stringent requirement on secure communication. Thus, with the assistance of a jammer UAV, the authors in [2,4,58] proposed a cooperative jamming scheme for secure UAV communications by jointly optimizing power allocation and trajectories. Yet, since the jammer UAV is only equipped with a single-antenna in these systems, the direction of artificial noise cannot be controlled properly which also causes strong interference to legitimate users due to the existence of strong LoS paths. Therefore, we propose to employ multiple antennas at the jammer UAV to focus the artificial noise to degrade the channel quality of eavesdroppers as well as to mitigate the interference upon legitimate users. However, designing a cooperative jamming policy with a multi-antenna jammer UAV is very challenging and remains to be explored. In Chapter 3, we aim to address the above issues by optimizing the resource allocation and trajectory design for the secure UAV communications with the assistance of a multiple-antenna jammer UAV.

1.3.4 IRS-Assisted UAV Communications

IRS is an enabling technology that can design the radio signal propagation in the wireless communications [59–61]. The IRS can dynamically change the

wireless channel to improve the performance of the communication by intelligently tuning the signal reflection. Most recently, IRS, a new technology, has attracted substantial attention in the field of wireless communications as it can reshape the signal propagation environment so as to improve the system performance [62–66]. For example, beamforming and discrete phase control of IRS-assisted systems were jointly optimized to minimize the total transmit power in [67, 68]. Besides, the authors in [5] proposed a jointly optimized active beamforming at the transmitter and passive beamforming at the IRS to maximize the received signal power at desired users. Furthermore, it is expected that deploying an IRS in UAV-enabled communication systems can help to improve the achievable data rate for ground users with a weak channel condition. In particular, the passive beamforming controlled by the IRS can reflect the dissipated signals transmitted from the UAV to the ground users. This unique feature not only increases the received signal strength at the desired users, but also improves the flexibility in the UAV's trajectory design. Thus, the integration of an IRS into UAV-based communication systems has been advocated lately. For instance, the authors in [69] maximized the average achievable data rate in IRS-assisted UAV communication systems by jointly optimizing the UAV's trajectory and the phase shift control of the IRS. Yet, this study only focused on the case of a single-user and the proposed result is not applicable to practical multi-user systems. Also, the joint design of 2D trajectory and passive beamforming was studied in [62,70] for multi-user IRS-aided UAV communications assuming the availability of perfectly known CSI, which is overly optimistic. Moreover, the considered system models in [69, 70] neglected the existence of a direct link between the UAV and ground users which leads to inevitable performance degradation. In fact, a joint resource allocation and phase shift control for power-efficient IRS-

assisted multi-user UAV communication systems are important and challenging, which has not been reported in the literature yet. In Chapters 4 and 5, we address the above issues by jointly optimizing the IRS's phase shift control and resource allocation for power-efficient IRS-assisted UAV communications taking into account multiple ground users.

1.3.5 UAV Communications over Multiple Access

Finally, to enable multiple access in UAV communication systems, UAVs based on time division multiple access (TDMA) are commonly adopted in the literature [40, 55], yet, their results are not applicable to a more general system supporting multiple users simultaneously. On the other hand, in order to support simultaneous energy-efficient multi-user communications, orthogonal frequency division multiple access (OFDMA) is an ideal candidate, as it has been commonly adopted in various conventional communication systems [19,22,71]. In particular, OFDMA provides a high flexibility in resource allocation for exploiting multi-user diversity to improve the system energy efficiency. For instance, in [66, 72], OFDMA was adopted for UAV communication systems and a joint trajectory and resource allocation design was proposed to maximize the minimum data rate for fairness the QoS constraints. Moreover, as a multiple access technology beyond OFDM, NOMA provides a higher flexibility in resource allocation for improving the system spectral efficiency, especially considering the diverse QoS requirements of users. In [73, 74], the UAV-NOMA communication systems were designed to maximize the achievable data rate or minimizing the power consumption of the system. Thus, diverse channel conditions need to be explored for UAV communication systems.

1.3.6 Summary

In this part, we summarize the main issue of UAV communications studied in the literature review, which motivates the thesis.

- Due to the total energy budget for maintaining both stable flight and communication is limited by the onboard battery capacity, the resource allocation and trajectory for the UAV communication systems are need to be designed.

- Since the LoS paths dominate the air-to-ground communication channels, UAV-based communication systems are susceptible to potential eavesdropping, physical layer security is an important point for UAV communications requiring a thorough investigation.

- Since the Rician factor is related to the UAV's flight altitude and there is a non-trivial trade-off between the outage probability and channel gain, the design of UAV's 3D trajectory taking into account the altitude-dependent Rician fading channel is necessary.

- To improve the end-to-end channel quality between the UAV and users, adopting IRS to reflect the spread communication power from the environment towards users needs to be explored.

- NOMA protocol for UAV communications can fully adopt the mobility of the UAV to transmit information for two users with near-farness pairing, which strongly improve the DoF for resource allocation design. Yet, the efficient resource allocation optimizations for UAV-NOMA communications are remain unknown.

1.4 Thesis Outline and Main Contributions

1.4.1 Thesis Organization

In this subsection, the outline of each chapter in this thesis is given. There are six chapters in total, including an introduction of the thesis, the necessary background knowledge, the technical details of the conducted research, and the conclusion of this thesis.

Chapter 1

This chapter provides an overview of 5G communications and the motivation of the considered research questions of the thesis and the existing works are presented. It also provides the outline and the main contributions of this thesis.

Chapter 2

This chapter presents some background knowledge including the types of UAVs, channel model, energy efficiency, and resource allocation design methodologies.

Chapter 3

This chapter discusses the joint trajectory and resource allocation design for energy-efficient secure UAV communication systems, which taking into account the maximum tolerable leakage signal-to-interference-plus-noise ratio (SINR) to eavesdroppers and the minimum individual user data rate requirement. A low-complexity suboptimal iterative algorithm is provided for maximizing the system energy efficiency. The proposed schemes and approaches in this chapter serve as building blocks for the studies in the following chapters.

Chapter 4

This chapter studies the resource allocation for power-efficient IRS-assisted UAV communications considering pure LoS dominated channel with perfect

CSI, the energy budget of the IRS, 2D trajectory design of the multiple-antenna allocated UAV, and TDMA protocol. A joint design of user scheduling, power allocation, UAV's trajectory, UAV's flight velocity, the transformer's beamforming precoder, and the phase control policy of the IRS for minimize the total power consumption is formulated and solved. The study of this chapter can be extended to a more practical model considering 3D trajectory design and NOMA transmission which will be studied in Chapter 5.

Chapter 5

This chapter proposes the resource allocation and 3D trajectory design for power-efficient IRS-assisted UAV-NOMA communications by taking into account the altitude dependent Rician fading, minimum individual data rate requirement, and the outage probability limitation. A suboptimal resource allocation design for minimizing the average total power consumption is also presented in this chapter.

The proposed schemes in Chapters 3-5 can be utilized in practice, e.g., adopting the UAV as a temporary base station for the specific situation if the tradition base station is damaged, adopting the UAV as a patrol jammer for the emergency scenario maintaining security, and adopting the IRS to reuse the spread signal in the energy crisis area or situation.

Chapter 6

This chapter presents the conclusions of this thesis and the contribution of the works during my Ph.D. research. The potential future work related to this thesis are also introduced.

Appendix

Appendixes A-D discuss some fundamental knowledge about convex optimization techniques, the proof of theories, and algorithm convergence of Chapters 3-5.

1.4.2 Research Contributions

This thesis studies the resource allocation and trajectory design of the UAV communications. The developed theoretical results can serve as guidelines for the practical implementation of UAV in future wireless communication systems. A detail presented of the research contribution in Chapters 3-5 are listed in the following.

- Chapter 3 studies the joint trajectory, resource allocation, and jamming policy design for energy-efficient secure UAV-OFDMA communication systems. In particular, an information UAV provides energy-efficient secure communication for multiple legitimate users adopting OFDMA in the existence of multiple eavesdroppers, with the assistance of a multiple-antenna jammer UAV patrolling with a fixed trajectory. The joint design is formulated as a non-convex optimization problem to maximize the system energy efficiency taking into account the maximum tolerable leakage signal-to-interference-plus-noise ratio (SINR) to eavesdroppers and the minimum individual user data rate requirement. Since the formulated problem is non-convex which is generally intractable, we propose an iterative algorithm to achieve a suboptimal solution of the formulated problem.

  The results in Chapter 3 have been presented in the following publications:

  – **Y. Cai**, Z. Wei, R. Li, D. W. K. Ng, and J. Yuan, "Energy-Efficient Resource Allocation for Secure UAV Communication Systems," in 2019 IEEE Wireless Commun. Netw. Conf. (WCNC), Apr. 2019, pp. 18.

  – **Y. Cai**, Z. Wei, R. Li, D. W. K. Ng, and J. Yuan, "Joint Trajectory and Resource Allocation Design for Energy-Efficient Secure UAV

Communication Systems," IEEE Trans. Commun., vol. 68, no. 7, pp. 4536-4553, Mar. 2020.

- Chapter 4 aims to minimize the average total power consumption of the system via jointly optimizing the resource allocation and trajectory while considering the minimum data rate requirement of each user. We propose an iterative algorithm based on the alternating optimization technique to achieve a suboptimal solution efficiently. The numerical results evaluate the system performance gain of the proposed algorithm over baseline schemes without IRS or a fixed straight flight trajectory with a constant flight speed.

  The results in Chapter 4 have been presented in the following publications:

  – **Y. Cai**, Z. Wei, S. Hu, D. W. K. Ng, and J. Yuan, "Resource Allocation for Power-Efficient IRS-Assisted UAV Communications," in Proc. IEEE Intern. Commun. Conf. Workshops (ICC Workshops), Jun. 2020, pp. 17.

- Chapter 5 studies the joint design of the resource allocation, UAV's 3D trajectory, and its flight velocity, as well as the phase shift control of the IRS in a practical altitude-dependent Rician fading channel for power-efficient IRS-assisted UAV-NOMA communications. The joint design is formulated as a non-convex optimization problem to minimize the average total power consumption of the system taking into account the minimum data rate requirement of each user and the maximum tolerable outage probability constraint. Since the formulated problem is non-convex and highly intractable, we first propose a closed-form phase control policy for IRS. Then, to handle the intractability caused by the altitude-dependent Rician fading channel, we employ a deep neural network (DNN) technique

to approximate the outage-guaranteed effective channel gain. Furthermore, the obtained results are exploited to serve as a building block for the design of an iterative optimization algorithm for addressing the design problem.

The results in Chapter 5 have been presented in the following publications:

– **Y. Cai**, Z. Wei, S. Hu, C. Liu, D. W. K. Ng, and J. Yuan, "Resource Allocation and 3D Trajectory Design for Power-Efficient IRS-Assisted UAV-NOMA Communications," IEEE Trans. Commun., major revision, Apr. 2021.

1.5 Summary

This chapter briefly introduces of the 5G wireless networks and UAV communication techniques, including the research challenges and related works. Besides, the thesis outline and the main contributions of this thesis are listed in this chapter.

Chapter 2

Background

2.1 Introduction

In this chapter, we first introduce the related background information of unmanned arial vehicle (UAV), e.g., different types of UAV and the adopted flight power consumption model. Subsequently, we briefly introduce the fundamental knowledge of UAV communications, e.g., the channel models, the definition of energy eiciency, and the potential multiple access techniques for UAV communications. Finally, we introduce the optimization-based resource allocation design framework for UAV communication systems. The materials in this chapter serve as technical guidelines to provide the necessary background to understand the works in the later chapters.

2.2 UAV's Flight Power Consumption Model

There are generally two types of UAVs adopted in wireless communication systems, i.e., the fixed wing UAV [1] and the rotary wing UAV [3]. In this thesis, we adopt a rotary wing UAV since it has a higher flexibility than that

of the fixed wing UAV for trajectory and resource allocation design. Due to the size, weight, and power (SWaP) limitation of the UAV, taking into account the flight power consumption of the UAV is necessary for the design of the UAV's trajectory. The flight power consumption of a rotary wing UAV is given by [3]

$$P_{\text{flight}} = \underbrace{P_o\left(1+\frac{3v^2}{\Omega^2 r^2}\right)}_{\text{Blade profile}} + \underbrace{P_i\left(\sqrt{1+\frac{v^4}{4v_0^4}}-\frac{v^2}{2v_0^2}\right)^2}_{\text{Induced}} + \underbrace{\frac{1}{2}d_0\rho s A_{\text{r}} v^3}_{\text{Parasite}} \tag{2.1}$$

$$\approx P_o\left(1+\frac{3v^2}{\Omega^2 r^2}\right) + \frac{P_i v_0}{v} + \frac{1}{2}d_0\rho s A_{\text{r}} v^3, \tag{2.2}$$

where $v \in \mathbb{R}$ denotes the UAV's horizontal flight velocity. The physical meanings of the parameters in (2.1) and (2.2) are summarized in Table 2.1. Note that since the total power in (2.1) is a non-convex function with respect to (w.r.t.) flight velocity, which is approximated by a convex function in (2.2) to improve the model tractability. Fig. 2.1 illustrates the total power in (2.1), the approximated total power in (2.2), the blade profile power, the induced power, and the parasite power consumptions in (2.1) versus the flight velocity. We can observe that the flight velocity with the highest power-efficiency located in the medial range to strike a balance between the cruising speed and the power consumption. Note that the power consumption models will be adopted in Chapters 3-5 to facilitate effective resource allocation design.

2.3 Channel Models

Generally, wireless communication systems operate with electromagnetic (EM) waves. In theory, a communication channel in the space can be characterized by

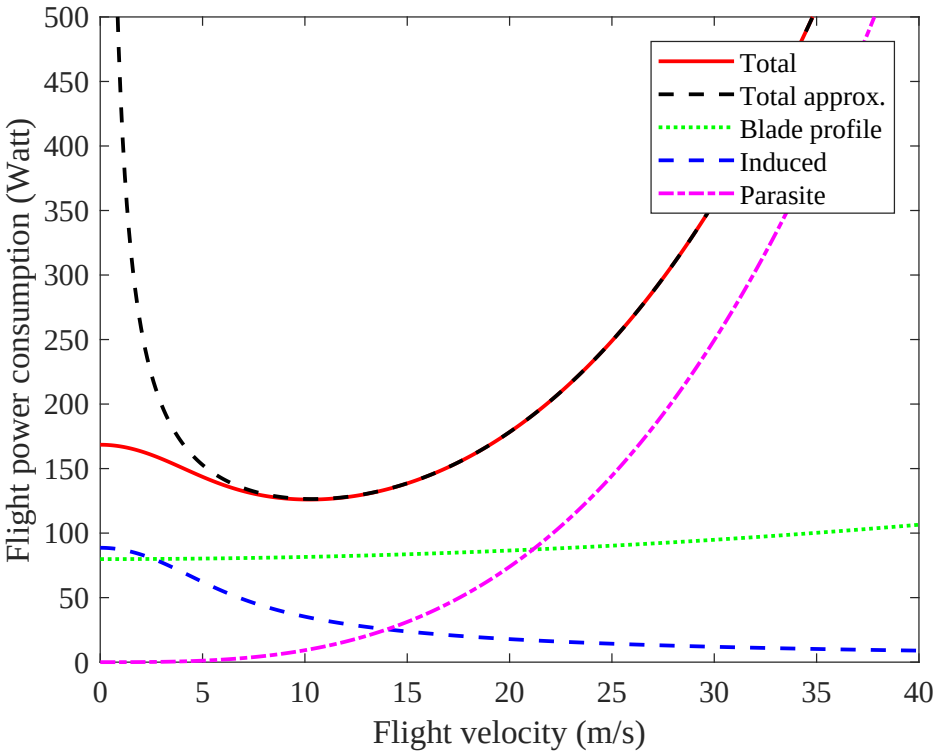

Figure 2.1: The flight power consumption of the rotary-wing UAV.

the Maxwell's equations [75]:

$$\frac{\partial \mathbf{B}}{\partial t} + \nabla \times \mathbf{E} = 0, \tag{2.3}$$

$$\nabla \cdot \mathbf{D} = \rho, \tag{2.4}$$

$$\frac{\partial \mathbf{D}}{\partial t} + \nabla \times \mathbf{H} = -\mathbf{J}, \tag{2.5}$$

$$\nabla \cdot \mathbf{B} = 0, \tag{2.6}$$

where $t \in \mathbb{R}$, ρ, and $\mathbf{J}$ are the time, the total electric charge density, and the total electric current density, respectively. $\frac{\partial \cdot}{\partial t}$ denotes the partial derivative of a function w.r.t. t. Note that $\mathbf{E}$, $\mathbf{D}$, $\mathbf{H}$, $\mathbf{B}$ denote the electric field intensities, the electric displacement, the magnetic field intensities, and the magnetic induction, respectively. In particular, equation (2.3) is Faraday's law and illustrates the

Table 2.1: Notations and physical meaning of variables in power consumption model.

Notations	Physical meaning
Ω	Blade angular velocity in radians/second
r	Rotor radius in meter
ρ	Air density in kg/m^3
s	Rotor solidity in m^3
A_{r}	Rotor disc area in m^2
P_o	Blade profile power in hovering status in watt
P_i	Induced power in hovering status in watt
v_0	Mean rotor induced velocity in forwarding flight in m/s
d_0	Fuselage drag ratio

effect of a altering magnetic field on the electric field. Besides, the Gauss's law in divergence condition (2.4) denotes the influence of the changing density on the electric displacement. Also, the Ampère's circuital law as in (2.5) is modified by Maxwell. Finally, (2.6) denotes the fact that the magnetic induction $\mathbf{B}$ is solenoidal.

Despite the high accuracy of the Maxwell's equations, they are not commonly adopted in developing communications theory due to their intractabilities. For example, these equations require the complete knowledge of all physical objects in the channel such as the distances and the reflecting indices which are generally not available in ad-hoc wireless communication networks. To strike a balance between accuracy and model tractability, in wireless communications, stochastic based channel fading models are introduced to simplify the performance analysis of wireless communication systems. Roughly speaking, the channel fading in the area of wireless communication research can be divided into two types:

- *Large-scale fading*: It is caused by the path loss attenuation of the signal as a function of distance and shadowing caused by large objects such as buildings and hills.

- *Small-scale fading*: It is caused by the constructive and destructive additions of the multi-path signals between the transmitter and receiver.

We will discuss both types of fading modelings in the following.

2.3.1 Large-scale Fading Models

Free Space Path Loss Model:

Consider a signal transmitted through the free space without any obstructions between the transmitter and the receiver. The free-space path loss is defined as the path loss of the free-space model [76]:

$$P_{\mathrm{L}}(d)\,[\mathrm{dB}] = 10\log_{10}\frac{P_{\mathrm{t}}}{P_{\mathrm{r}}} = 10\log_{10}\frac{(4\pi d)^2}{G_t G_r \lambda^2}, \tag{2.7}$$

where d is the distance between the transmitter and the receiver, λ is the wavelength of the information-carrying signal, P_{t} denotes the transmit power, P_{r} denotes the received power, G_{t} represents the transmit antenna gain, and G_{r} is the receiving antenna gain.

Simplified Distance-based Path Loss Model

Depending on the potential application, a further simplified distance-based path loss model has been widely used in the literature [77, 78] for the ease of system design and performance analysis. This model emphasizes the impact of propagation distance d, which is given by:

$$P_{\mathrm{L}}(d) = \frac{1}{1 + d^{n_{\mathrm{L}}}}, \tag{2.8}$$

where n_{L} is the path loss exponent. In this model, the path loss is only a simple function w.r.t. the distance d between the corresponded transmitter and the

receiver. The simplified distance-based path loss model is adopted in Chapters 3-5 of this thesis.

Shadowing Model

The shadowing effect is the influence on the received signal power fluctuation due to the objects blocking the propagation path between the transmitter and the receiver. These fluctuations are experienced through the local-mean square power, which means that the short-term average eliminates the fluctuations caused by multi-path fading. The received power fluctuates with a "log-normal" distribution is given by

$$P_{\mathrm{L}}^{\mathrm{Total}}(d)[\mathrm{dB}] = P_{\mathrm{L}}(d)[\mathrm{dB}] + \Delta P_{\mathrm{L}}[\mathrm{dB}], \tag{2.9}$$

where $\Delta P_{\mathrm{L}} \sim \mathcal{N}(0, \sigma^2)$ and σ^2 means the variance of the Gaussian distribution.

In UAV communication systems proposed in this thesis, the shadowing is negligible since the line-of-sight (LoS) paths dominate the air-to-ground wireless channel as discussed in the following.

2.3.2 Small-scale Fading Models

The large-scale fading model parameters are associated with the macro-scattering environment and change relatively slowly over time. In contrast, small-scale fading models are established primarily to characterize the constructive and destructive patterns in different multi-path components introduced by the channel, often showing rapid fluctuations in the signal's envelope across a small distance.

Rician Fading Model

When a LoS path dominates the wireless channel than other non-line-of-sight

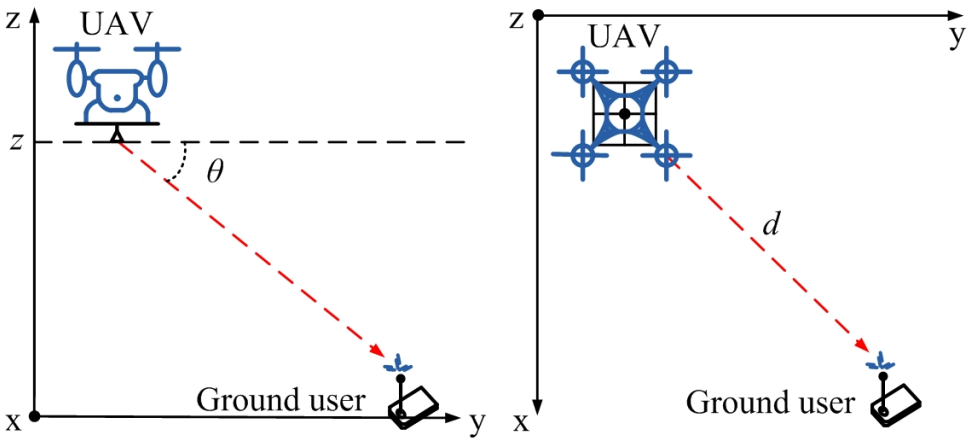

Figure 2.2: The vertical AoDs between the UAV and GU.

(NLoS) paths, the commonly adopted channel model is Rician fading model. In this case, the narrow band channel h can be modeled as

$$h = \sqrt{\frac{\kappa}{\kappa+1}} h^{\mathrm{LoS}} + \sqrt{\frac{1}{\kappa+1}} \Delta h, \tag{2.10}$$

where h^{LoS} denotes the LoS component of the channel h and $\Delta h \sim \mathcal{CN}(0, \sigma^2)$. The Rician factor κ is the ratio of the energy in the LoS path to the energy in the scattered paths. The magnitude $|h|$ follows a Rician distribution. Thus, this channel model is referred to as the Rician fading model [79].

Altitude-Dependent Rician Fading Model

In fact, for UAV communication systems, the altitude-dependent Rician factor for UAV-ground user (GU) link can be modeled by an exponential function [40, 80], which is given by

$$\kappa = A_1 \exp\left(A_2 \theta\right), \tag{2.11}$$

where θ is the elevation angle-of-departure (AoD) from the UAV to GU, as shown in Fig. 2.2, and is given by

$$\theta = \arctan\left(\frac{z}{d}\right), \tag{2.12}$$

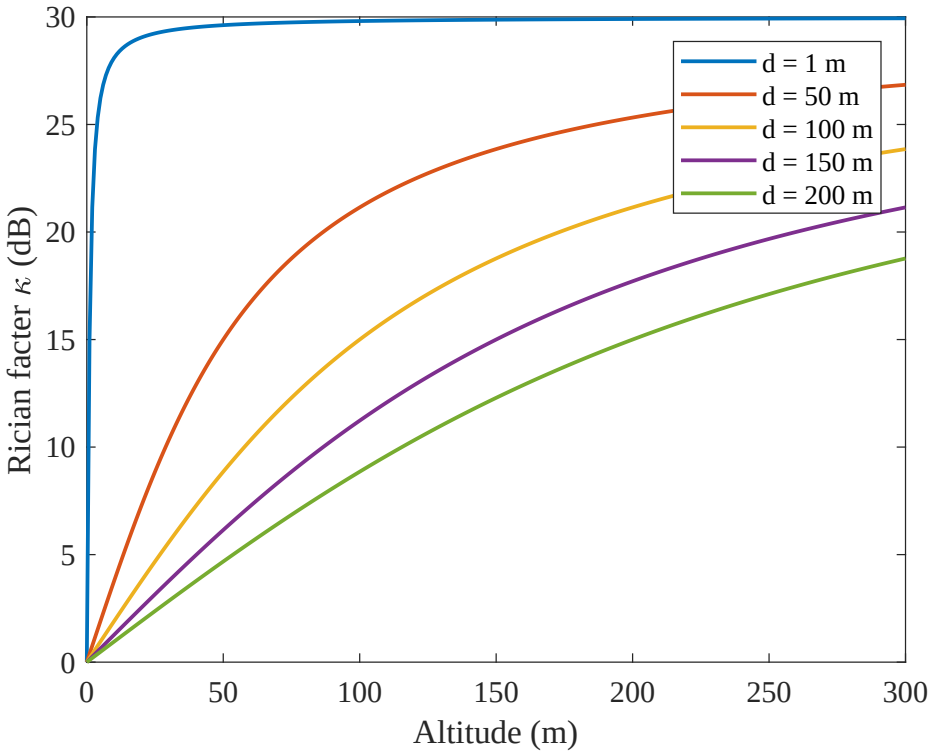

Figure 2.3: The Rician factor κ versus the UAV's flight altitude with different horizontal distances between the UAV and the GU.

where d denotes the horizontal distance between the UAV and the GU. Note that $A_1 > 0$ and $A_2 > 0$ are constant parameters related to the terrain environment and can be obtained via long-term measurements. Then, we can observe that the Rician factor is bounded by $\kappa_{\min} \leq \kappa \leq \kappa_{\max}$, where $\kappa_{\min} = A_1$ and $\kappa_{\max} = A_1 e^{A_2 \pi/2}$. Fig. 2.3 illustrates the Rician factor κ versus the UAV's flight altitude with difference horizontal distances between the UAV and GU. We can observe that the Rician factor κ increases as the UAV's flight altitude increases for all the considered horizontal distances. In specific, both the Rician factor κ and its increasing slop are higher when the UAV is horizontally closer to the GU. The altitude-dependent Rician fading model will be adopted in Chapter 5 of this thesis.

2.4 Energy Efficiency

In this section, we introduce the basic definitions of the energy efficiency adopted in this thesis.

In UAV communication systems, the energy efficiency has emerged as a new pivotal and fundamental figure of merit since the limited energy capacity equipped at the UAV. Besides, energy consumptions and related environmental issues become a hot topic today. In general, energy efficiency is essentially in the form of a cost-benefit ratio[1] to evaluate the amount of data successfully delivered by utilizing the limited energy resource (bits/Joule) of the system. The energy efficiency is defined as [10, 19, 20]

$$\mathcal{EE} = \frac{W \log_2 \left(1 + \frac{p|h|^2}{\sigma^2}\right)}{\delta p + P_{\mathrm{C}} + P_{\text{flight}}}, \tag{2.13}$$

where W, p, h, and σ^2 in the numerator represent the bandwidth, the transmission power, the channel gain, and the noise power, respectively. Note that P_{C} denotes the static circuit power consumption associated with communications, P_{flight} represents the UAV's flight power consumption as in (2.2), and $\delta > 1$ captures the inefficiency of the transmit power amplifier[2]. In the following chapters, the energy-efficient communication systems are adopted by maximizing the energy efficiency or minimizing the total power consumption with system performance requirements. The detail discussion about maximizing the energy efficiency as the objective is given in Section 2.6.1 and Chapter 3.

[1]It should be noted that there are alternative types of energy efficiency definitions, such as from facility level, equipment level, and network level, respectively [81], depending on the design of specific systems.

[2]Here, we assume that the power amplifier operates in its linear region and the hardware power consumption P_{C} is a constant.

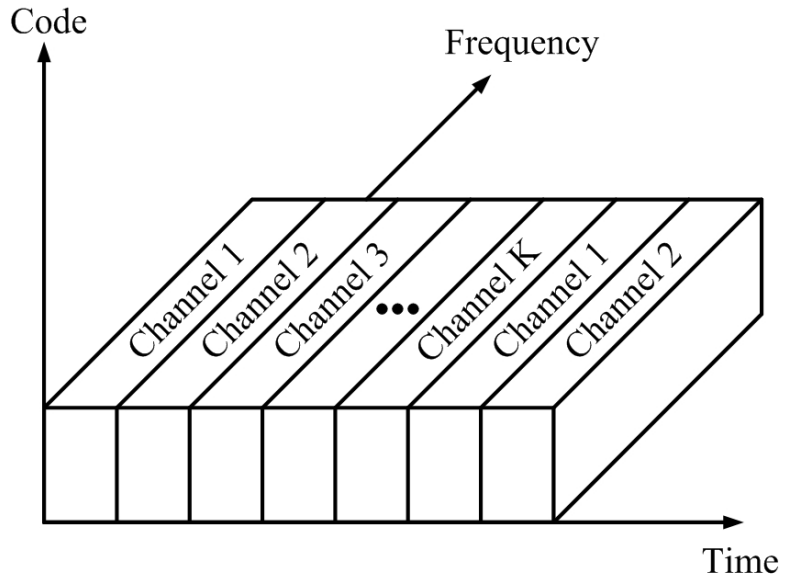

Figure 2.4: Time-division multiple access.

2.5 Fundamental of Multiple Access

Multiple access techniques divide the total dimension of the signaling into channels and then assign these channels to different users. The multiple access schemes enable the UAV communications to serve multiple users via limited system resources. The most commonly adopted methods are to divide the signal space along the time, frequency, and/or code dimension. In particular, the different users are allocated by an orthogonal division along these dimension: time-division multiple access (TDMA), frequency-division multiple access (FDMA), and code-division multiple access (CDMA).

2.5.1 Orthogonal Multiple Access (OMA)

Time-Division Multiple Access (TDMA)

For TDMA protocol, e.g., global system for mobile communications (GSM) in the second-generation (2G) communication systems, the time dimension is

divided into non-overlapping channels and each user is allocated to a different cyclically repeating time slot, as shown in Fig. 2.4. These TDMA partitive channels occupy the entire system bandwidth, usually a narrow band for simplicity. The cyclically repeating time slots imply that the transmission of each user is bursty across time. As such, a digital transmission technology that allows buffering is required. Also, TDMA has the advantage that it allows the flexibility of assigning multiple channels to a single user simply by assigning multiple time slots, e.g., general packet radio service (GPRS) in 2G, for handling data-hungry tasks. However, the main difficulty with TDMA is the requirement for synchronization among different users with different receive distances. For example, to maintain orthogonal time slots in the received signals, the different uplink transmitters must be synchronized. In such a way, after transmission through their respective channels, the received signals remain orthogonal in time. Besides, multi-path can also destroy time-division orthogonality if the multi-path delays are a significant fraction of a time slot. Therefore, TDMA channels often have guard bands between them to compensate for time synchronization errors and multi-path. In Chapter 5 of this thesis, the TDMA protocol is adopted as a baseline scheme.

Frequency-Division Multiple Access (FDMA)

In FDMA, the system is divided across the frequency dimension into non-overlapping channels and each user is allocated to a different frequency channel, as shown in Fig. 2.5. The channels often have guard bands between them to compensate for imperfect filters, adjacent channel interference, and spectral spread due to Doppler. In contrast to TDMA, the transmission is continuous in time, which requiring real-time signal processing.

Code-Division Multiple Access (CDMA)

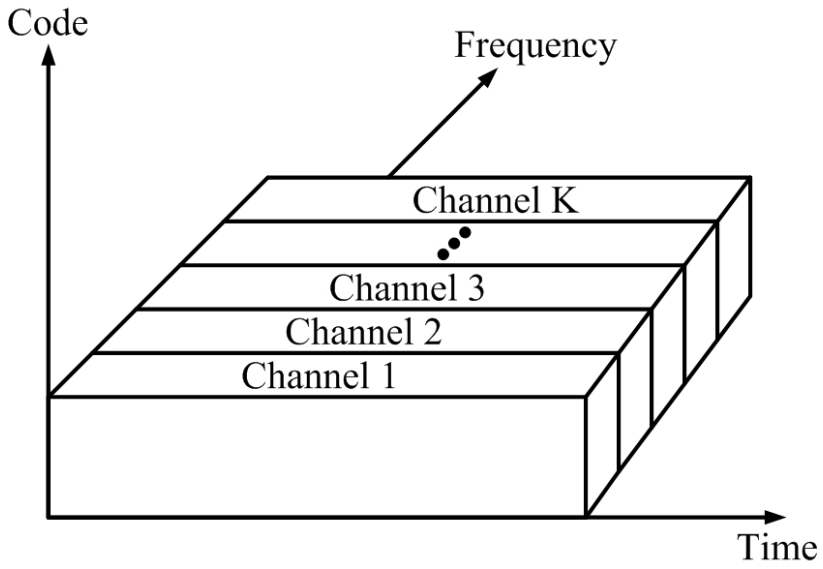

Figure 2.5: Frequency-division multiple access.

In CDMA, the information signals from different users are modulated by orthogonal spreading codes, e.g., interim standard 95 (IS-95) in the 2G and wideband-CDMA (WCDMA) in the third-generation (3G) wireless communication systems. The resulting spread signals simultaneously occupy the same bandwidth at the same time, as shown in Fig. 2.6. The receiver exploits the spreading code structure to separate the different users. However, the system performance is limited by the numbers of code, i.e., 64 code channels in the downlink of IS-95 while it is interference-limited in the uplink.

2.5.2 Non-Orthogonal Multiple Access (NOMA)

In this section, we follow a similar approach as in [23] to discuss the basic knowledge of non-orthogonal multiple access (NOMA). Recently, NOMA has drawn a lot of attentions as an important enabling technique to fulfill the challenging requirements of the next generation wireless networks, such as massive connectivity, high spectral efficiency, and improved energy efficiency [82–88]. In

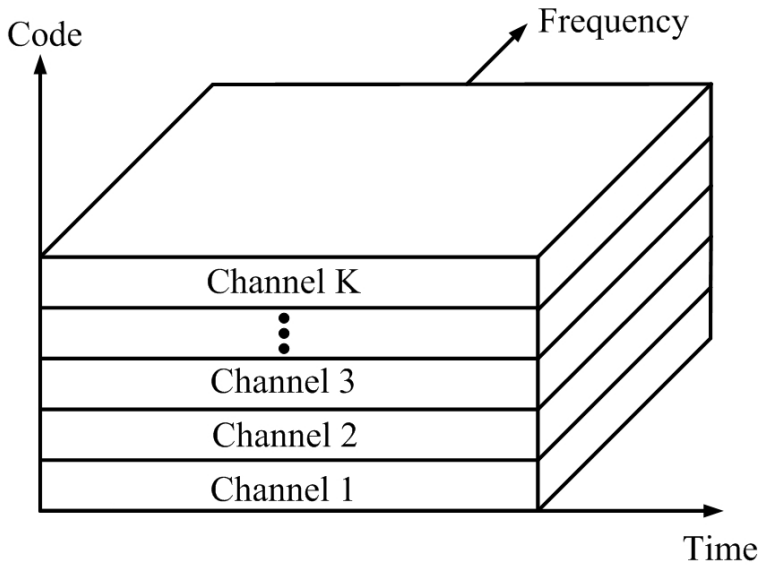

Figure 2.6: Code-division multiple access.

contrast to conventional orthogonal multiple access (OMA) schemes, NOMA allows multiple users to share the same degrees of freedom (DoF) via power-domain and/or code-domain multiplexing at transmitter side and to perform multi-user detection (MUD) at receiver side to retrieve the messages of multiple users [83–85]. One can refer to various survey papers in [83–85] for more details. It is known that NOMA is beneficial to supporting a large number of connections to achieve resource allocation fairness by introducing controllable symbol collisions in the same DoF. In recent years, NOMA has been extensively studied in the literature, e.g., [10, 89–93] and it has been shown that NOMA can achieve a considerable performance gain over conventional OMA schemes in terms of spectral efficiency and energy efficiency. In fact, the concept of non-orthogonal transmissions can be dated back to the 1990s, e.g., [94, 95], which serves as a foundation for the recent development of NOMA [36, 96–98]. However, NOMA has rekindled the interests of researchers, due to the benefit of the recent advances in signal processing and silicon technologies [99, 100]. For example, the industrial

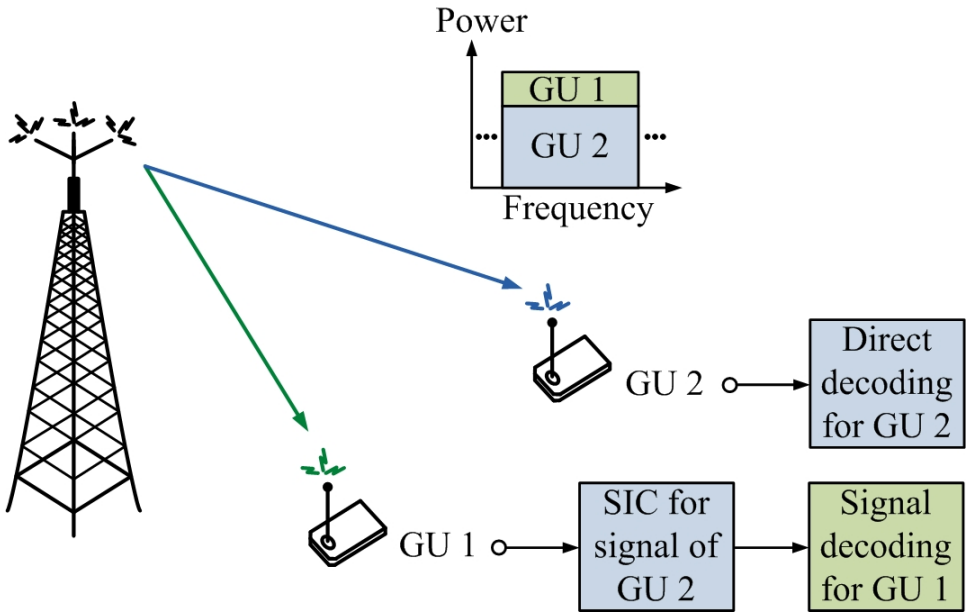

Figure 2.7: A downlink NOMA system model.

community has proposed up to 16 various forms of NOMA as the potential multiple access schemes for the fifth-generation (5G) networks [101]. Specifically, the NOMA can be applied on the top of other multiple access protocols.

Fig. 2.7 illustrates a multi-carrier downlink NOMA system with one base station (BS) and two GUs. In this NOMA system, each subcarrier is multiplexed with two users concurrently. According to the conventional approach, for GU 1 who has a better channel quality, it should decode and remove the messages of GU 2 via successive interference cancelation (SIC) before it decodes its own signal. The power allocation of GU 2 is higher than GU 1 to facilitate decoding.

The application of NOMA to UAVs wireless communication systems have various advantages, compared with the non-scalable OMA scheme. In particular, NOMA allows UAVs to reuse the resource blocks which already occupied by ground users, thus increasing the number of air users that can be supported even in the case of a high ground user density. For the case where all users located on the ground, the mobility of the UAV can fully adopt near-farness pairing of

the GUs to transmit information, which strongly improve the DoF for resource allocation design.

2.6 Optimization and Resource Allocation Designs

In UAV wireless communications, resource allocation is the concept of making the best use of limited communication resources based on the information available at the resource allocator to improve the system performance, as shown in Fig. 2.8. Specifically, resource allocation designs rely on the application of the optimization theory to optimize the system performance taking into account various quality of service (QoS) constraints. The available information at the resource allocator usually includes the channel state information (CSI), the transmit power budget, the UAV's trajectory design, and the available bandwidth as well as time resources. Typically, the resource allocation design objectives are maximizing the system sum-rate [32, 88, 102], maximizing the system energy efficiency [19, 20, 53], or minimizing the system power consumption [93, 103, 104]. In the following, we adopt a similar approach as in [23] to discuss the basic knowledge of resource allocation for wireless communication systems with UAV.

2.6.1 Design Objectives

In the following, we briefly introduce three kinds of design objectives commonly used in the literature.

System Sum-rate Maximization

Considering a communication system with K users, the objective function for

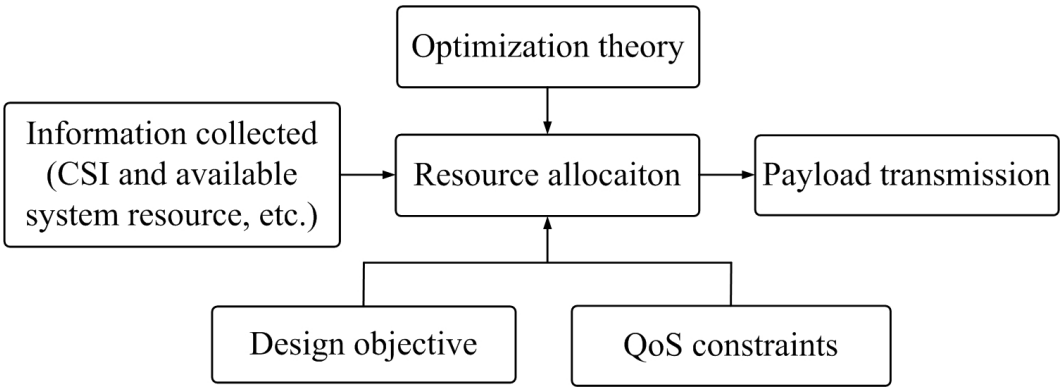

Figure 2.8: Optimization-based resource allocation design framework.

maximizing the system sum-rate is given by

$$\mathcal{P}_1 : \underset{\mathbf{x}\in\mathcal{S}}{\text{maximize}} \sum_{k=1}^{K} R_k\left(\mathbf{x}\right), \tag{2.14}$$

where $\mathbf{x} \in \mathbb{C}^{n\times n}$ denotes the optimization variables, e.g., power allocation, user scheduling and UAV's trajectory, and $\mathcal{S}$ represents the feasible solution set. The individual transmission data rate of user k can be expressed as $R_k(\mathbf{x})$.

System Power Consumption Minimization

When the resource allocation design is applied to minimize the system total power consumption, the objective function is given by

$$\mathcal{P}_2 : \underset{\mathbf{x}\in\mathcal{S}}{\text{minimize}} \sum_{k=1}^{K} p_k(\mathbf{x}) + P_{\text{flight}}(\mathbf{x}), \tag{2.15}$$

where $p_k(\mathbf{x})$ and $P_{\text{flight}}(\mathbf{x})$ represent the transmit power for user k and the flight power consumption of the UAV, respectively, which are functions of optimization variables $\mathbf{x}$, e.g., user scheduling, power allocation, UAV's trajectory, and rate allocation, etc. The power consumption minimization as the objective function is adopted in Chapter 4 and Chapter 5 of this thesis.

System Energy Efficiency Maximization

When the resource allocation design is applied to maximize the system energy efficiency, the objective function is given by

$$\mathcal{P}_3 : \underset{\mathbf{x}\in\mathcal{S}}{\text{maximize}} \ \frac{\sum_{k=1}^{K} R_k(\mathbf{x})}{\sum_{k=1}^{K} \left(\delta p_k(\mathbf{x}) + P_{\mathrm{C},k}\right) + P_{\text{flight}}(\mathbf{x})}. \tag{2.16}$$

In the denominator, $\frac{1}{\delta}$ and $P_{\mathrm{C},k}$, represent the efficiency of the power amplifier of the transmit antenna and the static circuit power consumption associated with user k, respectively. The system energy-efficiency as the objective function is adopted in Chapter 3.

2.6.2 QoS Constraint

To satisfy diverse QoS requirements for different applications, different types of QoS constraints can be incorporated in the problem formulation of resource allocation designs. In fact, QoS constraints combined with the system resource limitations usually span the feasible solution set $\mathcal{S}$ for the optimization variable, i.e., $\mathbf{x} \in \mathcal{S}$. In general, the minimum data rate constraint commonly adopted in the literature is introduced in the following.

Minimum Data Rate Requirement

The minimum data rate requirement limits the minimum data rate $R_k^{\min}$ for user k, i.e.,

$$R_k(\mathbf{x}) \geq R_k^{\min}, \tag{2.17}$$

where $R_k^{\min}$ is usually preset and obtained during the information collection phase in Fig. 2.8. The minimum data rate requirement is imposed for resource allocation design to guarantee the QoS of each user. Hence, introducing a minimum data rate requirement can effectively balance the system performance and each user's QoS requirement, which will be adopted in Chapters $3-5$ of this

thesis.

2.6.3 Channel Uncertainty Model

The robust resource allocation design is necessary to offer wireless communication systems to against the channel uncertainty. In this part, we introduce two models for the robust communications adopted in this thesis, i.e., the probabilistic model and the worst case model.

Probabilistic Model

For the probabilistic model, the channel uncertainty can be expressed as:

$$\mathbf{h} = \hat{\mathbf{h}} + \Delta\mathbf{h}, \tag{2.18}$$

where $\Delta\mathbf{h} \in \mathbb{C}^{n\times 1} \sim \mathcal{CN}(\mu, \sigma^2)$ denotes the distribution of the channel uncertainty, which is adopted in Chapter 5 of the thesis and the commonly adopted the related outage probability constraint is introduced in the following.

Outage Probability Requirement

For a communication system with imperfect CSI at transmitter side, there exists a non-zero probability that the scheduled data rate exceeds the instantaneous channel capacity. In this case, even applying powerful error correction coding cannot prevent packet error and thus an outage occurs. As a result, the outage probability for the communication link of user k for given estimated channel $\hat{\mathbf{h}}$ can be defined as

$$\mathrm{P}_{\mathrm{out},k}(\mathbf{x}) = \Pr\{C_k(\mathbf{x}) < R_k(\mathbf{x})|\hat{\mathbf{h}}\}, \tag{2.19}$$

where $R_k(\mathbf{x})$ is the allocated data rate for user k and $C_k(\mathbf{x})$ is the channel capacity of the communication link for user k. They both depend on the resource

allocation policy and the channel fading between the UAV and the users. Thus the outage probability is a function of the resource allocation variables and UAV's trajectory, i.e., $\mathbf{x}$. The outage probability constraint has been employed for resource allocation design to enhance the communication reliability [93, 105]. In particular, the outage probability of user k should be smaller than the maximum tolerable outage probability $\overline{\mathrm{P}}_{\mathrm{out},k}$, i.e.,

$$\mathrm{P}_{\mathrm{out},k}\left(\mathbf{x}\right) \leq \overline{\mathrm{P}}_{\mathrm{out},k}. \tag{2.20}$$

This probabilistic constraint takes the CSI imperfectness into consideration and hence is very useful for robust resource allocation in wireless communications. We note that the robust resource allocation design based on outage probability only needs to know the statistical CSI at the transmitter, rather than the instantaneous CSI. This makes the outage-constrained resource allocation design more practical since statistical CSI is usually available based on the long term measurements and does not change so fast as the instantaneous CSI. The outage probability requirement will be adopted in Chapter 5 of this thesis.

Worst-Case Model

For the worst case model, the channel uncertainty can be expressed as the same function in (2.18), where $|\Delta\mathbf{h}| \leq \rho$ denotes the channel estimation error. $\rho \geq 0$ represents the maximum value of the estimation error. The worst case model will be adopted in Chapter 3 of this thesis.

2.7 Summary

In this chapter, we present the background materials on wireless communications and resource allocation which are closely related to and required by the research

work in this thesis. The main points presented in this chapter are summarized as follows.

- We briefly introduced the adopted UAV's flight power consumption model.
- We introduced the channel fading in wireless communications and presented the typical channel models adopted in the later chapters.
- We provided some basic knowledge and definitions on the system energy efficiency.
- We also presented the optimization-based resource allocation design framework, including the commonly adopted design objectives and the QoS constraints.

Chapter 3

Joint Trajectory and Resource Allocation Design for Energy-Efficient Secure UAV Communication Systems

3.1 Introduction

In this chapter, we study the joint trajectory, resource allocation, and jamming policy design for energy-efficient secure unmanned aerial vehicle (UAV)-orthogonal frequency division multiple access (OFDMA) communication systems. In particular, an information UAV provides energy-efficient secure communication for multiple legitimate users adopting OFDMA in the existence of multiple eavesdroppers, with the assistance of a multiple-antenna jammer UAV patrolling with a fixed trajectory. The joint design is formulated as a non-convex optimization problem to maximize the system energy efficiency taking into

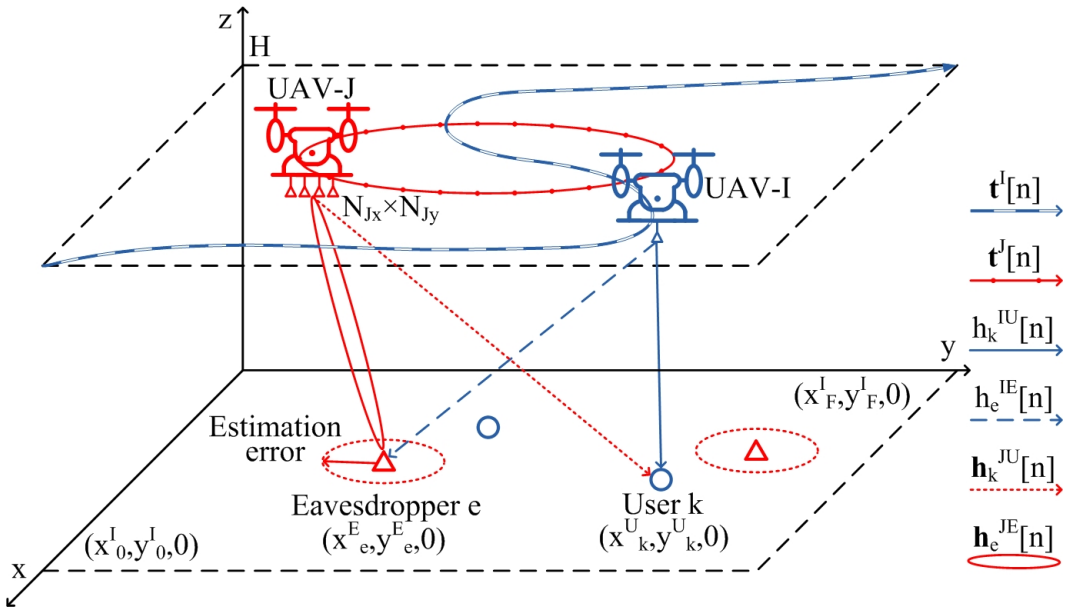

Figure 3.1: A UAV-OFDMA system with a multi-antenna jammer UAV, multiple legitimate users, and multiple potential eavesdroppers. The dotted circles denote the uncertainty of the eavesdroppers.

account the maximum tolerable leakage signal-to-interference-plus-noise ratio (SINR) to eavesdroppers and the minimum individual user data rate requirement. Since the formulated problem is non-convex which is generally intractable, we propose an iterative algorithm to achieve a suboptimal solution of the formulated problem. To this end, we first divide the formulated problem into two sub-problems and solve them alternatively via alternating optimization. In each iteration, a suboptimal solution can be achieved by employing successive convex approximation (SCA) and the Dinkelbach method with fast convergence.

3.2 System Model

A UAV-based OFDMA[1] communication system is considered which consists of a UAV serving as an information transmitter, K legitimate users, and another UAV serving as a jammer to combat E non-cooperative potential eavesdroppers, as shown in Fig. 3.1. The information UAV, the legitimate users, and the potential eavesdroppers are single-antenna devices. On the other hand, we assume that the jammer UAV is equipped with $N_{\mathrm{J}} = N_{\mathrm{J}x} \times N_{\mathrm{J}y}$ antennas such that $N_{\mathrm{J}} > E$. Besides, artificial noise is generated from the jammer UAV and is steered towards eavesdroppers for ensuring communication security. To facilitate the system design and simplicity, the jammer UAV patrols the service area with a fixed trajectory and a constant flight velocity[2] Note that although the jammer UAV cruises with a defined trajectory, it can generate focused artificial noise to interference the eavesdroppers via exploiting the spatial degrees of freedom (DoF) brought by the multiple antennas. We assume that the total bandwidth and the time duration of the system are divided equally into N_{F} subcarriers and N time slots, respectively. Besides, in the system, we assume that the information UAV and the jammer UAV operate at a constant altitude[3] H and all the ground

[1]In this chapter, we consider a more general problem formulation where user scheduling is performed in subcarrier-level. This study is applicable to the special case where resource allocation is performed in resource block levels.

[2]In this paper, we assume that the jammer UAV has a fixed trajectory and a constant flight velocity to simplify the design of resource allocation. Note that the proposed framework can achieve a superior performance compared to existing designs, e.g., [35,44], as will be verified in the simulation section. Optimizing multi-antenna information UAVs trajectory is an interesting but challenging work and will be considered in our future study.

[3]We note that since the channel between the UAV and the ground terminals are LoS dominated [44, 57, 58], the UAVs would fly at the lowest allowable flight altitude to obtain a higher channel gain for maximizing the system energy efficiency. Thus, we consider a fixed UAVs' flight altitude of $H = 100$ m. Since the constant flight altitude does not affect our design, it can be easily extended to different scenarios when the information UAV and the jammer UAV have different flight altitudes. The design of variable H is an interesting topic which will be left for future work.

nodes, i.e., legitimate users and eavesdroppers, are fixed during N time slots. To facilitate secure communication, artificial noise is generated $\mathbf{z}_i^{\mathrm{J}}[n] \in \mathbb{C}^{N_{\mathrm{J}} \times 1}$ on subcarrier $i \in \{1, \ldots, N_{\mathrm{F}}\}$ at time slot $n \in \{1, \ldots, N\}$ by the jammer UAV. Note that the duration of each time slot n is denoted by τ. Furthermore, we assume that $\mathbf{z}_i^{\mathrm{J}}[n]$ can be modeled by a complex Gaussian random vector:

$$\mathbf{z}_i^{\mathrm{J}}[n] \sim \mathcal{CN}(\mathbf{0}, \mathbf{Z}_i^{\mathrm{J}}[n]), \tag{3.1}$$

where $\mathbf{Z}_i^{\mathrm{J}}[n] \in \mathbb{H}^{N_{\mathrm{J}}}$ with $\mathbf{Z}_i^{\mathrm{J}}[n] \succeq \mathbf{0}$ represents the covariance matrix of the artificial noise on subcarrier i at time slot n. The artificial noise signal $\mathbf{z}_i^{\mathrm{J}}[n]$ is unknown to both the legitimate receivers and the potential eavesdroppers. We introduce a multi-antenna jammer UAV to assist the UAV-based communication system to guarantee secure communication. Although the additional artificial noise generated by the jammer UAV may cause interference to legitimate ground users, the artificial noise is optimized and mainly focused on the eavesdroppers. If the jamming does not improve the system performance, the proposed optimization framework will set $\mathbf{Z}_i^{\mathrm{J}}[n] = \mathbf{0}$ automatically to shut down the artificial noise transmission. In the considered system, the air-to-ground channel is dominated by line-of-sight (LoS) links with a reasonable flight height and all size [106, 107]. To simplify the design in the sequel, we assume that the channel is modeled by pure LoS links as commonly adopted in the literature, e.g., [1, 38, 43, 57]. As the UAV communication channel is dominated by the LoS links[4], the channel state information (CSI) between each node and each UAV can be determined by its location [4, 43, 44, 57, 58, 108]. Besides, the desired ground

[4]Based on field measurements [106, 107], the air-to-ground links between the UAVs and the ground terminals are LoS channels in rural areas when the flight altitude of a UAV is 100 meters and the length of side of the service area is 500 meters. Besides, the adopted LoS model can facilitate the design of resource allocation and trajectory in the sequel.

node users perform handshaking with the system regularly such that accurate location information is available for resource allocation design. In contrast, since potential eavesdroppers are usually less active in the systems, we assume that only the estimations of their locations are available. Thus, the distances between the information UAV and user $k \in \{1, \ldots, K\}$ as well as the jammer UAV[5] and user k at time slot n are given by

$$d_k^{\mathrm{IU}}[n] = \sqrt{\|\mathbf{t}_k^{\mathrm{U}} - \mathbf{t}^{\mathrm{I}}[n]\|^2 + H^2} \text{ and} \tag{3.2}$$

$$d_k^{\mathrm{JU}}[n] = \sqrt{\|\mathbf{t}_k^{\mathrm{U}} - \mathbf{t}^{\mathrm{J}}[n]\|^2 + H^2}, \tag{3.3}$$

respectively. $\mathbf{t}_k^{\mathrm{U}} = [x_k^{\mathrm{U}}, y_k^{\mathrm{U}}]^{\mathrm{T}} \in \mathbb{R}^{2\times 1}$ represents the location of ground user k, $\mathbf{t}^{\mathrm{I}}[n] = [x^{\mathrm{I}}[n], y^{\mathrm{I}}[n]]^{\mathrm{T}} \in \mathbb{R}^{2\times 1}$ and $\mathbf{t}^{\mathrm{J}}[n] = [x^{\mathrm{J}}[n], y^{\mathrm{J}}[n]]^{\mathrm{T}} \in \mathbb{R}^{2\times 1}$ represent the horizontal location of the information UAV and the jammer UAV at time slot n, respectively. Similarly, the distance between the information UAV and potential eavesdropper $e \in \{1, \ldots, E\}$ is given by

$$d_e^{\mathrm{IE}}[n] = \sqrt{\|\hat{\mathbf{t}}_e^{\mathrm{E}} + \Delta\mathbf{t}_e^{\mathrm{E}} - \mathbf{t}^{\mathrm{I}}[n]\|^2 + H^2} \tag{3.4}$$

and the distance between the jammer UAV and eavesdropper e at time slot n is given by

$$d_e^{\mathrm{JE}}[n] = \sqrt{\|\hat{\mathbf{t}}_e^{\mathrm{E}} + \Delta\mathbf{t}_e^{\mathrm{E}} - \mathbf{t}^{\mathrm{J}}[n]\|^2 + H^2}, \tag{3.5}$$

where $\hat{\mathbf{t}}_e^{\mathrm{E}} = [\hat{x}_e^{\mathrm{E}}, \hat{y}_e^{\mathrm{E}}]^{\mathrm{T}} \in \mathbb{R}^{2\times 1}$ represents the estimated location of potential eavesdropper e and $\Delta\mathbf{t}_e^{\mathrm{E}} = [\Delta x_e^{\mathrm{E}}, \Delta y_e^{\mathrm{E}}]^{\mathrm{T}} \in \mathbb{R}^{2\times 1}$ denotes the estimation error of

[5]We assume that all the antennas have roughly the same distance between the jammer UAV and user k. In fact, this assumption generally holds as antenna separation at the jammer is generally much shorter compared to the distance between the jammer UAV and ground users.

Table 3.1: Notations and physical meaning of variables in power consumption model.

Notations	Physical meaning
Ω	Blade angular velocity in radians/second
r	Rotor radius in meter
ρ	Air density in kg/m^3
s	Rotor solidity in m^3
A_{r}	Rotor disc area in m^2
P_o	Blade profile power in hovering status in watt
P_i	Induced power in hovering status in watt
v_0	Mean rotor induced velocity in forwarding flight in m/s
d_0	Fuselage drag ratio

$\hat{\mathbf{t}}_e^{\mathrm{E}}$. Without loss of generality, we assume that the estimation error satisfies [44]

$$\|\Delta \mathbf{t}_e^{\mathrm{E}}\|^2 \leq (Q_e^{\mathrm{E}})^2, \tag{3.6}$$

where Q_e^{E} is the radius defining the circular uncertain region centered at the estimated location of eavesdropper e. In this chapter, we adopt this worst case model instead of the probabilistic model [19] as the probabilistic model can be easily converted to the deterministic model under some mild conditions [109].

3.2.1 UAV Power Consumption Model

To facilitate the design of energy-efficient resource allocation, the system power consumption is defined as follows. The flight power consumption for the rotary-wing UAV is a function of its flight velocity. In particular, the flight power consumption models of the information UAV and the jammer UAV are given

by [3]:

$$P^{\mathrm{I}}_{\mathrm{flight}}[n] = P_o\left(1+\frac{3\|\mathbf{v}^{\mathrm{I}}[n]\|^2}{\Omega^2 r^2}\right) + \frac{P_i v_0}{\|\mathbf{v}^{\mathrm{I}}[n]\|} + \frac{1}{2}d_0\rho s A_{\mathrm{r}}\|\mathbf{v}^{\mathrm{I}}[n]\|^3 \text{ and} \tag{3.7}$$

$$P^{\mathrm{J}}_{\mathrm{flight}}[n] = P_o\left(1+\frac{3\|\mathbf{v}^{\mathrm{J}}[n]\|^2}{\Omega^2 r^2}\right) + \frac{P_i v_0}{\|\mathbf{v}^{\mathrm{J}}[n]\|} + \frac{1}{2}d_0\rho s A_{\mathrm{r}}\|\mathbf{v}^{\mathrm{J}}[n]\|^3, \tag{3.8}$$

respectively, where $\mathbf{v}^{\mathrm{I}}[n] = [v^{\mathrm{I}}_x[n], v^{\mathrm{I}}_y[n]]^{\mathrm{T}} \in \mathbb{R}^{2\times 1}$ and $\mathbf{v}^{\mathrm{J}}[n] = [v^{\mathrm{J}}_x[n], v^{\mathrm{J}}_y[n]]^{\mathrm{T}} \in \mathbb{R}^{2\times 1}$. The notations and the physical meanings of the variables in (3.7) and (3.8) are summarized in Table 3.1. We can observe that the flight power consumption is a convex function with respect to (w.r.t.) the flight velocity for both the information UAV and the jammer UAV. In this work, we assume that the trajectory of the jammer UAV follows a fixed path with a fixed velocity [110]. In fact, $\mathbf{v}^{\mathrm{J}}[n]$ is selected by the most energy-efficient flying velocity according to the setting in [3]. Since the jammer UAV is equipped with an antenna array, the beamformed artificial noise can combat the channels of eavesdroppers deliberately for providing secure communication to legitimate users. The total power consumption of the information UAV and the jammer UAV at time slot n in Joules-per-second (J/sec) includes the communication power and the flight power which can be modeled as

$$P^{\mathrm{I}}_{\mathrm{total}}[n] = \underbrace{\sum_{k=1}^{K}\sum_{i=1}^{N_{\mathrm{F}}} s^{\mathrm{I}}_{k,i}[n]p^{\mathrm{I}}_{k,i}[n]\zeta^{\mathrm{I}}}_{\text{Information signals power}} + P^{\mathrm{I}}_{\mathrm{C}} + P^{\mathrm{I}}_{\mathrm{flight}}[n] \text{ and} \tag{3.9}$$

$$P^{\mathrm{J}}_{\mathrm{total}}[n] = \underbrace{\sum_{i=1}^{N_{\mathrm{F}}} \mathrm{Tr}(\mathbf{Z}^{\mathrm{J}}_i[n])}_{\text{Jamming signals power}} \zeta^{\mathrm{J}} + P^{\mathrm{J}}_{\mathrm{C}} + P^{\mathrm{J}}_{\mathrm{flight}}[n], \tag{3.10}$$

respectively. The constants $\zeta^{\mathrm{I}}, \zeta^{\mathrm{J}} \geq 1$ denote the power inefficiency of the power amplifier at the information UAV and the jammer UAV, respectively. Variable

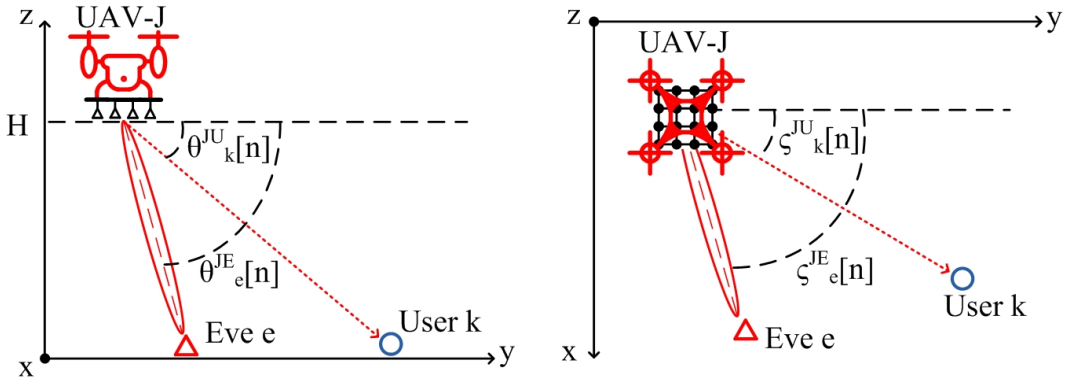

Figure 3.2: Downlink LoS channel model between the jammer UAV and the ground terminals. The left hand side figure shows the vertical AoDs, $\theta_k^{\mathrm{JU}}[n]$ and $\theta_e^{\mathrm{JE}}[n]$, for user k and eavesdropper e, respectively. The right hand side figure shows the horizontal AoDs, $\varsigma_k^{\mathrm{JU}}[n]$ and $\varsigma_e^{\mathrm{JE}}[n]$, for user k and eavesdropper e, respectively.

$p_{k,i}^{\mathrm{I}}[n]$ denotes the information transmit power allocation for user k on subcarrier i at time slot n. $P_{\mathrm{C}}^{\mathrm{I}}$ and $P_{\mathrm{C}}^{\mathrm{J}}$ denote the constant circuit power consumptions of the information UAV and the jammer UAV, respectively. The binary variable $s_{k,i}^{\mathrm{I}}[n] = 1$ represents that subcarrier i is assigned to user k at time slot n. Otherwise, $s_{k,i}^{\mathrm{I}}[n] = 0$.

3.2.2 Downlink Channel Model

We assume that the channels from the UAVs to all ground receivers are dominated by the LoS paths and the Doppler effect is well compensated. Thus, the channel power gain between the information UAV and user k as well as eavesdropper e at time slot n can be characterized by the commonly adopted free-space path loss model, [3, 31], which are given by

$$h_k^{\mathrm{IU}}[n] = \frac{\beta_0}{(d_k^{\mathrm{IU}}[n])^2} = \frac{\beta_0}{\|\mathbf{t}_k - \mathbf{t}^{\mathrm{I}}[n]\|^2 + H^2} \text{ and} \tag{3.11}$$

$$h_e^{\mathrm{IE}}[n] = \frac{\beta_0}{(d_e^{\mathrm{IE}}[n])^2} = \frac{\beta_0}{\|\hat{\mathbf{t}}_e + \Delta\mathbf{t}_e - \mathbf{t}^{\mathrm{I}}[n]\|^2 + H^2}, \tag{3.12}$$

respectively. The constant β_0 represents the channel power gain at a reference distance. Besides, the channel vectors between the jammer UAV and user k as well as between eavesdropper e at time slot n are given by

$$\mathbf{h}_k^{\mathrm{JU}}[n] = \left(1, e^{-\mathrm{j}\frac{2\pi\Delta_{\mathrm{J}}}{\lambda_{\mathrm{c}}}\sin\theta_k^{\mathrm{JU}}[n]\cos\varsigma_k^{\mathrm{JU}}[n]}, \dots e^{-\mathrm{j}\frac{2\pi\Delta_{\mathrm{J}}}{\lambda_{\mathrm{c}}}\sin\theta_k^{\mathrm{JU}}[n](N_{\mathrm{J}x}-1)\cos\varsigma_k^{\mathrm{JU}}[n]}\right)^{\mathrm{T}} \otimes \left(1, e^{-\mathrm{j}\frac{2\pi\Delta_{\mathrm{J}}}{\lambda_{\mathrm{c}}}\sin\theta_k^{\mathrm{JU}}[n]\sin\varsigma_k^{\mathrm{JU}}[n]}, \dots e^{-\mathrm{j}\frac{2\pi\Delta_{\mathrm{J}}}{\lambda_{\mathrm{c}}}\sin\theta_k^{\mathrm{JU}}[n](N_{\mathrm{J}y}-1)\sin\varsigma_k^{\mathrm{JU}}[n]}\right)^{\mathrm{T}} \quad (3.13)$$

and

$$\mathbf{h}_e^{\mathrm{JE}}[n] = \left(1, e^{-\mathrm{j}\frac{2\pi\Delta_{\mathrm{J}}}{\lambda_{\mathrm{c}}}\sin\theta_e^{\mathrm{JE}}[n]\cos\varsigma_e^{\mathrm{JE}}[n]}, \dots e^{-\mathrm{j}\frac{2\pi\Delta_{\mathrm{J}}}{\lambda_{\mathrm{c}}}\sin\theta_e^{\mathrm{JE}}[n](N_{\mathrm{J}x}-1)\cos\varsigma_e^{\mathrm{JE}}[n]}\right)^{\mathrm{T}} \otimes \left(1, e^{-\mathrm{j}\frac{2\pi\Delta_{\mathrm{J}}}{\lambda_{\mathrm{c}}}\sin\theta_e^{\mathrm{JE}}[n]\sin\varsigma_e^{\mathrm{JE}}[n]}, \dots e^{-\mathrm{j}\frac{2\pi\Delta_{\mathrm{J}}}{\lambda_{\mathrm{c}}}\sin\theta_e^{\mathrm{JE}}[n](N_{\mathrm{J}y}-1)\sin\varsigma_e^{\mathrm{JE}}[n]}\right)^{\mathrm{T}}, \quad (3.14)$$

respectively[6] [79], [111]. λ_{c} represents the wavelength of the carrier center frequency and Δ_{J} is the antenna separation at the jammer UAV. $N_{\mathrm{J}x}$ and $N_{\mathrm{J}y}$ represent the number of the rows and columns of the antenna array. As shown in Fig. 3.2, $\theta_k^{\mathrm{JU}}[n]$ and $\theta_e^{\mathrm{JE}}[n]$ denote the vertical angle of departure (AoD) from the jammer antenna array to user k and eavesdropper e, respectively. $\varsigma_k^{\mathrm{JU}}[n]$ and $\varsigma_e^{\mathrm{JE}}[n]$ denote the horizontal AoD from the jammer antenna array to user k and eavesdropper e, respectively. We note that $\sin\theta_k^{\mathrm{JU}}[n] = \frac{H}{\sqrt{\|\mathbf{t}_k^{\mathrm{U}}-\mathbf{t}^{\mathrm{J}}[n]\|^2+H^2}}$, $\sin\theta_e^{\mathrm{JE}}[n] = \frac{H}{\sqrt{\|\hat{\mathbf{t}}_e^{\mathrm{E}}+\Delta\mathbf{t}_e^{\mathrm{E}}-\mathbf{t}^{\mathrm{J}}[n]\|^2+H^2}}$, $\sin\varsigma_k^{\mathrm{JU}}[n] = \frac{\|x_k^{\mathrm{U}}-x^{\mathrm{J}}[n]\|}{\|\mathbf{t}_k^{\mathrm{U}}-\mathbf{t}^{\mathrm{J}}[n]\|}$, $\sin\varsigma_e^{\mathrm{JE}}[n] = \frac{\|\hat{x}_e^{\mathrm{E}}+\Delta x_e^{\mathrm{E}}-x^{\mathrm{J}}[n]\|}{\|\hat{\mathbf{t}}_e^{\mathrm{E}}+\Delta\mathbf{t}_e^{\mathrm{E}}-\mathbf{t}^{\mathrm{J}}[n]\|}$ $\cos\varsigma_k^{\mathrm{JU}}[n] = \frac{\|y_k^{\mathrm{U}}-y^{\mathrm{J}}[n]\|}{\|\mathbf{t}_k^{\mathrm{U}}-\mathbf{t}^{\mathrm{J}}[n]\|}$, and $\cos\varsigma_e^{\mathrm{JE}}[n] = \frac{\|\hat{y}_e^{\mathrm{E}}+\Delta y_e^{\mathrm{E}}-y^{\mathrm{J}}[n]\|}{\|\hat{\mathbf{t}}_e^{\mathrm{E}}+\Delta\mathbf{t}_e^{\mathrm{E}}-\mathbf{t}^{\mathrm{J}}[n]\|}$. Specifically, the multi-antenna wireless channel between the jammer UAV and the potential eavesdroppers captures the location uncertainty

[6]Note that $\mathbf{h}_k^{\mathrm{JU}}[n]$ and $\mathbf{h}_e^{\mathrm{JE}}[n]$ are known when the jammer UAV has a fixed trajectory.

in $\cos\varsigma_e^{\mathrm{JE}}[n]$. For notational simplicity, we define

$$\mathbf{H}_k^{\mathrm{JU}}[n] = \mathbf{h}_k^{\mathrm{JU}}[n](\mathbf{h}_k^{\mathrm{JU}}[n])^{\mathrm{H}} \text{ and} \tag{3.15}$$

$$\mathbf{H}_e^{\mathrm{JE}}[n] = \mathbf{h}_e^{\mathrm{JE}}[n](\mathbf{h}_e^{\mathrm{JE}}[n])^{\mathrm{H}}, \tag{3.16}$$

where $\mathbf{H}_k^{\mathrm{JU}}[n] \succeq \mathbf{0}$, $\mathbf{H}_e^{\mathrm{JE}}[n] \succeq \mathbf{0}$, $\mathbf{H}_k^{\mathrm{JU}}[n] \in \mathbb{H}^{N_{\mathrm{J}}}$, and $\mathbf{H}_e^{\mathrm{JE}}[n] \in \mathbb{H}^{N_{\mathrm{J}}}$. Subsequently, the received interference power from the jammer UAV to users and eavesdroppers can be written as $\mathrm{Tr}(\mathbf{H}_k^{\mathrm{JU}}[n]\mathbf{Z}_i^{\mathrm{J}}[n])$ and $\mathrm{Tr}(\mathbf{H}_e^{\mathrm{JE}}[n]\mathbf{Z}_i^{\mathrm{J}}[n])$, respectively.

3.3 Resource Allocation and Trajectory Design

3.3.1 System Achievable Rate and Energy Efficiency

The achievable data rate for user k on subcarrier i at time slot n is given by

$$R_{k,i}^{\mathrm{U}}[n] = W s_{k,i}^{\mathrm{I}}[n] \log_2(1 + \Gamma_{k,i}^{\mathrm{IU}}[n]), \tag{3.17}$$

where $\Gamma_{k,i}^{\mathrm{IU}}[n]$ denotes the received signal-to-interference-plus-noise ratio (SINR) at user k on subcarrier i in time slot n and it is given by

$$\Gamma_{k,i}^{\mathrm{IU}}[n] = \frac{p_{k,i}^{\mathrm{I}}[n] h_k^{\mathrm{IU}}[n]}{A_k^{\mathrm{U}}[n]\mathrm{Tr}(\mathbf{H}_k^{\mathrm{JU}}[n]\mathbf{Z}_i^{\mathrm{J}}[n]) + WN_0}, \tag{3.18}$$

where $A_k^{\mathrm{U}}[n] = \frac{\beta_0}{\|\mathbf{t}_k^{\mathrm{U}} - \mathbf{t}^{\mathrm{J}}[n]\|^2 + H^2}$ denotes the attenuation in the LoS path between the jammer UAV to user k at time slot n. W represents the subcarrier bandwidth and N_0 is the power spectral density of the additive white Gaussian noise (AWGN). On the other hand, the information data rate leakage to potential eavesdropper

e on subcarrier i for user k at time slot n is given by

$$R^{\mathrm{E}}_{k,e,i}[n] = W s^{\mathrm{I}}_{k,i}[n] \log_2(1 + \Gamma^{\mathrm{IE}}_{k,e,i}[n]), \tag{3.19}$$

where $\Gamma^{\mathrm{IE}}_{k,e,i}[n]$ denotes the received SINR at eavesdropper e on subcarrier i in time slot n and it is given by

$$\Gamma^{\mathrm{IE}}_{k,e,i}[n] = \frac{p^{\mathrm{I}}_{k,i}[n] h^{\mathrm{IE}}_e[n]}{A^{\mathrm{E}}_e[n] \mathrm{Tr}(\mathbf{H}^{\mathrm{JE}}_e[n] \mathbf{Z}^{\mathrm{J}}_i[n]) + W N_0}, \tag{3.20}$$

where $A^{\mathrm{E}}_e[n] = \frac{\beta_0}{\|\hat{\mathbf{t}}^{\mathrm{E}}_e + \Delta \mathbf{t}^{\mathrm{E}}_e - \mathbf{t}^{\mathrm{J}}[n]\|^2 + H^2}$ denotes the attenuation in the LoS path between the jammer UAV and eavesdropper e at time slot n. Clearly, the artificial noise generated by the jammer UAV interferes the channels of both legitimate user k and eavesdropper e.

Thus, the system energy efficiency in bits-per-Joule (bits/J) is defined as

$$\mathrm{EE}(\mathcal{A}, \mathcal{P}, \mathcal{Z}, \mathcal{T}_{\mathcal{I}}, \mathcal{V}_{\mathcal{I}}) = \frac{\sum_{n=1}^{N} \sum_{k=1}^{K} \sum_{i=1}^{N_{\mathrm{F}}} R^{\mathrm{U}}_{k,i}[n]}{\sum_{n=1}^{N} P^{\mathrm{I}}_{\mathrm{total}}[n] + P^{\mathrm{J}}_{\mathrm{total}}[n]}, \tag{3.21}$$

where $\mathcal{A} = \{s^{\mathrm{I}}_{k,i}[n], \forall k, i, n\}$ is the user scheduling variable set, $\mathcal{P} = \{p^{\mathrm{I}}_{k,i}[n], \forall k, i, n\}$ is the transmit power[7] variable set, $\mathcal{Z} = \{\mathbf{Z}^{\mathrm{J}}_i[n], \forall i, n\}$ is the covariance matrix set of the artificial noises, $\mathcal{T}_{\mathcal{I}} = \{\mathbf{t}^{\mathrm{I}}[n], \forall n\}$ is the set of the information UAV's trajectory variables, and $\mathcal{V}_{\mathcal{I}} = \{\mathbf{v}^{\mathrm{I}}[n], \forall n\}$ is the set of the information UAV's flight velocity variables.

[7]In the considered system, although the flight power consumption is larger than the communication power, optimizing both the flight power and the communication power consumption are important to improve the system energy efficiency and to guarantee communication security.

3.3.2 Optimization Problem Formulation

The energy-efficient design of user scheduling, transmit power allocation, UAVs' trajectory, and UAV's flight velocity is formulated as the following optimization problem[8]:

$$\underset{\mathcal{A},\mathcal{P},\mathcal{Z},\mathcal{T}_\mathcal{I},\mathcal{V}_\mathcal{I}}{\text{maximize}} \ \text{EE}(\mathcal{A},\mathcal{P},\mathcal{Z},\mathcal{T}_\mathcal{I},\mathcal{V}_\mathcal{I}) \tag{3.22}$$

$$\text{s.t. C1}: s^{\text{I}}_{k,i}[n] \in \{0,1\}, \forall k,i,n,$$

$$\text{C2}: \sum_{k=1}^{K} s^{\text{I}}_{k,i}[n] \leq 1, \forall i,n,$$

$$\text{C3a}: p^{\text{I}}_{k,i}[n] \geq 0, \forall k,i,n, \qquad \text{C3b}: \mathbf{Z}^{\text{J}}_i[n] \succeq \mathbf{0}, \forall i,n,$$

$$\text{C4a}: \sum_{k=1}^{K}\sum_{i=1}^{N_\text{F}} s^{\text{I}}_{k,i}[n]p^{\text{I}}_{k,i}[n] \leq P^{\text{I}}_{\text{peak}}, \forall n, \qquad \text{C4b}: \sum_{i=1}^{N_\text{F}} \text{Tr}(\mathbf{Z}^{\text{J}}_i[n]) \leq P^{\text{J}}_{\text{peak}}, \forall n,$$

$$\text{C5a}: P^{\text{I}}_{\text{total}}[n] \leq P^{\text{I}}_{\max}, \forall n, \qquad \text{C5b}: P^{\text{J}}_{\text{total}}[n] \leq P^{\text{J}}_{\max}, \forall n,$$

$$\text{C6}: \frac{1}{N}\sum_{n=1}^{N}\sum_{i=1}^{N_\text{F}} R^{\text{U}}_{k,i}[n] \geq R_{\min}, \forall k,$$

$$\text{C7}: \max_{\|\Delta\mathbf{t}^{\text{E}}_e\| \leq Q^{\text{E}}_e} \Gamma^{\text{IE}}_{k,e,i}[n] \leq \Gamma_{\text{th}}, \forall k,e,i,n,$$

$$\text{C8}: \mathbf{t}^{\text{I}}[0] = \mathbf{t}^{\text{I}}_0,$$

$$\text{C9}: \mathbf{t}^{\text{I}}[N] = \mathbf{t}^{\text{I}}_{\text{F}},$$

$$\text{C10}: \mathbf{t}^{\text{I}}[n+1] = \mathbf{t}^{\text{I}}[n] + \mathbf{v}^{\text{I}}[n]\tau, n = 1,...,N-1,$$

$$\text{C11}: \|\mathbf{v}^{\text{I}}[n]\| \leq V^{\text{I}}_{\max}, \forall n,$$

$$\text{C12}: \|\mathbf{v}^{\text{I}}[n+1] - \mathbf{v}^{\text{I}}[n]\| \leq V^{\text{I}}_{\text{acc}}, n = 1,...,N-1,$$

$$\text{C13}: \|\mathbf{t}^{\text{I}}[n] - \mathbf{t}^{\text{J}}[n]\|^2 \geq d^2_{\min}, \forall n.$$

[8]Note that the solution proposed in the chapter can be easily extended to the case of 3D aviation.

Note that C1 and C2 are user scheduling constraints such that each subcarrier can be assigned to at most one user at each time slot to avoid multiple access interference (MAI). C3a and C3b are the non-negative transmit power constraints for information and jammer UAVs, respectively. $P^{\mathrm{I}}_{\mathrm{peak}}$ and $P^{\mathrm{J}}_{\mathrm{peak}}$ in C4a and C4b are the peak transmit power for the information UAV and the jammer UAV at each time slot, respectively, which is limited by the output range of the corresponding power amplifier. Constants $P^{\mathrm{I}}_{\mathrm{max}}$ and $P^{\mathrm{J}}_{\mathrm{max}}$ in C5a and C5b are the maximum budget for total power consumption of information UAV and jammer UAV at each time slot, respectively, which are limited by the corresponding battery maximum output power. R_{min} in C6 denotes the minimum required individual user data rate over the whole flight duration. Γ_{th} in C7 is the maximum tolerable SINR threshold for eavesdropper e attempting to eavesdrop the information of user k on subcarrier i at timeslot n. Note that constraint C7 takes into account the location uncertainty of the potential eavesdroppers. C8 and C9 indicate the required UAV's initial and final locations, respectively. C10 draws the connections between the UAV's velocity and the displacement between two consecutive time slots for the information UAV[9]. $V^{\mathrm{I}}_{\mathrm{max}}$ in C11 is the maximum flight velocity constraint for the information UAV. $V^{\mathrm{I}}_{\mathrm{acc}}$ in constraint C12 is the maximum allowable acceleration for the information UAV in a given time slot. C13 limits the minimum distance between the information UAV and the jammer UAV to avoid possible collision.

Remark 1. *In the considered system, secure communication can be guaranteed when* $R_{\mathrm{min}} > \log_2(1+\Gamma_{\mathrm{th}}), \forall k$, *holds with a minimum secrecy rate given by* $R_{\mathrm{min}} - \log_2(1+\Gamma_{\mathrm{th}})$. *Compared to some works directly optimizing the system*

[9]Note that the flight velocity of a UAV can be expressed as a function of its trajectory for a given constant time slot duration τ. Yet, expressing the flight power consumption as a function of trajectory would complicate the resource allocation design. Therefore, we introduce the flight velocity variable $\mathbf{v}^{\mathrm{I}}[n]$ to simplify the problem formulation.

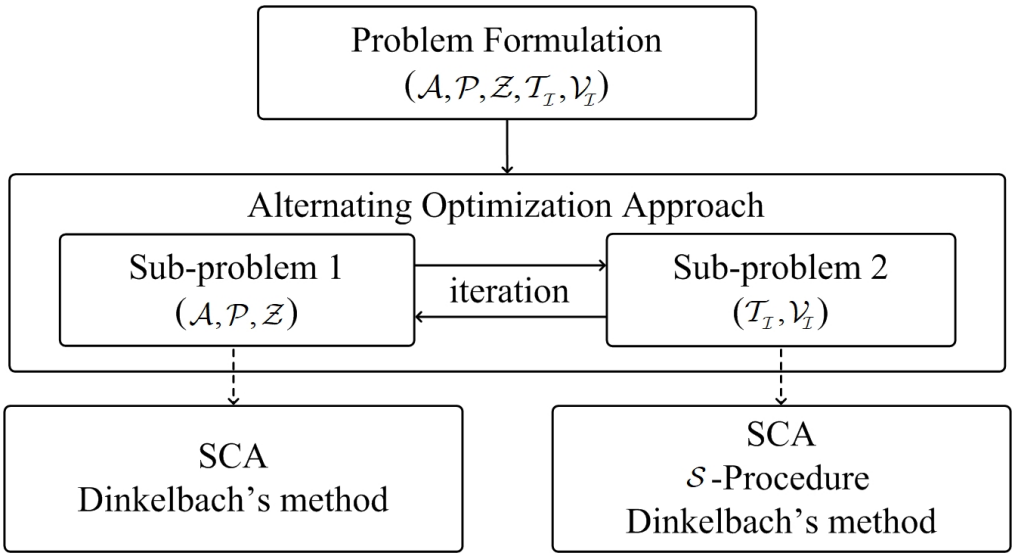

Figure 3.3: A flow chart of the proposed iterative algorithm.

secrecy rate, the parameters $R_{\min}$ *and* Γ_{th} *in our work are chosen by the system operator which can be adopted for different applications requiring different levels of communication security. This formulation provides flexibility in designing resource allocation algorithms and has been widely adopted, e.g., [11, 104].*

3.4 Problem Solution

The formulated problem in (3.22) is non-convex. In general, a brute force approach is required to obtain a globally optimal solution which is computationally intractable even for a moderate size of system. To facilitate a low computational complexity design of resource allocation and trajectory, we aim at designing an efficient suboptimal solution. In particular, the divide and conquer philosophy is adopted, where the global problem is divided into several subproblems and he subproblems are solved iteratively. In particular, we divide the problem (3.22) into two sub-problems and solve them iteratively utilizing the alternating optimization to achieve a suboptimal solution of the original problem [112].

Specifically, as shown in Fig. 3.3, sub-problem 1 optimizes the user scheduling, $\mathcal{A}$, the information transmit power allocation, $\mathcal{P}$, and the artificial noise, $\mathcal{Z}$, for a given feasible information UAV's trajectory, $\mathcal{T}_{\mathcal{I}}$, and its flight velocity, $\mathcal{V}_{\mathcal{I}}$. Sub-problem 2 aims to optimize the information UAV's trajectory, $\mathcal{T}_{\mathcal{I}}$, and its flight velocity, $\mathcal{V}_{\mathcal{I}}$, under a given feasible user scheduling, $\mathcal{A}$, transmit power allocation, $\mathcal{P}$, and artificial noise, $\mathcal{Z}$. The proof details on the convergence of the alternating optimization approach can be found in [112]. Now, we first study the solution of sub-problem 1.

3.4.1 Sub-problem 1: Optimizing User Scheduling, Communication Transmit Power Allocation, and Artificial Noise

For a given information UAV's trajectory $\mathcal{T}_{\mathcal{I}}$ and its flight velocity $\mathcal{V}_{\mathcal{I}}$, we can express sub-problem 1 as the following optimization problem:

$$\begin{aligned} \underset{\mathcal{A},\mathcal{P},\mathcal{Z}}{\text{maximize}} \ & \frac{\sum_{n=1}^{N}\sum_{k=1}^{K}\sum_{i=1}^{N_{\mathrm{F}}} R_{k,i}^{\mathrm{U}}[n]}{\sum_{n=1}^{N}\left(P_{\text{total}}^{\mathrm{I}}[n]+P_{\text{total}}^{\mathrm{J}}[n]\right)} \\ \text{s.t.} \ & \mathrm{C1}, \mathrm{C2}, \mathrm{C3a}-\mathrm{C5a}, \mathrm{C3b}-\mathrm{C5b}, \mathrm{C6}, \mathrm{C7}, \end{aligned} \tag{3.23}$$

where $R_{k,i}^{\mathrm{U}}[n]$ in (3.17) is a non-convex function w.r.t. the joint optimization of $s_{k,i}^{\mathrm{I}}[n]$, $p_{k,i}^{\mathrm{I}}[n]$, and $\mathbf{Z}_i^{\mathrm{J}}[n]$ since the division between $p_{k,i}^{\mathrm{I}}[n]$ and $\mathbf{Z}_i^{\mathrm{J}}[n]$. Thus, we can rewrite it to a substraction function as

$$\begin{aligned} R_{k,i}^{\mathrm{U}}[n] = & \, W s_{k,i}^{\mathrm{I}}[n] \log_2\left(\mathrm{Tr}(\mathbf{H}_k^{\mathrm{JU}}[n]\mathbf{Z}_i^{\mathrm{J}}[n]) + WN_0 + p_{k,i}^{\mathrm{I}}[n] h_k^{\mathrm{IU}}[n]\right) \\ & - W s_{k,i}^{\mathrm{I}}[n] \log_2\left(WN_0 + \mathrm{Tr}(\mathbf{H}_k^{\mathrm{JU}}[n]\mathbf{Z}_i^{\mathrm{J}}[n])\right). \end{aligned} \tag{3.24}$$

The problem in (3.23) is non-convex and the non-convexity arises from the objective function and constraints C1, C4a, C5a, C6, and C7. In order to solve sub-problem 1 in (3.23), we first handle the coupling of $s^{\mathrm{I}}_{k,i}[n]p^{\mathrm{I}}_{k,i}[n]$ and $s^{\mathrm{I}}_{k,i}[n]\mathbf{Z}^{\mathrm{J}}_{i}[n]$ by introduce two auxiliary variables $\tilde{p}^{\mathrm{I}}_{k,i}[n] = s^{\mathrm{I}}_{k,i}[n]p^{\mathrm{I}}_{k,i}[n], \forall k,i,n$, and $\tilde{\mathbf{Z}}^{\mathrm{J}}_{k,i}[n] = s^{\mathrm{I}}_{k,i}[n]\mathbf{Z}^{\mathrm{J}}_{i}[n], \forall k,i,n$. Then, by applying the big-M reformulation [97, 113, 114], the couplings are resolved by introducing the following equivalent constraints:

$$\begin{aligned}
&\mathrm{C14}: \tilde{p}^{\mathrm{I}}_{k,i}[n] \leq p^{\mathrm{I}}_{k,i}[n], \forall k,i,n,\\
&\mathrm{C15}: \tilde{p}^{\mathrm{I}}_{k,i}[n] \geq p^{\mathrm{I}}_{k,i}[n] - (1 - s^{\mathrm{I}}_{k,i}[n])P^{\mathrm{I}}_{\mathrm{peak}}, \forall k,i,n,\\
&\mathrm{C16}: \tilde{p}^{\mathrm{I}}_{k,i}[n] \geq 0, \forall k,i,n,\\
&\mathrm{C17}: \tilde{p}^{\mathrm{I}}_{k,i}[n] \leq s^{\mathrm{I}}_{k,i}[n]P^{\mathrm{I}}_{\mathrm{peak}}, \forall k,i,n,\\
&\mathrm{C18}: \tilde{\mathbf{Z}}^{\mathrm{J}}_{k,i}[n] \preceq \mathbf{Z}^{\mathrm{J}}_{i}[n], \forall k,i,n,\\
&\mathrm{C19}: \tilde{\mathbf{Z}}^{\mathrm{J}}_{k,i}[n] \succeq \mathbf{Z}^{\mathrm{J}}_{i}[n] - (1 - s^{\mathrm{I}}_{k,i}[n])P^{\mathrm{J}}_{\mathrm{peak}}\mathbf{I}_{N_{\mathrm{J}}}, \forall k,i,n,\\
&\mathrm{C20}: \tilde{\mathbf{Z}}^{\mathrm{J}}_{k,i}[n] \succeq \mathbf{0}, \forall k,i,n,\\
&\mathrm{C21}: \tilde{\mathbf{Z}}^{\mathrm{J}}_{k,i}[n] \preceq s^{\mathrm{I}}_{k,i}[n]P^{\mathrm{J}}_{\mathrm{peak}}, \forall k,i,n.
\end{aligned}$$

Then, we handle the binary user scheduling constraint C1 in optimization problem (3.23) by rewriting constraint C1 in its equivalent form as:

$$\mathrm{C1a}: \sum_{n=1}^{N}\sum_{k=1}^{K}\sum_{i=1}^{N_{\mathrm{F}}} s^{\mathrm{I}}_{k,i}[n] - (s^{\mathrm{I}}_{k,i}[n])^2 \leq 0, \tag{3.25}$$

$$\mathrm{C1b}: 0 \leq s^{\mathrm{I}}_{k,i}[n] \leq 1, \forall k,i,n, \tag{3.26}$$

where $s^{\mathrm{I}}_{k,i}[n]$ is a continuous variable with a value between zero and one. Specifically, the continuous version of $s^{\mathrm{I}}_{k,i}[n]$ serves as a time-sharing factor for user k in utilizing subcarrier i at time slot n. However, constraint C1a is a

reverse convex function [103, 115]. In order to handle this non-convexity [97], based on [103,116,117] and for $\chi \gg 1$, the problem in (3.23) can be equivalently transformed as:

$$\begin{aligned}
&\underset{\mathcal{A},\mathcal{P},\tilde{\mathcal{P}},\mathcal{Z},\tilde{\mathcal{Z}}}{\text{maximize}} \ \frac{\sum_{n=1}^{N}\sum_{k=1}^{K}\sum_{i=1}^{N_{\mathrm{F}}} \tilde{R}^{\mathrm{U}}_{k,i}[n] - \chi\big(s^{\mathrm{I}}_{k,i}[n] - (s^{\mathrm{I}}_{k,i}[n])^2\big)}{\sum_{n=1}^{N}(\tilde{P}^{\mathrm{I}}_{\mathrm{total}}[n] + P^{\mathrm{J}}_{\mathrm{total}}[n])} \qquad (3.27)\\
&\qquad \text{s.t. C1b, C2, C3a, C3b} - \text{C5b, C7, C14} - \text{C21},\\
&\widetilde{\text{C4a}}: \ \sum_{k=1}^{K}\sum_{i=1}^{N_{\mathrm{F}}} \tilde{p}^{\mathrm{I}}_{k,i}[n] \le P^{\mathrm{I}}_{\mathrm{peak}}, \forall n,\\
&\widetilde{\text{C5a}}: \ \tilde{P}^{\mathrm{I}}_{\mathrm{total}}[n] \le P^{\mathrm{I}}_{\mathrm{max}}, \forall n,\\
&\widetilde{\text{C6}}: \ \frac{1}{N}\sum_{n=1}^{N}\sum_{i=1}^{N_{\mathrm{F}}} \tilde{R}^{\mathrm{U}}_{k,i}[n] \ge R_{\mathrm{min}}, \forall k,
\end{aligned}$$

where $\tilde{\mathcal{P}} = \{\tilde{p}^{\mathrm{I}}_{k,i}[n], \forall k, i, n\}$, $\tilde{\mathcal{Z}} = \{\tilde{\mathbf{Z}}^{\mathrm{J}}_{k,i}[n], \forall k, i, n\}$,

$$\tilde{R}^{\mathrm{U}}_{k,i}[n] = D^{\mathrm{I}}_{k,i}[n] - D^{\mathrm{II}}_{k,i}[n] \qquad (3.28)$$

$$D^{\mathrm{I}}_{k,i}[n] = W s^{\mathrm{I}}_{k,i}[n] \log_2\left(WN_0 + \frac{\mathrm{Tr}(\mathbf{H}^{\mathrm{JU}}_{k}[n]\tilde{\mathbf{Z}}^{\mathrm{J}}_{k,i}[n]) + \tilde{p}^{\mathrm{I}}_{k,i}[n] h^{\mathrm{IU}}_{k}[n]}{s^{\mathrm{I}}_{k,i}[n]}\right), \forall k, i, n, \qquad (3.29)$$

$$D^{\mathrm{II}}_{k,i}[n] = W s^{\mathrm{I}}_{k,i}[n] \log_2\left(\frac{\mathrm{Tr}(\mathbf{H}^{\mathrm{JU}}_{k}[n]\tilde{\mathbf{Z}}^{\mathrm{J}}_{k,i}[n])}{s^{\mathrm{I}}_{k,i}[n]} + WN_0\right), \forall k, i, n, \text{ and} \qquad (3.30)$$

$$\tilde{P}^{\mathrm{I}}_{\mathrm{total}}[n] = \sum_{k=1}^{K}\sum_{i=1}^{N_{\mathrm{F}}} \tilde{p}^{\mathrm{I}}_{k,i}[n] + P^{\mathrm{I}}_{\mathrm{C}} + P^{\mathrm{I}}_{\mathrm{flight}}[n]. \qquad (3.31)$$

The variable $\chi \gg 1$ acts as a penalty factor for accounting the objective function for any $s^{\mathrm{I}}_{k,i}[n]$ that is not equal to 0 or 1. Note that the problem in (3.27) is still non-convex and the non-convexity arises from the objective function and constraint $\widetilde{\text{C6}}$. Thus, we handle the data rate in the objective function and constraint $\widetilde{\text{C6}}$ since it is the difference of convex (DC) functions. Based on the

SCA and [110, 116], for given feasible points $(s^{\mathrm{I}}_{k,i}[n])^{j^{\mathrm{A1}}}$ and $(\tilde{\mathbf{Z}}^{\mathrm{J}}_{k,i}[n])^{j^{\mathrm{A1}}}$, a lower bound of the data rate can be obtained by its first-order Taylor expansion as

$$\begin{aligned}\tilde{R}^{\mathrm{U}}_{k,i}[n] \geq\ & (\tilde{R}^{\mathrm{U}}_{k,i,\mathrm{lb}}[n])^{j^{\mathrm{A1}}} \\ =\ & D^{\mathrm{I}}_{k,i}[n] - (D^{\mathrm{II}}_{k,i,\mathrm{ub}}[n])^{j^{\mathrm{A1}}} \\ =\ & D^{\mathrm{I}}_{k,i}[n] - \big[(D^{\mathrm{II}}_{k,i}[n])^{j^{\mathrm{A1}}} + \nabla_{\mathcal{A}} D^{\mathrm{II}}_{k,i}[n] \times (s^{\mathrm{I}}_{k,i}[n] - (s^{\mathrm{I}}_{k,i}[n])^{j^{\mathrm{A1}}}) \\ & + \nabla_{\{\tilde{\mathcal{Z}}\}_{r,c}} D^{\mathrm{II}}_{k,i}[n] \times (\{\tilde{\mathbf{Z}}^{\mathrm{J}}_{k,i}[n]\}_{r,c} - \{(\tilde{\mathbf{Z}}^{\mathrm{J}}_{k,i}[n])^{j^{\mathrm{A1}}}\}_{r,c})\big], \end{aligned} \tag{3.32}$$

where $r \in \{1, ..., N_{\mathrm{J}x}N_{\mathrm{J}y}\}$, $c \in \{1, ..., N_{\mathrm{J}x}N_{\mathrm{J}y}\}$, $(D^{\mathrm{II}}_{k,i,\mathrm{ub}}[n])^{j^{\mathrm{A1}}}$, $\nabla_{\mathcal{A}} D^{\mathrm{II}}_{k,i}[n](s^{\mathrm{I}}_{k,i}[n] - (s^{\mathrm{I}}_{k,i}[n])^{j^{\mathrm{A1}}})$, and $\nabla_{\{\tilde{\mathcal{Z}}\}_{r,c}} D^{\mathrm{II}}_{k,i}[n](\{\tilde{\mathbf{Z}}^{\mathrm{J}}_{k,i}[n]\}_{r,c} - \{(\tilde{\mathbf{Z}}^{\mathrm{J}}_{k,i}[n])^{j^{\mathrm{A1}}}\}_{r,c})$ are given by

$$(D^{\mathrm{II}}_{k,i}[n])^{j^{\mathrm{A1}}} = W(s^{\mathrm{I}}_{k,i}[n])^{j^{\mathrm{A1}}} \log_2 \left(\frac{\mathrm{Tr}(\mathbf{H}^{\mathrm{JU}}_k[n](\tilde{\mathbf{Z}}^{\mathrm{J}}_{k,i}[n])^{j^{\mathrm{A1}}})}{(s^{\mathrm{I}}_{k,i}[n])^{j^{\mathrm{A1}}}} + WN_0 \right), \forall k, i, n, \tag{3.33}$$

$$\begin{aligned}&\nabla_{\mathcal{A}} D^{\mathrm{II}}_{k,i}[n](s^{\mathrm{I}}_{k,i}[n] - (s^{\mathrm{I}}_{k,i}[n])^{j^{\mathrm{A1}}}) \\ &= W \log_2 \left(\frac{\mathrm{Tr}(\mathbf{H}^{\mathrm{JU}}_k[n](\tilde{\mathbf{Z}}^{\mathrm{J}}_{k,i}[n])^{j^{\mathrm{A1}}})}{(s^{\mathrm{I}}_{k,i}[n])^{j^{\mathrm{A1}}}} + WN_0 \right)(s^{\mathrm{I}}_{k,i}[n] - (s^{\mathrm{I}}_{k,i}[n])^{j^{\mathrm{A1}}}) \\ &- \frac{W\mathrm{Tr}\big(\mathbf{H}^{\mathrm{JU}}_k[n](\tilde{\mathbf{Z}}^{\mathrm{J}}_{k,i}[n])^{j^{\mathrm{A1}}}\big)(s^{\mathrm{I}}_{k,i}[n] - (s^{\mathrm{I}}_{k,i}[n])^{j^{\mathrm{A1}}})}{(\mathrm{Tr}(\mathbf{H}^{\mathrm{JU}}_k[n](\tilde{\mathbf{Z}}^{\mathrm{J}}_{k,i}[n])^{j^{\mathrm{A1}}}) + WN_0(s^{\mathrm{I}}_{k,i}[n])^{j^{\mathrm{A1}}}) \ln 2}, \forall k, i, n, \text{ and} \end{aligned} \tag{3.34}$$

$$\begin{aligned}&\nabla_{\{\tilde{\mathcal{Z}}\}_{r,c}} D^{\mathrm{II}}_{k,i}[n](\{\tilde{\mathbf{Z}}^{\mathrm{J}}_{k,i}[n]\}_{r,c} - \{(\tilde{\mathbf{Z}}^{\mathrm{J}}_{k,i}[n])^{j^{\mathrm{A1}}}\}_{r,c}) \\ &= \frac{W(s^{\mathrm{I}}_{k,i}[n])^{j^{\mathrm{A1}}}\{\mathbf{H}^{\mathrm{JU}}_k[n]\}_{c,r}(\{\tilde{\mathbf{Z}}^{\mathrm{J}}_{k,i}[n]\}_{r,c} - \{(\tilde{\mathbf{Z}}^{\mathrm{J}}_{k,i}[n])^{j^{\mathrm{A1}}}\}_{r,c})}{(\mathrm{Tr}(\mathbf{H}^{\mathrm{JU}}_k[n](\tilde{\mathbf{Z}}^{\mathrm{J}}_{k,i}[n])^{j^{\mathrm{A1}}}) + WN_0(s^{\mathrm{I}}_{k,i}[n])^{j^{\mathrm{A1}}}) \ln 2}, \forall k, i, n, r, c. \end{aligned} \tag{3.35}$$

respectively. Similarly, we can obtain an upper bound of the penalty part as

$$\begin{aligned} & s^{\mathrm{I}}_{k,i}[n] - (s^{\mathrm{I}}_{k,i}[n])^2 \\ \leq & (A_{k,i,\mathrm{ub}}[n])^{j^{\mathrm{A1}}} \\ = & s^{\mathrm{I}}_{k,i}[n] - \big((s^{\mathrm{I}}_{k,i}[n])^{j^{\mathrm{A1}}}\big)^2 + 2(s^{\mathrm{I}}_{k,i}[n])^{j^{\mathrm{A1}}}\big(s^{\mathrm{I}}_{k,i}[n] - (s^{\mathrm{I}}_{k,i}[n])^{j^{\mathrm{A1}}}\big). \end{aligned} \tag{3.36}$$

Then, we handle constraint C7 in (3.27) by considering its subset:

$$\begin{aligned} & \max_{\|\Delta\mathbf{t}_e^{\mathrm{E}}\|\le Q_e^{\mathrm{E}}} \frac{p_{k,i}^{\mathrm{I}}[n]h_e^{\mathrm{IE}}[n]}{\mathrm{Tr}(\mathbf{H}_e^{\mathrm{JE}}[n]\mathbf{Z}_i^{\mathrm{J}}[n])+WN_0} \\ \le & \max_{\|\Delta\mathbf{t}_e^{\mathrm{E}}\|\le Q_e^{\mathrm{E}}} \frac{p_{k,i}^{\mathrm{I}}[n]h_e^{\mathrm{IE}}[n]}{\min\limits_{\|\Delta\mathbf{t}_e^{\mathrm{E}}\|\le Q_e^{\mathrm{E}}} \mathrm{Tr}(\mathbf{H}_e^{\mathrm{JE}}[n]\mathbf{Z}_i^{\mathrm{J}}[n])+WN_0} \\ = & \frac{\max\limits_{\|\Delta\mathbf{t}_e^{\mathrm{E}}\|\le Q_e^{\mathrm{E}}} p_{k,i}^{\mathrm{I}}[n]h_e^{\mathrm{IE}}[n]}{\min\limits_{\|\Delta\mathbf{t}_e^{\mathrm{E}}\|\le Q_e^{\mathrm{E}}} \mathrm{Tr}(\mathbf{H}_e^{\mathrm{JE}}[n]\mathbf{Z}_i^{\mathrm{J}}[n])+WN_0} \le \Gamma_{\mathrm{th}}. \end{aligned} \tag{3.37}$$

This safe approximation [12, 118] imposes a more stringent constraint on the leakage SINR and solving the corresponding problem provides a performance lower bound of the original problem.

After applying (3.32)-(3.37) to (3.27), a suboptimal solution of (3.27) can be obtained by solving

$$\begin{aligned} \underset{\mathcal{A},\mathcal{P},\tilde{\mathcal{P}},\mathcal{Z},\tilde{\mathcal{Z}}}{\text{maximize}} \; & \frac{\sum_{n=1}^{N}\sum_{k=1}^{K}\sum_{i=1}^{N_{\mathrm{F}}}(\tilde{R}_{k,i,\mathrm{lb}}^{\mathrm{U}}[n])^{j^{\mathrm{A1}}} - \chi(A_{k,i,\mathrm{ub}}[n])^{j^{\mathrm{A1}}}}{\sum_{n=1}^{N}(\tilde{P}_{\mathrm{total}}^{\mathrm{I}}[n]+P_{\mathrm{total}}^{\mathrm{J}}[n])} \\ \text{s.t. } & \mathrm{C1b}, \mathrm{C2}, \mathrm{C3a}, \widetilde{\mathrm{C4}}\mathrm{a}, \widetilde{\mathrm{C5}}\mathrm{a}, \mathrm{C3b}-\mathrm{C5b}, \mathrm{C14}-\mathrm{C21}, \\ \widetilde{\widetilde{\mathrm{C6}}}: \; & \frac{1}{N}\sum_{n=1}^{N}\sum_{i=1}^{N_{\mathrm{F}}}(\tilde{R}_{k,i,\mathrm{lb}}^{\mathrm{U}}[n])^{j^{\mathrm{A1}}} \ge R_{\min}, \forall k, \\ \widetilde{\mathrm{C7}}: \; & p_{k,i}^{\mathrm{I}}[n]\max_{\|\Delta\mathbf{t}_e^{\mathrm{E}}\|\le Q_e^{\mathrm{E}}} h_e^{\mathrm{IE}}[n] \\ & \le \Gamma_{\mathrm{th}}\big(\mathrm{Tr}(\min_{\|\Delta\mathbf{t}_e^{\mathrm{E}}\|\le Q_e^{\mathrm{E}}} \mathbf{H}_e^{\mathrm{JE}}[n]\mathbf{Z}_i^{\mathrm{J}}[n])+WN_0\big), \forall k,e,i,n. \end{aligned} \tag{3.38}$$

Then, for improving the quality of the obtained suboptimal solutions, we update the feasible solution, $(s_{k,i}^{\mathrm{I}}[n])^{j^{\mathrm{A1}}}$ and $(\tilde{\mathbf{Z}}_{k,i}^{\mathrm{J}}[n])^{j^{\mathrm{A1}}}$, obtained by solving (3.38) in the SCA iteratively, cf. Main loop in **Algorithm 3.1**.

Now, we discuss the methodology for solving sub-problem 1 in (3.38). In particular, we tackle the fractional form objective function in (3.38). Let q_1^* be

Algorithm 3.1 Proposed Algorithm for Solving Sub-problem 1 in (3.23)

1: Initialize the convergence tolerance $\epsilon_1 \rightarrow 0$, the maximum number of iterations for main loop $J_{\max}^{\mathrm{A1}}$, the initial iteration index $j^{\mathrm{A1}} = 1$, and the initial system energy efficiency $q_1^{j^{\mathrm{A1}}} = 0$
2: **repeat** {Main Loop: SCA}
3: Set $j^{\mathrm{A1}} = j^{\mathrm{A1}} + 1$
4: Using **Algorithm 3.2** to obtain $\{\underline{\mathcal{A}}^{(j^{\mathrm{A1}})}, \underline{\mathcal{P}}^{(j^{\mathrm{A1}})}, \underline{\tilde{\mathcal{P}}}^{(j^{\mathrm{A1}})}, \underline{\mathcal{Z}}^{(j^{\mathrm{A1}})}, \underline{\tilde{\mathcal{Z}}}^{(j^{\mathrm{A1}})}\}$ and $q_1^{(j^{\mathrm{A1}})}$
5: **until** $j^{\mathrm{A1}} = J_{\max}^{\mathrm{A1}}$ or $\frac{|q_1^{(j^{\mathrm{A1}})} - q_1^{(j^{\mathrm{A1}}+1)}|}{q_1^{(j^{\mathrm{A1}})}} \leq \epsilon_1$
6: Return $\{\mathcal{A}^*, \mathcal{P}^*, \tilde{\mathcal{P}}^*, \mathcal{Z}^*, \tilde{\mathcal{Z}}^*\} = \{\underline{\mathcal{A}}^{(j^{\mathrm{A1}})}, \underline{\mathcal{P}}^{(j^{\mathrm{A1}})}, \underline{\tilde{\mathcal{P}}}^{(j^{\mathrm{A1}})}, \underline{\mathcal{Z}}^{(j^{\mathrm{A1}})}, \underline{\tilde{\mathcal{Z}}}^{(j^{\mathrm{A1}})}\}$ and $q_1^* = q_1^{(j^{\mathrm{A1}})}$

the maximum system energy efficiency of sub-problem 1 which is given by

$$q_1^* = \frac{R(\mathcal{A}^*, \tilde{\mathcal{P}}^*, \tilde{\mathcal{Z}}^*)}{P(\tilde{\mathcal{P}}^*, \mathcal{Z}^*)} = \underset{\mathcal{A},\mathcal{P},\tilde{\mathcal{P}},\mathcal{Z},\tilde{\mathcal{Z}}\in\mathcal{F}}{\text{maximize}} \frac{R(\mathcal{A}, \tilde{\mathcal{P}}, \tilde{\mathcal{Z}})}{P(\tilde{\mathcal{P}}, \mathcal{Z})}, \tag{3.39}$$

where $\mathcal{A}^*$, $\mathcal{P}^*$, $\tilde{\mathcal{P}}^*$, $\mathcal{Z}^*$, and $\tilde{\mathcal{Z}}^*$ are the optimal value sets of the optimization variables in (3.27). $\mathcal{F}$ is the feasible solution set spanned by constraints C1b, C2, C3a, $\widetilde{\text{C4a}}$, $\widetilde{\text{C5a}}$, C3b − C5b, $\widetilde{\widetilde{\text{C6}}}$, $\widetilde{\text{C7}}$, and C14 − C21. Now, by applying the fractional programming theory [19], the objective function of (3.38) can be equivalently transformed into a subtractive form.

Theorem 3.1. *In particular, the optimal value of* q_1^* *in* (3.38) *can be achieved if and only if*

$$\begin{aligned} &\underset{\mathcal{A},\mathcal{P},\tilde{\mathcal{P}},\mathcal{Z},\tilde{\mathcal{Z}}\in\mathcal{F}}{\text{maximize}}\ R(\mathcal{A}, \tilde{\mathcal{P}}, \tilde{\mathcal{Z}}) - q_1^* P(\tilde{\mathcal{P}}, \mathcal{Z}) \\ &= R(\mathcal{A}^*, \tilde{\mathcal{P}}^*, \tilde{\mathcal{Z}}^*) - q_1^* P(\tilde{\mathcal{P}}^*, \mathcal{Z}^*) = 0, \end{aligned} \tag{3.40}$$

for $R(\mathcal{A}, \tilde{\mathcal{P}}, \tilde{\mathcal{Z}}) \geq 0$ *and* $P(\mathcal{P}, \mathcal{Z}) > 0$.

Proof: Please refer to Appendix B.1. □

Therefore, we can apply the iterative Dinkelbach method [119] to solve (3.38). In particular, for the j^{A1}-th iteration for sub-problem 1 and a given intermediate value $q_1^{(j_{\mathrm{in}}^{\mathrm{A1}})}$, we need to solve a convex optimization as follows:

$$\begin{aligned}
&\{\underline{\mathcal{A}}, \underline{\mathcal{P}}, \underline{\tilde{\mathcal{P}}}, \underline{\mathcal{Z}}, \underline{\tilde{\mathcal{Z}}}\} \qquad (3.41)\\
&= \arg \underset{\mathcal{A},\mathcal{P},\tilde{\mathcal{P}},\mathcal{Z},\tilde{\mathcal{Z}}}{\text{maximize}} \sum_{n=1}^{N}\sum_{k=1}^{K}\sum_{i=1}^{N_{\mathrm{F}}}(\tilde{R}^{\mathrm{U}}_{k,i,\mathrm{lb}}[n])^{j^{\mathrm{A1}}}\\
&\qquad -\chi(A_{k,i,\mathrm{ub}}[n])^{j^{\mathrm{A1}}} - q_1^{(j_{\mathrm{in}}^{\mathrm{A2}})}\sum_{n=1}^{N}(\tilde{P}^{\mathrm{I}}_{\mathrm{total}}[n] + P^{\mathrm{J}}_{\mathrm{total}}[n])\\
&\qquad \text{s.t. C1b, C2, C3a} - \text{C5a, C3b} - \text{C5b, } \widetilde{\widetilde{\text{C6}}}, \widetilde{\text{C7}}, \text{C14} - \text{C21},
\end{aligned}$$

where $\{\underline{\mathcal{A}}, \underline{\mathcal{P}}, \underline{\tilde{\mathcal{P}}}, \underline{\mathcal{Z}}, \underline{\tilde{\mathcal{Z}}}\}$ is the optimal solution of (3.41) for a given $q_1^{(j_{\mathrm{in}}^{\mathrm{A2}})}$. Then, the intermediate energy efficiency value $q_1^{(j_{\mathrm{in}}^{\mathrm{A2}})}$ should be updated as $q_1^{(j_{\mathrm{in}}^{\mathrm{A2}})} = \frac{R(\underline{\mathcal{A}},\underline{\tilde{\mathcal{P}}},\underline{\tilde{\mathcal{Z}}})}{P(\underline{\tilde{\mathcal{P}}},\underline{\mathcal{Z}})}$ for each iteration of the Dinkelbach method until convergence[10]. Sine the problem in (3.41) is jointly convex w.r.t. the optimization variables, it can be solved efficiently via convex programm solvers, e.g., CVX [120]. On the other hand, it is interesting to study structure of the generated artificial noise which is summarised in the following theorem.

Theorem 3.2. *If the optimization problem in* (3.41) *is feasible, the rank of the optimal artificial noise matrix* $\mathrm{Rank}(\mathbf{Z}) \leq 1$.

Proof: Please refer to Appendix B.2. □

Although there are multiple eavesdroppers in the system, rank-one beamforming is optimal for (3.41) to guarantee secure and energy efficient communication.

The proposed algorithm for solving sub-problem 1 is summarized in **Algorithm 3.1**

[10]Note that the convergence of the Dinkelbach method is guaranteed if the problem in (3.41) can be solved optimally in each iteration [119].

Algorithm 3.2 Dinkelbach Method

1: Initialize the convergence tolerance $\epsilon_2 \rightarrow 0$, the maximum number of iterations $J_{\text{in,max}}^{\text{A2}}$, the iteration index $j_{\text{in}}^{\text{A2}} = 1$, and the initial system energy efficiency $q_1^{(j_{\text{in}}^{\text{A2}})} = 0$
2: **repeat** {Inner Loop: Dinkelbach Method}
3: Solve (3.41) for the given $q_1^{(j_{\text{in}}^{\text{A2}})}$ to obtain $\{\underline{\mathcal{A}}^{(j_{\text{in}}^{\text{A2}})}, \underline{\mathcal{P}}^{(j_{\text{in}}^{\text{A2}})}, \underline{\tilde{\mathcal{P}}}^{(j_{\text{in}}^{\text{A2}})}, \underline{\mathcal{Z}}^{(j_{\text{in}}^{\text{A2}})}, \underline{\tilde{\mathcal{Z}}}^{(j_{\text{in}}^{\text{A2}})}\}$
4: **if** $R(\underline{\mathcal{A}}^{(j_{\text{in}}^{\text{A2}})}, \underline{\tilde{\mathcal{P}}}^{(j_{\text{in}}^{\text{A2}})}, \underline{\tilde{\mathcal{Z}}}^{(j_{\text{in}}^{\text{A2}})}) - q_1^{j_{\text{in}}^{\text{A2}}} P(\underline{\tilde{\mathcal{P}}}^{(j_{\text{in}}^{\text{A2}})}, \underline{\mathcal{Z}}^{(j_{\text{in}}^{\text{A2}})}) < \epsilon_2$ **then**
5: Inner Loop Convergence = **true**
6: **return** $\{\underline{\mathcal{A}}^{(j^{\text{A1}})}, \underline{\mathcal{P}}^{(j^{\text{A1}})}, \underline{\tilde{\mathcal{P}}}^{(j^{\text{A1}})}, \underline{\mathcal{Z}}^{(j^{\text{A1}})}, \underline{\tilde{\mathcal{Z}}}^{(j^{\text{A1}})}\} = \{\underline{\mathcal{A}}^{(j_{\text{in}}^{\text{A2}})}, \underline{\mathcal{P}}^{(j_{\text{in}}^{\text{A2}})}, \underline{\tilde{\mathcal{P}}}^{(j_{\text{in}}^{\text{A2}})}, \underline{\mathcal{Z}}^{(j_{\text{in}}^{\text{A2}})}, \underline{\tilde{\mathcal{Z}}}^{(j_{\text{in}}^{\text{A2}})}\}$ and $q_1^{\text{A1}} = \frac{R(\underline{\mathcal{A}}^{(j_{\text{in}}^{\text{A2}})}, \underline{\tilde{\mathcal{P}}}^{(j_{\text{in}}^{\text{A2}})}, \underline{\tilde{\mathcal{Z}}}^{(j_{\text{in}}^{\text{A2}})})}{P(\underline{\tilde{\mathcal{P}}}^{(j_{\text{in}}^{\text{A2}})}, \underline{\mathcal{Z}}^{(j_{\text{in}}^{\text{A2}})})}$
7: **else**
8: Set $q_1^{(j_{\text{in}}^{\text{A2}}+1)} = \frac{R(\underline{\mathcal{A}}^{(j_{\text{in}}^{\text{A2}})}, \underline{\tilde{\mathcal{P}}}^{(j_{\text{in}}^{\text{A2}})}, \underline{\tilde{\mathcal{Z}}}^{(j_{\text{in}}^{\text{A2}})})}{P(\underline{\tilde{\mathcal{P}}}^{(j_{\text{in}}^{\text{A2}})}, \underline{\mathcal{Z}}^{(j_{\text{in}}^{\text{A2}})})}$ and $j_{\text{in}}^{\text{A2}} = j_{\text{in}}^{\text{A2}} + 1$
9: Inner Loop Convergence = **false**
10: **end if**
11: **until** Inner Loop Convergence = **true** or $j_{\text{in}}^{\text{A2}} = J_{\text{in,max}}^{\text{A2}}$

which consists of two nested loops. Specifically, in each iteration of the main loop, we solve the inner loop problem, i.e., lines 2-11 of **Algorithm 3.2**, in (3.41) for a given parameter $q_1^{(j_{\text{in}}^{\text{A2}})}$ given by the initialization or last iteration. After obtaining the solution in the inner loop via the Dinkelbach method, we update parameter $q_1^{(j_{\text{in}}^{\text{A2}})}$ and use it for solving the inner loop problem in the next iteration. This procedure is repeated until the proposed algorithm converges. We note that the convergence of the SCA is guaranteed [1].

3.4.2 Sub-problem 2: Optimizing Information UAV's Trajectory and Flight Velocity

For a given user scheduling $\mathcal{A} = \{s_{k,i}^{\text{I}}[n], \forall k, i, n\}$, information transmit power allocation $\mathcal{P} = \{p_{k,i}^{\text{I}}[n], \forall k, i, n\}$, and jammer UAV's artificial noise $\mathcal{Z} =$

$\{\mathbf{Z}_i^{\mathrm{J}}[n], \forall i, n\}$, we can express sub-problem 2 as

$$\begin{aligned} \underset{\mathcal{T}_{\mathcal{I}}, \mathcal{V}_{\mathcal{I}}}{\text{maximize}} \; & \frac{\sum_{n=1}^{N} \sum_{k=1}^{K} \sum_{i=1}^{N_{\mathrm{F}}} R_{k,i}^{\mathrm{U}}[n]}{\sum_{n=1}^{N} (P_{\text{total}}^{\mathrm{I}}[n] + P_{\text{total}}^{\mathrm{J}}[n])} \\ \text{s.t.} \; & \mathrm{C5a}, \mathrm{C6}, \mathrm{C7}, \mathrm{C8} - \mathrm{C13}. \end{aligned} \tag{3.42}$$

The problem in (3.42) is non-convex and the non-convexity arises from the objective function and constraints C6 and C7. To facilitate the solution design, we introduce two slack optimization variables $u_k[n]$ and $v^{\mathrm{I}}[n]$ to transform the problem into its equivalent form as follows:

$$\begin{aligned} \underset{\mathcal{T}_{\mathcal{I}}, \mathcal{V}_{\mathcal{I}}, \mathcal{U}_{\mathcal{K}}, \boldsymbol{\Upsilon}_{\mathcal{I}}}{\text{maximize}} \; & \frac{\sum_{n=1}^{N} \sum_{k=1}^{K} \sum_{i=1}^{N_{\mathrm{F}}} \bar{R}_{k,i}^{\mathrm{U}}[n]}{\sum_{n=1}^{N} (\bar{P}_{\text{total}}^{\mathrm{I}}[n] + P_{\text{total}}^{\mathrm{J}}[n])} \\ \text{s.t.} \; & \mathrm{C5a}, \mathrm{C8} - \mathrm{C13}, \\ & \overline{\mathrm{C6}} : \frac{1}{N} \sum_{n=1}^{N} \sum_{i=1}^{N_{\mathrm{F}}} \bar{R}_{k,i}^{\mathrm{U}}[n] \geq R_{\min}, \forall k, \\ & \overline{\mathrm{C7}} : \min_{\|\Delta \mathbf{t}_e^{\mathrm{E}}\| \leq Q_e^{\mathrm{E}}} \|\mathbf{t}_e^{\mathrm{E}} + \Delta \mathbf{t}_e^{\mathrm{E}} - \mathbf{t}^{\mathrm{I}}[n]\|^2 + H^2 \geq \frac{\gamma_{k,e,i}^{\mathrm{IJE}}[n]}{\Gamma_{\text{th}}}, \forall k, e, i, n, \\ & \mathrm{C22} : \|\mathbf{t}_k^{\mathrm{U}} - \mathbf{t}^{\mathrm{I}}[n]\|^2 + H^2 \leq u_k[n], \forall k, n, \\ & \mathrm{C23} : \|\mathbf{v}^{\mathrm{I}}[n]\|^2 \geq (v^{\mathrm{I}}[n])^2, \forall n, \\ & \mathrm{C24} : v^{\mathrm{I}}[n] \geq 0, \forall n, \end{aligned} \tag{3.43}$$

where $\mathcal{U}_{\mathcal{K}} = \{u_k[n], \forall k, n\}$, $\boldsymbol{\Upsilon}_{\mathcal{I}} = \{\upsilon^{\mathrm{I}}[n], \forall n\}$,

$$\bar{R}^{\mathrm{U}}_{k,i}[n] = W s^{\mathrm{I}}_{k,i}[n] \log_2\left(1 + \frac{\gamma^{\mathrm{IJU}}_{k,i}[n]}{u_k[n]}\right), \tag{3.44}$$

$$\gamma^{\mathrm{IJU}}_{k,i}[n] = \frac{p^{\mathrm{I}}_{k,i}[n]\beta_0}{\mathrm{Tr}(\mathbf{H}^{\mathrm{JU}}_k[n]\mathbf{Z}^{\mathrm{J}}_i[n]) + WN_0}, \tag{3.45}$$

$$\bar{P}^{\mathrm{I}}_{\mathrm{total}}[n] = \sum_{k=1}^{K}\sum_{i=1}^{N_{\mathrm{F}}} s^i_k[n]p^i_k[n] + P_{\mathrm{C}} + \bar{P}^{\mathrm{I}}_{\mathrm{flight}}[n], \tag{3.46}$$

$$\bar{P}^{\mathrm{I}}_{\mathrm{flight}}[n] = P_o\left(1 + \frac{3\|\mathbf{v}^{\mathrm{I}}[n]\|^2}{\Omega^2 r^2}\right) + \frac{P_i v_0}{\upsilon^{\mathrm{I}}[n]} + \frac{1}{2}d_0\rho s A\|\mathbf{v}^{\mathrm{I}}[n]\|^3, \text{ and} \tag{3.47}$$

$$\gamma^{\mathrm{IJE}}_{k,e,i}[n] = \frac{p^{\mathrm{I}}_{k,i}[n]\beta_0}{\mathrm{Tr}(\mathbf{H}^{\mathrm{JE}}_e[n]\mathbf{Z}^{\mathrm{J}}_i[n]) + WN_0}. \tag{3.48}$$

Note that $\bar{R}^{\mathrm{U}}_{k,i}[n]$ and $\bar{P}^{\mathrm{I}}_{\mathrm{flight}}[n]$ are convex w.r.t. $u_k[n] > 0$ and $\upsilon^{\mathrm{I}}[n] > 0$, respectively. It can be proved that the problems in (3.42) and (3.43) are equivalent as inequality constraints C22 and C23 are always satisfied with equality at the optimal solution of (3.43). Then, we handle the location uncertainty of eavesdropper e by rewriting constraint $\overline{\mathrm{C7}}$ as:

$$\max_{\|\Delta\mathbf{t}^{\mathrm{E}}_e\| \le Q^{\mathrm{E}}_e} -\|\hat{\mathbf{t}}^{\mathrm{E}}_e + \Delta\mathbf{t}^{\mathrm{E}}_e - \mathbf{t}^{\mathrm{I}}[n]\|^2 - H^2 + \frac{\gamma^{\mathrm{IJE}}_{k,e,i}[n]}{\Gamma_{\mathrm{th}}} \le 0. \tag{3.49}$$

Note that the location uncertainty introduces an infinite number of constraints in $\overline{\mathrm{C7}}$. To circumvent this difficulty, we apply the $\mathcal{S}$-Procedure [44] and transform $\overline{\mathrm{C7}}$ into a finite number of linear matrix inequalities (LMIs) constraints. In particular, if there exists a variable $\psi[n] \ge 0$ such that

$$\Phi(\mathbf{t}^{\mathrm{I}}[n], \psi[n]) \succeq \mathbf{0}, \forall n, \tag{3.50}$$

holds, where

$$\Phi(\mathbf{t}^{\mathrm{I}}[n], \psi[n]) = \begin{bmatrix} (\psi[n]+1)\mathbf{I}_2 & \mathbf{t}^{\mathrm{I}}[n] - \hat{\mathbf{t}}_e^{\mathrm{E}} \\ (\mathbf{t}^{\mathrm{I}}[n] - \hat{\mathbf{t}}_e^{\mathrm{E}})^{\mathrm{T}} & -\psi[n](Q_e^{\mathrm{E}})^2 + c[n] \end{bmatrix} \tag{3.51}$$

and

$$c[n] = \|\mathbf{t}^{\mathrm{I}}[n]\|^2 - 2\|(\hat{\mathbf{t}}_e^{\mathrm{E}})^{\mathrm{T}}\mathbf{t}^{\mathrm{I}}[n]\| + \|\hat{\mathbf{t}}_e^{\mathrm{E}}\|^2 + H^2 - \frac{\gamma_{k,e,i}^{\mathrm{IJE}}[n]}{\Gamma_{\mathrm{th}}}, \tag{3.52}$$

then the implication (3.50)⇒(3.49) holds.

Next, the non-convexity arises from the numerator of the objective function, constraints C6, C13, and C23 since $\bar{R}_{k,i,\mathrm{lb}}^{\mathrm{U}}[n]$, $\|\mathbf{t}^{\mathrm{I}}[n] - \mathbf{t}^{\mathrm{J}}[n]\|^2$, and $\|\mathbf{v}^{\mathrm{I}}[n]\|^2$ are convex functions and differentiable w.r.t. $u_k[n]$, $\mathbf{t}^{\mathrm{I}}[n]$, and $\mathbf{v}^{\mathrm{I}}[n]$, respectively. Besides, $c[n]$ in constraint (3.50) is a non-convex function w.r.t. $\mathbf{t}^{\mathrm{I}}[n]$. In the following, we aim to establish a lower bound of the objective function and focus on a subset spanned by constraints C6, C13, and C23. By using the first-order Taylor expansion [1] and the SCA [**?**, **?**], for a given feasible solution $u_k^{(j^{\mathrm{A3}})}[n]$, $(\mathbf{t}^{\mathrm{I}}[n])^{j^{\mathrm{A3}}}$, and $(\mathbf{v}^{\mathrm{I}}[n])^{j^{\mathrm{A3}}}$, we have inequalities

$$\begin{aligned} \bar{R}_{k,i}^{\mathrm{U}}[n] \geq (\bar{R}_{k,i,\mathrm{lb}}^{\mathrm{U}}[n])^{j^{\mathrm{A3}}} &= Ws_{k,i}^{\mathrm{I}}[n]\log_2\left(1 + \frac{\gamma_{k,i}^{\mathrm{IJU}}[n]}{u_k^{(j^{\mathrm{A3}})}[n]}\right) \\ &\quad - \frac{Ws_{k,i}^{\mathrm{I}}[n]\gamma_{k,i}^{\mathrm{IJU}}[n](u_k[n] - u_k^{(j^{\mathrm{A3}})}[n])}{u_k^{(j^{\mathrm{A3}})}[n](u_k^{(j^{\mathrm{A3}})}[n] + \gamma_{k,i}^{\mathrm{IJU}}[n])\ln 2}, \forall k, i, n, \end{aligned} \tag{3.53}$$

$$\|\mathbf{t}^{\mathrm{I}}[n] - \mathbf{t}^{\mathrm{J}}[n]\|^2 \geq \|(\mathbf{t}^{\mathrm{I}}[n])^{j^{\mathrm{A3}}} - \mathbf{t}^{\mathrm{J}}[n]\|^2 + 2[(\mathbf{t}^{\mathrm{I}}[n])^{j^{\mathrm{A3}}}]^{\mathrm{T}}(\mathbf{t}^{\mathrm{I}}[n] - (\mathbf{t}^{\mathrm{I}}[n])^{j^{\mathrm{A3}}}), \text{ and} \tag{3.54}$$

$$\|\mathbf{v}^{\mathrm{I}}[n]\|^2 \geq \|(\mathbf{v}^{\mathrm{I}}[n])^{j^{\mathrm{A3}}}\|^2 + 2[(\mathbf{v}^{\mathrm{I}}[n])^{j^{\mathrm{A3}}}]^{\mathrm{T}}(\mathbf{v}^{\mathrm{I}}[n] - (\mathbf{v}^{\mathrm{I}}[n])^{j^{\mathrm{A3}}}), \tag{3.55}$$

respectively. Similarly, for a given feasible solution $(\mathbf{t}^{\mathrm{I}}[n])^{j^{\mathrm{A3}}}$, the following

constraint

$$\overline{\overline{\mathrm{C7}}} : \widetilde{\Phi}^{(j^{\mathrm{A3}})}(\mathbf{t}^{\mathrm{I}}[n], \psi[n]) \succeq \mathbf{0}, \forall n, \tag{3.56}$$

where $\widetilde{\Phi}^{(j^{\mathrm{A3}})}(\mathbf{t}^{\mathrm{I}}[n], \psi[n])$ is given by

$$\widetilde{\Phi}^{(j^{\mathrm{A3}})}(\mathbf{t}^{\mathrm{I}}[n], \psi[n]) = \begin{bmatrix} (\psi[n]+1)\mathbf{I}_2 & \mathbf{t}^{\mathrm{I}}[n] - \hat{\mathbf{t}}_e^{\mathrm{E}} \\ (\mathbf{t}^{\mathrm{I}}[n] - \hat{\mathbf{t}}_e^{\mathrm{E}})^{\mathrm{T}} & -\psi[n](Q_e^{\mathrm{E}})^2 + \tilde{c}^{(j^{\mathrm{A3}})}[n] \end{bmatrix} \tag{3.57}$$

and

$$\begin{aligned} \tilde{c}^{(j^{\mathrm{A3}})}[n] &= \|\hat{\mathbf{t}}_e^{\mathrm{E}}\|^2 + 2(\mathbf{t}^{\mathrm{I}}[n])^{\mathrm{T}}(\mathbf{t}^{\mathrm{I}}[n])^{j^{\mathrm{A3}}} - ((\mathbf{t}^{\mathrm{I}}[n])^{j^{\mathrm{A3}}})^2 \\ &\quad - 2(\hat{\mathbf{t}}_e^{\mathrm{E}})^{\mathrm{T}}\mathbf{t}^{\mathrm{I}}[n] + H^2 - \frac{\gamma_{k,e,i}^{\mathrm{IJE}}[n]}{\Gamma_{\mathrm{th}}} \leq c[n], \qquad (3.58) \\ &\Rightarrow \overline{\mathrm{C7}}. \qquad (3.59) \end{aligned}$$

Besides, a subset of C13 and C23 is given by

$$\overline{\mathrm{C13}} : \|(\mathbf{t}^{\mathrm{I}}[n])^{j^{\mathrm{A3}}} - \mathbf{t}^{\mathrm{J}}[n]\|^2 + 2[(\mathbf{t}^{\mathrm{I}}[n])^{j^{\mathrm{A3}}}]^{\mathrm{T}} \times (\mathbf{t}^{\mathrm{I}}[n] - (\mathbf{t}^{\mathrm{I}}[n])^{j^{\mathrm{A3}}}) \geq d_{\min}^2, \forall n, \tag{3.60}$$

$$\overline{\mathrm{C23}} : \|(\mathbf{v}^{\mathrm{I}}[n])^{j^{\mathrm{A3}}}\|^2 + 2[(\mathbf{v}^{\mathrm{I}}[n])^{j^{\mathrm{A3}}}]^{\mathrm{T}} \times (\mathbf{v}^{\mathrm{I}}[n] - (\mathbf{v}^{\mathrm{I}}[n])^{j^{\mathrm{A3}}}) \geq {v^{\mathrm{I}}}^2[n], \forall n. \tag{3.61}$$

Now, we obtain a lower bound of the objective function via replacing the denominator and the numerator of the original objective function in (3.43) by its equivalent form in (3.46) and the lower bound of average total data rate in (3.53), respectively. Besides, we replace constraints C13 and C23 by $\overline{\mathrm{C13}}$ and $\overline{\mathrm{C23}}$, respectively. Therefore, we can obtain a suboptimal solution of (3.43) via

Algorithm 3.3 Proposed Algorithm for Solving Sub-problem 2 in (3.42)

1: Initialize the convergence tolerance $\epsilon_3 \rightarrow 0$, the maximum number of iterations for main loop $J^{\mathrm{A3}}_{\max}$, the initial iteration index $j^{\mathrm{A3}} = 1$, and the initial system energy efficiency $q_3^{j^{\mathrm{A3}}} = 0$
2: **repeat** {Main Loop: SCA}
3: Set $j^{\mathrm{A3}} = j^{\mathrm{A3}} + 1$
4: Using **Algorithm 3.2** with replacing the maximum number of iterations as $J^{\mathrm{A3}}_{\mathrm{in,max}}$, the iteration index as $j^{\mathrm{A3}}_{\mathrm{in}}$, the initial system energy efficiency as $q_3^{(j^{\mathrm{A3}}_{\mathrm{in}})}$, variables as $\{\underline{\mathcal{T}_{\mathcal{I}}}^{(j^{\mathrm{A3}}_{\mathrm{in}})}, \underline{\mathcal{V}_{\mathcal{I}}}^{(j^{\mathrm{A3}}_{\mathrm{in}})}, \underline{\mathcal{U}_{\mathcal{K}}}^{(j^{\mathrm{A3}}_{\mathrm{in}})}, \underline{\Upsilon_{\mathcal{I}}}^{(j^{\mathrm{A3}}_{\mathrm{in}})}\}$, the total achievable data rate function as $\bar{R}(\underline{\mathcal{U}_{\mathcal{K}}}^{(j^{\mathrm{A3}}_{\mathrm{in}})})$, and the total power consumption as $\bar{P}(\underline{\mathcal{V}_{\mathcal{I}}}^{(j^{\mathrm{A3}}_{\mathrm{in}})}, \underline{\Upsilon_{\mathcal{I}}}^{(j^{\mathrm{A3}}_{\mathrm{in}})})$ to obtain $\{\underline{\mathcal{T}_{\mathcal{I}}}^{(j^{\mathrm{A3}})}, \underline{\mathcal{V}_{\mathcal{I}}}^{(j^{\mathrm{A3}})}, \underline{\mathcal{U}_{\mathcal{K}}}^{(j^{\mathrm{A3}})}, \underline{\Upsilon_{\mathcal{I}}}^{(j^{\mathrm{A3}})}\}$ and $q_3^{(j^{\mathrm{A3}})}$
5: **until** $j^{\mathrm{A3}} = J^{\mathrm{A3}}_{\max}$ or $\frac{|q_3^{(j^{\mathrm{A3}})} - q_3^{(j^{\mathrm{A3}}+1)}|}{q_3^{(j^{\mathrm{A3}})}} \leq \epsilon_3$
6: Return $\{\mathcal{T_{\mathcal{I}}}^*, \mathcal{V_{\mathcal{I}}}^*, \mathcal{U_{\mathcal{K}}}^*, \Upsilon_{\mathcal{I}}^*\} = \{\underline{\mathcal{T}_{\mathcal{I}}}^{(j^{\mathrm{A3}})}, \underline{\mathcal{V}_{\mathcal{I}}}^{(j^{\mathrm{A3}})}, \underline{\mathcal{U}_{\mathcal{K}}}^{(j^{\mathrm{A3}})}, \underline{\Upsilon_{\mathcal{I}}}^{(j^{\mathrm{A3}})}\}$ and $q_3^* = q_3^{(j^{\mathrm{A3}})}$

solving the following optimization problem:

$$
\begin{aligned}
\underset{\mathcal{T}_{\mathcal{I}},\mathcal{V}_{\mathcal{I}},\mathcal{U}_{\mathcal{K}},\boldsymbol{\Upsilon}_{\mathcal{I}},\boldsymbol{\Psi}}{\text{maximize}} \quad & \frac{\sum_{n=1}^{N}\sum_{k=1}^{K}\sum_{i=1}^{N_{\mathrm{F}}}(\bar{R}^{\mathrm{U}}_{k,i,\mathrm{lb}}[n])^{j^{\mathrm{A3}}}}{\sum_{n=1}^{N}(\bar{P}^{\mathrm{I}}_{\mathrm{total}}[n] + P^{\mathrm{J}}_{\mathrm{total}}[n])} \\
\text{s.t.} \quad & \overline{\overline{\mathrm{C7}}}, \mathrm{C8} - \mathrm{C12}, \overline{\mathrm{C13}}, \mathrm{C22}, \overline{\mathrm{C23}}, \mathrm{C24}, \\
& \overline{\mathrm{C5a}} : \bar{P}^{\mathrm{I}}_{\mathrm{total}}[n] \leq P^{\mathrm{I}}_{\max}, \forall n, \\
& \overline{\overline{\mathrm{C6}}} : \frac{1}{N}\sum_{n=1}^{N}\sum_{i=1}^{N_{\mathrm{F}}}(\bar{R}^{\mathrm{U}}_{k,i,\mathrm{lb}}[n])^{j^{\mathrm{A3}}} \geq R_{\min}, \forall k, \\
& \mathrm{C25} : \psi[n] \geq 0, \forall n,
\end{aligned}
\tag{3.62}
$$

where $\boldsymbol{\Psi} = \{\psi[n], \forall n\}$. Note that a solution satisfies the constraints in (3.62) would satisfy the one in (3.43). Now, similar to the approach for solving sub-problem 1, we apply the Dinklebach's method for a given $\{(\mathbf{t}^{\mathrm{I}}[n])^{j^{\mathrm{A3}}}, (\mathbf{v}^{\mathrm{I}}[n])^{j^{\mathrm{A3}}}\}$

Algorithm 3.4 Overall Algorithm for Solving Problem in (3.22)

1: Initialize the convergence tolerance $\epsilon_4 \rightarrow 0$, the maximum number of iterations $J_{\max}^{\mathrm{A4}}$, the initial iteration index $j^{\mathrm{A4}} = 1$, and the initial trajectory $\{\mathbf{t}^{\mathrm{I}}[n], \mathbf{v}^{\mathrm{I}}[n], \mathbf{t}^{\mathrm{J}}[n], \mathbf{v}^{\mathrm{J}}[n]\}$
2: **repeat**
3: Set $j^{\mathrm{A4}} = j^{\mathrm{A4}} + 1$
4: Using **Algorithm 3.1** obtain the suboptimal result q_1, $\{s_k^i[n], p_k^i[n], \mathbf{Z}_i^{\mathrm{J}}[n]\}$
5: Using **Algorithm 3.3** obtain the suboptimal result q_3, $\{\mathbf{t}^{\mathrm{I}}[n], \mathbf{v}^{\mathrm{I}}[n]\}$
6: **until** $j^{\mathrm{A4}} = J_{\max}^{\mathrm{A4}}$ or $\frac{|q_3^{(j^{\mathrm{A4}})} - q_3^{(j^{\mathrm{A4}}+1)}|}{q_3^{(j^{\mathrm{A4}})}} \leq \epsilon$
7: **return** $s_k^{i\,*}[n] = s_k^i[n], p_k^{i\,*}[n] = p_k^i[n], \mathbf{Z}_i^{\mathrm{J}*}[n] = \mathbf{Z}_i^{\mathrm{J}}[n], \mathbf{t}^{\mathrm{I}*}[n] = \mathbf{t}^{\mathrm{I}}[n], \mathbf{v}^{\mathrm{I}*}[n] = \mathbf{v}^{\mathrm{I}}[n]$, and $q^* = q_3^{(j^{\mathrm{A4}})}$

and $q_3^{(j^{\mathrm{A3}})}$, we solve the following convex optimization problem iteratively[11]:

$$\begin{aligned}
&\{\underline{\mathcal{T}_{\mathcal{I}}}, \underline{\mathcal{V}_{\mathcal{I}}}, \underline{\mathcal{U}_{\mathcal{K}}}, \underline{\Upsilon_{\mathcal{I}}}\} \\
&= \arg \underset{\mathcal{T}_{\mathcal{I}}, \mathcal{V}_{\mathcal{I}}, \mathcal{U}_{\mathcal{K}}, \boldsymbol{\Psi}, \boldsymbol{\Upsilon}_{\mathcal{I}}}{\text{maximize}} \sum_{n=1}^{N} \sum_{k=1}^{K} \sum_{i=1}^{N_{\mathrm{F}}} (\bar{R}_{k,i,\mathrm{lb}}^{\mathrm{U}}[n])^{j^{\mathrm{A3}}} \\
&- q_3^{(j_{\mathrm{in}}^{\mathrm{A3}})} \sum_{n=1}^{N} (\bar{P}_{\mathrm{total}}^{\mathrm{I}}[n] + P_{\mathrm{total}}^{\mathrm{J}}[n]) \qquad (3.63) \\
\text{s.t.} \quad &\overline{\mathrm{C5a}}, \overline{\overline{\mathrm{C6}}}, \overline{\overline{\mathrm{C7}}}, \mathrm{C8} - \mathrm{C12}, \overline{\mathrm{C13}}, \mathrm{C22}, \overline{\mathrm{C23}}, \mathrm{C24}, \mathrm{C25},
\end{aligned}$$

where $\{\underline{\mathcal{T}_{\mathcal{I}}}, \underline{\mathcal{V}_{\mathcal{I}}}, \underline{\mathcal{U}_{\mathcal{K}}}, \underline{\Upsilon_{\mathcal{I}}}\}$ is the optimal solution of (3.63) for a given $q_3^{(j_{\mathrm{in}}^{\mathrm{A3}})}$. The problem optimization in (3.63) is a convex formulation which can be easily solved by CVX [120]. The proposed algorithm for solving sub-problem 2 is summarized in **Algorithm 3.3**.

3.4.3 Overall Algorithm

The overall proposed iterative algorithms for solving the two sub-problems

[11]The problem in (3.63) can be easily solved by dual decomposition or numerical convex program solvers.

(3.23) and (3.42) are summarized in **Algorithm 3.4**. Since the feasible solution set of (3.22) is compact and its objective value is non-decreasing over iterations via solving the sub-problem in (3.23) and (3.42), iteratively, the solution of the proposed algorithm is guaranteed to converge [112]. The proof of the convergence please refer to Appendix B.3. □

Since we handle the problem with SCA and $\mathcal{S}$-Procedure, the obtained solution converges to a suboptimal optimal solution [110, 112, 121–123] of the original problem in (3.22).

On the other hand, as the computational complexity of solving sub-problem 1 is dominated by the semidefinite programming (SDP), the computational complexity of the proposed suboptimal algorithm is given by [124, 125]

$$\mathcal{O}\Bigg(J_{\max}^{\mathrm{A4}}\Bigg(\underbrace{(\mathcal{M}_1\mathcal{N}_1^3+\mathcal{M}_1^2\mathcal{N}_1^2+\mathcal{M}_1^3\mathcal{N}_1)\times J_{\max}^{\mathrm{A1}}J_{\mathrm{in,max}}^{\mathrm{A2}}\left(\sqrt{\mathcal{N}_1}\log\left(\frac{1}{\Delta_1}\right)\right)}_{\text{Sub-problem 1}}$$
$$\underbrace{+\mathcal{M}_2\mathcal{N}_2^2\times J_{\max}^{\mathrm{A3}}J_{\mathrm{in,max}}^{\mathrm{A3}}\left(\sqrt{\mathcal{N}_2}\log\left(\frac{1}{\Delta_2}\right)\right)}_{\text{Sub-problem 2}}\Bigg)\Bigg). \tag{3.64}$$

Note that $\mathcal{M}_1 = 10NKN_{\mathrm{F}} + NKEN_{\mathrm{F}} + 2NN_{\mathrm{F}} + 4N + K$, $\mathcal{N}_1 = 3NKN_{\mathrm{F}} + N_{\mathrm{J}}^2NN_{\mathrm{F}} + N_{\mathrm{J}}^2NKN_{\mathrm{F}}$, $\mathcal{M}_2 = 9N + NK + K$, and $\mathcal{N}_2 = 4N + NK$. Besides, $\Delta_1 > 0$, and $\Delta_2 > 0$ denote the solutions of the sub-problem 1 and sub-problem 2, respectively. We note that the proposed suboptimal algorithm has a polynomial time computational complexity.

3.5 Numerical Results

In this section, we evaluate the performance of the proposed algorithm via simulations. The simulation setups are summarized in Table 3.2. In our

Table 3.2: Simulation parameters [1–4].

Notations	Simulation value	Notations	Simulation value
Ω	300 radians/second	K	2
r	0.4 meter	E	2
ρ	1.225 kg/m^3	τ	0.1 s
s	0.05	N_{F}	128
A_{r}	0.503 m^2	B	1 MHz
P_o	79.86 W	W	7.8 kHz
P_i	88.63 W	N_0	-160 dBm/Hz
v_0	4.03 m/s	$P_{\mathrm{C}}^{\mathrm{I}}$	30 dBm
d_0	0.3	$P_{\mathrm{C}}^{\mathrm{J}}$	30 dBm
$V_{\max}^{\mathrm{I}}$	30 m/s	ζ^{I}	2
$V_{\mathrm{acc}}^{\mathrm{I}}$	4 m/s^2	ζ^{J}	2
$P_{\max}^{\mathrm{I}}$	65 dBm	λ_{c}	10^{-10} m
$P_{\max}^{\mathrm{J}}$	65 dBm	Δ_{J}	0.1 m
$N_{\mathrm{J}x}$	5	$R_{\min}$	6 Mbits/s
$N_{\mathrm{J}y}$	5	Γ_{th}	10^{-3} bps/subcarrier
$\mathbf{t}_0$	$[0, 0]$ m	$\mathbf{t}_1^{\mathrm{U}}$	$[350, 100]$ m
$\mathbf{t}_{\mathrm{F}}$	$[500, 500]$ m	$\mathbf{t}_2^{\mathrm{U}}$	$[150, 400]$ m
$\hat{\mathbf{t}}_1^{\mathrm{E}}$	$[400, 100]$ m	Q_e^{E}	$[71, 141]$ m
$\hat{\mathbf{t}}_2^{\mathrm{E}}$	$[250, 250]$ m	H	100 m
$P_{\mathrm{peak}}^{\mathrm{I}}$	30 dBm	$d_{\min}$	1 m
$P_{\mathrm{peak}}^{\mathrm{J}}$	30 dBm	$J_{\max}^{\mathrm{A1}}$	10
$J_{\max}^{\mathrm{A3}}$	10	$J_{\max}^{\mathrm{A4}}$	5
$J_{\mathrm{in,max}}^{\mathrm{A3}}$	10		

simulations, we compare the system energy efficiency of the proposed algorithm "PA", with the other three baseline schemes: (a) *No jammer UAV (NJ)*, which has only an information UAV in this scheme. The suboptimal resource allocation and UAV's trajectory for "NJ" can be obtained by using a similar approach as in our previous work [53]. (b) *Single-antenna jammer UAV (SAJ)*, in which both the information UAV and jammer UAV are all equipped with a single-antenna to provide secure communication. Since the problem formulation of the "PA" subsumes "SAJ", the system performance of "SAJ" can be achieved by solving the designed problem with "PA" and setting the number of antenna

array $N_{\mathrm{J}x} = N_{\mathrm{J}y} = 1$; (c) *Zero-acceleration information UAV (ZAI)*, where the information UAV's flight velocity remains unchanged but is optimized by our proposed scheme; (d) *Straight locus information UAV (SLI)*, where the information UAV cruises with a straight locus trajectory from the initial point to the final point with a constant speed and the jammer UAV has the same setting as in the "PA". Since "SLI" is another subcase of the problem formulation for "PA", the suboptimal solution can be obtained by optimizing resource allocation with fixing the information UAV's trajectory. Since the initial information-UAV trajectory will affect the performance of the proposed suboptimal solution, we have tried different reasonable trajectories as an initial point, e.g., (1) *Straight forward flight from the initial point to the destination* (SFF); (2) *A path passing through all users' location once*; (3) *A path along the boundary of the service area*, and found out that "SFF" provides the best performance. As a result, in the simulation section, we adopt "SFF" as the initial trajectory for the proposed algorithm.

3.5.1 Convergence of the Proposed Algorithm and Baseline Schemes

Fig. 3.4 illustrates the convergence behavior of the alternating optimization **Algorithm 3.4** for the maximization of the system energy efficiency. We compare the system energy efficiency of our proposed scheme for three different mission time durations, $T = 50$ s, $T = 25$ s, and $T = 13$ s, which correspond to the number of time slot $N = 500$, $N = 200$, and $N = 130$, respectively. The jammer UAV orbits around the *center of the eavesdroppers areas (CEA)* [110], as shown in Fig. 3.6. It can be seen from Fig. 3.4 that the system energy efficiency of the proposed scheme with different T converges to the corresponding suboptimal

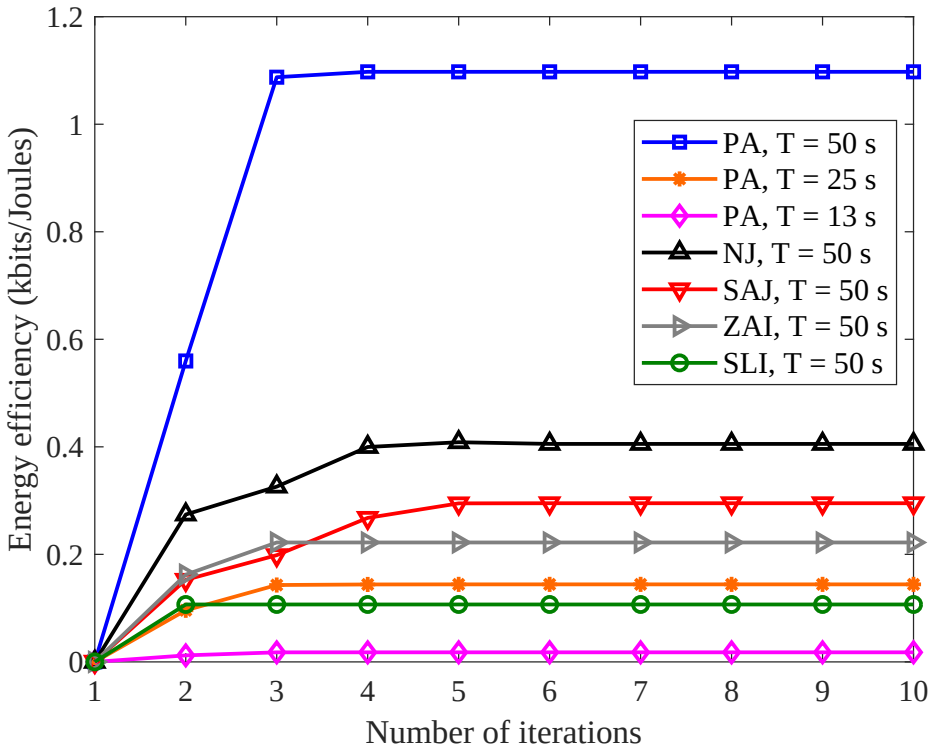

Figure 3.4: Energy efficiency versus the number of iterations.

solutions within only 5 iterations which demonstrates the fast convergence of the proposed alternating optimization algorithm. Thus, in the following simulations, we set the maximum number of iterations as 5 to illustrate the performance of the proposed algorithm. For comparison, we also demonstrate the convergence behavior of four baseline schemes "NJ", "SAJ", "ACS", and "SLI" while the mission time duration for baseline schemes is fixed as $T = 50$ s, their performance and corresponding trajectory will be discussed in the following.

3.5.2 Impact of Number of Users

In order to show the impact of the number of users, K, on the system performance, we vary the number of users, from 1 to 9, and the location of these users in x-dimension and y-dimension are given by $x_k^{\mathrm{U}} = [300; 200; 100; 300; 500; 900; 700;$

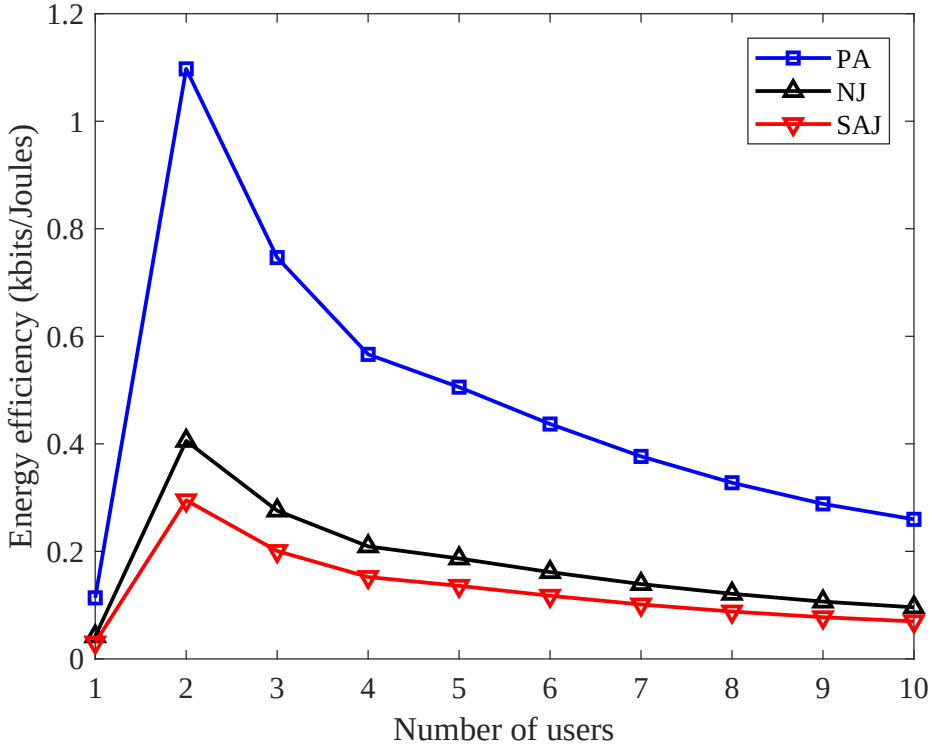

Figure 3.5: Energy efficiency versus the number of users.

$300; 500; 100]$ and $y_k^{\mathrm{U}} = [800; 700; 100; 300; 800; 900; 700; 200; 500; 300]$, respectively. The minimum data rate requirement for each user is set $R_{\min} = 1$ Mbits/s in this simulation. Other setups remain the same as before. The corresponding system energy efficiency versus number of users is shown in Fig. 3.5. We can observe that for all the mentioned schemes, the energy efficiency achieved with $K = 2$ is much higher than that with $K = 1$. In fact, when the number of users is small, the UAV can exploit the multiuser diversity via the proposed scheduling for improving the system performance. However, when there are more than 2 users, the minimum data rate constraints C6 become stringent and the resource allocator becomes less flexible in optimizing the usage of system resources leading to the decrease of the system energy efficiency. Besides, the system performance of "PA" is always better than that of other baseline schemes while increasing the

number of user K.

3.5.3 Impact of Jammer UAV's Trajectory

Fig. 3.6 shows the corresponding information UAV's trajectories for different predetermined trajectories of the jammer UAV with $T = 50$ s. In this chapter, we consider six commonly adopted trajectories of the jammer UAV, which have the same flight velocity[12] at 10.4 m/s, with the following proposed scheme. (a) *Center of the service area (CSA)*, in which the jammer UAV adopts a circular trajectory centered at the center of the service area [250, 250] with a radius of 150 meters [2]; (b) *Center of the eavesdroppers area (CEA)*, where the jammer UAV patrols also with a circular trajectory but centered at [312.5, 187.5] (centroid of all estimated eavesdroppers' locations) with a radius of 159 meters [110]; (c) *Shuttling flight between the eavesdroppers (SFE)*, where the jammer UAV flight is shuttled back and forth between the estimated locations of the two eavesdroppers during the given time frame; (d) *Centered at [400, 100] (CA1)*, (e) *Centered at [375, 175] (CA2)*, and (f) *Centered at [250, 250] (CA3)*, in which the jammer UAV has a circular trajectory with a radius of 10 meters centered at the eavesdropper 1's estimated location [400, 100], the middle of two eavesdroppers' estimated locations [375, 175], and the eavesdropper 2's estimated location [250, 250], respectively. Note that in these schemes, the jammer UAV is equipped with 25 antennas. We can observe in Fig. 3.6 that by setting a reasonable trajectory of the jammer UAV, e.g., a path cruises among all eavesdroppers, a high system energy efficiency can be achieved compared to the case without jamming UAV. In fact, the optimized artificial noise would try to compensate the suboptimality caused by the fixed trajectory. More importantly, the existence of jamming UAV

[12]Note that a UAV consumes the minimum flight power when it travels at 10.4 m/s for the considered setting in [3].

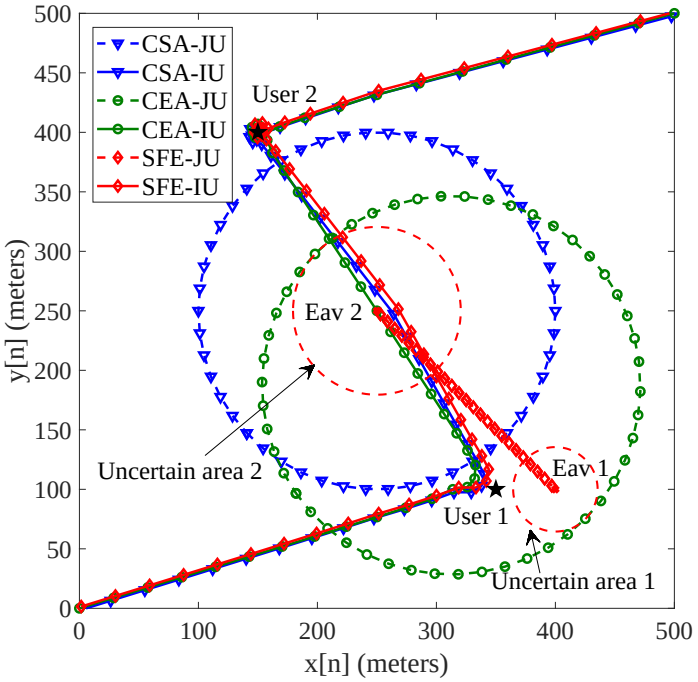

(a) The information UAV's trajectories of the proposed algorithm for CSA, CEA, and SFE.

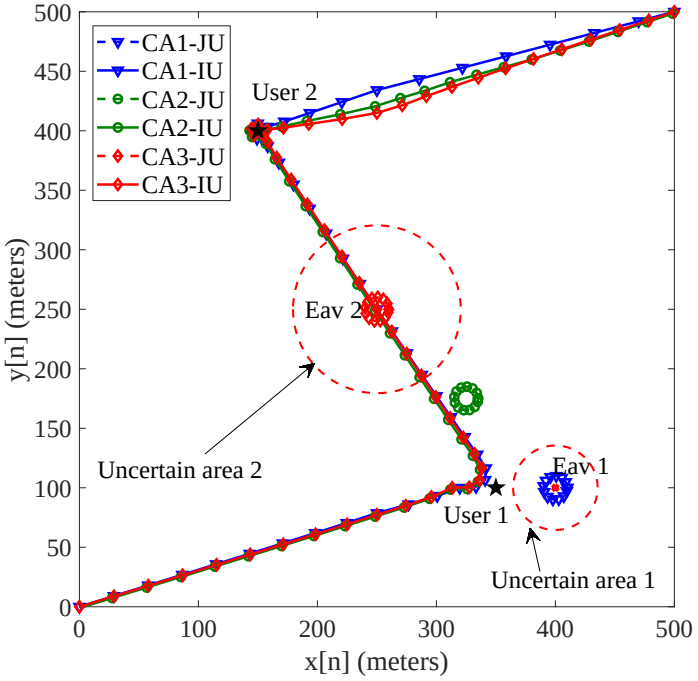

(b) The information UAV's trajectories of the proposed algorithm for CA1, CA2, and CA3.

Figure 3.6: The information UAV's trajectories of the proposed algorithm for different jammer UAV's trajectories.

and optimized jamming relieves the security constraint which provides a higher flexibility to the information UAV for adopting an energy efficient short route for communication. As a result, the information UAV's trajectories are almost the same (with short paths) for different jammer UAV's trajectories. This observation will be verified again when we compare our proposed scheme with no jammer in the next section. Therefore, in the following simulations, we fix the jammer UAV's trajectory as "CEA" for illustration.

3.5.4 Trajectories of Information UAV

Fig. 3.7 demonstrates the trajectory of the information UAV for the "PA" with three different mission time durations, $T = 13$ s, $T = 25$ s, and $T = 50$ s, respectively. Note that the flight velocity of the information UAV in each time slot can be calculated from the distance between each two adjacent points along its trajectory. Besides, the corresponding communication transmit power and artificial noise transmit power versus time slots are illustrated in Fig. 3.8, where the communication power for user 1, user 2, and the noise power are denoted as "PA-U1", "PA-U2", and "PA-Z", respectively. Besides, a longer mission completion time enables a higher system energy efficiency for our proposed scheme. This is because the information UAV's trajectory design becomes more flexible with increasing T. As a result, the mobility of the information UAV can be more efficiently exploited to improve the system energy efficiency. In the following, for different mission time durations T, we will discuss simulation results of the information UAV's trajectory, communication power allocation, and noise power allocation.

It is observed that when the mission time duration is sufficiently large (e.g., $T = 50$ s), the information UAV would maintain a high velocity when it is

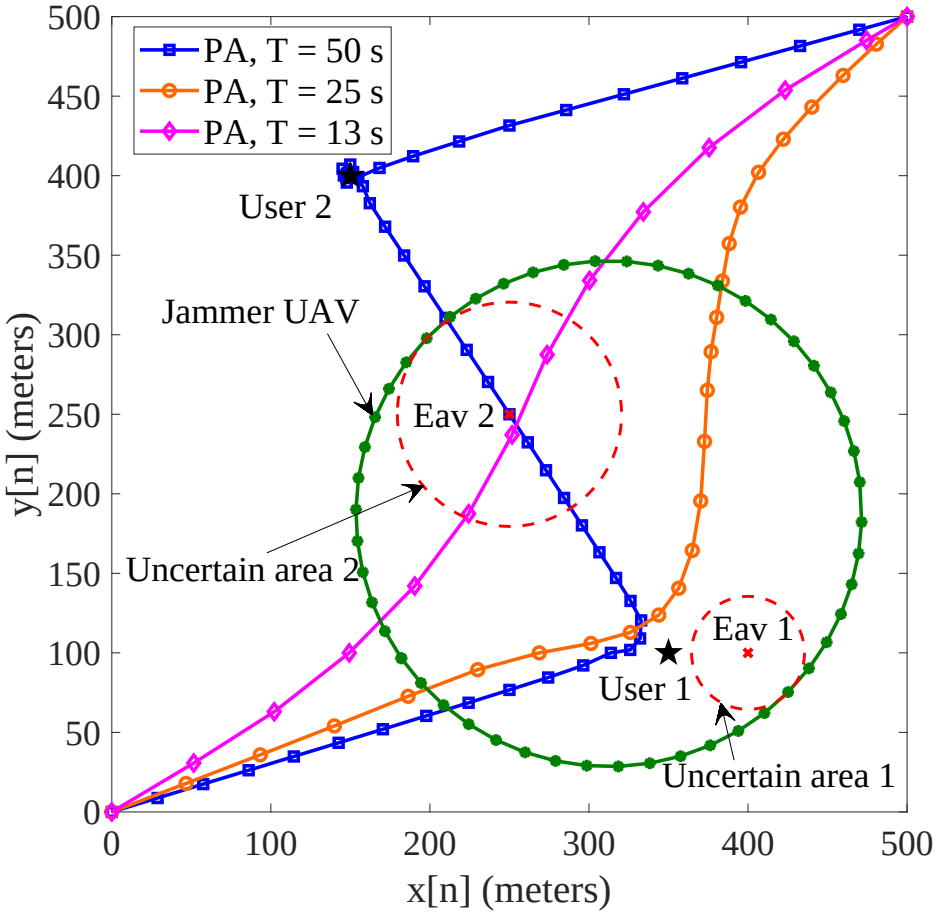

Figure 3.7: The UAVs' trajectories of the proposed algorithm with different service time durations.

far away from the users and only fly slowly whenever it is close to any desired user. This behavior aims to save more time slots for the information UAV to provide high data rate communication when it is close to the users. Besides, with $T = 50$ s, the information UAV would strike a balance between energy consumption and velocity. In particular, the information UAV hovers above user 2 with the optimized velocity for a long period of time to achieve a high throughput. In contrast, the information UAV does not hover above user 1 as user 1 is closer to one of the eavesdroppers than user 2 which has a higher potential in information leakage. Correspondingly, as shown in Fig. 3.8, for $T = 50$ s,

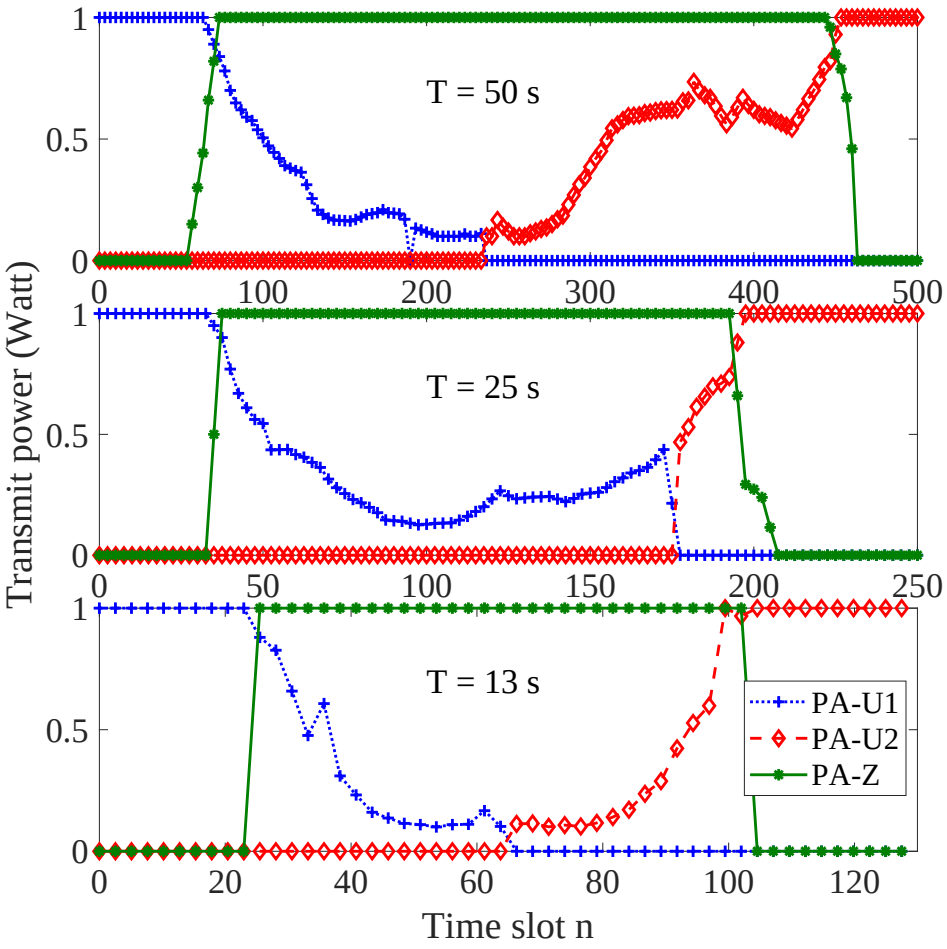

Figure 3.8: The communication transmit power to user 1 and user 2 as well as the artificial noise transmit power versus time slots.

the communication power is allocated solely to user 1 at first half of total time slots, then the remaining time slots are allocated to user 2. Moreover, when the information UAV is faraway from all the users and eavesdroppers, e.g., at the beginning and ending time slots, the information UAV transmits the highest available communication power and the jammer transmits small power of artificial noise as the leakage SINR of each eavesdropper are relatively small. However, for those time slots having a high potential of information leakage, not only the jammer UAV transmits the highest artificial noise, but also the information

UAV decreases its transmit power to reduce the potential information leakage. Specifically, by exploiting the spatial DoF brought by the multiple antennas, the jammer UAV creates a sharp artificial noise beam with full power and steers towards a direction with can impair both eavesdroppers efficiently. In contrast, when the mission time duration T is 25 s as shown in Fig. 3.7, the information UAV first flies towards to user 1 with a relatively higher velocity then flies slowly to the destination. Note that the UAV would slow down but with a reasonable speed when it is close to user 2 instead of stationing since the flight power consumption of the rotary UAV is relatively high when its flight speed is sufficiently low [3]. It can also be observed that the information UAV detours a bit towards user 2 for a more efficient communication. From Fig. 3.8, for $T = 25$ s, the information UAV first communicates with user 1 until the 36-th time slot, where it just crosses outside the locus of the jammer UAV. Then, the maximum transmit power is allocated solely to user 2 to achieve the minimum data rate requirement. Additionally, when the total time duration is relatively short (e.g., $T = 13$ s), the information UAV flies with the highest speed from the initial point to the final point. Besides, due to the limited mission completed time, the information UAV flies slightly closer to user 1 at the beginning and later to user 2 for satisfying the individual user's minimum data rate requirement of security communication. Moreover, the information power allocation and the jamming policy have a similar pattern for the "PA" with different total time durations, c.f. Fig. 3.8. These illustrate that the information UAV's trajectory plays an extremely important role in achieving high system energy efficiency and secure communication.

Fig. 3.9 illustrates the information UAV's trajectories for different schemes, as "SLI", "NJ", "SAJ", and "PA". In this figure, we assume that the mission

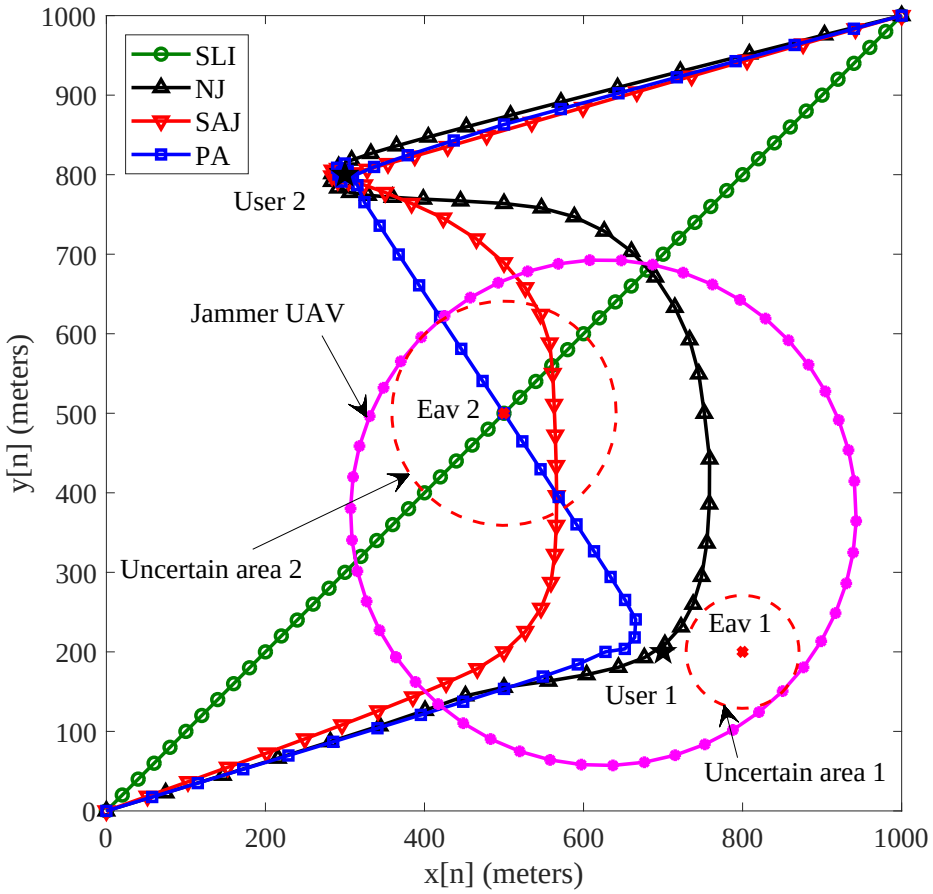

Figure 3.9: The UAVs' trajectories of the proposed algorithm and the baseline schemes.

time duration T is 50 s for all the schemes. As it can be observed, for "SLI", the information UAV flies at a constant speed and following a predefined straight trajectory from the initial point to the destination, which have the lowest energy efficiency in all the considered schemes, c.f. Fig. 3.4 and Fig. 3.11. The information UAV in "NJ" scheme first flies towards user 1. Meanwhile, the information UAV keeps decreasing its transmit power allocated to user 1 for reducing the potential of information leakage. After passing by user 1, the information UAV starts communicate with user 2 with a small transmit power which adopts an arc trajectory and fly towards user 2. The detouring trajectory

of the information UAV aims to decrease the leakage SINR to eavesdropper 2. Note that the information UAV only communicates with user 2 with high transmit power when the UAV is far away from eavesdropper 2. In contrast, the information UAV in "SAJ" scheme flies a shorter distance than that of "NJ" due to the artificial noise generated by the jammer UAV which relaxes the security requirement on "SAJ". Additionally, comparing all the baseline schemes, the trajectory of information UAV in the "PA" does not detour and fly around the uncertain area of the eavesdroppers. In other words, "PA" has a higher flexibility in design the trajectory of the information UAV. This is a clear evidence of the benefit in utilizing an antenna array at the jammer UAV as it can always focus the artificial noise on the threatened eavesdroppers for guaranteeing secure communication.

3.5.5 Energy Efficiency

Fig. 3.10 shows the energy efficiency versus the number of antennas equipped at the jammer UAV. In this simulation, we consider the circuit power consumption for each antenna of the jammer UAV, with $P_{\mathrm{CJ}} = 0.1$ Watt. It is obviously that the energy efficiency increases with the number of antennas equipped at the jammer UAV as the associated spatial DoF improve the flexibility in resource allocation. Besides, the energy efficiency become saturated when the jammer UAV's antenna number is sufficiently large. This is due to the fact that the circuit power consumption of antennas become a dominate factor in the system performance outweighing the associated performance gain. In particular, the increase trend of the system energy efficiency presents the contribution of the multiple antennas equipped in the jammer UAV to the system.

Fig. 3.11 shows the energy efficiency versus communication peak transmit

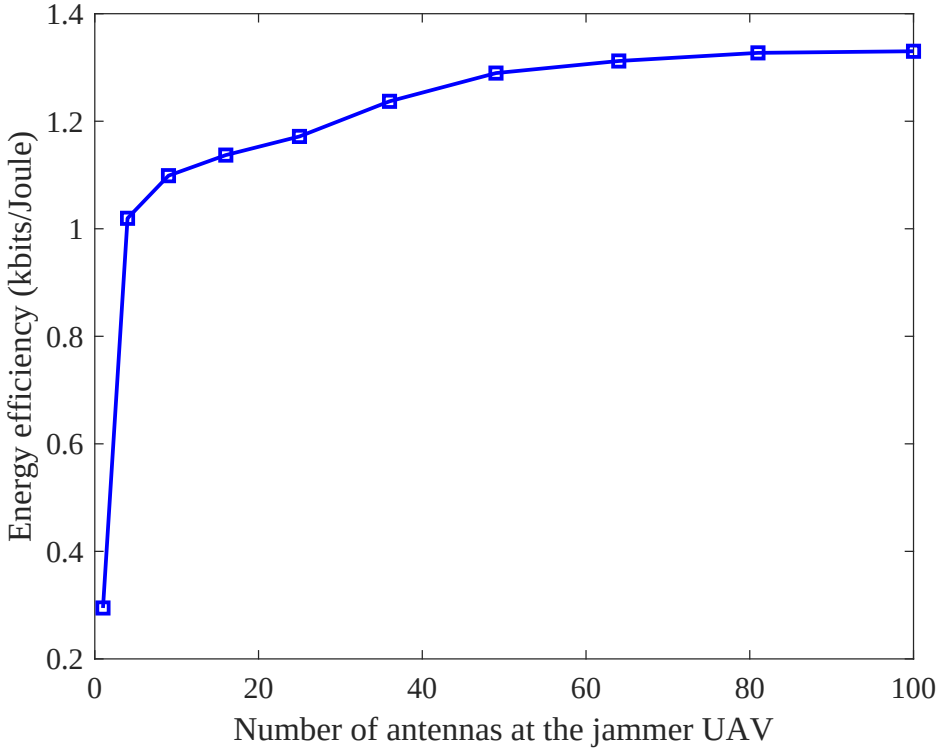

Figure 3.10: Energy efficiency versus the number of antennas equipped at the jammer UAV.

power $P_{\text{peak}}^{\text{I}}$ for the "PA", "NJ", "SAJ", and "SLI" when the mission time duration T is 50 s. It can be observed that the energy efficiencies achieved by the "PA" and baseline schemes first increase with the communication peak transmit power budget. This is due to the fact that increasing the communication transmit power budget can achieve a higher achievable data rate. In particular, for low to moderate transmit power, the data rate gain due to a higher transmit power outweighs the cost of transmit power consumption leading to a rise in system energy efficiency. However, the energy efficiency gain due to a higher values of $P_{\text{peak}}^{\text{I}}$ is diminishing and becomes saturated as the maximum system energy efficiency is achieved and the information UAV would clip the transmit power at the optimal value. Moreover, the security constraint becomes more

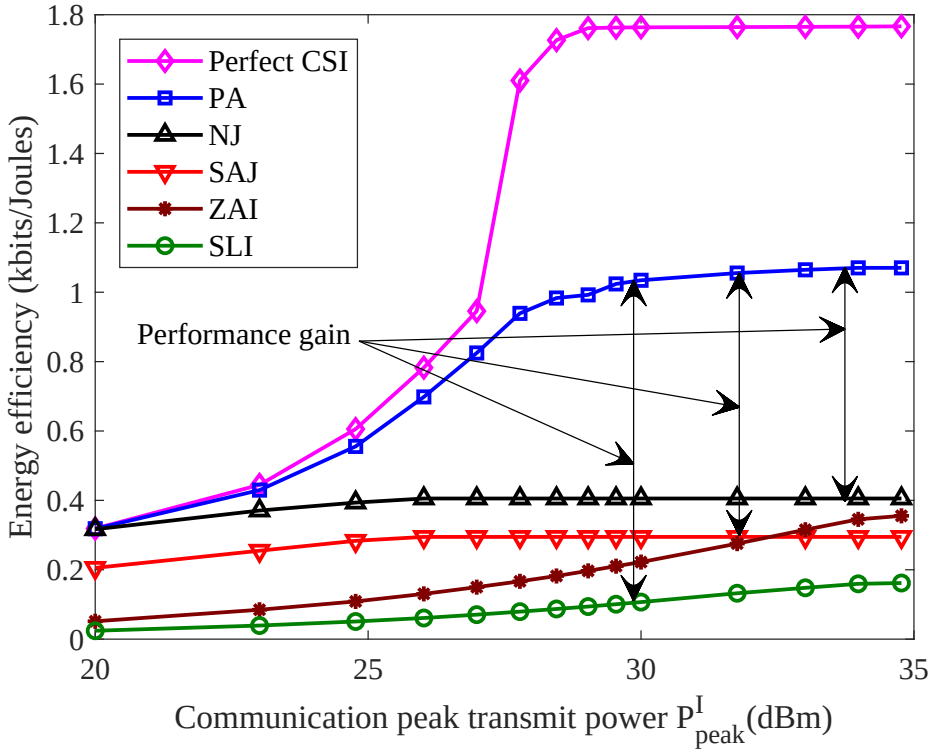

Figure 3.11: Energy efficiency versus communication peak transmit power.

stringent for a larger $P^{\mathrm{I}}_{\mathrm{peak}}$ when the peak transmit power of artificial noise is fixed. As a result, to guarantee communication security, the information UAV may not always transmit with its full power in the high transmit power regime. Besides, it is observed that the system energy efficiency with perfect CSI is higher than that of "PA". In fact, the CSI error arises from the uncertain area of eavesdroppers, which imposes a stringent information leakage constraints for the proposed scheme. Therefore, more system resources are required to achieve secure communication. As a result, the system performance degrades dramatically when there is an CSI error. However, our proposed scheme can achieve the best performance among all the considered baseline schemes in the case of imperfect CSI. Also, we can observe that the energy efficiency of "ZAI" is much lower than that of "PA" which presents the importance of variable UAV's

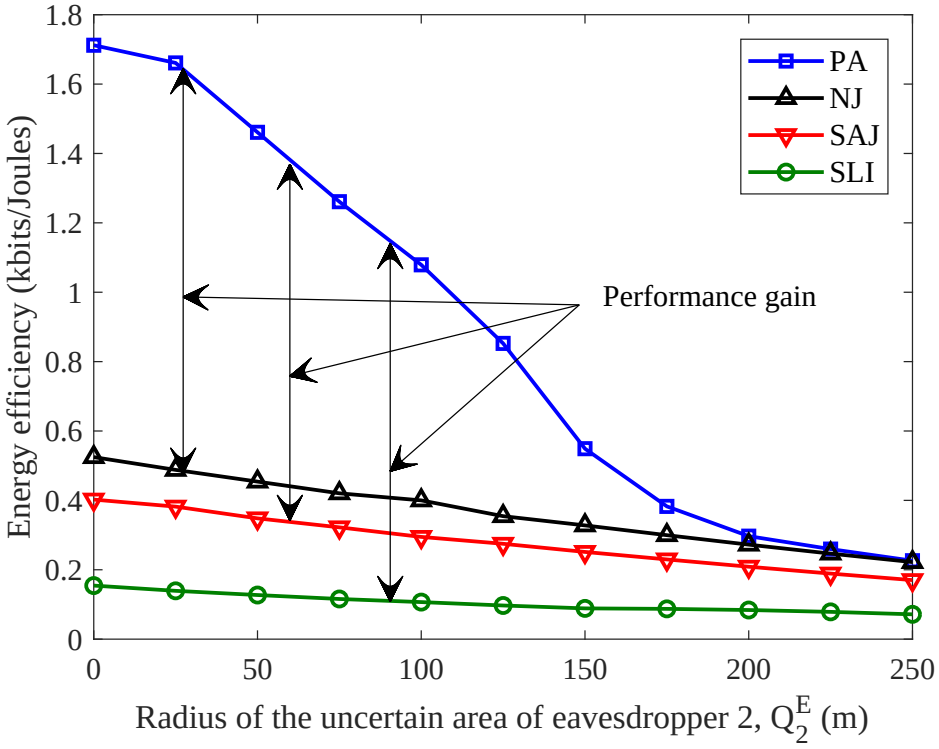

Figure 3.12: Energy efficiency versus the radius of eavesdropper 2's uncertain area.

flight speed for system performance. In other words, varying the speed of UAV can help the system to exploit the system resources efficiently. Furthermore, we can observe that the increasing slope of "PA" is substantially higher than that of other baseline schemes. In fact, the proper design of the artificial noise strategy of the multi-antenna jammer UAV offers the flexibility in designing the trajectory of information UAV and thus facilitates the efficient exploitation of power in our proposed scheme.

Fig. 3.12 depicts the energy efficiency of the considered system versus the radius of the uncertain area of potential eavesdropper 2 for the same schemes as in Fig. 3.11. Note that we choose eavesdropper 2 instead of eavesdropper 1 in this figure. The reason is that the uncertainty of eavesdropper 2 affects the trajectory

of information UAV more significantly since its estimated location is on the straight locus from the initial location to the final location. Although all schemes can guarantee communication security in all the considered cases, it can be observed that the energy efficiencies of both "PA" and baseline schemes decrease with the radius of uncertain areas. Indeed, a larger eavesdropper's uncertain area imposes a more stringent security constraint on the system design, which reduces the flexibility in resource allocation leading to a lower system energy efficiency. Furthermore, even with exact location information of eavesdroppers, all the three baseline schemes can only achieves a much smaller system energy efficiency compared to "PA", which again indicates the contribution of employing a multi-antenna jammer UAV and our proposed design.

3.6 Summary

In this chapter, we jointly designed the information UAV's trajectory, the communication resource allocation strategy, and the jamming policy to maximize the system energy efficiency of a secure UAV-OFDMA communication system. The joint design was formulated as a non-convex optimization problem taking into account the minimum data rate requirement, the maximum tolerable SINR leakage, the minimum safety distance between UAVs, and the imperfect location information of the potential eavesdroppers. An iterative algorithm based on alternating optimization was proposed to achieve a suboptimal solution with a low computational complexity. Simulation results illustrated that the proposed algorithm converges within a small number of iterations and demonstrated some interesting insights. In particular, (1) deploying a decided multiple-antenna UAV serves as a key to improve the system performance in both energy efficiency and communication security; (2) employing a multi-antenna jammer UAV offers an

enhanced flexibility in designing the trajectory of information UAV, which can combat the eavesdropper efficiently to improve the system energy efficiency; (3) optimizing the trajectory of information UAV is important to improve the system energy efficiency.

Chapter 4

Resource Allocation for Power-Efficient IRS-assisted UAV Communications

4.1 Introduction

In the previous chapter, we have studied the joint trajectory, resource allocation, and jamming policy design for energy-efficient secure unmanned aerial vehicle (UAV)-orthogonal frequency division multiple access (OFDMA) communication systems. However, most of the radiated power is wasted due to the broadcast nature of wireless communication channels. Indeed, the increasing concern for energy efficiency calls for advanced energy-efficient UAV communication system designs. On the other hand, intelligent reflection surface (IRS) serves as an emerging technology to customize the communication channels via passive beamforming. Therefore, in this chapter, we aim to minimize the average total power consumption of the IRS-assisted UAV communication system via jointly

optimizing the resource allocation and trajectory while considering the minimum data rate requirement of each user. We propose an iterative algorithm based on alternating optimization to achieve a suboptimal solution efficiently. The numerical results evaluate the system performance gain of the proposed algorithm over baseline schemes without IRS or a fixed straight flight trajectory with a constant flight speed.

4.2 System Model

We consider a UAV-enabled narrowband downlink time division multiple access (TDMA) wireless communication system serving K ground users (GUs) with the assistance of an IRS as shown in Fig. 4.1. The UAV is equipped with $M_{\mathrm{A}x} \times M_{\mathrm{A}y} = M_{\mathrm{A}} > 1$ antennas. To reduce the hardware complexity and the UAV's load weight, we assume that all the M_{A} antennas share a single radio frequency (RF) chain but each antenna has an individual phase shifter. Besides, the IRS consists of $M_{\mathrm{R}x} \times M_{\mathrm{R}y} = M_{\mathrm{R}} > 1$ passive reflecting elements and all the GUs are single-antenna devices. Also, the total service time T is divided into N equal-length time slots with duration time τ (s) for each slot, i.e., $T = N\tau$. Besides, the UAV operates at a constant altitude $H_{\mathrm{A}} > 0$ with a variable flight velocity, while the locations of all the GUs and the IRS are fixed during the whole service time. Since the air-to-ground communication channel is dominated by the line-of-sight (LoS) propagation [44, 45, 57, 58] and the Doppler effect can be well compensated by adopting existing frequency synchronization algorithms, e.g., [126], the channel state information (CSI) of the UAV-to-IRS and UAV-to-GUs links can be determined by their locations[1]. Besides, we assume that the channel between the IRS and GUs are also dominated by LoS links. Thus, the

[1]The more general channel model with Rician fading will be considered in the future work.

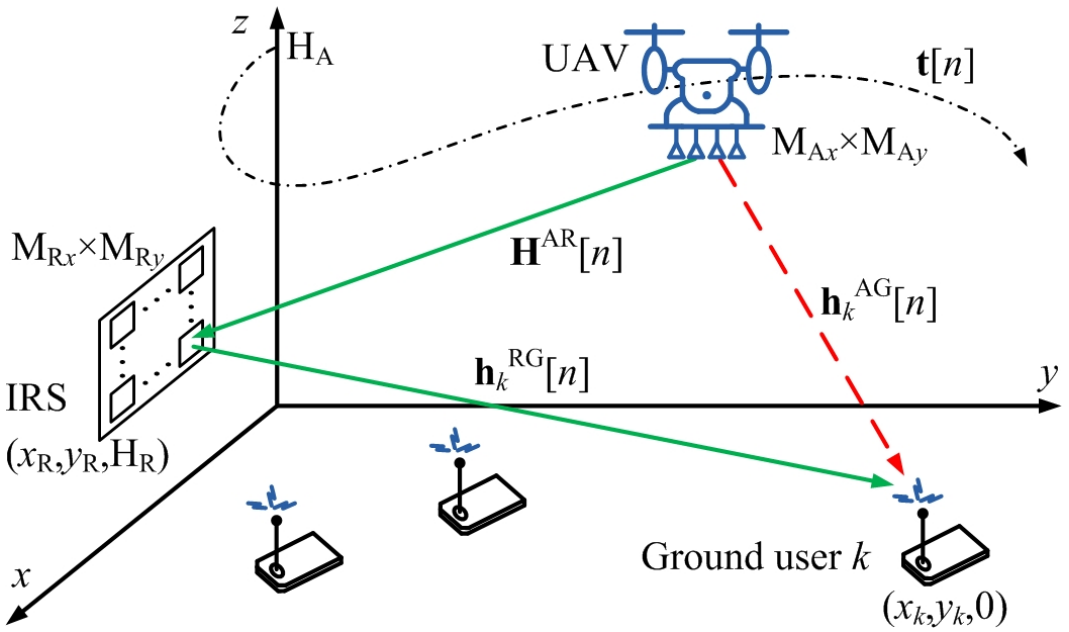

Figure 4.1: The system model of an IRS-assisted UAV communication system.

distances between the UAV and the IRS, the UAV and the GU $k \in \{1, \ldots, K\}$, as well as the IRS and GU k at time slot n are given by

$$d^{\mathrm{AR}}[n] = \sqrt{\|\mathbf{l}_{\mathrm{R}} - \mathbf{t}[n]\|^2 + (H_{\mathrm{A}} - H_{\mathrm{R}})^2}, \tag{4.1}$$

$$d_k^{\mathrm{AG}}[n] = \sqrt{\|\mathbf{l}_k - \mathbf{t}[n]\|^2 + H_{\mathrm{A}}^2}, \text{ and} \tag{4.2}$$

$$d_k^{\mathrm{RG}} = \sqrt{\|\mathbf{l}_{\mathrm{R}} - \mathbf{l}_k\|^2 + H_{\mathrm{R}}^2}, \tag{4.3}$$

respectively. Note that $\mathbf{l}_{\mathrm{R}} = [x_{\mathrm{R}}, y_{\mathrm{R}}]^{\mathrm{T}} \in \mathbb{R}^{2\times 1}$ and $\mathbf{l}_k = [x_k, y_k]^{\mathrm{T}} \in \mathbb{R}^{2\times 1}$ denote the Cartesian coordinate of the IRS[2] and GU k, respectively, while $\mathbf{t}[n] = [x[n], y[n]]^{\mathrm{T}} \in \mathbb{R}^{2\times 1}$ denotes the horizontal trajectory of the UAV at time slot $n \in \{1, \ldots, N\}$.

[2]Since the typical size of each element in a small-scale IRS is of the same order of the wavelength of the carrier frequency (λ_{c}) [127], e.g., $\frac{\lambda_{\mathrm{c}}}{2}$, the distance between elements of the IRS, Δ_{R}, is much shorter than that of the distance between the UAV and the IRS, $d^{\mathrm{AR}}[n]$. Thus, in the proposed system model, we assume that the locations of each element of the IRS are the same, as commonly adopted in the literature [69].

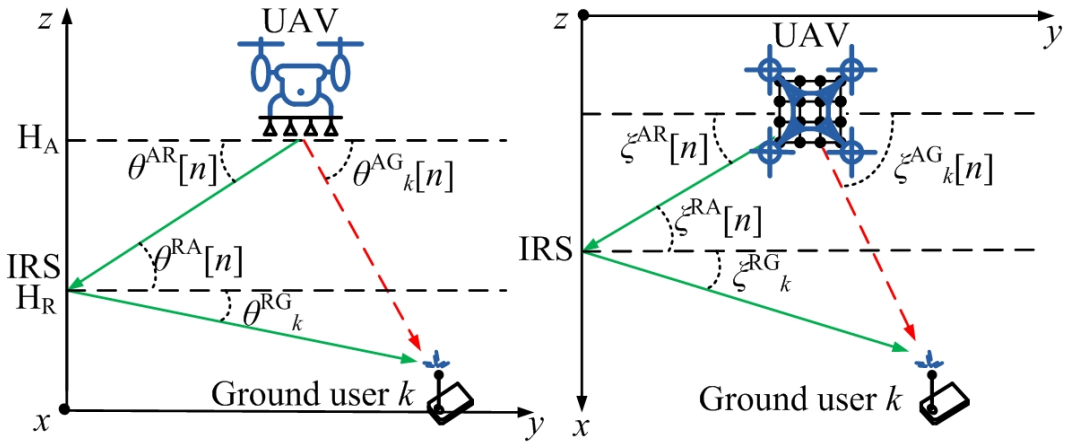

Figure 4.2: The vertical and horizontal AoDs/AoAs between the UAV, IRS, and GU k in the considered downlink communication system are shown on the left hand side and the right side, respectively.

4.2.1 Downlink Channel Model

In the considered system, a GU can be served either by direct transmission, i.e., mode 1, or via the assistance of the IRS, i.e., mode 2. For mode 1, the LoS channel between the UAV and GU k at time slot n is given by

$$\begin{aligned}&\mathbf{h}_{k,1}[n]\\&=\sqrt{\frac{\beta_0}{(d_k^{\mathrm{AG}}[n])^2}}\left[1,e^{-j\frac{2\pi\Delta_{\mathrm{A}x}}{\lambda_{\mathrm{c}}}\sin\theta_k^{\mathrm{AG}}[n]\cos\xi_k^{\mathrm{AG}}[n]},\ldots,e^{-j\frac{2\pi\Delta_{\mathrm{A}x}}{\lambda_{\mathrm{c}}}(M_{\mathrm{A}x}-1)\sin\theta_k^{\mathrm{AG}}[n]\cos\xi_k^{\mathrm{AG}}[n]}\right]^{\mathrm{H}}\\&\otimes\left[1,e^{-j\frac{2\pi\Delta_{\mathrm{A}y}}{\lambda_{\mathrm{c}}}\sin\theta_k^{\mathrm{AG}}[n]\sin\xi_k^{\mathrm{AG}}[n]},\ldots,e^{-j\frac{2\pi\Delta_{\mathrm{A}y}}{\lambda_{\mathrm{c}}}(M_{\mathrm{A}y}-1)\sin\theta_k^{\mathrm{AG}}[n]\sin\xi_k^{\mathrm{AG}}[n]}\right]^{\mathrm{H}}\in\mathbb{C}^{M_{\mathrm{A}}\times 1},\end{aligned}\tag{4.4}$$

where $\theta_k^{\mathrm{AG}}[n]$ and $\xi_k^{\mathrm{AG}}[n]$ represent the vertical and horizontal angle-of-departures (AoDs) from the UAV to GU k at time slot n, respectively. β_0 denotes the reference distance channel power gain and λ_{c} denotes the wavelength of the center carrier frequency. Constants $\Delta_{\mathrm{A}x}$ and $\Delta_{\mathrm{A}y}$ represent the antenna separation at the UAV in x-dimension and y-dimension, respectively. Fig. 4.2 shows the geographic

relations of $\sin\theta_k[n] = \frac{H_{\mathrm{A}}}{d_k^{\mathrm{AG}}[n]}$, $\sin\xi_k[n] = \frac{\|x_k - x[n]\|}{\|\mathbf{l}_k - \mathbf{t}[n]\|}$, and $\cos\xi_k[n] = \frac{\|y_k - y[n]\|}{\|\mathbf{l}_k - \mathbf{t}[n]\|}$. On the other hand, for mode 2, the LoS channel from the UAV to the IRS at time slot n is denoted as

$$
\begin{aligned}
&\mathbf{H}^{\mathrm{AR}}[n] \\
&= \mathbf{h}^{\mathrm{RA}}[n] \otimes (\mathbf{h}^{\mathrm{AR}}[n])^{\mathrm{H}} \in \mathbb{C}^{M_{\mathrm{R}} \times M_{\mathrm{A}}} \\
&= \sqrt{\frac{\beta_0}{(d^{\mathrm{AR}}[n])^2}} \big[1, e^{-j\frac{2\pi\Delta_{\mathrm{R}x}}{\lambda_{\mathrm{c}}}\sin\theta^{\mathrm{RA}}[n]\cos\xi^{\mathrm{RA}}[n]}, \ldots, e^{-j\frac{2\pi\Delta_{\mathrm{R}x}}{\lambda_{\mathrm{c}}}(M_{\mathrm{R}x}-1)\sin\theta^{\mathrm{RA}}[n]\cos\xi^{\mathrm{RA}}[n]}\big]^{\mathrm{H}} \\
&\otimes \big[1, e^{-j\frac{2\pi\Delta_{\mathrm{R}y}}{\lambda_{\mathrm{c}}}\sin\theta^{\mathrm{RA}}[n]\sin\xi^{\mathrm{RA}}[n]}, \ldots, e^{-j\frac{2\pi\Delta_{\mathrm{R}y}}{\lambda_{\mathrm{c}}}(M_{\mathrm{R}y}-1)\sin\theta^{\mathrm{RA}}[n]\sin\xi^{\mathrm{RA}}[n]}\big]^{\mathrm{H}} \\
&\otimes \big[1, e^{-j\frac{2\pi\Delta_{\mathrm{A}x}}{\lambda_{\mathrm{c}}}\sin\theta^{\mathrm{AR}}[n]\cos\xi^{\mathrm{AR}}[n]}, \ldots, e^{-j\frac{2\pi\Delta_{\mathrm{A}x}}{\lambda_{\mathrm{c}}}(M_{\mathrm{A}x}-1)\sin\theta^{\mathrm{AR}}[n]\cos\xi^{\mathrm{AR}}[n]}\big] \\
&\otimes \big[1, e^{-j\frac{2\pi\Delta_{\mathrm{A}y}}{\lambda_{\mathrm{c}}}\sin\theta^{\mathrm{AR}}[n]\sin\xi^{\mathrm{AR}}[n]}, \ldots, e^{-j\frac{2\pi\Delta_{\mathrm{A}y}}{\lambda_{\mathrm{c}}}(M_{\mathrm{A}y}-1)\sin\theta^{\mathrm{AR}}[n]\sin\xi^{\mathrm{AR}}[n]}\big],
\end{aligned} \tag{4.5}
$$

where $\mathbf{h}^{\mathrm{RA}}[n]$ and $\mathbf{h}^{\mathrm{AR}}[n]$ are the channel vectors containing the angle-of-arrival (AoA) and AoD, respectively. Constants $\Delta_{\mathrm{R}x}$ and $\Delta_{\mathrm{R}y}$ represent the reflecting element separation at the IRS in x-dimension and y-dimension, respectively. As shown in Fig. 4.2, $\theta^{\mathrm{AR}}[n]$ and $\xi^{\mathrm{AR}}[n]$ are the vertical and horizontal AoDs from the UAV to the IRS, respectively. $\theta^{\mathrm{RA}}[n]$ and $\xi^{\mathrm{RA}}[n]$ denote the vertical and horizontal AoAs between the UAV and the IRS, respectively. It can be observed that $\theta^{\mathrm{AR}}[n] = \theta^{\mathrm{RA}}[n]$ and $\xi^{\mathrm{AR}}[n] = \xi^{\mathrm{RA}}[n]$. Note that $\sin\theta^{\mathrm{AR}}[n] = \sin\theta^{\mathrm{RA}}[n] = \frac{\|H_{\mathrm{A}} - H_{\mathrm{R}}\|}{d^{\mathrm{AR}}[n]}$, $\sin\xi^{\mathrm{AR}}[n] = \sin\xi^{\mathrm{RA}}[n] = \frac{\|x_{\mathrm{R}} - x[n]\|}{\|\mathbf{l}_{\mathrm{R}} - \mathbf{t}[n]\|}$, and $\cos\xi^{\mathrm{AR}}[n] = \cos\xi^{\mathrm{RA}}[n] = \frac{\|y_{\mathrm{R}} - y[n]\|}{\|\mathbf{l}_{\mathrm{R}} - \mathbf{t}[n]\|}$. Besides, the LoS channel from the IRS to GU k is given by

$$
\begin{aligned}
\mathbf{h}_k^{\mathrm{RG}} = &\sqrt{\frac{\beta_0}{(d_k^{\mathrm{RG}})^2}} \big[1, e^{-j\frac{2\pi\Delta_{\mathrm{R}x}}{\lambda_{\mathrm{c}}}\sin\theta_k^{\mathrm{RG}}\cos\xi_k^{\mathrm{RG}}}, \ldots, e^{-j\frac{2\pi\Delta_{\mathrm{R}x}}{\lambda_{\mathrm{c}}}(M_{\mathrm{R}x}-1)\sin\theta_k^{\mathrm{RG}}\cos\xi_k^{\mathrm{RG}}}\big]^{\mathrm{H}} \\
&\otimes \big[1, e^{-j\frac{2\pi\Delta_{\mathrm{R}y}}{\lambda_{\mathrm{c}}}\sin\theta_k^{\mathrm{RG}}\sin\xi_k^{\mathrm{RG}}}, \ldots, e^{-j\frac{2\pi\Delta_{\mathrm{R}y}}{\lambda_{\mathrm{c}}}(M_{\mathrm{R}y}-1)\sin\theta_k^{\mathrm{RG}}\sin\xi_k^{\mathrm{RG}}}\big]^{\mathrm{H}} \in \mathbb{C}^{M_{\mathrm{R}} \times 1},
\end{aligned} \tag{4.6}
$$

where θ_k^{RG} and ξ_k^{RG} denote the vertical and horizontal AoDs from the IRS to GU k, respectively. Note that we have $\sin\theta_k^{\mathrm{RG}} = \frac{H_{\mathrm{R}}}{d_k^{\mathrm{RG}}}$, $\sin\xi_k^{\mathrm{RG}} = \frac{\|x_{\mathrm{R}}-x_k\|}{\|\mathbf{l}_{\mathrm{R}}-\mathbf{l}_k\|}$, and $\cos\xi_k^{\mathrm{RG}} = \frac{\|y_{\mathrm{R}}-y_k\|}{\|\mathbf{l}_{\mathrm{R}}-\mathbf{l}_k\|}$ as shown in Fig. 4.2.

Moreover, the IRS manipulates the reflected signals to GUs by introducing controlled phase shifts. The phase control matrix imposed by the IRS for GU k at time slot n is given by

$$\mathbf{\Phi}_k[n] = \mathrm{diag}(e^{j\phi_{1,1,k}[n]}, \ldots, e^{j\phi_{m_{\mathrm{R}x},m_{\mathrm{R}y},k}[n]}, \ldots, e^{j\phi_{M_{\mathrm{R}x},M_{\mathrm{R}y},k}[n]}) \in \mathbb{C}^{M_{\mathrm{R}}\times M_{\mathrm{R}}}, \quad (4.7)$$

where $\phi_{m_{\mathrm{R}x},m_{\mathrm{R}y},k}[n] \in [0, 2\pi)$, $m_{\mathrm{R}x} = \{1, \ldots, M_{\mathrm{R}x}\}$, $m_{\mathrm{R}y} = \{1, \ldots, M_{\mathrm{R}y}\}$ represents the phase control introduced to the $(m_{\mathrm{R}x}, m_{\mathrm{R}y})$-th reflecting element of the IRS at time slot n. Without loss of generality, for mode 2, we define the end-to-end effective channel between the UAV and ground GU k reflected by the IRS at time slot n is given by

$$(\mathbf{h}_{k,2}[n])^{\mathrm{H}} = (\mathbf{h}_k^{\mathrm{RG}}[n])^{\mathrm{H}}\mathbf{\Phi}_k[n]\mathbf{H}^{\mathrm{AR}}[n] \in \mathbb{C}^{1\times M_{\mathrm{A}}}. \quad (4.8)$$

4.2.2 Signal Model

In the considered system, transmission from the UAV is scheduled to either via reflected path with the help of IRS or through the direct path from the UAV to the GUs. Thus, the received signal of the ground GU k at time slot n is given by

$$y_k^{\mathrm{Rx}}[n] = s_{k,i}[n](\mathbf{h}_{k,i}[n])^{\mathrm{H}}\boldsymbol{w}_{k,i}[n]p_{k,i}[n]x_k^{\mathrm{Tx}}[n] + z_k[n], \quad (4.9)$$

where $\boldsymbol{w}_{k,i}[n] \in \mathbb{C}^{M_{\mathrm{A}}\times 1}$ denotes a unit-power beamformer adopted by the UAV to serve GU k with mode $i \in \{1, 2\}$. Running index i is the mode index, where $i = 1$ and $i = 2$ denote the direct transmission mode from the UAV to GUs and

Table 4.1: Physical meaning of parameters in flight power consumption model of UAV [3].

Parameters	Physical meaning	Simulation values
Ω	Blade angular velocity	300 (radians/second)
r	Rotor radius	0.4 (meter)
ρ	Air density	1.225 (kg/m^3)
s	Rotor solidity	0.05 (m^3)
A_{r}	Rotor disc area	0.503 (m^2)
v_0	Induced velocity for rotor in forwarding flight	4.03 (meter/second)
d_0	Fuselage drag ratio	0.3
P_o	Blade profile power in hovering status	79.86 (watt)
P_i	Induced power in hovering status	88.63 (watt)

the reflection mode through the IRS, respectively. We represent $s_{k,i}[n] = 1$ when user k selects mode i at time slot n. Otherwise, $s_{k,i}[n] = 0$. The transmit power allocated to user k with mode i at time slot n is presented as $p_{k,i}[n]$. Complex scalar $x_k^{\mathrm{Tx}}[n] \in \mathbb{C}$ denotes a modulated symbol and $z_k[n] \sim \mathcal{CN}(0, \sigma^2)$ denotes the background noise at GU k at time slot n, where σ^2 denotes the noise power. In (4.9), $s_{k,i}[n]$ denotes that mode i is scheduled to user k at time slot n. In particular, since a single RF chain is equipped at the UAV transmitter, only one transmission mode can be supported to user k at time slot n, i.e., direct mode or reflection mode. Meanwhile, all the other users $k' \neq k$ ignore the signal of user k from the reflected path or direct path as TDMA is adopted. Then, the achievable data rate of GU k at time slot n associated with mode i is given by

$$R_{k,i}[n] = s_{k,i}[n] \log_2 \left(1 + \frac{p_{k,i}[n] |\mathbf{h}_{k,i}^{\mathrm{H}}[n] \boldsymbol{w}_{k,i}[n]|^2}{\sigma^2} \right). \tag{4.10}$$

4.2.3 UAV Power Consumption Model

The flight power consumption of the UAV is finite and plays an important role in UAV-based communications due to the limited battery capacity of the UAV. In this system, we consider a rotary wing UAV since it has a higher mobility than that of the fixed wing UAV. According to [3], the flight power consumption of a rotary wing UAV is given by

$$P_{\text{flight}}^{\text{UAV}}[n] = \underbrace{P_o\left(1+\frac{3\|\mathbf{v}[n]\|^2}{\Omega^2 r^2}\right)}_{\text{Bladeprofile}} + \underbrace{\frac{P_i v_0}{\|\mathbf{v}[n]\|}}_{\text{Induced}} + \underbrace{\frac{1}{2}d_0\rho s A_{\text{r}}\|\mathbf{v}[n]\|^3}_{\text{Parasite}}, \tag{4.11}$$

where $\mathbf{v}[n] = [v_x[n], v_y[n]]^{\text{T}} \in \mathbb{R}^{2\times 1}$. The physical meanings of the parameters in (4.11) are summarized in Table 4.1.

4.2.4 IRS Power Consumption Model

In practice, an IRS is an energy-limited device [128] which cannot be always turned on to alter the condition of the communication channels. Thus, it is important to take the power consumption of the IRS into account when it is active. The total energy consumption of the IRS during the service period is given by

$$P_{\text{total}}^{\text{IRS}} = \sum_{n=1}^{N}\sum_{k=1}^{K} s_{k,2}[n] M_{\text{R}} p^{\text{IRS}}, \tag{4.12}$$

where $p^{\text{IRS}} > 0$ denotes the power consumption of each element of the IRS for controlling the phase of the reflected signal when it is active.

4.3 Problem Formulation

The optimization problem for minimizing the total power consumption via jointly designing the user scheduling $\mathcal{S} = \{s_{k,i}[n], \forall n, k, i\}$, power allocation $\mathcal{P} = \{p_{k,i}[n], \forall n, k, i\}$, the UAV's trajectory $\mathcal{T} = \{\mathbf{t}[n], \forall n\}$, the UAV's flight velocity $\mathcal{V} = \{\mathbf{v}[n], \forall n\}$, the beamforming precoder $\mathcal{W} = \{\mathbf{w}_{k,i}[n], \forall n, k, i\}$, and phase control policy of the IRS $\mathbf{\Phi} = \{\mathbf{\Phi}_k[n], \forall n, k\}$ is formulated as:

$$\underset{\mathcal{S},\mathcal{P},\mathcal{T},\mathcal{V},\mathcal{W},\mathbf{\Phi}}{\text{minimize}} \sum_{n=1}^{N}\sum_{k=1}^{K}\sum_{i=1}^{2} s_{k,i}[n]p_{k,i}[n] + P_{\text{total}}^{\text{IRS}} + \sum_{n=1}^{N} P_{\text{flight}}^{\text{UAV}}[n] \tag{4.13}$$

$$\begin{aligned}
\text{s.t. C1}: & \; s_{k,i}[n] \in \{0,1\}, \forall n, k, i, \\
\text{C2}: & \sum_{k=1}^{K}\sum_{i=1}^{2} s_{k,i}[n] \leq 1, \forall n, \\
\text{C3}: & \; p_{k,i}[n] \geq 0, \forall n, k, i, \\
\text{C4}: & \sum_{k=1}^{K}\sum_{i=1}^{2} s_{k,i}[n]p_{k,i}[n] \leq P_{\max}^{\text{UAV-Tx}}, \forall n, k, \\
\text{C5}: & \; P_{\text{total}}^{\text{IRS}}\tau \leq E_{\max}^{\text{IRS}}, \\
\text{C6}: & \sum_{n=1}^{N}\sum_{i=1}^{2} R_{k,i}[n] \geq R_{\min}, \forall k, \\
\text{C7}: & \; \mathbf{t}[n+1] = \mathbf{t}[n] + \mathbf{v}[n]\tau, n = 1, \ldots, N-1, \\
\text{C8}: & \; \mathbf{t}[1] = \mathbf{t}_0, \\
\text{C9}: & \; \mathbf{t}[N] = \mathbf{t}_{\text{F}}, \\
\text{C10}: & \; \|\mathbf{v}[n]\| \leq V_{\max}, \forall n, \\
\text{C11}: & \; \|\mathbf{v}[n+1] - \mathbf{v}[n]\| \leq V_{\text{acc}}\tau, \forall n.
\end{aligned}$$

Note that C1 and C2 are user scheduling constraints such at most one user is scheduled through at most one transmission mode in each time slot, i.e.,

TDMA. C3 is the non-negative constraint for the transmit power from the UAV. $P_{\max}^{\mathrm{UAV-Tx}}$ in C4 denotes the maximum transmission power of the UAV. $E_{\max}^{\mathrm{IRS}}$ in C5 represents the energy budget of the IRS for N time slots. C6 is introduced to guarantee the minimum achievable data rate for each GU. Constraint C7 denotes the relationship between the UAV's trajectory and its flight velocity. C8 and C9 are the starting location and the final location of the UAV, respectively. $V_{\max}$ and V_{acc} in constraints C10 and C11 denote the maximum flight velocity and the maximum flight acceleration, respectively.

4.4 Problem Solution

The formulated problem in (4.13) is a non-convex optimization problem and there is no standard method to obtain the globally optimal solution. In the following, we first simplify the studied problem by exploiting its special structure at the optimality. It can be observed that the minimum power consumption in (4.13) is achieved when the maximum ratio transmission (MRT)[3] is employed by the UAV which maximizes the transmission efficiency, i.e., that $\boldsymbol{w}_{k,1}[n] = \frac{1}{\sqrt{\mathrm{M_A}}}\mathbf{h}_{k,1}[n] \in \mathbb{C}^{M_{\mathrm{A}}\times 1}$ and $\boldsymbol{w}_{k,2}[n] = \frac{1}{\sqrt{\mathrm{M_A}}}\mathbf{h}^{\mathrm{AR}}[n] \in \mathbb{C}^{M_{\mathrm{A}}\times 1}$. Thus, with the optimal beamforming at the UAV, the direct transmission mode channel from the UAV to the GUs and

[3]Note that the adopted MRT is indeed a kind of analog beamforming as the amplitude of each element of the beamformer is 1.

the reflection mode with the IRS are given by

$$h_{k,1}[n] = \mathbf{h}_{k,1}^{\mathrm{H}}[n]\boldsymbol{w}_{k,1}[n] = \frac{\sqrt{M_{\mathrm{A}}}\beta_0}{d_k^{\mathrm{AG}}[n]} \text{ and} \tag{4.14}$$

$$\begin{aligned} h_{k,2}[n] &= (\mathbf{h}_k^{\mathrm{RG}})^{\mathrm{H}}\boldsymbol{\Phi}_k[n]\big(\mathbf{h}^{\mathrm{RA}}[n] \otimes (\mathbf{h}^{\mathrm{AR}}[n])^{\mathrm{H}}\big)\boldsymbol{w}_{k,2}[n] \\ &= \sqrt{M_{\mathrm{A}}}(\mathbf{h}_k^{\mathrm{RG}})^{\mathrm{H}}\boldsymbol{\Phi}_k[n]\mathbf{h}^{\mathrm{RA}}[n] \\ &= \sqrt{M_{\mathrm{A}}}\beta_0 \sum_{m_{\mathrm{R}x}=1}^{M_{\mathrm{R}x}} \sum_{m_{\mathrm{R}y}=1}^{M_{\mathrm{R}y}} \Bigg[\sqrt{\frac{\kappa}{1+\kappa}} e^{-j\frac{2\pi\Delta_{\mathrm{R}}}{\lambda_{\mathrm{c}}}\Theta_k^{\mathrm{RG}}} \\ &+ \sqrt{\frac{1}{1+\kappa}}\Delta h_{m_{\mathrm{R}x},m_{\mathrm{R}y},k}\Bigg] e^{j\phi_{m_{\mathrm{R}x},m_{\mathrm{R}y},k}[n]} e^{-j\frac{2\pi\Delta_{\mathrm{R}}}{\lambda_{\mathrm{c}}}\Theta^{\mathrm{RA}}[n]} \\ &= \frac{\sqrt{M_{\mathrm{A}}}M_{\mathrm{R}}\beta_0}{d_k^{\mathrm{RG}}d^{\mathrm{AR}}[n]}, \end{aligned} \tag{4.15}$$

respectively. Note that $\Theta_k^{\mathrm{RG}} = \big[(m_{\mathrm{R}x}-1)\sin\theta_k^{\mathrm{RG}}\cos\xi_k^{\mathrm{RG}} + (m_{\mathrm{R}y}-1)\sin\theta_k^{\mathrm{RG}}\sin\xi_k^{\mathrm{RG}}\big]$, $\Theta^{\mathrm{RA}}[n] = \big[(m_{\mathrm{R}x}-1)\sin\theta^{\mathrm{RA}}[n]\cos\xi^{\mathrm{RA}}[n] + (m_{\mathrm{R}y}-1)\sin\theta^{\mathrm{RA}}[n]\sin\xi^{\mathrm{RA}}[n]\big]$. Next, we introduce the optimal phase shift adopted at the IRS in the following theorem.

Theorem 4.1. *The optimal phase control policy $\phi_{m_{\mathrm{R}x},m_{\mathrm{R}y},k}[n]$ in each element of the IRS for serving GU k at time slot n when $s_{k,i}[n] = 1$ is given by*

$$\begin{aligned} &\phi_{m_{\mathrm{R}x},m_{\mathrm{R}y},k}[n] \\ &= \frac{2\pi\Delta_{\mathrm{R}}}{\lambda_{\mathrm{c}}}\big[(m_{\mathrm{R}x}-1)(\sin\theta^{\mathrm{RA}}[n]\cos\xi^{\mathrm{RA}}[n] + \sin\theta_k^{\mathrm{RG}}\cos\xi_k^{\mathrm{RG}}) \\ &+ (m_{\mathrm{R}y}-1)(\sin\theta^{\mathrm{RA}}[n]\sin\xi^{\mathrm{RA}}[n] + \sin\theta_k^{\mathrm{RG}}\sin\xi_k^{\mathrm{RG}})\big], \forall m_{\mathrm{R}x}, m_{\mathrm{R}y}, n, k, \end{aligned} \tag{4.16}$$

to maximize the reflection mode channel gain in the sense of power consumption minimization.

Proof: Please refer to appendix C.1 for a proof of Theorem 4.1. □

Then, the achievable data rate of GU k at time slot n with mode i is given by

$$R_{k,i}[n] = s_{k,i}[n] \log_2 \left(1 + \frac{p_{k,i}[n]|h_{k,i}[n]|^2}{\sigma^2}\right). \tag{4.17}$$

Thus, the proposed optimization problem in (4.13) can be rewritten as

$$\begin{aligned} \underset{\mathcal{S},\mathcal{P},\mathcal{T},\mathcal{V}}{\text{minimize}} \quad & \sum_{n=1}^{N}\sum_{k=1}^{K}\sum_{i=1}^{2} s_{k,i}[n]p_{k,i}[n] + P_{\text{total}}^{\text{IRS}} + \sum_{n=1}^{N} P_{\text{flight}}^{\text{UAV}}[n] \\ \text{s.t.} \quad & \text{C1} - \text{C11}, \end{aligned} \tag{4.18}$$

which is still non-convex. Next, to facilitate the design of an efficient method to obtain a suboptimal solution of the formulated problem, similar to Chapter 3, we adopt the alternating optimization method by dividing the optimization problem in (4.13) into two subproblems and solve them iteratively to achieve a suboptimal solution. In particular, sub-problem 1 optimizes user scheduling $\mathcal{S}$ and power allocation strategy $\mathcal{P}$ for a given UAV's trajectory design $\mathcal{T}$ and flight velocity $\mathcal{V}$, while sub-problem 2 optimizes the UAV's trajectory $\mathcal{T}$ and flight velocity $\mathcal{V}$ for a given user scheduling $\mathcal{S}$ and power allocation strategy $\mathcal{P}$. Now, we study the solution of sub-problem 1.

4.4.1 Sub-problem 1: Optimizing User Scheduling and Power Allocation

In this subproblem, for any given trajectory and flight velocity of the UAV, the problem formulation can be expressed as follows:

$$\begin{aligned} \underset{\mathcal{S},\mathcal{P}}{\text{minimize}} \ & \sum_{n=1}^{N}\sum_{k=1}^{K}\sum_{i=1}^{2} s_{k,i}[n]p_{k,i}[n] + P_{\text{total}}^{\text{IRS}} + \sum_{n=1}^{N} P_{\text{flight}}^{\text{UAV}}[n] \\ \text{s.t. } & \text{C1} - \text{C6}. \end{aligned} \tag{4.19}$$

Note that constraints C2 and C5 are linear constraints with respect to (w.r.t.) user scheduling $s_{k,i}[n]$. Thus, in order to handle the nonconvexity of the problem, we relax the binary constraint C1 as

$$\widetilde{\text{C1}} : 0 \leq s_{k,i}[n] \leq 1, \forall n, k, \tag{4.20}$$

which can be interpreted as a time-sharing factor [129]. Then, we introduce a slack variable $\tilde{p}_{k,i}[n] = s_{k,i}[n]p_{k,i}[n]$ to the optimization problem. Thus, the optimization problem in (4.19) can be rewritten as its equivalent form

$$\begin{aligned} \underset{\mathcal{S},\tilde{\mathcal{P}}}{\text{minimize}} \ & \tilde{P}_{\text{total}} \\ \text{s.t. } & \widetilde{\text{C1}}, \text{C2}, \text{C5}, \\ & \widetilde{\text{C3}} : \tilde{p}_{k,i}[n] \geq 0, \forall n, k, i, \\ & \widetilde{\text{C4}} : \sum_{k=1}^{K}\sum_{i=1}^{2} \tilde{p}_{k,i}[n] \leq P_{\text{max}}^{\text{UAV}-\text{Tx}}, \forall n, \\ & \widetilde{\text{C6}} : \sum_{n=1}^{N}\sum_{i=1}^{2} \tilde{R}_{k,i}[n] \geq R_{\text{min}}, \forall k, \end{aligned} \tag{4.21}$$

where $\tilde{\mathcal{P}} = \{\tilde{p}_{k,i}[n], \forall n, k, i\}$,

$$\tilde{P}_{\text{total}} = \sum_{n=1}^{N}\sum_{k=1}^{K}\sum_{i=1}^{2}\tilde{p}_{k,i}[n] + P_{\text{total}}^{\text{IRS}} + \sum_{n=1}^{N}P_{\text{flight}}^{\text{UAV}}[n], \text{ and} \tag{4.22}$$

$$\tilde{R}_{k,i}[n] = s_{k,i}[n]\log_2\left(1 + \frac{\tilde{p}_{k,i}[n]|h_{k,i}[n]|^2}{s_{k,i}[n]\sigma^2}\right). \tag{4.23}$$

Note that the optimization problem in (4.21) is jointly convex w.r.t. user scheduling $s_{k,i}[n]$ and power allocation $\tilde{p}_{k,i}[n]$. Besides, it satisfies the Slater's constraint qualification. Thus, the strong duality holds and the duality gap is zero [22]. Therefore, solving the dual problem is equivalent to solving the primal optimization problem of sub-problem 1 in (4.21). Next, we focus on solving the dual problem and the Lagrangian function of (4.21) is given by

$$\begin{aligned}
&\mathcal{L}(\boldsymbol{\vartheta}, \boldsymbol{\zeta}, \delta, \boldsymbol{\eta}, \mathcal{S}, \tilde{\mathcal{P}}) \qquad (4.24)\\
&= \sum_{n=1}^{N}(1+\zeta_n)\sum_{k=1}^{K}\sum_{i=1}^{2}\tilde{p}_{k,i}[n] + \sum_{n=1}^{N}P_{\text{flight}}^{\text{UAV}}[n]\\
&+ \sum_{n=1}^{N}\vartheta_n\left(\sum_{k=1}^{K}\sum_{i=1}^{2}s_{k,i}[n] - 1\right) - \sum_{n=1}^{N}\zeta_n P_{\max}^{\text{UAV-Tx}}\\
&+ \delta\left(P_{\text{total}}^{\text{IRS}}\tau - E_{\max}^{\text{IRS}}\right) + \sum_{k=1}^{K}\eta_k\left(R_{\min} - \sum_{n=1}^{N}\sum_{i=1}^{2}\tilde{R}_{k,i}[n]\right),
\end{aligned}$$

where $\boldsymbol{\vartheta} = \{\vartheta_n, \forall n\}$, $\boldsymbol{\zeta} = \{\zeta_n, \forall n\}$, δ, and $\boldsymbol{\eta} = \{\eta_k, \forall k\}$ represent the non-negative Lagrange multipliers corresponding to constraints C2, $\widetilde{\text{C4}}$, C5, and $\widetilde{\text{C6}}$, respectively. Constraints $\widetilde{\text{C1}}$ and $\widetilde{\text{C3}}$ will be considered in the Karush-Kuhn-Tucker (KKT) conditions when designing the optimal solution of the transformed problem in the following. Then, the dual problem of (4.21) is given by

$$\mathcal{D} = \underset{\boldsymbol{\vartheta},\boldsymbol{\zeta},\delta,\boldsymbol{\eta},\geq 0}{\text{maximize}}\ \underset{\mathcal{S},\tilde{\mathcal{P}}}{\text{minimize}}\ \mathcal{L}(\boldsymbol{\vartheta}, \boldsymbol{\zeta}, \delta, \boldsymbol{\eta}, \mathcal{S}, \tilde{\mathcal{P}}). \tag{4.25}$$

In the following, the dual problem in (4.25) can be solved iteratively by dual decomposition. In particular, we divide the dual problem into two nested layers: Layer 1, minimizing the Lagrangian over user scheduling $\mathcal{S}$ and power allocation $\tilde{\mathcal{P}}$ in (4.25) for given the Lagrange multipliers $\boldsymbol{\vartheta}, \boldsymbol{\zeta}, \delta$, and $\boldsymbol{\eta}$; Layer 2, maximizing the Lagrangian function over $\boldsymbol{\vartheta}, \boldsymbol{\zeta}, \delta$, and $\boldsymbol{\eta}$ for given user scheduling $\mathcal{S}$ and power allocation $\tilde{\mathcal{P}}$.

Solution of Layer 1 (User Scheduling and Power Allocation): The optimal power allocation for GU k at time slot n with mode i is given by

$$\tilde{p}^*_{k,i}[n] = s_{k,i}[n] p^*_{k,i}[n] = s_{k,i}[n] \left[\frac{\eta_k}{(1+\zeta_n)\ln 2} - \frac{\sigma^2}{|h_{k,i}[n]|^2} \right]^+, \forall n, k, i. \tag{4.26}$$

Note that the optimal power allocation strategy in (4.26) is the classic multiuser water-filling solution. The GUs' water-levels, i.e., $\frac{\eta_k}{(1+\zeta_n)\ln 2}$, are normally different at time slot n. In particular, the Lagrange multiplier η_k drives the UAV to increase the communication power such that the minimum data rate requirement $R_{\min}$ can be achieved for GU k. In contrast, the Lagrange multiplier ζ_n reduces the water-level to satisfy the maximum communication power constraint. Then, in order to find the optimal user scheduling, we perform the derivatives of the Lagrangian function w.r.t. $s_{k,1}[n]$ and $s_{k,2}[n]$ which are given by

$$A_{k,1}[n] = \vartheta_n - \eta_k \log_2 \left(1 + \frac{p_{k,1}[n]|h_{k,1}[n]|^2}{\sigma^2} \right) \text{ and} \tag{4.27}$$

$$A_{k,2}[n] = \vartheta_n - \eta_k \log_2 \left(1 + \frac{p_{k,2}[n]|h_{k,2}[n]|^2}{\sigma^2} \right) + \delta M_{\mathrm{R}} p^{\mathrm{IRS}} \tau, \tag{4.28}$$

respectively. Note that $A_{k,i}[n] \geq 0$ represents the benefit of the system performance if time slot n is allocated to user k with mode i. Since $A_{k,i}[n]$ in (4.27) and (4.28) is independent of $s_{k,i}[n]$, based on constraint C2, the optimal

user scheduling for GU k at time slot n with mode i is given by

$$s^*_{k,i}[n] = \begin{cases} 1, & k,i = \arg\min\limits_{k',i'}\{A_{k',i'}[n]\}, \\ 0, & \text{otherwise}, \end{cases} \quad \forall n. \tag{4.29}$$

As the relationship between $A_{k,1}[n]$ and $A_{k,2}[n]$ shown in (4.28), time slot n is allocated to user k with reflection mode if the cost in using the IRS, i.e., $\delta M_{\mathrm{R}} p^{\mathrm{IRS}} \tau$, is less than the gain obtained by switching from direct transmission to reflection mode, i.e., $\eta_k \left[\log_2\left(1+\frac{p_{k,2}[n]|h_{k,2}[n]|^2}{\sigma^2}\right) - \log_2\left(1+\frac{p_{k,1}[n]|h_{k,1}[n]|^2}{\sigma^2}\right)\right]$.

Solution of Layer 2 (Master Problem): In order to solve the master maximization problem in (4.25), we adopt the gradient method to update the Lagrange multipliers via

$$\zeta_n(j_1+1) = \left[\zeta_n(j_1) - \lambda_2(j_1) \times \left(P^{\mathrm{UAV-Tx}}_{\max} - \sum_{k=1}^{K}\sum_{i=1}^{2} \tilde{p}_{k,i}[n]\right)\right]^+, \forall n, \tag{4.30}$$

$$\delta(j_1+1) = \left[\delta(j_1) - \lambda_3(j_1) \times \left(E^{\mathrm{IRS}}_{\max} - P^{\mathrm{IRS}}_{\mathrm{total}}\tau\right)\right]^+, \text{and} \tag{4.31}$$

$$\eta_k(j_1+1) = \left[\eta_k(j_1) - \lambda_4(j_1) \times \left(\sum_{n=1}^{N}\sum_{i=1}^{2} \tilde{R}_{k,i}[n] - R_{\min}\right)\right]^+, \forall k, \tag{4.32}$$

respectively, where $j_1 \geq 0$ and $\lambda_\alpha(j_1) \geq 0, \alpha \in \{1,\ldots,4\}$, represent the iteration index for iteratively solving sub-problem 1 and the step size satisfying the infinite travel condition, respectively [20]. Next, we solve Layer 1 minimization problem in (4.25) by updating the resource allocation with the updated Lagrange multipliers in (4.30)–(4.32). The convergence of the proposed algorithm and obtaining the optimal solution of sub-problem 1 is guaranteed [20], as the objective in sub-problem 1 is finite and non-increasing over iterations for solving the optimization problem in (4.21).

4.4.2 Sub-problem 2: Optimizing UAV's Trajectory and Flight Velocity

In this subproblem, for a given user scheduling and power allocation strategy, we can express the optimization problem as

$$\begin{aligned} \underset{\mathcal{T},\mathcal{V}}{\text{minimize}} \ & \sum_{n=1}^{N}\sum_{k=1}^{K}\sum_{i=1}^{2} s_{k,i}[n]p_{k,i}[n] + P_{\text{total}}^{\text{IRS}} + \sum_{n=1}^{N} P_{\text{flight}}^{\text{UAV}}[n] \\ \text{s.t. } & \text{C6} - \text{C11}. \end{aligned} \tag{4.33}$$

Note that the optimization problem in (4.33) is nonconvex and the nonconvexity is due to constraint C6 and the function of the UAV's flight power consumption $P_{\text{flight}}^{\text{UAV}}[n]$ w.r.t. $\mathbf{t}[n]$ and $\mathbf{v}[n]$, respectively. Thus, to tackle this nonconvexity, we first introduce two slack variables $u_{k,i}[n]$ and $m[n]$, to rewrite the problem in (4.33) into its equivalent form:

$$\begin{aligned} \underset{\mathcal{T},\mathcal{V},\mathcal{U},\mathcal{M}}{\text{minimize}} \ & \bar{P}_{\text{total}} \\ \text{s.t. } & \text{C7} - \text{C11}, \\ & \text{C6}: \sum_{n=1}^{N}\sum_{i=1}^{2} \bar{R}_{k,i}[n] \geq R_{\min}, \forall k, \\ & \text{C12}: \|\mathbf{l}_k - \mathbf{t}[n]\|^2 + H_{\text{A}}^2 \leq u_{k,1}[n], \forall n, k, \\ & \text{C13}: \|\mathbf{l}_{\text{R}} - \mathbf{t}[n]\|^2 + (H_{\text{A}} - H_{\text{R}})^2 \leq u_{k,2}[n], \forall n, k, \\ & \text{C14}: m[n] \geq 0, \forall n, \\ & \text{C15}: \|\mathbf{v}[n]\|^2 \geq m^2[n], \forall n, \end{aligned} \tag{4.34}$$

where $\mathcal{U} = \{u_{k,i}[n], \forall n, k, i\}$ and $\mathcal{M} = \{m[n], \forall n\}$,

Algorithm 4.1 Overall Algorithm for Solving Problem in (4.13)

1: Initialize the convergence tolerance $\epsilon_1 \rightarrow 0$, the maximum number of iterations $J_{1,\max}$, the initial iteration index $j_1 = 0$, and the initial trajectory $\{\mathbf{t}[n], \mathbf{v}[n]\}$
2: **repeat**
3: Set $j_1 = j_1 + 1$
4: Solving optimization problem in (4.21) to obtain the optimal solutions $\tilde{P}_{\text{total}}$, $\{s_{k,i}[n], p_{k,i}[n]\}$
5: Use **Algorithm 4.2** to obtain the suboptimal result $\bar{P}_{\text{total}}$, $\{\mathbf{t}[n], \mathbf{v}[n]\}$ given the resource allocation design $\{s_{k,i}[n], p_{k,i}[n]\}$
6: Update $\bar{P}^{j_1}_{\text{total}} = \bar{P}_{\text{total}}$
7: **until** $j_1 = J_{1,\max}$ or $\frac{|\bar{P}^{j_1}_{\text{total}} - \bar{P}^{(j_1-1)}_{\text{total}}|}{\bar{P}^{j_1}_{\text{total}}} \leq \epsilon_1$
8: **return** $\{s^*_{k,i}[n], p^*_{k,i}[n], \mathbf{t}^*[n], \mathbf{v}^*[n]\} = \{s_{k,i}[n], p_{k,i}[n], \mathbf{t}[n], \mathbf{v}[n]\}$ and $P^*_{\text{total}} = \bar{P}^{j_1}_{\text{total}}$

Algorithm 4.2 Proposed Algorithm for Solving Sub-problem in (4.33)

1: Initialize the convergence tolerance $\epsilon_2 \rightarrow 0$, the maximum number of iterations $J_{2,\max}$, the initial iteration index $j_2 = 0$, the initial variables $\{\mathbf{v}[n], u_{k,i}[n]\}$, and the initial objective value $\bar{P}_{\text{total}}$.
2: **repeat** {Main Loop: SCA}
3: Set $j_2 = j_2 + 1$ and $\{\mathbf{v}^{j_2}[n], u^{j_2}_{k,i}[n]\} = \{\mathbf{v}[n], u_{k,i}[n]\}$
4: Solving optimization problem in (4.42) to obtain $\{\mathbf{t}[n], \mathbf{v}[n], u_{k,i}[n], m[n]\}$ and $\bar{P}_{\text{total}}$
5: Update $\bar{P}^{j_2}_{\text{total}} = \bar{P}_{\text{total}}$
6: **until** $j_2 = J_{2,\max}$ or $\frac{|\bar{P}^{j_2}_{\text{total}} - \bar{P}^{(j_2-1)}_{\text{total}}|}{\bar{P}^{j_2}_{\text{total}}} \leq \epsilon_2$
7: Return $\{\mathbf{t}^*[n], \mathbf{v}^*[n]\} = \{\mathbf{t}[n], \mathbf{v}^{j_2}[n]\}$ and $\bar{P}^*_{\text{total}} = \bar{P}^{j_2}_{\text{total}}$

$$\bar{R}_{k,i}[n] = s_{k,i}[n] \log_2 \left(1 + \frac{\gamma_{k,i}[n]}{u_{k,i}[n]}\right), \tag{4.35}$$

$$\gamma_{k,1}[n] = \frac{p_{k,i}[n] M_{\mathrm{A}} \beta_0^2}{\sigma^2}, \tag{4.36}$$

$$\gamma_{k,2}[n] = \frac{p_{k,i}[n] M_{\mathrm{A}} M_{\mathrm{R}}^2 \beta_0^2}{(d_k^{\mathrm{RG}})^2 \sigma^2}, \tag{4.37}$$

$$\bar{P}_{\mathrm{flight}}^{\mathrm{UAV}}[n] = P_o \left(1 + \frac{3\|\mathbf{v}[n]\|^2}{\Omega^2 r^2}\right) + \frac{P_i v_0}{m[n]} + \frac{1}{2} d_0 \rho s A_{\mathrm{r}} \|\mathbf{v}[n]\|^3, \text{ and} \tag{4.38}$$

$$\bar{P}_{\mathrm{total}} = \sum_{n=1}^{N} \sum_{k=1}^{K} \sum_{i=1}^{2} s_{k,i}[n] p_{k,i}[n] + P_{\mathrm{total}}^{\mathrm{IRS}} + \sum_{n=1}^{N} \bar{P}_{\mathrm{flight}}^{\mathrm{UAV}}[n], \tag{4.39}$$

where $\gamma_{k,i}[n]$ in (4.35) is a constant for GU k at time slot n with mode i for given power allocation in sub-problem 2, i.e., as shown in (4.36) and (4.37). Note that the introduced inequality constraints C12, C13, and C15 in problem (4.34) are all active at the optimal point. Thus the formulated problems in (4.33) and (4.34) are equivalent to each other. Next, we handle the nonconvex constraints C6 and C15 in problem (4.34) via successive convex approximation (SCA) iteratively [78, 93, 130]. In particular, we can obtain a lower bound of the achievable data rate for a given feasible solution, $u_{k,i}^{j_2}[n]$ and $\mathbf{v}^{j_2}[n]$ in the j_2-th iteration, based on their first-order Taylor expansions [42], which are given by

$$\begin{aligned} \bar{R}_{k,i}[n] \geq (\bar{R}_{k,i}[n])^{j_2} &= s_{k,i}[n] \log_2 \left(1 + \frac{\gamma_{k,i}[n]}{u_{k,i}^{j_2}[n]}\right) \\ &\quad - \frac{s_{k,i}[n] \gamma_{k,i}[n] (u_{k,i}[n] - u_{k,i}^{j_2}[n])}{u_{k,i}^{j_2}[n] (u_{k,i}^{j_2}[n] + \gamma_{k,i}[n]) \ln 2} \text{ and} \end{aligned} \tag{4.40}$$

$$\|\mathbf{v}[n]\|^2 \geq \|\mathbf{v}^{j_2}[n]\|^2 + 2[\mathbf{v}^{j_2}[n]]^{\mathrm{T}} (\mathbf{v}[n] - \mathbf{v}^{j_2}[n]), \tag{4.41}$$

respectively.

Thus, applying the lower bounds in (4.40) and (4.41) to (4.34), we obtain a

convex optimization problem:

$$\begin{aligned}
&\underset{\mathcal{T},\mathcal{V},\mathcal{U},\mathcal{M}}{\text{minimize}}\ \bar{P}_{\text{total}} \\
&\quad \text{s.t. C7} - \text{C14}, \\
&\quad \overline{\text{C6}} : \sum_{n=1}^{N}\sum_{i=1}^{2}(\bar{R}_{k,i}[n])^{j_2} \geq R_{\min}, \forall k, \\
&\quad \overline{\text{C15}} : \|\mathbf{v}^{j_2}[n]\|^2 + 2[\mathbf{v}^{j_2}[n]]^{\mathrm{T}}(\mathbf{v}[n] - \mathbf{v}^{j_2}[n]) \geq m^2[n], \forall n,
\end{aligned} \tag{4.42}$$

which solving it yields an upper bound of the problem in (4.34). Furthermore, in order to tighten the obtained upper bound, we iteratively update the feasible solution, $u_{k,i}^{j_2}[n]$ and $\mathbf{v}^{j_2}[n]$, by solving the optimization problem in (4.42) with standard convex optimization solver, such as CVX [120] in j_2-th iteration. The proposed SCA-based algorithm is shown in **Algorithm 4.2**. Note that the convergence of the algorithm to a suboptimal solution is guaranteed [42].

The overall algorithm for solving two subproblems in (4.19) and (4.33) iteratively are summarized in **Algorithm 4.1**. Note that the convergence of the overall proposed algorithm to a suboptimal solution is guaranteed and it can be proved by following a similar approach as in [112]. Please refer to Appendix B.3 for the proof of the convergence. □

4.5 Numerical Results

In this section, we discuss the system performance of the proposed algorithm based on the simulation results with $K = 3$, $N = 50$, $M_{\mathrm{A}x} = M_{\mathrm{A}y} = 5$, $M_{\mathrm{R}x} = M_{\mathrm{R}y} = 50$, $\lambda_{\mathrm{c}} = 0.1$ m, $\beta_0 = -50$ dB, $\mathbf{l}_k = [250, 150; 50, 400; 100, 450]^{\mathrm{T}}$ m, $\mathbf{l}_{\mathrm{R}} = [0, 400]^{\mathrm{T}}$ m, $H_{\mathrm{A}} = 100$ m, $H_{\mathrm{R}} = 20$ m, $P_{\max}^{\mathrm{UAV-Tx}} = 30$ dBm, $R_{\min} = 50$ bits/Hz, $V_{\max} = 50$ m/s, $V_{\mathrm{acc}} = 4$ m/s^2, $\mathbf{t}_0 = [0, 0]^{\mathrm{T}}$ m, and $\mathbf{t}_{\mathrm{F}} = [500, 500]^{\mathrm{T}}$ m.

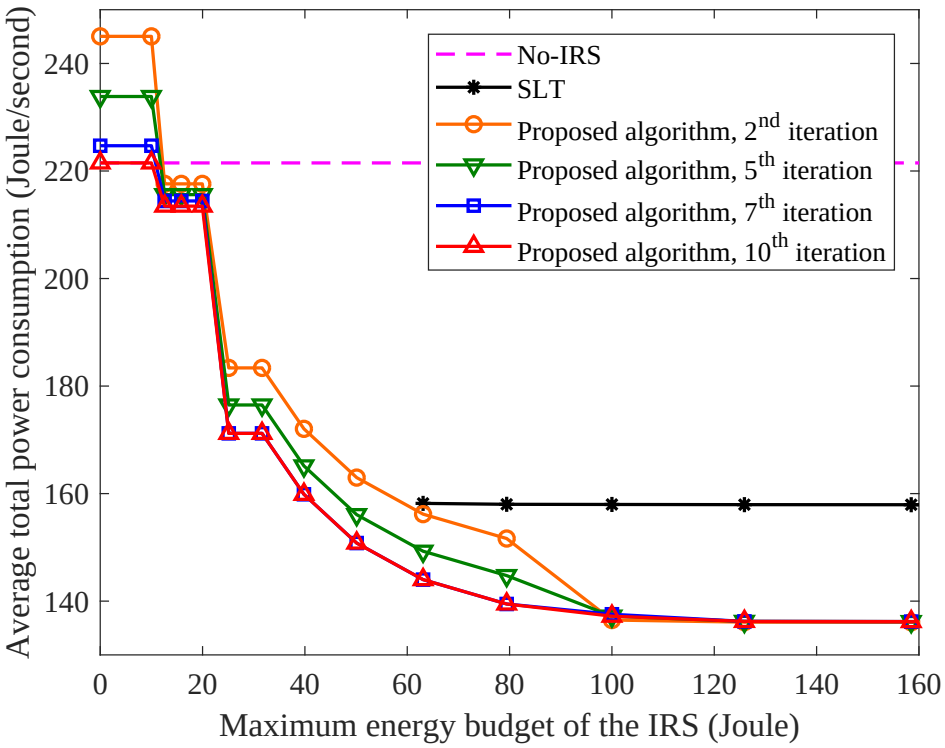

Figure 4.3: Average total power consumption versus the energy budget of the IRS.

In order to illustrate the contribution of the IRS to the UAV communications, we compare the system performance for the proposed algorithm with different energy budgets of the IRS and some baseline schemes. Besides, the initial trajectory of the UAV is set as a straight flight with a constant speed from the start point to the final point. The compared baseline schemes are no IRS consideration (No-IRS) and straight line trajectory with constant velocity (SLT).

4.5.1 Average Total Power Consumption

Figure 4.3 shows the average total power consumption of the UAV communications versus the energy budget of the IRS for different iterations of the proposed algorithm and a baseline scheme (SLT). We can observe that the proposed

algorithm converge quickly to a suboptimal solution within 10 iterations on average. Besides, the convergence of the proposed algorithm is accelerated by the increases of energy budget. This is because an effective solution can be easily achieved as the received signal-to-noise ratio (SNR) is improved in the time slots when the IRS is activated. Moreover, it can be observed that the energy budget of an IRS has a significant impact on the system performance. In particular, the average total power consumption of the system decreases with increasing the energy budget of the IRS which illustrates the benefit of introducing an IRS to UAV communication systems. On the other hand, for the baseline scheme (SLT), the proposed system is infeasible when the energy budget of the IRS is below 60 Joule and the average total power consumption is insensitive to the increase of energy budget of the IRS. This result indicates that IRS can only provide significant performance gain to UAV-based systems when resource allocation strategy and UAV's trajectory are jointly optimized.

4.5.2 2D Trajectory of the UAV

Figure 4.4 illustrates the UAV's trajectories for the proposed algorithm with 10 iterations and baseline schemes. For SLT, the UAV flies straightly from the initial point, $\mathbf{t}_0$, toward the final point, $\mathbf{t}_\mathrm{F}$, with a constant flight velocity. For No-IRS, due to the minimum data rate requirement for each user, the UAV has to fly with a high flight velocity and pass by each user to establish strong channel gain which consumes a significantly high flight power due to detoured path. Besides, we can observe that the UAV flies slowly when it close to any desired user to facilitate effective data communications. In contrast, thanks to the help of the IRS, the UAV's trajectory of the proposed scheme is shorter compared to No-IRS. In particular, for $E_{\max}^{\mathrm{IRS}} = 30$ Joule and $E_{\max}^{\mathrm{IRS}} = 100$ Joule, the IRS can offer

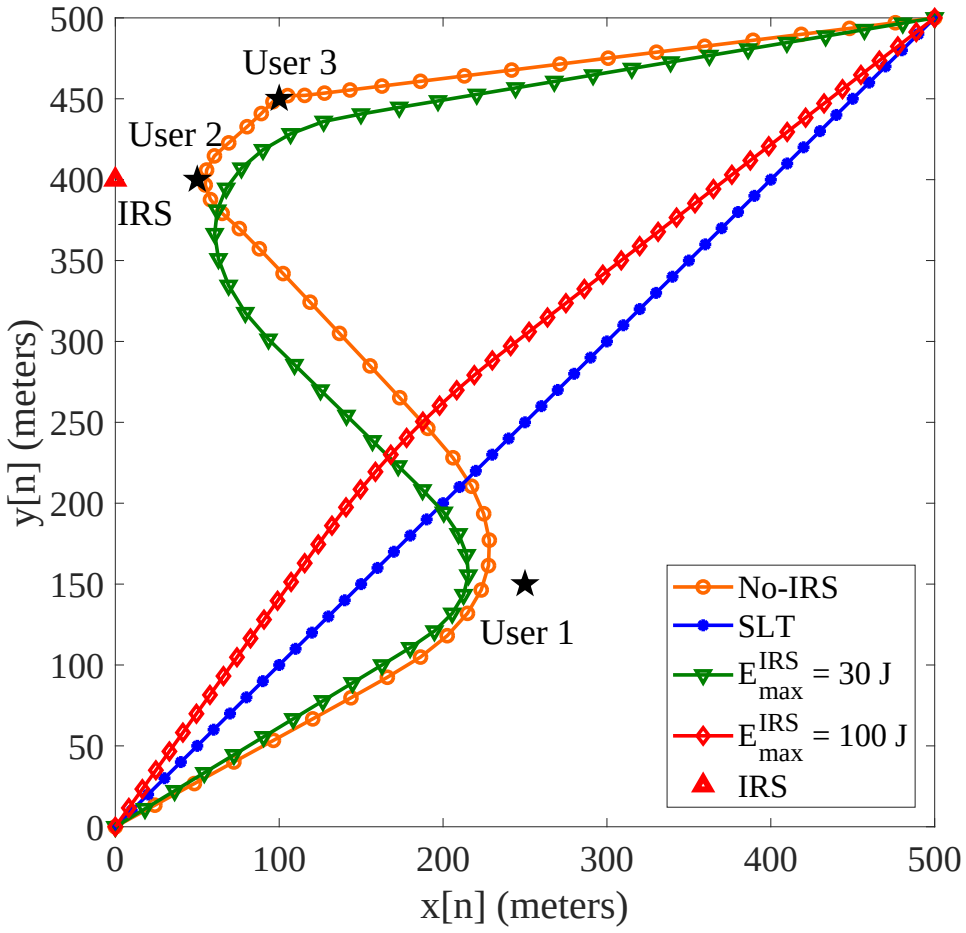

Figure 4.4: UAV's trajectories of the proposed algorithm and baseline scheme.

temporary assistance to the UAV for efficient communication. Hence, the UAV of the proposed scheme does not hover the desired users as the No-IRS scheme, since it would cause a longer flight route and power consumption. In other words, the UAV of the proposed scheme can enjoy a higher flexibility in designing UAV's trajectory which can reduce the flight power consumption substantially compared to other baseline schemes.

4.6 Summary

In this chapter, we studied a non-convex power minimization problem for IRS-assisted UAV communication systems via jointly optimizing the UAVs trajectory design and resource allocation strategy. We proposed an alternating algorithm to achieve a suboptimal solution efficiently. The proposed algorithm supports the high flexibility to the UAVs trajectory in the communications with the assistance of the IRS. The numerical results illustrate the fast convergence and system performance gain achieved by the proposed algorithm with different energy budgets of the IRS compared to various baseline schemes.

Chapter 5

Resource Allocation and 3D Trajectory Design for Power-Efficient IRS-Assisted UAV-NOMA Communications

5.1 Introduction

In the previous two chapters, we have introduced two creative trajectory design and resource allocation algorithms for unmanned arial vehicle (UAV) communications. However, these considered scenarios adopted orthogonal multiple access (OMA) protocols, i.e., orthogonal frequency division multiple access (OFDMA) and time division multiple access (TDMA), which are not applicable to the case of a large number of users with stringent quality of service (QoS) requirements. As we discussed in Chapter 2, non-orthogonal multiple access (NOMA) protocol provides higher degrees of freedom (DoF) for optimizing the UAV communication

systems. Moreover, the adopted pure line-of-sight (LoS) channel in Chapters 3 and 4 are need to be explored to a more universal channel model. Therefore, in this chapter, we study the joint design of the resource allocation, UAV's three-dimensional (3D) trajectory, and its flight velocity, as well as the phase shift control of the intelligent reflection surface (IRS) in a practical altitude-dependent Rician fading channel for power-efficient IRS-assisted UAV-NOMA communications. The joint design is formulated as a non-convex optimization problem to minimize the average total power consumption of the system taking into account the minimum data rate requirement of each user and the maximum tolerable outage probability constraint. Since the formulated problem is non-convex and highly intractable, we first propose a closed-form phase control policy for IRS. Then, to handle the intractability caused by the altitude-dependent Rician fading channel, we employ a deep neural network (DNN) technique to approximate the outage-guaranteed effective channel gain. Furthermore, the obtained results are exploited to serve as a building block for the design of an iterative optimization algorithm for addressing the design problem. In particular, we divide the problem at hand into two subproblems and solve them iteratively based on the alternating optimization method. In each iteration, a suboptimal solution of these two subproblems are obtained by the successive convex approximation (SCA) with a fast convergence.

5.2 System Model

We consider a rotary UAV-enabled downlink NOMA wireless communication system serving K ground users (GUs) with the assistance of an IRS[1] as shown

[1]Note that a more complex scenario can be considered in the future work with more IRSs adopted in the communications [131, 132], considering IRS selection and the coorperation between the IRSs.

in Fig. 5.1. Particularly, the IRS is coated on the surface of a building located at the edge of the service area such that all the GUs have the opportunity to be assisted by the IRS. We assume that the UAV is equipped with a single antenna[2]. Besides, the IRS consists of $M_{\mathrm{R}x} \times M_{\mathrm{R}y} = M_{\mathrm{R}} > 1$ passive reflecting elements and all the GUs are single-antenna devices. Also, the total service time duration T is divided into N equal-length time slots with duration time τ (s), i.e., $T = N\tau$. In each time slot, the UAV selects two GUs[3] and serves them through NOMA. Moreover, the UAV operates in 3D space with a variable flight velocity, while the locations of all the GUs and the IRS are fixed during the whole service time, e.g., [40, 46, 58]. Also, we assume that the IRS is deployed at a high altitude above all obstacles. The distances between the UAV and the IRS, the UAV and GU $k \in \{1, \ldots, K\}$, as well as the IRS and GU k at time slot $n \in \{1, \ldots, N\}$ are given by

$$d^{\mathrm{AR}}[n] = \|\mathbf{l}_{\mathrm{R}} - \mathbf{t}[n]\|,\ d_k^{\mathrm{AG}}[n] = \|\mathbf{l}_k - \mathbf{t}[n]\|,\ \text{and}\ d_k^{\mathrm{RG}} = \|\mathbf{l}_{\mathrm{R}} - \mathbf{l}_k\|, \tag{5.1}$$

respectively. Note that $\mathbf{l}_{\mathrm{R}} = [x_{\mathrm{R}}, y_{\mathrm{R}}, H_{\mathrm{R}}]^{\mathrm{T}} \in \mathbb{R}^{3\times 1}$, $\mathbf{l}_k = [x_k, y_k, z_k]^{\mathrm{T}} \in \mathbb{R}^{3\times 1}$, and $\mathbf{t}[n] = [x[n], y[n], z[n]]^{\mathrm{T}} \in \mathbb{R}^{3\times 1}$ denote the Cartesian coordinate of the IRS[4], GU k, and the UAV at time slot n, respectively.

[2]Note that single-antenna UAV is commonly assumed in the literature, e.g., [3,42], to reduce the signal processing burden at the UAV.

[3]In this chapter, we consider to select two GUs to form a NOMA group since it enjoys a lower computational complexity and a shorter signal processing delay for successive interference cancellation (SIC) decoding at GUs, compared with that of grouping more NOMA users [93,97]. Moreover, as shown in [78,133], the performance gain of NOMA over OMA diminishes rapidly with increasing the number of users in one NOMA group. Therefore, the considered two-user NOMA scheme can achieve a considerable performance improvement than conventional OMA scheme.

[4]Since the typical size of each element in a small-scale IRS is the same order of the wavelength of the carrier frequency, λ_{c}, [127], e.g., $\frac{\lambda_{\mathrm{c}}}{2}$, the separations between reflecting elements of the IRS in the x-dimension and the y-dimension, denoted as $\Delta_{\mathrm{R}x}$ and $\Delta_{\mathrm{R}y}$, respectively, are much shorter than that of the distance between the UAV and the IRS, $d^{\mathrm{AR}}[n]$, as well as the distance between the IRS and GUs, d_k^{RG}. Thus, we assume that the distance of each element of the IRS to a GU/UAV is the same, as commonly adopted in the literature [69].

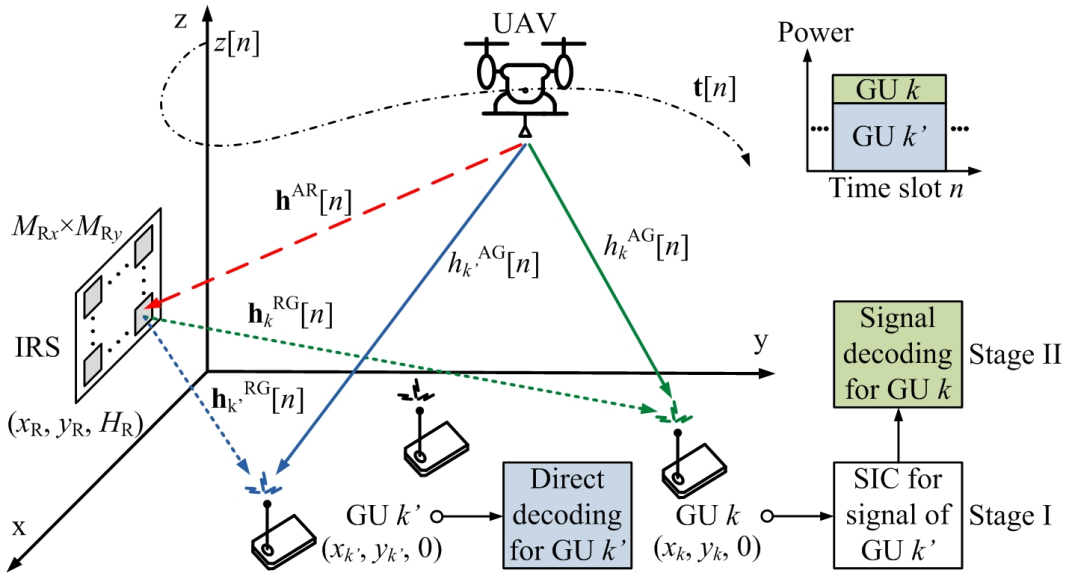

Figure 5.1: An IRS-assisted UAV-NOMA communication system with multiple ground users.

5.2.1 Channel Model

In the considered system, we assume that the channels between the UAV and the GUs as well as the IRS and the GUs follow a frequency flat Rician fading channel model with an altitude-dependent Rician factor [40, 80]. Note that the Doppler effect caused by the movement of the UAV can be well compensated by adopting existing frequency synchronization algorithms, e.g., [126]. According to [40], the Rician factor of the direct link between the UAV and different GUs is non-identical caused by the UAV's mobility and their surrounding environment. In fact, the altitude-dependent Rician factor for UAV-GUs link can be modeled by an exponential function [40, 80], which is given by

$$\kappa_k^{\mathrm{AG}}[n] = A_1 \exp\left(A_2 \theta_k^{\mathrm{AG}}[n]\right), \tag{5.2}$$

where $\theta_k^{\mathrm{AG}}[n]$ is the elevation angle-of-departure (AoD) from the UAV to GU k at time slot n, as shown in Fig. 5.2, and is given by

$$\theta_k^{\mathrm{AG}}[n] = \arcsin\left(\frac{z[n]}{d_k^{\mathrm{AG}}[n]}\right). \tag{5.3}$$

Note that $A_1 > 0$ and $A_2 > 0$ are constant parameters related to the terrain environment and can be obtained via long-term measurements. Then, we can observe that the Rician factor is bounded by $\kappa_{\min} \leq \kappa_k^{\mathrm{AG}}[n] \leq \kappa_{\max}$, where $\kappa_{\min} = A_1$ and $\kappa_{\max} = A_1 e^{A_2\pi/2}$.

Hence, the Rician channel between the UAV and GU k at time slot n is given by

$$h_k^{\mathrm{AG}}[n] = \sqrt{\frac{\beta_0}{(d_k^{\mathrm{AG}}[n])^{\alpha^{\mathrm{AG}}}}}\left[\sqrt{\frac{\kappa_k^{\mathrm{AG}}[n]}{1+\kappa_k^{\mathrm{AG}}[n]}}h_k^{\mathrm{AG,LoS}}[n] + \sqrt{\frac{1}{1+\kappa_k^{\mathrm{AG}}[n]}}\Delta h_k^{\mathrm{AG}}[n]\right] \in \mathbb{C}, \tag{5.4}$$

where $h_k^{\mathrm{AG,LoS}}[n] = e^{-j2\pi d_k^{\mathrm{AG}[n]}/\lambda_{\mathrm{c}}}$ and the associated phase rotation is caused by the delay of the LoS component of UAV-GUs link, which is determined solely by their locations and is known to the system. $\Delta h_k^{\mathrm{AG}}[n] \in \mathbb{C} \sim \mathcal{CN}(0,1)$ denotes the randomly scattered component of the channel experienced by GU k at time slot n. Note that $\beta_0 \in \mathbb{R}$ and $\alpha^{\mathrm{AG}} > 0$ denote the average channel power gain at the reference distance and the path loss exponent of the UAV-GUs channel, respectively. Besides, we use $\xi_k^{\mathrm{AG}}[n]$ to represent the horizontal AoD from the UAV to GU k at time slot n and λ_{c} denotes the wavelength of the carrier frequency. Fig. 5.2 shows the geographic relations of $\sin\xi_k^{\mathrm{AG}}[n] = \frac{|x_k - x[n]|}{\sqrt{(x_k-x[n])^2+(y_k-y[n])^2}}$ and $\cos\xi_k^{\mathrm{AG}}[n] = \frac{|y_k - y[n]|}{\sqrt{(x_k-x[n])^2+(y_k-y[n])^2}}$. On the other hand, the pure LoS channel[5] from the UAV to the IRS at time slot n

[5]In practice, the IRS is mounted at the wall of a building that has a similar height with traditional base stations deployed in outdoor wireless communication systems [134], e.g., $20-30$ meters. Based on the field measurements in [106, 107], the LoS probability of the air-to-air

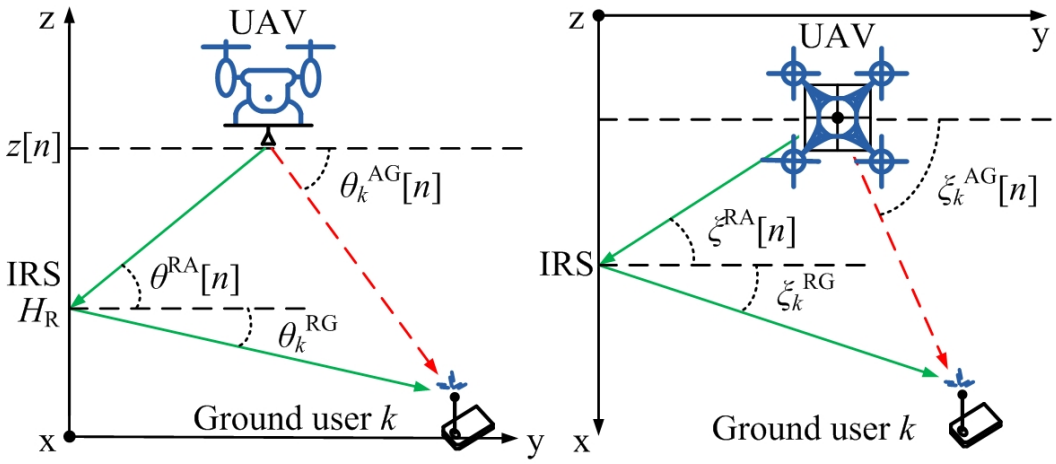

Figure 5.2: The vertical and horizontal AoDs/AoAs between the UAV, IRS, and GU k in the considered downlink communication system are shown on the left-hand side and the right-hand side, respectively.

is denoted as

$$\begin{aligned}
&\mathbf{h}^{\mathrm{AR}}[n] \\
&= \sqrt{\frac{\beta_0}{(d^{\mathrm{AR}}[n])^{\alpha^{\mathrm{AR}}}}} e^{-j\frac{2\pi d^{\mathrm{AR}}[n]}{\lambda_c}} \\
&\times \left[1, e^{-j\frac{2\pi\Delta_{\mathrm{R}x}}{\lambda_c}\sin\theta^{\mathrm{RA}}[n]\cos\xi^{\mathrm{RA}}[n]}, \ldots, e^{-j\frac{2\pi\Delta_{\mathrm{R}x}}{\lambda_c}(M_{\mathrm{R}x}-1)\sin\theta^{\mathrm{RA}}[n]\cos\xi^{\mathrm{RA}}[n]}\right]^{\mathrm{H}} \\
&\otimes \left[1, e^{-j\frac{2\pi\Delta_{\mathrm{R}y}}{\lambda_c}\sin\theta^{\mathrm{RA}}[n]\sin\xi^{\mathrm{RA}}[n]}, \ldots, e^{-j\frac{2\pi\Delta_{\mathrm{R}y}}{\lambda_c}(M_{\mathrm{R}y}-1)\sin\theta^{\mathrm{RA}}[n]\sin\xi^{\mathrm{RA}}[n]}\right]^{\mathrm{H}} \in \mathbb{C}^{M_{\mathrm{R}}\times 1},
\end{aligned} \tag{5.5}$$

where $\alpha^{\mathrm{AR}} > 0$ is the path loss exponent of the UAV-IRS link. As shown in Fig. 5.2, $\theta^{\mathrm{RA}}[n]$ and $\xi^{\mathrm{RA}}[n]$ denote the vertical and horizontal angle-of-arrivals (AoAs) between the UAV and the IRS, respectively. Note that $\sin\theta^{\mathrm{RA}}[n] = \frac{|z[n]-H_{\mathrm{R}}|}{d^{\mathrm{AR}}[n]}$, $\sin\xi^{\mathrm{RA}}[n] = \frac{|x_{\mathrm{R}}-x[n]|}{\sqrt{(x_{\mathrm{R}}-x[n])^2+(y_{\mathrm{R}}-y[n])^2}}$, and $\cos\xi^{\mathrm{RA}}[n] = \frac{|y_{\mathrm{R}}-y[n]|}{\sqrt{(x_{\mathrm{R}}-x[n])^2+(y_{\mathrm{R}}-y[n])^2}}$. Besides, the Rician channel from the IRS to GU k at time

communication channel closely approaches one. Thus, in our proposed system, we assume that the UAV-IRS link experiences the pure LoS channel which the corresponding channel coefficients can be determined by their locations.

slot n can be modeled as

$$\mathbf{h}_k^{\mathrm{RG}}[n] = \sqrt{\frac{\beta_0}{(d_k^{\mathrm{RG}})^{\alpha^{\mathrm{RG}}}}} \left[\sqrt{\frac{\kappa^{\mathrm{RG}}}{1+\kappa^{\mathrm{RG}}}} \mathbf{h}_k^{\mathrm{RG,LoS}} + \sqrt{\frac{1}{1+\kappa^{\mathrm{RG}}}} \Delta \mathbf{h}_k^{\mathrm{RG}}[n] \right] \in \mathbb{C}^{M_{\mathrm{R}} \times 1}, \tag{5.6}$$

where

$$\begin{aligned} \mathbf{h}_k^{\mathrm{RG,LoS}} = e^{-j\frac{2\pi d_k^{\mathrm{RG}}}{\lambda_{\mathrm{c}}}} \left[1, e^{-j\frac{2\pi \Delta_{\mathrm{R}x}}{\lambda_{\mathrm{c}}} \sin\theta_k^{\mathrm{RG}} \cos\xi_k^{\mathrm{RG}}}, \ldots, e^{-j\frac{2\pi \Delta_{\mathrm{R}x}}{\lambda_{\mathrm{c}}}(M_{\mathrm{R}x}-1) \sin\theta_k^{\mathrm{RG}} \cos\xi_k^{\mathrm{RG}}}\right]^{\mathrm{H}} \\ \otimes \left[1, e^{-j\frac{2\pi \Delta_{\mathrm{R}y}}{\lambda_{\mathrm{c}}} \sin\theta_k^{\mathrm{RG}} \sin\xi_k^{\mathrm{RG}}}, \ldots, e^{-j\frac{2\pi \Delta_{\mathrm{R}y}}{\lambda_{\mathrm{c}}}(M_{\mathrm{R}y}-1) \sin\theta_k^{\mathrm{RG}} \sin\xi_k^{\mathrm{RG}}}\right]^{\mathrm{H}} \end{aligned} \tag{5.7}$$

is the LoS component that is known to the system. $\Delta \mathbf{h}_k^{\mathrm{RG}}[n] \in \mathbb{C}^{M_{\mathrm{R}} \times 1} \sim \mathcal{CN}(0, \mathbf{I}_{M_{\mathrm{R}}})$, $\alpha^{\mathrm{RG}} \geq 0$, and $\kappa^{\mathrm{RG}} \geq 0$ represent the randomly scattered component, the path loss exponent, and the fixed Rician factor of the IRS-GUs channel, respectively. θ_k^{RG} and ξ_k^{RG} denote the vertical and horizontal AoDs from the IRS to GU k, respectively. As shown in Fig. 5.2, we have $\sin\theta_k^{\mathrm{RG}} = \frac{H_{\mathrm{R}}}{d_k^{\mathrm{RG}}}$, $\sin\xi_k^{\mathrm{RG}} = \frac{|x_{\mathrm{R}} - x_k|}{\sqrt{(x_{\mathrm{R}}-x_k)^2 + (y_{\mathrm{R}}-y_k)^2}}$, and $\cos\xi_k^{\mathrm{RG}} = \frac{|y_{\mathrm{R}} - y_k|}{\sqrt{(x_{\mathrm{R}}-x_k)^2 + (y_{\mathrm{R}}-y_k)^2}}$.

Moreover, the IRS can manipulate the reflected signals to GUs by introducing controllable phase shifts. The phase control matrix imposed by the IRS at time slot n is given by[6]

$$\mathbf{\Phi}[n] = \mathrm{diag}(e^{j\phi_{1,1}[n]}, \ldots, e^{j\phi_{m_{\mathrm{R}x}, m_{\mathrm{R}y}}[n]}, \ldots, e^{j\phi_{M_{\mathrm{R}x}, M_{\mathrm{R}y}}[n]}) \in \mathbb{C}^{M_{\mathrm{R}} \times M_{\mathrm{R}}}, \tag{5.8}$$

where $\phi_{m_{\mathrm{R}x}, m_{\mathrm{R}y}}[n] \in [0, 2\pi)$, $m_{\mathrm{R}x} = \{1, \ldots, M_{\mathrm{R}x}\}$, $m_{\mathrm{R}y} = \{1, \ldots, M_{\mathrm{R}y}\}$, represents the phase control introduced by the $(m_{\mathrm{R}x}, m_{\mathrm{R}y})$-th reflecting element of the IRS at time slot n. Now, we define the end-to-end effective channel[7] between

[6]Note that although continuous phase control is considered in this chapter, it can be extended to the case discrete phase control via a similar approach as in [63,64] and with the IRS channel estimation as in [65,135].

[7]The signal propagation delay between the direct link and the reflection link is negligible as it is about 2 μs in an 500×500 m^2 service area, which is much shorter than the symbol duration in long-term evolution (LTE) systems (around 70 μs) [136].

the UAV and GU k at time slot n as

$$h_k[n] = h_k^{\mathrm{AG}}[n] + (\mathbf{h}_k^{\mathrm{RG}}[n])^{\mathrm{H}} \mathbf{\Phi}[n] \mathbf{h}^{\mathrm{AR}}[n] \in \mathbb{C}. \tag{5.9}$$

Meanwhile, at the UAV side, the deterministic components of all channels, including the LoS components, path loss as well as the Rician factors can be determined that are available for the designed trajectory of the UAV. Apart from the deterministic components, the distributions of the randomly scattered components in the UAV-GUs and IRS-GUs links are also available [137].

5.2.2 NOMA Transmission and Achievable Data Rate

We consider NOMA transmission at the UAV to serve two GUs at each time slot as it is potential to achieve a higher power efficiency than that of the conventional OMA schemes[8] [93]. Without loss of generality, when the UAV selects GU k and GU k' to form a NOMA group and instructs GU k to perform SIC decoding at time slot n, we denote $s_{k,k'}[n] = 1$, $\forall k, k'$. Otherwise, $s_{k,k'}[n] = 0$. When $s_{k,k'}[n] = 1$, the UAV transmits the superimposed signals for GU k and GU k' simultaneously. As illustrated in Fig. 5.1, GU k is assumed as the user performing SIC which first decodes the information of GU k' before decoding its own information. Besides, GU k' is assumed as the non-SIC user which directly decodes its own information while treating the interference of GU k as noise. For $s_{k,k'}[n] = 1$, the achievable data rates of the two stages of SIC decoding at GU k serving as a SIC user and that of GU k' serving as a non-SIC user can be

[8]The proposed optimization framework is a generalized one which subsumes TDMA as a special case.

formulated as

$$C_{k,k'}^{\mathrm{I,SIC}}[n] = \log_2\left(1 + \frac{p_{k'}[n]|h_k[n]|^2}{p_k[n]|h_k[n]|^2 + \sigma_k^2}\right), \forall n, k \neq k', \tag{5.10}$$

$$C_{k,k'}^{\mathrm{II,SIC}}[n] = \log_2\left(1 + \frac{p_k[n]|h_k[n]|^2}{\sigma_k^2}\right), \forall n, k, \text{and} \tag{5.11}$$

$$C_{k,k'}^{\mathrm{NSIC}}[n] = \log_2\left(1 + \frac{p_{k'}[n]|h_{k'}[n]|^2}{p_k[n]|h_{k'}[n]|^2 + \sigma_{k'}^2}\right), \forall n, k \neq k', \tag{5.12}$$

respectively, where $p_k[n]$, $p_{k'}[n]$, σ_k^2, and $\sigma_{k'}^2$ denote the power allocation variables and the background noise powers for GU k and GU k' at time slot n, respectively. Note that when $k = k'$, $s_{k,k}[n] = 1$ models the case of TDMA where only GU k is served at time slot n and the achievable rate can be given by $C_{k,k}^{\mathrm{II,SIC}}[n]$ in (5.11). However, due to the existence of randomly scattered components in Rician fading channels, an outage event occurs when the transmission rate exceeds the achievable data rate. To capture the potential outage events, we define the effective rate allocation for GU k and GU k' at time slot n as $r_k[n]$ and $r_{k'}[n]$, respectively. When $s_{k,k'}[n] = 1$, $r_k[n]$ can be achieved when the two stages of SIC decoding at GU k are successful, i.e., $r_{k'}[n] \leq C_{k,k'}^{\mathrm{I,SIC}}[n]$ and $r_k[n] \leq C_{k,k'}^{\mathrm{II,SIC}}[n]$. Meanwhile, $r_{k'}[n]$ can be achieved when the direct decoding at GU k' is successful, i.e., $r_{k'}[n] \leq C_{k,k'}^{\mathrm{NSIC}}[n]$. Besides, when $s_{k,k}[n] = 1$, $r_k[n]$ can be achieved when $r_k[n] \leq C_{k,k}^{\mathrm{II,SIC}}[n]$.

Our design aims to satisfy the minimum data rate requirement of each user while taking into account the potential outages of both SIC decoding and direct decoding. Therefore, we formulate the average transmission rate of user k during

the whole flight period as follows:

$$\bar{R}_k = \underbrace{\frac{1}{N}\sum_{n=1}^{N}\sum_{\substack{k'=1\\k'\neq k}}^{K} s_{k,k'}[n]r_k[n]}_{\text{GU } k \text{ as a SIC user}} + \underbrace{\frac{1}{N}\sum_{n=1}^{N}\sum_{\substack{k'=1\\k'\neq k}}^{K} s_{k',k}[n]r_k[n]}_{\text{GU } k \text{ as a non-SIC user}} + \underbrace{\frac{1}{N}\sum_{n=1}^{N} s_{k,k}[n]r_k[n]}_{\text{GU } k \text{ as an OMA user}}, \tag{5.13}$$

where the first term denotes the average transmission rate of GU k as a SIC user, the second term denotes the average transmission rate of GU k as a non-SIC user, and the third term represents the average transmission rate of GU k as an OMA user.

5.2.3 Power Consumption Model

The power consumption of the UAV plays an important role in UAV-based communications due to its small-size onboard battery with limited energy capacity. The system power consumption consists of the UAV's communication power and the flight power. The communication power of the UAV at time slot n can be given by

$$P_{\text{comm}}[n] = \eta\left(\sum_{k=1}^{K}\sum_{k'\neq k}^{K} s_{k,k'}[n]\left(p_k[n]+p_{k'}[n]\right) + \sum_{k=1}^{K} s_{k,k}[n]p_k[n]\right), \tag{5.14}$$

where $\frac{1}{\eta} > 0$ denotes the efficiency of the power amplifier of the transmit antenna. Note that the first term denotes the communication power consumption for NOMA users and the second term represents the communication power of the users selected to operate in OMA mode. In this system, we consider a rotary wing UAV as it has a higher maneuverability than fixed wing UAVs. According to [3, 31], the flight power consumption of a rotary wing UAV at time slot n is

Table 5.1: Physical meaning of parameters in flight power consumption model of UAV [3].

Parameters	Physical meaning	Simulation values
G	Weight of UAV	20 (Newton)
Ω	Blade angular velocity	300 (radians/second)
r	Rotor radius	0.4 (meter)
ρ	Air density	1.225 (kg/m^3)
s	Rotor solidity	0.05 (m^3)
A_{r}	Rotor disc area	0.503 (m^2)
v_0	Induced velocity for rotor in forwarding flight	4.03 (meter/second)
d_0	Fuselage drag ratio	0.3
P_o	Blade profile power in hovering status	79.86 (watt)
P_i	Induced power in hovering status	88.63 (watt)

given by

$$P_{\mathrm{fly}}[n] = \underbrace{P_o\left(1+\frac{3(v_x^2[n]+v_y^2[n])}{\Omega^2 r^2}\right)}_{\text{Bladeprofile power}} + \underbrace{\frac{P_i v_0}{v_x^2[n]+v_y^2[n]}}_{\text{Induced power}} + \underbrace{\frac{1}{2}d_0\rho s A_{\mathrm{r}}(v_x^2[n]+v_y^2[n])^{3/2}}_{\text{Parasite power}} + \underbrace{Gv_{\mathrm{z}}[n]}_{\text{Vertical flight power}}, \tag{5.15}$$

where the velocity of the UAV in 3D Cartesian coordinate is denoted as $\mathbf{v}[n] = [v_x[n], v_y[n], v_z[n]]^{\mathrm{T}} \in \mathbb{R}^{3\times 1}$. The physical meanings of the parameters in (5.15) are summarized in Table 5.1. In (5.15), the first three components are related to horizontal flight power and the last component, the vertical flight power consumption, plays an important role in controlling the UAV's flight altitude. In particular, it is expected that optimizing the vertical velocity, $v_{\mathrm{z}}[n]$, can affect the flight endurance and the flight power consumption.

On the other hand, in practice, the IRS is usually mounted on the building exterior which is accessible to energy source. Besides, the IRS is nearly passive and its operation power is a constant which is much lower than that of the

communication and flight power consumption of the UAV [3, 5]. Therefore, we ignore the IRS power consumption in the considered system.

5.3 Problem Formulation

The optimization problem for minimizing the average total power consumption via jointly designing the user scheduling $\mathcal{S} = \{s_{k,k'}[n], \forall n, k, k'\}$, the power allocation $\mathcal{P} = \{p_k[n], \forall n, k\}$[9], the effective transmission rate $\mathcal{R} = \{r_k[n], \forall n, k\}$[10], the UAV's 3D trajectory $\mathcal{T} = \{\mathbf{t}[n], \forall n\}$, the UAV's 3D flight velocity $\mathcal{V} = \{\mathbf{v}[n], \forall n\}$, and the phase control policy of the IRS $\mathbf{\Phi} = \{\phi_{m_{\mathrm{R}x}, m_{\mathrm{R}y}}[n], \forall n, m_{\mathrm{R}x}, m_{\mathrm{R}y}\}$ is

[9]In practise, the total power draws by the power amplifier can be comparable to the flight power consumption, e.g., roughly $\frac{1}{3}$ of the latter. As such, we optimize both $p_k[n]$ and $P_{\mathrm{fly}}[n]$ in the objective function since the transmit power allocation affects substantially the UAV's trajectory, which is directly related to flight power consumption.

[10]Note that the transmission rate $r_k[n]$ is optimized to satisfy the outage probability constraints based on the practical altitude-dependent Rician fading channel model while only the statistical CSI is available for resource allocation.

formulated as:

$$\underset{\mathcal{S},\mathcal{P},\mathcal{R},\mathcal{T},\mathcal{V},\mathbf{\Phi}}{\text{minimize}} \ \frac{1}{N}\sum_{n=1}^{N} P_{\text{comm}}[n] + \frac{1}{N}\sum_{n=1}^{N} P_{\text{fly}}[n] \tag{5.16}$$

$$\text{s.t. C1}: s_{k,k'}[n] \in \{0,1\}, \forall n, k, k',$$

$$\text{C2}: \sum_{k=1}^{K}\sum_{k'=1}^{K} s_{k,k'}[n] \leq 1, \forall n,$$

$$\text{C3}: p_k[n] \geq 0, \forall n, k,$$

$$\text{C4}: P_{\text{comm}}[n] \leq P_{\text{peak}}, \forall n,$$

$$\text{C5}: \bar{R}_k \geq R_{\min_k}, \forall k,$$

$$\text{C6}: \Pr\Big(s_{k,k'}[n] r_{k'}[n] \leq s_{k,k'}[n] C_{k,k'}^{\text{I,SIC}}[n], s_{k,k'}[n] r_k[n] \leq s_{k,k'}[n] C_{k,k'}^{\text{II,SIC}}[n]\Big)$$
$$\geq 1 - \varepsilon_k^{\text{SIC}}, \forall n, k' \neq k,$$

$$\text{C7}: \Pr\Big(s_{k',k}[n] r_k[n] \leq s_{k',k}[n] C_{k',k}^{\text{NSIC}}[n]\Big) \geq 1 - \varepsilon_k^{\text{NSIC}}, \forall n, k' \neq k,$$

$$\text{C8}: \Pr\Big(s_{k,k}[n] r_k[n] \leq s_{k,k}[n] C_{k,k}^{\text{II,SIC}}[n]\Big) \geq 1 - \varepsilon_k^{\text{OMA}}, \forall n, k,$$

$$\text{C9}: \mathbf{t}[n+1] = \mathbf{t}[n] + \mathbf{v}[n]\tau, n = 1, \ldots, N-1,$$

$$\text{C10}: \mathbf{t}[1] = \mathbf{t}_0,$$

$$\text{C11}: \mathbf{t}[N] = \mathbf{t}_{\text{F}},$$

$$\text{C12}: \mathbf{t}_{\min} \leq \mathbf{t}[n] \leq \mathbf{t}_{\max}, \forall n,$$

$$\text{C13}: \|\mathbf{v}[n+1] - \mathbf{v}[n]\| \leq V_{\text{acc}}\tau, \forall n,$$

$$\text{C14}: \|\mathbf{v}[n]\| \leq V_{\max}, \forall n,$$

$$\text{C15}: 0 \leq \phi_{m_{\text{R}}x, m_{\text{R}}y}[n] < 2\pi, \forall n, m_{\text{R}}x, m_{\text{R}}y.$$

Note that C1 defines the user scheduling variable and C2 guarantees that at most two users are scheduled at each time slot. C3 is the non-negative constraint for the transmit power from the UAV to GU k and P_{peak} in C4 represents the peak transmission power of the UAV at each time slot. Constraint C5 is introduced

to limit the minimum data rate for each user. Constraints C6 − C8 represent the maximum outage probability constraints for the SIC decoding at SIC users, the direct decoding at non-SIC users[11], and the direct decoding at OMA users, respectively, where $\varepsilon_k^{\mathrm{SIC}} > 0$, $\varepsilon_k^{\mathrm{NSIC}} > 0$, and $\varepsilon_k^{\mathrm{OMA}} > 0$ are corresponding maximum tolerable outage probabilities. Constraint C9 denotes the relationship between the UAV's 3D trajectory and its flight velocity[12]. C10 and C11 denote the starting and the final locations of the UAV, respectively. Parameters $\mathbf{t}_{\min}$ and $\mathbf{t}_{\max}$ in constraint C12 limit the maximum service area of the UAV. V_{acc} and $V_{\max}$ in constraints C13 and C14 denote the maximum flight acceleration and the maximum flight velocity, respectively. C15 limits the range of phase control of the IRS.

5.4 Problem Solution

The formulated problem in (5.16) is a non-convex optimization problem and there is no systematic and efficient method to obtain the globally optimal solution. In the following, we first simplify the studied problem by exploiting its special structure at the optimality. Then, a computationally-efficient suboptimal algorithm is proposed to obtain a high-quality solution.

[11]In this system, we assume that the SIC user did not tempt to decode its own message if the first stage is failed, as commonly adopted in [18, 36, 93].

[12]Note that the UAV's flight velocity is a function of its trajectory for a given time slot duration τ. However, directly expressing the total power consumption in terms of UAV's trajectory or expressing the effective channel gain in terms of UAV's flight velocity would lead to an intractable formulation. Thus, we introduce variables of the UAV's trajectory and flight velocity to simplify the problem at hand.

5.4.1 Phase Control and Outage-guaranteed Effective Channel Gain

Since the randomly scattered components of the channels, e.g., $\Delta h_k^{\mathrm{AG}}[n]$ and $\Delta \mathbf{h}_k^{\mathrm{RG}}[n]$, are unknown, optimizing the phase control policy of the IRS has to rely on the LoS components of the channels, $\mathbf{h}^{\mathrm{AR}}[n]$, $h_k^{\mathrm{AG,LoS}}[n]$, and $\mathbf{h}_k^{\mathrm{RG,LoS}}$. To facilitate our design, we propose a efficient closed-form suboptimal phase control policy and derive the effective channel gain based on the distributions of $\Delta h_k^{\mathrm{AG}}[n]$ and $\Delta \mathbf{h}_k^{\mathrm{RG}}[n]$. Note that the proposed design can significantly reduce the required signaling overhead for CSI acquisition and phase control.

To determine the IRS phase control, since GU k is designed to perform SIC decoding and it is more likely to suffer from the channel outage than GU k', we assume that the IRS is always controlled to coherently combine the LoS channels of GU k when $s_{k,k'}[n] = 1$. In the following, we summarize a suboptimal phase control policy in a theorem.

Theorem 5.1. *A suboptimal phase control policy of the IRS at time slot n $\phi_{m_{\mathrm{R}x},m_{\mathrm{R}y}}[n]$ for minimizing the total system power consumption is given by*

$$\begin{aligned}
&\phi_{m_{\mathrm{R}x},m_{\mathrm{R}y}}[n] \\
&= \sum_{k=1}^{K}\sum_{k'=1}^{K} s_{k,k'}[n]\left(\frac{2\pi\Delta_{\mathrm{R}x}}{\lambda_{\mathrm{c}}}(m_{\mathrm{R}x}-1)\left(\sin\theta_k^{\mathrm{RG}}\cos\xi_k^{\mathrm{RG}} - \sin\theta^{\mathrm{RA}}[n]\cos\xi^{\mathrm{RA}}[n]\right)\right. \\
&+ \frac{2\pi\Delta_{\mathrm{R}y}}{\lambda_{\mathrm{c}}}(m_{\mathrm{R}y}-1)\left(\sin\theta_k^{\mathrm{RG}}\sin\xi_k^{\mathrm{RG}} - \sin\theta^{\mathrm{RA}}[n]\sin\xi^{\mathrm{RA}}[n]\right) \\
&\left.+ \frac{2\pi}{\lambda_{\mathrm{c}}}\left(d_k^{\mathrm{AR}}[n] + d_k^{\mathrm{RG}} - d_k^{\mathrm{AG}}[n]\right)\right). \qquad (5.17)
\end{aligned}$$

Proof: Please refer to appendix D.1 for a proof of Theorem 5.1. □

Applying (5.17) to (5.4)–(5.7) yields the effective channels from the UAV to

GU k and GU k' at time slot n are given by

$$h_k[n] = \sqrt{\frac{\beta_0 \kappa_k^{\mathrm{AG}}[n]}{A_k[n]}} + \sqrt{\frac{\beta_0^2 \kappa^{\mathrm{RG}} M_{\mathrm{R}}^2}{B_k[n]}} + \sqrt{\frac{\beta_0}{A_k[n]}} \Delta h_k^{\mathrm{AG}}[n] + \sqrt{\frac{\beta_0^2 M_{\mathrm{R}}^2}{B_k[n]}} \Delta h_k^{\mathrm{RG}}[n] \text{ and} \tag{5.18}$$

$$\begin{aligned} h_{k'}[n] =& \sqrt{\frac{\beta_0 \kappa_{k'}^{\mathrm{AG}}[n]}{A_{k'}[n]}} e^{-j\frac{2\pi}{\lambda}(d_{k'}^{\mathrm{AG}}[n] + d_k^{\mathrm{AG}}[n])} + \sqrt{\frac{\beta_0^2 \kappa^{\mathrm{RG}}}{B_{k'}[n]}} e^{-j\frac{2\pi}{\lambda}(d_{k'}^{\mathrm{RG}} - d_k^{\mathrm{RG}})} \\ & \sum_{m_{\mathrm{R}x}=1}^{M_{\mathrm{R}x}} \sum_{m_{\mathrm{R}y}=1}^{M_{\mathrm{R}y}} \exp\Bigg(-j\frac{2\pi}{\lambda} \big[\Delta_{\mathrm{R}x}(m_{\mathrm{R}x}-1)(\sin\theta_{k'}^{\mathrm{RG}} \cos\xi_{k'}^{\mathrm{RG}} - \sin\theta_k^{\mathrm{RG}} \cos\xi_k^{\mathrm{RG}}) \\ & + \Delta_{\mathrm{R}y}(m_{\mathrm{R}y}-1)(\sin\theta_{k'}^{\mathrm{RG}} \sin\xi_{k'}^{\mathrm{RG}} - \sin\theta_k^{\mathrm{RG}} \sin\xi_k^{\mathrm{RG}}) \big] \Bigg) \\ & + \sqrt{\frac{\beta_0}{A_{k'}[n]}} \Delta h_{k'}^{\mathrm{AG}}[n] + \sqrt{\frac{\beta_0^2}{B_{k'}[n]}} \Delta h_{k'}^{\mathrm{RG}}[n], \end{aligned} \tag{5.19}$$

respectively, where $A_k[n] = (d_k^{\mathrm{AG}}[n])^{\alpha^{\mathrm{AG}}}(1+\kappa_k^{\mathrm{AG}}[n])$, $B_k[n] = (d^{\mathrm{AR}}[n])^{\alpha^{\mathrm{AR}}}(d_k^{\mathrm{RG}})^{\alpha^{\mathrm{RG}}}(1+\kappa^{\mathrm{RG}})$, $A_{k'}[n] = (d_{k'}^{\mathrm{AG}}[n])^{\alpha^{\mathrm{AG}}}(1+\kappa_{k'}^{\mathrm{AG}}[n])$, and $B_{k'}[n] = (d^{\mathrm{AR}}[n])^{\alpha^{\mathrm{AR}}}(d_{k'}^{\mathrm{RG}})^{\alpha^{\mathrm{RG}}}(1+\kappa^{\mathrm{RG}})$. We can observe that $h_k[n]$ and $h_{k'}[n]$ follow the Gaussian distribution with mean, $\sqrt{\frac{\beta_0 \kappa_k^{\mathrm{AG}}[n]}{A_k[n]}} + \sqrt{\frac{\beta_0^2 \kappa^{\mathrm{RG}} M_{\mathrm{R}}^2}{B_k[n]}}$ and $\sqrt{\frac{\beta_0 \kappa_{k'}^{\mathrm{AG}}[n]}{A_{k'}[n]}} + \sqrt{\frac{\beta_0^2 \kappa^{\mathrm{RG}}}{B_{k'}[n]}}$, as well as variance, $\frac{\beta_0}{A_k[n]} + \frac{\beta_0^2 M_{\mathrm{R}}^2}{B_k[n]}$ and $\frac{\beta_0}{A_{k'}[n]} + \frac{\beta_0^2}{B_{k'}[n]}$, respectively. In other words, the end-to-end effective channels of GUs still follows the altitude-dependent Rician fading with our proposed phase control policy[13]. Note that the outage probability constraints C6 – C8 of the formulated optimization problem (5.16) are active at the optimal

[13]The obtained closed-form IRS phase shift in (5.17) is the optimal solution for the case of OMA.

point. Then, constraints C6 − C8 can be rewritten as[14]

$$\begin{aligned}1-\varepsilon_k^{\mathrm{SIC}} &= \Pr\left(s_{k,k'}[n]r_{k'}[n] \le s_{k,k'}[n]C_{k,k'}^{\mathrm{I,SIC}}[n], s_{k,k'}[n]r_k[n] \le s_{k,k'}[n]C_{k,k'}^{\mathrm{II,SIC}}[n]\right)\\ &= \Pr\left(\frac{\sigma_k^2(2^{r_{k'}[n]}-1)}{p_{k'}[n]-p_k[n](2^{r_{k'}[n]}-1)} \le |h_k[n]|^2, \frac{\sigma_k^2(2^{r_k[n]}-1)}{p_k[n]} \le |h_k[n]|^2\right)\\ &= \max\left\{1-F_{n,k}\left(\frac{\sigma_k^2(2^{r_{k'}[n]}-1)}{p_{k'}[n]-p_k[n](2^{r_{k'}[n]}-1)}\right),\right.\\ &\quad \left.1-F_{n,k}\left(\frac{\sigma_k^2(2^{r_k[n]}-1)}{p_k[n]}\right)\right\}, \qquad (5.20)\end{aligned}$$

$$\begin{aligned}1-\varepsilon_k^{\mathrm{NSIC}} &= \Pr\left(s_{k',k}[n]r_k[n] \le s_{k',k}[n]C_{k',k}^{\mathrm{NSIC}}[n]\right)\\ &= \Pr\left(\frac{\sigma_k^2(2^{r_k[n]}\upsilon-1)}{p_k[n]-p_{k'}[n](2^{r_k[n]}-1)} \le |h_k[n]|^2\right)\\ &= 1-F_{n,k}\left(\frac{\sigma_k^2(2^{r_k[n]}-1)}{p_k[n]-p_{k'}[n](2^{r_k[n]}-1)}\right), \qquad (5.21)\end{aligned}$$

$$\begin{aligned}1-\varepsilon_k^{\mathrm{OMA}} &= \Pr\left(s_{k,k}[n]r_k[n] \le s_{k,k}[n]C_{k,k}^{\mathrm{II,SIC}}[n]\right)\\ &= \Pr\left(\frac{\sigma_k^2(2^{r_k[n]}-1)}{p_k[n]} \le |h_k[n]|^2\right) = 1-F_{n,k}\left(\frac{\sigma_k^2(2^{r_k[n]}-1)}{p_k[n]}\right), \qquad (5.22)\end{aligned}$$

respectively. Note that $F_{n,k}(\cdot)$ is the cumulative distribution function (CDF) of the random variable $|h_k[n]|^2$, which is given by [40, 138]

$$\begin{aligned}&F_{n,k}(\chi)\\ &= 1-Q_1\left(\sqrt{\frac{\beta_0\kappa_k^{\mathrm{AG}}[n]B_k[n]}{D_k[n]}}+\sqrt{\frac{\beta_0^2\kappa^{\mathrm{RG}}M_{\mathrm{R}}^2A_k[n]}{D_k[n]}}, \sqrt{\frac{A_k[n]B_k[n]}{D_k[n]}}\chi\right) \text{ and } \qquad (5.23)\\ &F_{n,k}(f_k^{\mathrm{NSIC}}[n])\\ &= 1-Q_1\left(\sqrt{\frac{\beta_0\kappa_k^{\mathrm{AG}}[n]B_k[n]}{D_k[n]}}+\sqrt{\frac{\beta_0^2\kappa^{\mathrm{RG}}A_k[n]}{D_k[n]}}, \sqrt{\frac{A_k[n]B_k[n]}{D_k[n]}}f_k^{\mathrm{NSIC}}[n]\right), \qquad (5.24)\end{aligned}$$

where $\chi \in \{f_k^{\mathrm{I,SIC}}[n], f_k^{\mathrm{II,SIC}}[n], f_k^{\mathrm{OMA}}[n]\}$, $f_k^{\mathrm{SIC}}[n] = \min\left\{f_k^{\mathrm{I,SIC}}[n], f_k^{\mathrm{II,SIC}}[n]\right\}$, and

[14]Note that since outage constraints C6 − C8 are inactive if $s_{k,k'}[n] = 0$, we only consider the situation of $s_{k,k'}[n] = 1$ while handling the intractable constraints C6 − C8 in the following process.

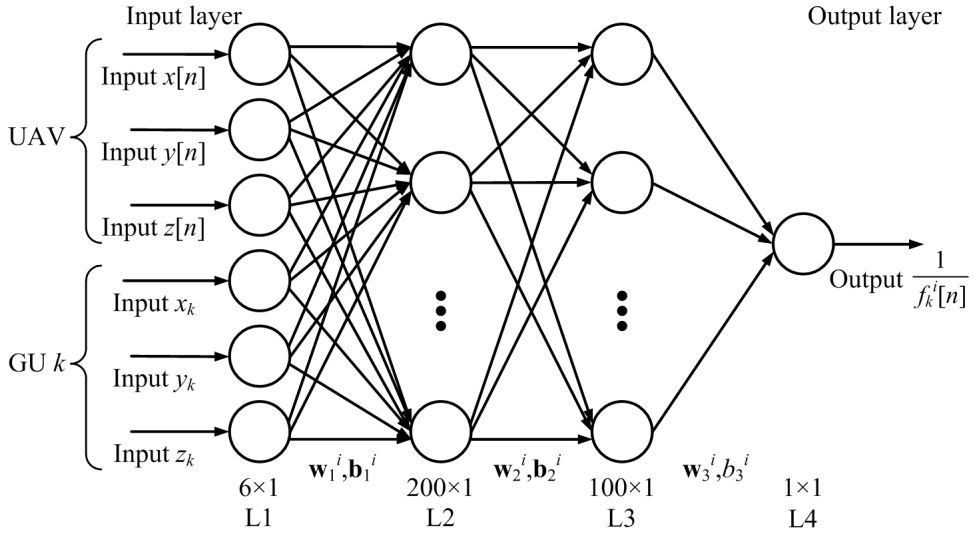

Figure 5.3: The structure of the employed three-layer feedforward neural network.

$D_k[n] = \beta_0 B_k[n] + \beta_0^2 M_{\mathrm{R}}^2 A_k[n]$. Note that $f_k^{\mathrm{SIC}}[n]$, $f_k^{\mathrm{NSIC}}[n]$, and $f_k^{\mathrm{OMA}}[n]$ denote the outage-guaranteed effective channel gain for GU k when it is selected as a SIC user, a non-SIC user, and an OMA user, respectively. Function $Q_1(a, b)$ is the standard Marcum-Q function [139]. In general, there is no closed-form expression for (5.23) and (5.24). More importantly, their inverse functions, i.e., $F_{n,k}^{-1}(f_k^{\mathrm{I,SIC}}[n])$, $F_{n,k}^{-1}(f_k^{\mathrm{II,SIC}}[n])$, $F_{n,k}^{-1}(f_k^{\mathrm{NSIC}}[n])$, and $F_{n,k}^{-1}(f_k^{\mathrm{OMA}}[n])$, for returning outage-guaranteed effective channel gains, $f_k^{\mathrm{I,SIC}}[n]$, $f_k^{\mathrm{II,SIC}}[n]$, $f_k^{\mathrm{NSIC}}[n]$, and $f_k^{\mathrm{OMA}}[n]$ are intractable functions with respect to (w.r.t.) the 3D trajectory of the UAV, $\mathbf{t}[n]$. On the other hand, although the value of the Marcum-Q function can be found via a lookup table, it does not facilitate the overall resource allocation design.

To strike a balance between the system performance and the computational complexity, in this chapter, we adopt a DNN approach[15] [140,141] to approximate the outage-guaranteed effective channel gain $f_k^i[n]$ for different schemes $i \in$

[15]Note that although existing data regression methods, e.g., discriminant analysis and stochastic modeling, have been proposed to approximate the sophisticated effective channel gain, the obtained results are generally intractable which do not facilitate the design of computationally efficient resource allocation.

$\{\text{SIC}, \text{NSIC}, \text{OMA}\}$ as a tractable function w.r.t. the 3D trajectory of the UAV and location of GUs. Fig. 5.3 shows the structure of a three-layer feedforward neural network [142, 143]. Thus, for each location of the UAV, $\mathbf{t}[n]$, the location of GU k, $\mathbf{l}_k$, and a given outage probability, ε_k^i, we can generate the numerical data of $\frac{1}{f_k^i[n]}$ based on (5.2)–(5.7), (5.20)–(5.24) which serve as labels for neural network training[16]. After offline training based on the generated samplings, we can then obtain a well-trained neural network. That is, for given maximum tolerable outage probabilities ε_k^i, we obtain the approximated outage-guaranteed user location-aware effective channel gain for GU k as

$$f_k^i[n] \approx \frac{1}{(\mathbf{w}_3^i)^{\mathrm{H}} \left[\mathbf{w}_2^i \left[\mathbf{w}_1^i \mathbf{q}_k[n] + \mathbf{b}_1^i\right]^+ + \mathbf{b}_2^i\right]^+ + b_3^i}. \tag{5.25}$$

Note that $[\mathbf{w}_1^i \mathbf{q}_k[n] + \mathbf{b}_1^i]^+$ is the rectified linear unit (ReLU) function for GU k adopting scheme i, which is a convex function w.r.t. $\mathbf{q}_k[n]$. Vector $\mathbf{q}_k[n] = [\mathbf{t}[n]; \mathbf{l}_k] \in \mathbb{R}^{6\times 1}$ collects the trajectory of the UAV and the location of GU k at time slot n. Parameters $\mathbf{w}_1^i \in \mathbb{R}^{200\times 6}$, $\mathbf{b}_1^i \in \mathbb{R}^{200\times 1}$, $\mathbf{w}_2^i \in \mathbb{R}^{100\times 200}$, $\mathbf{b}_2^i \in \mathbb{R}^{100\times 1}$, $\mathbf{w}_3^i \in \mathbb{R}^{100\times 1}$, and $b_3^i \in \mathbb{R}$ are the well-trained weights and biases for scheme i between layer 1 and layer 2, layer 2 and layer 3, as well as layer 3 and layer 4, respectively, as shown in Fig. 5.3. To verify the approximation accuracy, as shown in Fig. 5.4 and Fig. 5.5, we present the numerical result of $f_k^i[n]$ based on (5.23) and (5.24) as well as the approximated value by the neural network model according to (5.25) for different dimensions, respectively. We can observe from them that the numerical result of $f_k^i[n]$ based on (5.2)–(5.7), (5.20)–(5.24) closely match their predicted effective channel gains obtained by

[16]The reason for adopting $\frac{1}{f_k^i[n]}$ as a label rather than $f_k^i[n]$ is that the former can be interpreted as the path loss between the UAV and the desired GU's location which directly depends on the UAV's trajectory.

our well-trained numerical network model. Besides, the normalized mean square error (NMSE) between the numerical channel gain and the outage-guaranteed effective channel gain via the DNN approach is less than 0.005. In particular, there is a non-trivial trade-off between the flight altitude, outage-guaranteed effective channel gain, and the horizontal distance between the UAV and the GUs. For example, as shown in Fig. 5.5, when the horizontal distance between the UAV and the desired users (e.g., GU 1 and GU 2) is large, increasing the flight altitude to a certain extent would increase the effective channel gain. Specifically, a higher flight altitude can reduce the variance of Rician fading channel in (5.4) which facilitates a more power-efficient UAV communication. However, an exceedingly high flight altitude would cause the decrease in outage-guaranteed effective channel gain, as the increased path loss outweights the gain brought by reduced channel uncertainty. On the other hand, when the horizontal distance between the UAV and the user (e.g., GU 3) is short, increasing the flight altitude is not beneficial to the effective channel gain since the increased path loss is dominated. As a result, we set the outage-guaranteed transmission rate for GU k as a SIC user, a non-SIC user, and an OMA user[17] are given by

$$r_k[n] = \log_2\left(1 + \frac{p_k[n] f_k^{\mathrm{SIC}}[n]}{\sigma_k^2}\right), \forall n, k \neq k', \text{ if } s_{k,k'}[n] = 1, \tag{5.26}$$

$$r_k[n] = \log_2\left(1 + \frac{p_k[n] f_k^{\mathrm{NSIC}}[n]}{p_{k'}[n] f_k^{\mathrm{NSIC}}[n] + \sigma_k^2}\right), \forall n, k \neq k', \text{ if } s_{k',k}[n] = 1, \text{ and} \tag{5.27}$$

$$r_k[n] = \log_2\left(1 + \frac{p_k[n] f_k^{\mathrm{OMA}}[n]}{\sigma_k^2}\right), \forall n, k, \text{ if } s_{k,k}[n] = 1, \tag{5.28}$$

respectively. Then, by applying (5.26) and (5.27) to constraint C5a, we can readily reformulate the original optimization formulation in (5.16) as the following

[17]Note that we will verify the accuracy of the outage probability obtained by using (5.25) as the outage-guaranteed effective channel gain in the simulation section.

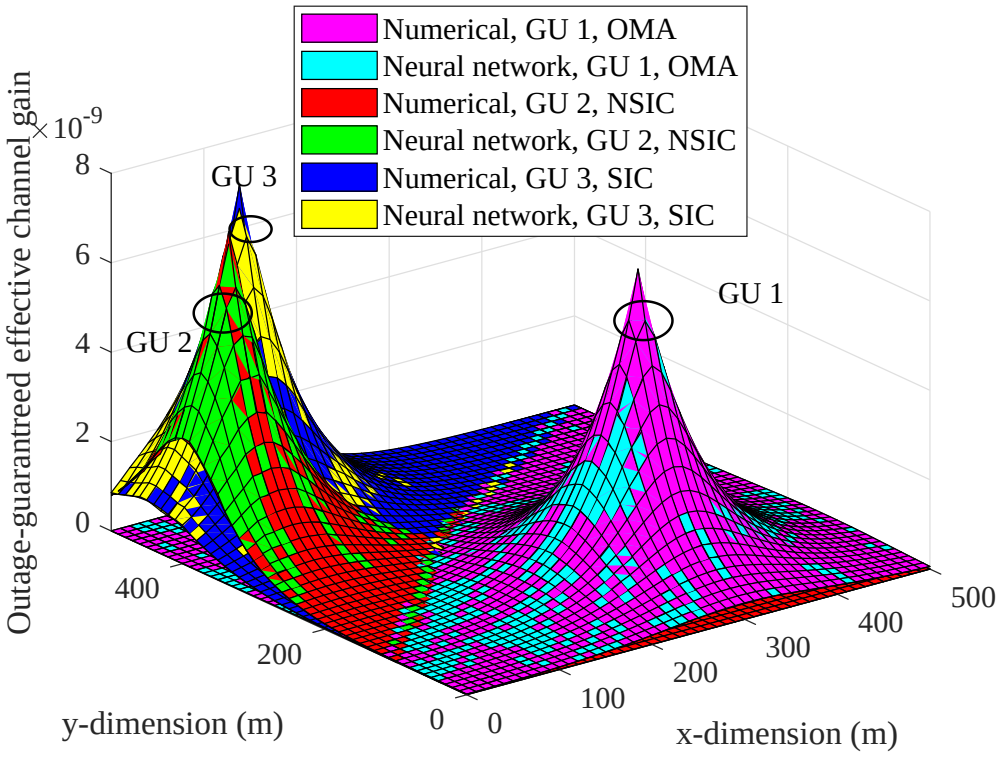

Figure 5.4: Comparisons between the numerical data and the neural network model versus the UAV's location at the x-dimension and the y-dimension for a specific altitude, i.e., 140 m, when the maximum tolerable outage probability = 0.01 and $\kappa_{\min} = 0$ dB. The location of GUs and the IRS are listed in Table 5.2.

problem:

$$\underset{\mathcal{S},\mathcal{P},\mathcal{T},\mathcal{V},\mathcal{Q}}{\text{minimize}} \ \frac{1}{N}\sum_{n=1}^{N} P_{\text{comm}}[n] + \frac{1}{N}\sum_{n=1}^{N} P_{\text{fly}}[n] \tag{5.29}$$

$$\text{s.t.C1} - \text{C4}, \text{C9} - \text{C14},$$

$$\overline{\text{C5}} : \frac{1}{N}\sum_{n=1}^{N}\left[\sum_{\substack{k'=1\\k'\neq k}}^{K}\left(s_{k,k'}[n]\log_2\left(1+\frac{p_k[n]f_k^{\text{SIC}}[n]}{\sigma_k^2}\right)\right.\right.$$

$$\left. + s_{k',k}[n]\log_2\left(1+\frac{p_k[n]f_k^{\text{NSIC}}[n]}{p_{k'}[n]f_k^{\text{NSIC}}[n]+\sigma_k^2}\right)\right)$$

$$\left. + s_{k,k}[n]\log_2\left(1+\frac{p_k[n]f_k^{\text{OMA}}[n]}{\sigma_k^2}\right)\right] \geq R_{\min_k}, \forall k,$$

$$\text{C16} : \mathbf{q}_k[n] = [\mathbf{t}[n]; \mathbf{l}_k], \forall n, k,$$

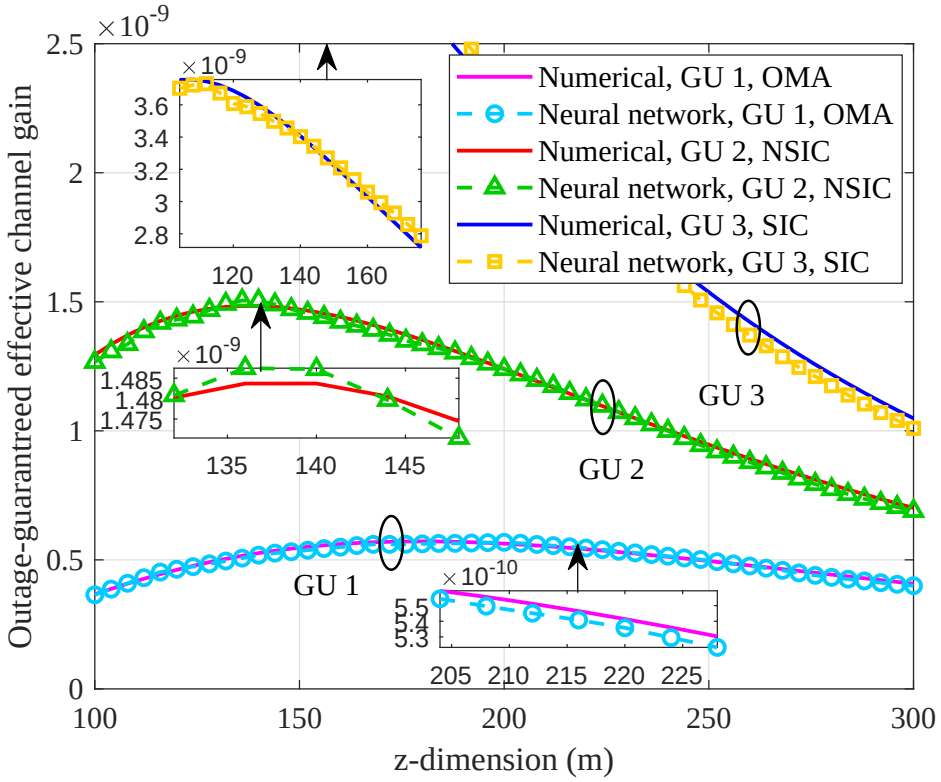

Figure 5.5: Comparisons between the numerical data and the neural network model versus the UAV's vertical location at z-dimension with horizontal locations, i.e., $(170, 200)$, $(180, 300)$, and $(60, 400)$, calculated for GU 1, GU 2, and GU 3, respectively, when the maximum tolerable outage probability $= 0.01$ and $\kappa_{\min} = 0$ dB.

where $\mathcal{Q} = \{\mathbf{q}_k[n], \forall n, k\}$. Note that we can rewrite $\overline{\text{C5}}$ as

$$\overline{\overline{\text{C5}}}: \frac{1}{N}\sum_{n=1}^{N}\left[\sum_{\substack{k'=1\\k'\neq k}}^{K} R_{k,k'}^{\text{SIC}}[n] + \sum_{\substack{k'=1\\k'\neq k}}^{K}\left(R_{k',k}^{\text{I}}[n] - R_{k',k}^{\text{II}}[n]\right) + R_{k,k}^{\text{OMA}}[n]\right] \geq R_{\min_k}, \forall k, \tag{5.30}$$

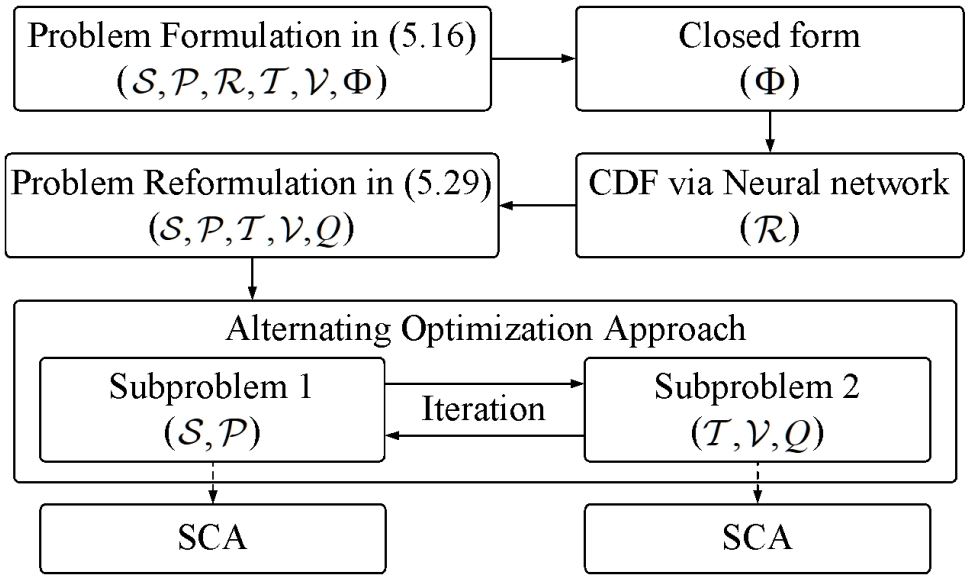

Figure 5.6: A flow chart for the illustration of the proposed iterative algorithm.

where

$$R_{k,k'}^{\mathrm{SIC}}[n] = s_{k,k'}[n]\log_2\left(1+\frac{p_k[n]f_k^{\mathrm{SIC}}[n]}{\sigma_k^2}\right), \tag{5.31}$$

$$R_{k',k}^{\mathrm{I}}[n] = s_{k',k}[n]\log_2\big((p_k[n]+p_{k'}[n])f_k^{\mathrm{NSIC}}[n]+\sigma_k^2\big), \tag{5.32}$$

$$R_{k',k}^{\mathrm{II}}[n] = s_{k',k}[n]\log_2\big(p_{k'}[n]f_k^{\mathrm{NSIC}}[n]+\sigma_k^2\big), \text{ and} \tag{5.33}$$

$$R_{k,k}^{\mathrm{OMA}}[n] = s_{k,k}[n]\log_2\left(1+\frac{p_k[n]f_k^{\mathrm{OMA}}[n]}{\sigma_k^2}\right). \tag{5.34}$$

Although the reformulated problem in (5.29) is more tractable, it is still non-convex due to the coupling between the communication resource allocation variables and the UAV's trajectory design variables. Now, to obtain an efficient suboptimal solution, we adopt the alternating optimization (AO) method [112] by separating the optimization problem in (5.29) into two subproblems and address them iteratively. The solution structure is shown in a flow chart in Fig. 5.6. In particular, subproblem 1 optimizes the user scheduling $\mathcal{S} = \{s_{k,k'}[n], \forall n,k,k'\}$ and the power allocation $\mathcal{P} = \{p_k[n], \forall n,k\}$ for a given UAV's 3D trajectory

$\mathcal{T} = \{\mathbf{t}[n], \forall n\}$, 3D flight velocity $\mathcal{V} = \{\mathbf{v}[n], \forall n\}$, and $\mathcal{Q} = \{\mathbf{q}_k[n], \forall n, k\}$; Subproblem 2 optimizes the UAV's 3D trajectory $\mathcal{T} = \{\mathbf{t}[n], \forall n\}$, its 3D flight velocity $\mathcal{V} = \{\mathbf{v}[n], \forall n\}$, and $\mathcal{Q} = \{\mathbf{q}_k[n], \forall n, k\}$ for a given user scheduling $\mathcal{S} = \{s_{k,k'}[n], \forall n, k, k'\}$ and power allocation $\mathcal{P} = \{p_k[n], \forall n, k\}$. Now, we study the solution of subproblem 1.

5.4.2 Subproblem 1: Optimizing User Scheduling and Power Allocation

In this subproblem, for any given UAV's trajectory and flight velocity, the user scheduling and power allocation can be formulated as:

$$\begin{aligned} \underset{\mathcal{S},\mathcal{P}}{\text{minimize}} \ & \frac{1}{N}\sum_{n=1}^{N} P_{\text{comm}}[n] + \frac{1}{N}\sum_{n=1}^{N} P_{\text{fly}}[n] \\ \text{s.t. } & \text{C1} - \text{C4}, \overline{\text{C5}}. \end{aligned} \tag{5.35}$$

Note that constraint C2 is an affine constraint w.r.t. the user scheduling $s_{k,k'}[n]$. First, to address the nonconvexity of the problem, we handle the coupling between the paired user scheduling $s_{k,k'}[n]$ and transmit power allocation $p_k[n]$ variables by introducing one slack variable[18] $\tilde{p}_{k,k',k}[n] = s_{k,k'}[n]p_k[n]$. Then, by adopting the big-M formulation [45, 97, 113], we introduce the following auxiliary

[18]Note that the slack variable with different subscripts have different physical meanings, i.e., $\tilde{p}_{k,k',k}[n] = s_{k,k'}[n]p_k[n]$, $\tilde{p}_{k,k',k'}[n] = s_{k,k'}[n]p_{k'}[n]$, $\tilde{p}_{k',k,k}[n] = s_{k',k}[n]p_k[n]$, $\tilde{p}_{k',k,k'}[n] = s_{k',k}[n]p_{k'}[n]$, and $\tilde{p}_{k,k,k}[n] = s_{k,k}[n]p_k[n]$ are the power allocation for GU k and k' when GU k as the SIC user and GU k' as the non-SIC user, the power allocation for GU k and k' when GU k' as the SIC user and GU k as the non-SIC user, and the power allocation for GU k when it as the OMA user, respectively. In this chapter, we adopt $\tilde{p}_{k,k',k}[n]$ to represent the slack variable to simplify the presentation.

constraints:

$$\begin{aligned}
&\text{C17}: \tilde{p}_{k,k',k}[n] \leq p_k[n], \forall n, k, k', \\
&\text{C18}: \tilde{p}_{k,k',k}[n] \leq s_{k,k'}[n] P_{\text{peak}}, \forall n, k, k', \\
&\text{C19}: \tilde{p}_{k,k',k}[n] \geq 0, \forall n, k, k', \\
&\text{C20}: \tilde{p}_{k,k',k}[n] \geq p_k[n] - (1 - s_{k,k'}[n]) P_{\text{peak}}, \forall n, k, k'.
\end{aligned} \tag{5.36}$$

Then, we can rewrite the binary constraint C1 in its equivalent form as

$$\begin{aligned}
&\text{C1a}: \sum_{n=1}^{N} \sum_{k=1}^{K} \sum_{k'=1}^{K} \left(s_{k,k'}[n] - (s_{k,k'}[n])^2 \right) \leq 0, \\
&\text{C1b}: 0 \leq s_{k,k'}[n] \leq 1, \forall n, k, k',
\end{aligned} \tag{5.37}$$

where variable $s_{k,k'}[n]$ is a continuous value between zero and one. However, constraint C1a is a reverse convex function [103, 115]. To handle this non-convexity, we reformulate the problem formulation in (5.35) based on [45, 93, 103] as its equivalent form:

$$\begin{aligned}
\underset{\mathcal{S},\mathcal{P},\tilde{\mathcal{P}}}{\text{minimize}} \; & \frac{1}{N} \sum_{n=1}^{N} \sum_{k=1}^{K} \Bigg[\eta \Bigg(\sum_{\substack{k'=1 \\ k' \neq k}}^{K} (\tilde{p}_{k,k',k}[n] + \tilde{p}_{k,k',k'}[n]) + \tilde{p}_{k,k,k}[n] \Bigg) \\
& + \sum_{k'=1}^{K} \zeta \left(s_{k,k'}[n] - (s_{k,k'}[n])^2 \right) \Bigg] + \frac{1}{N} \sum_{n=1}^{N} P_{\text{fly}}[n] \qquad (5.38) \\
\text{s.t.} \; & \text{C1b}, \text{C2}, \text{C17} - \text{C20}, \\
& \widetilde{\text{C3}}: \tilde{p}_{k,k',k}[n] \geq 0, \forall n, k, k', \\
& \widetilde{\text{C4}}: \sum_{k=1}^{K} \left(\sum_{k' \neq k}^{K} (\tilde{p}_{k,k',k}[n] + \tilde{p}_{k,k',k'}[n]) + \tilde{p}_{k,k,k}[n] \right) \leq P_{\text{peak}}, \forall n, \\
& \widetilde{\text{C5}}: \frac{1}{N} \sum_{n=1}^{N} \left[\sum_{\substack{k'=1 \\ k' \neq k}}^{K} \tilde{R}^{\text{SIC}}_{k,k'}[n] + \sum_{\substack{k'=1 \\ k' \neq k}}^{K} \left(\tilde{R}^{\text{I}}_{k',k}[n] - \tilde{R}^{\text{II}}_{k',k}[n] \right) + \tilde{R}^{\text{OMA}}_{k,k}[n] \right] \geq R_{\min_k}, \forall k,
\end{aligned}$$

where

$$\tilde{R}_{k,k'}^{\mathrm{SIC}}[n] = s_{k,k'}[n]\log_2\left(1+\frac{\tilde{p}_{k,k',k}[n]f_k^{\mathrm{SIC}}[n]}{s_{k,k'}[n]\sigma_k^2}\right), \tag{5.39}$$

$$\tilde{R}_{k',k}^{\mathrm{I}}[n] = s_{k',k}[n]\log_2\left(\frac{(\tilde{p}_{k',k,k}[n]+\tilde{p}_{k',k,k'}[n])f_k^{\mathrm{NSIC}}[n]}{s_{k',k}[n]}+\sigma_k^2\right), \tag{5.40}$$

$$\tilde{R}_{k',k}^{\mathrm{II}}[n] = s_{k',k}[n]\log_2\left(\frac{\tilde{p}_{k',k,k'}[n]f_k^{\mathrm{NSIC}}[n]}{s_{k',k}[n]}+\sigma_k^2\right), \text{ and} \tag{5.41}$$

$$\tilde{R}_{k,k}^{\mathrm{OMA}}[n] = s_{k,k}[n]\log_2\left(1+\frac{\tilde{p}_{k,k,k}[n]f_k^{\mathrm{OMA}}[n]}{s_{k,k}[n]\sigma_k^2}\right), \tag{5.42}$$

$\tilde{\mathcal{P}} = \{\tilde{p}_{k,k',k}[n], \forall n,k,k'\}$, and $\zeta \gg 1$. Note that the optimization problem in (5.38) is still non-convex and the non-convexity arises from the objective function and constraint $\widetilde{\mathrm{C5}}$. Thus, we handle the penalty terms in the objective function and $\tilde{R}_{k',k}^{\mathrm{II}}[n]$ in nonconvex constraints $\widetilde{\mathrm{C5}}$ in problem (5.38) via the iterative successive convex approximation (SCA) technique [78,130]. Specifically, for given $s_{k,k'}^{j_1}[n]$ and $p_{k,k',k}^{j_1}[n]$ in the j_1-th iteration, an upper bound of the penalty term and $\tilde{R}_{k',k}^{\mathrm{II}}[n]$ can be obtained by their first-order Taylor expansions as

$$\begin{aligned}
&s_{k,k'}[n]-(s_{k,k'}[n])^2 \le (A_{k,k'}^{\mathrm{up}}[n])^{j_1}\\
&= s_{k,k'}[n]-(s_{k,k'}^{j_1}[n])^2+2s_{k,k'}^{j_1}[n](s_{k,k'}[n]-s_{k,k'}^{j_1}[n]) \text{ and}
\end{aligned} \tag{5.43}$$

$$\begin{aligned}
&\tilde{R}_{k',k}^{\mathrm{II}}[n] \le (\tilde{R}_{k',k}^{\mathrm{II,up}}[n])^{j_1}\\
&= s_{k',k}^{j_1}[n]\log_2\left(\frac{\tilde{p}_{k',k,k'}^{j_1}[n]f_k^{\mathrm{NSIC}}[n]}{s_{k',k}^{j_1}[n]}+\sigma_k^2\right)\\
&+\log_2\left(\frac{\tilde{p}_{k',k,k'}^{j_1}[n]f_k^{\mathrm{NSIC}}[n]}{s_{k',k}^{j_1}[n]}+\sigma_k^2\right)(s_{k',k}[n]-s_{k',k}^{j_1}[n])\\
&-\frac{\tilde{p}_{k',k,k'}^{j_1}[n]f_k^{\mathrm{NSIC}}[n](s_{k',k}[n]-s_{k',k}^{j_1}[n])}{(\tilde{p}_{k',k,k'}^{j_1}[n]f_k^{\mathrm{NSIC}}[n]+s_{k',k}^{j_1}[n]\sigma_k^2)\ln 2}+\frac{s_{k',k}^{j_1}[n]f_k^{\mathrm{NSIC}}[n](\tilde{p}_{k',k,k'}[n]-\tilde{p}_{k',k,k'}^{j_1}[n])}{(\tilde{p}_{k',k,k'}^{j_1}[n]f_k^{\mathrm{NSIC}}[n]+s_{k',k}^{j_1}[n]\sigma_k^2)\ln 2},
\end{aligned} \tag{5.44}$$

respectively.

After applying (5.43) and (5.44) to the transformed optimization problem in (5.38), we obtain a suboptimal solution by

$$\begin{aligned}
&\underset{\mathcal{S},\mathcal{P},\tilde{\mathcal{P}}}{\text{minimize}} \sum_{n=1}^{N}\sum_{k=1}^{K}\left[\frac{\eta}{N}\left(\sum_{\substack{k'=1\\k'\neq k}}^{K}(\tilde{p}_{k,k',k}[n]+\tilde{p}_{k,k',k'}[n])+\tilde{p}_{k,k,k}[n]\right)+\sum_{k'=1}^{K}\zeta(A_{k,k'}^{\text{up}}[n])^{j_1}\right] \\
&\qquad\qquad +\frac{1}{N}\sum_{n=1}^{N}P_{\text{fly}}[n] \\
&\quad \text{s.t. C1b, C2, } \widetilde{\text{C3}}, \widetilde{\text{C4}}, \text{C17}-\text{C20}, \qquad (5.45)\\
&\widetilde{\widetilde{\text{C5}}}: \frac{1}{N}\sum_{n=1}^{N}\left[\sum_{\substack{k'=1\\k'\neq k}}^{K}\tilde{R}_{k,k'}^{\text{SIC}}[n]+\sum_{\substack{k'=1\\k'\neq k}}^{K}\left(\tilde{R}_{k',k}^{\text{I}}[n]-(\tilde{R}_{k',k}^{\text{II,up}}[n])^{j_1}\right)+\tilde{R}_{k,k}^{\text{OMA}}[n]\right] \\
&\qquad \geq R_{\min_k}, \forall k.
\end{aligned}$$

Note that solving (5.45) leads to an upper bound of the optimal objective value of problem (5.38). Furthermore, in order to tighten the obtained upper bound, we iteratively update the feasible solution, $s_{k,k'}^{j_1}[n]$ and $\tilde{p}_{k',k,k'}^{j_1}[n]$, by solving the optimization problem in (5.45) with a standard convex optimization solver, such as CVX [120] in the j_1-th iteration. The proposed SCA-based algorithm is summarized in **Algorithm 5.1** and the convergence of the algorithm to a suboptimal solution is guaranteed [42].

Algorithm 5.1 Proposed Algorithm for Handling Sub-problem 1 in (5.35)

1: Initialize the convergence tolerance $\epsilon_1 \rightarrow 0$, the maximum number of iterations $I_{1,\max}$, the initial iteration index $j_1 = 0$, the initial variables $\{s_{k,k'}^{j_1}[n], \tilde{p}_{k',k,k'}^{j_1}[n]\}$, and the initial objective value $\tilde{P}_{\text{total}}$

2: **repeat** {Main Loop: SCA}

3: Set $j_1 = j_1 + 1$ and $\{s_{k,k'}^{j_1}[n], \tilde{p}_{k',k,k'}^{j_1}[n]\} = \{s_{k,k'}[n], \tilde{p}_{k',k,k'}[n]\}$

4: Solving optimization problem in (5.45) to obtain $\{s_{k,k'}[n], p_k[n], \tilde{p}_{k,k',k}[n]\}$ and $\tilde{P}_{\text{total}}$

5: Update $\tilde{P}_{\text{total}}^{j_1} = \tilde{P}_{\text{total}}$

6: **until** $j_1 = I_{1,\max}$ or $\frac{|\tilde{P}_{\text{total}}^{j_1} - \tilde{P}_{\text{total}}^{(j_1-1)}|}{\tilde{P}_{\text{total}}^{j_1}} \leq \epsilon_1$

7: Return $\{s_{k,k'}^*[n], p_k^*[n]\} = \{s_{k,k'}[n], \tilde{p}_{k,k',k}[n]\}$ and $\tilde{P}_{\text{total}}^* = \tilde{P}_{\text{total}}^{j_1}$

5.4.3 Subproblem 2: Optimizing UAV's 3D Trajectory and Flight Velocity

In this subproblem, for a given user scheduling and power allocation strategy, we can express the optimization problem as

$$\underset{\mathcal{T},\mathcal{V},\mathcal{Q}}{\text{minimize}} \ \frac{1}{N}\sum_{n=1}^{N} P_{\text{comm}}[n] + \frac{1}{N}\sum_{n=1}^{N} P_{\text{fly}}[n] \tag{5.46}$$
$$\text{s.t. } \overline{\text{C5}}, \text{C9} - \text{C14}, \text{C16}.$$

Note that the optimization problem in (5.46) is nonconvex and the nonconvexity arises from constraint $\overline{\text{C5}}$ and the function of the UAV's flight power consumption $P_{\text{fly}}[n]$ w.r.t. $\mathbf{t}[n]$ and $\mathbf{v}[n]$, respectively. Thus, to tackle these nonconvexities, we first introduce two slack variables $\nu[n]$ and $u_k^i[n]$ to rewrite the problem in (5.46)

into its equivalent form:

$$\underset{\mathcal{T},\mathcal{V},\mathcal{Q},\Upsilon,\mathcal{U}}{\text{minimize}} \ \frac{1}{N}\sum_{n=1}^{N} P_{\text{comm}}[n] + \frac{1}{N}\sum_{n=1}^{N} \hat{P}_{\text{fly}}[n] \tag{5.47}$$

$$\text{s.t. C9} - \text{C14, C16,}$$

$$\widehat{\text{C5}} : \frac{1}{N}\sum_{n=1}^{N}\left(\sum_{\substack{k'=1\\k'\neq k}}^{K}\hat{R}^{\text{SIC}}_{k,k'}[n] + \sum_{\substack{k'=1\\k'\neq k}}^{K}\left(\hat{R}^{\text{I}}_{k',k}[n] - \hat{R}^{\text{II}}_{k',k}[n]\right) + \hat{R}^{\text{OMA}}_{k,k}[n]\right) \geq R_{\min_k}, \forall k,$$

$$\text{C21} : v_x^2[n] + v_y^2[n] \geq \nu^2[n], \forall n,$$

$$\text{C22} : \nu[n] \geq 0, \forall n,$$

$$\text{C23} : u_k^i[n] \geq (\mathbf{w}_3^i)^{\text{H}}\left[\mathbf{w}_2^i\left[\mathbf{w}_1^i\mathbf{q}_k[n] + \mathbf{b}_1^i\right]^+ + \mathbf{b}_2^i\right]^+ + b_3^i, \forall n, k, i,$$

where $\Upsilon = \{\nu[n], \forall n\}$, $\mathcal{U} = \{u_k^i[n], \forall k, n\}$,

$$\hat{R}^{\text{SIC}}_{k,k'}[n] = s_{k,k'}[n]\log_2\left(1 + \frac{\tilde{p}_{k,k',k}[n]}{u_k^{\text{SIC}}[n]\sigma_k^2}\right), \tag{5.48}$$

$$\hat{R}^{\text{I}}_{k',k}[n] = s_{k',k}[n]\log_2\left(\frac{\tilde{p}_{k',k,k'}[n] + \tilde{p}_{k',k,k}[n]}{u_k^{\text{NSIC}}[n]} + \sigma_k^2\right), \tag{5.49}$$

$$\hat{R}^{\text{II}}_{k',k}[n] = s_{k',k}[n]\log_2\left(\frac{\tilde{p}_{k',k,k'}[n]}{u_k^{\text{NSIC}}[n]} + \sigma_k^2\right), \tag{5.50}$$

$$\hat{R}^{\text{OMA}}_{k,k}[n] = s_{k,k}[n]\log_2\left(1 + \frac{\tilde{p}_{k,k,k}[n]}{u_k^{\text{OMA}}[n]\sigma_k^2}\right), \text{and} \tag{5.51}$$

$$\hat{P}_{\text{fly}}[n] = P_o\left(1 + \frac{3(v_x^2[n] + v_y^2[n])}{\Omega^2 r^2}\right) + \frac{P_i v_0}{\nu[n]} + \frac{1}{2}d_0\rho s A_{\text{r}}(v_x^2[n] + v_y^2[n])^{3/2} + G v_{\text{z}}[n]. \tag{5.52}$$

Note that the additional inequality constraints C21 − C25 in problem (5.47) are all active at the optimal point. Thus, the formulated problems in (5.46) and (5.47) are equivalent to each other. Moreover, the nonconvexity of constraint C23 in problem (5.47) is attributed to the vector parameter $\mathbf{w}_2^i$ involving both positive and negative values, although the ReLU function is convex w.r.t. $\mathbf{q}_k[n]$.

To address this issue, we introduce two indicator variables $\mathbf{a}_{1,k}^{i}[n] \in \mathbb{R}^{200\times 200}$ and $\mathbf{a}_{2,k}^{i}[n] \in \mathbb{R}^{100\times 100}$ as

$$\begin{aligned} &\mathrm{C24}: \mathbf{a}_{1,k}^{i}[n] \in \{0,1\}, \forall n,k,i, \\ &\mathrm{C25}: \mathbf{a}_{2,k}^{i}[n] \in \{0,1\}, \forall n,k,i, \end{aligned} \tag{5.53}$$

where $\mathbf{a}_{1,k}^{i}[n] = 1$ when $\mathbf{w}_1^i \mathbf{q}_k[n] + \mathbf{b}_1^i > 0$. Otherwise, $\mathbf{a}_{1,k}^{i}[n] = 0$. Similarly, $\mathbf{a}_{2,k}^{i}[n] = 1$ when $\mathbf{w}_2^i \left(\mathbf{w}_1^i \mathbf{q}_k[n] + \mathbf{b}_1^i\right) + \mathbf{b}_2^i > 0$. Otherwise, $\mathbf{a}_{2,k}^{i}[n] = 0$. Thus, constraint C23 can be rewritten as

$$\widehat{\mathrm{C23}}: u_k^i[n] \geq (\mathbf{w}_3^i)^{\mathrm{H}} \mathbf{a}_{2,k}^{i}[n] \left(\mathbf{w}_2^i \mathbf{a}_{1,k}^{i}[n] \left(\mathbf{w}_1^i \mathbf{q}_k[n] + \mathbf{b}_1^i\right) + \mathbf{b}_2^i\right) + b_3^i, \forall n,k,i. \tag{5.54}$$

Note that similar to the solution of subproblem 1, we handle the coupling of $\mathbf{a}_{1,k}^{i}[n]$, $\mathbf{a}_{2,k}^{i}[n]$, and $\mathbf{q}_k[n]$ by introducing two slack variables $\hat{\mathbf{q}}_k^i[n] = \mathbf{a}_{1,k}^{i}[n] \left(\mathbf{w}_1^i \mathbf{q}_k[n] + \mathbf{b}_1^i\right) \in \mathbb{R}^{200\times 1}$ and $\hat{\hat{\mathbf{q}}}_k^i[n] = \mathbf{a}_{2,k}^{i}[n] \left(\mathbf{w}_2^i \hat{\mathbf{q}}_k^i[n] + \mathbf{b}_2^i\right) \in \mathbb{R}^{100\times 1}$, and introduce the following constraints based on big-M formulation:

$$\begin{aligned} &\mathrm{C26}: \hat{\mathbf{q}}_k^i[n] \geq \mathbf{w}_1^i \mathbf{q}_k[n] + \mathbf{b}_1^i, \forall n,k,i, \\ &\mathrm{C27}: \hat{\mathbf{q}}_k^i[n] \geq 0, \forall n,k,i, \\ &\mathrm{C28}: \hat{\mathbf{q}}_k^i[n] \leq \mathbf{a}_{1,k}^{i}[n] \left(\mathbf{w}_1^i \left[\mathbf{t}_{\max}; \mathbf{l}_k\right] + \mathbf{b}_1^i\right), \forall n,k,i, \\ &\mathrm{C29}: \hat{\mathbf{q}}_k^i[n] \leq \mathbf{w}_1^i \mathbf{q}_k[n] + \mathbf{b}_1^i + \left(1 - \mathbf{a}_{1,k}^{i}[n]\right) \left(\mathbf{w}_1^i \left[\mathbf{t}_{\max}; \mathbf{l}_k\right] + \mathbf{b}_1^i\right), \forall n,k,i, \\ &\mathrm{C30}: \hat{\hat{\mathbf{q}}}_k^i[n] \geq \mathbf{w}_2^i \hat{\mathbf{q}}_k^i[n] + \mathbf{b}_2^i, \forall n,k,i, \\ &\mathrm{C31}: \hat{\hat{\mathbf{q}}}_k^i[n] \geq 0, \forall n,k,i, \\ &\mathrm{C32}: \hat{\hat{\mathbf{q}}}_k^i[n] \leq \mathbf{a}_{2,k}^{i}[n] \left(\mathbf{w}_2^i \left(\mathbf{w}_1^i \left[\mathbf{t}_{\max}; \mathbf{l}_k\right] + \mathbf{b}_1^i\right) + \mathbf{b}_2^i\right), \forall n,k,i, \\ &\mathrm{C33}: \hat{\hat{\mathbf{q}}}_k^i[n] \leq \mathbf{w}_2^i \hat{\mathbf{q}}_k^i[n] + \mathbf{b}_2^i + \left(1 - \mathbf{a}_{2,k}^{i}[n]\right) \left(\mathbf{w}_2^i \left(\mathbf{w}_1^i \left[\mathbf{t}_{\max}; \mathbf{l}_k\right] + \mathbf{b}_1^i\right) + \mathbf{b}_2^i\right), \forall n,k,i. \end{aligned} \tag{5.55}$$

Then, we rewrite the binary constraints C24 and C25 in their equivalent forms as

$$\begin{aligned}
&\text{C24a}: \mathbf{a}_{1,k}^{i}[n] - \left(\mathbf{a}_{1,k}^{i}[n]\right)^2 \leq 0, \forall n, k, i, \\
&\text{C24b}: 0 \leq \mathbf{a}_{1,k}^{i}[n] \leq 1, \forall n, k, i, \\
&\text{C25a}: \mathbf{a}_{2,k}^{i}[n] - \left(\mathbf{a}_{2,k}^{i}[n]\right)^2 \leq 0, \forall n, k, i, \\
&\text{C25b}: 0 \leq \mathbf{a}_{2,k}^{i}[n] \leq 1, \forall n, k, i,
\end{aligned} \tag{5.56}$$

respectively. Next, we handle the nonconvex constraints $\widehat{\text{C5}}$, C21, C24a, and C25a via SCA. In particular, for a given feasible solution, $(u_k^i[n])^{j_2}$, $v_x^{j_2}[n]$, $v_y^{j_2}[n]$, $(\mathbf{a}_{1,k}^{i}[n])^{j_2}$, and $(\mathbf{a}_{2,k}^{i}[n])^{j_2}$ in the j_2-th iteration, the lower bound function of $\widehat{\text{C5}}$, C21, C24a, and C25a can be constructed based on their first-order Taylor

expansions [42], respectively, which are given by

$$\hat{R}^{\mathrm{SIC}}_{k,k'}[n] \geq (\hat{R}^{\mathrm{SIC,lb}}_{k,k'}[n])^{j_2} \tag{5.57}$$
$$= s_{k,k'}[n]\log_2\left(1+\frac{\tilde{p}_{k,k',k}[n]}{(u^{\mathrm{SIC}}_k[n])^{j_2}\sigma_k^2}\right) - \frac{s_{k,k'}[n]\tilde{p}_{k,k',k}[n](u^{\mathrm{SIC}}_k[n]-(u^{\mathrm{SIC}}_k[n])^{j_2})}{(u^{\mathrm{SIC}}_k[n])^{j_2}((u^{\mathrm{SIC}}_k[n])^{j_2}\sigma_k^2+\tilde{p}_{k,k',k}[n])\ln 2},$$

$$\hat{R}^{\mathrm{I}}_{k',k}[n] \geq (\hat{R}^{\mathrm{I,lb}}_{k',k}[n])^{j_2} = s_{k',k}[n]\log_2\left(\frac{\tilde{p}_{k',k,k}[n]+\tilde{p}_{k',k,k'}[n]}{(u^{\mathrm{NSIC}}_k[n])^{j_2}}+\sigma_k^2\right) \tag{5.58}$$
$$- \frac{s_{k',k}[n](\tilde{p}_{k',k,k}[n]+\tilde{p}_{k',k,k'}[n])(u^{\mathrm{NSIC}}_k[n]-(u^{\mathrm{NSIC}}_k[n])^{j_2})}{(u^{\mathrm{NSIC}}_k[n])^{j_2}((u^{\mathrm{NSIC}}_k[n])^{j_2}\sigma_k^2+\tilde{p}_{k',k,k}[n]+\tilde{p}_{k',k,k'}[n])\ln 2},$$

$$\hat{R}^{\mathrm{OMA}}_{k,k}[n] \geq (\hat{R}^{\mathrm{OMA,lb}}_{k,k}[n])^{j_2} = s_{k,k}[n]\log_2\left(1+\frac{\tilde{p}_{k,k,k}[n]}{(u^{\mathrm{OMA}}_k[n])^{j_2}\sigma_k^2}\right) \tag{5.59}$$
$$- \frac{s_{k,k}[n]\tilde{p}_{k,k,k}[n](u^{\mathrm{OMA}}_k[n]-(u^{\mathrm{OMA}}_k[n])^{j_2})}{(u^{\mathrm{OMA}}_k[n])^{j_2}((u^{\mathrm{OMA}}_k[n])^{j_2}\sigma_k^2+\tilde{p}_{k,k,k}[n])\ln 2},$$

$$v_x^2[n]+v_y^2[n]$$
$$\geq (v_x^{j_2}[n])^2+(v_y^{j_2}[n])^2+2v_x^{j_2}[n](v_x[n]-v_x^{j_2}[n])+2v_y^{j_2}[n](v_y[n]-v_y^{j_2}[n]), \tag{5.60}$$

$$\mathbf{a}^i_{1,k}[n]-\left(\mathbf{a}^i_{1,k}[n]\right)^2$$
$$\leq \mathbf{a}^i_{1,k}[n]-\left((\mathbf{a}^i_{1,k}[n])^{j_2}\right)^2+2(\mathbf{a}^i_{1,k}[n])^{j_2}\left(\mathbf{a}^i_{1,k}[n]-(\mathbf{a}^i_{1,k}[n])^{j_2}\right), \text{ and} \tag{5.61}$$

$$\mathbf{a}^i_{2,k}[n]-\left(\mathbf{a}^i_{2,k}[n]\right)^2$$
$$\leq \mathbf{a}^i_{2,k}[n]-\left((\mathbf{a}^i_{2,k}[n])^{j_2}\right)^2+2(\mathbf{a}^i_{2,k}[n])^{j_2}\left(\mathbf{a}^i_{2,k}[n]-(\mathbf{a}^i_{2,k}[n])^{j_2}\right), \tag{5.62}$$

respectively.

Now, applying the lower bounds in (5.57)–(5.62) to (5.47) yields the following

convex optimization problem:

$$\underset{\mathcal{T},\mathcal{V},\mathcal{Q},\Upsilon,\mathcal{U},\mathcal{A},\hat{\mathcal{Q}}}{\text{minimize}} \ \frac{1}{N}\sum_{n=1}^{N} P_{\text{comm}}[n] + \frac{1}{N}\sum_{n=1}^{N} \hat{P}_{\text{fly}}[n] \tag{5.63}$$

$$\text{s.t. C9} - \text{C14}, \text{C16}, \text{C22}, \text{C24b}, \text{C25b}, \text{C26} - \text{C33},$$

$$\widehat{\widehat{\text{C5}}} : \frac{1}{N}\sum_{n=1}^{N}\left(\sum_{\substack{k'=1\\k'\neq k}}^{K}(\hat{R}_{k,k'}^{\text{SIC,lb}}[n])^{j_2} + \sum_{\substack{k'=1\\k'\neq k}}^{K}\left((\hat{R}_{k',k}^{\text{I,lb}}[n])^{j_2} - \hat{R}_{k',k}^{\text{II}}[n]\right)\right.$$
$$\left. + (\hat{R}_{k,k}^{\text{OMA,lb}}[n])^{j_2}\right) \geq R_{\min_k}, \forall k,$$

$$\widehat{\text{C21}} : (v_x^{j_2}[n])^2 + (v_y^{j_2}[n])^2 + 2v_x^{j_2}[n](v_x[n] - v_x^{j_2}[n])$$
$$+ 2v_y^{j_2}[n](v_y[n] - v_y^{j_2}[n]) \geq \nu^2[n], \forall n,$$

$$\widehat{\widehat{\text{C23}}} : u_k^i[n] \geq (\mathbf{w}_3^i)^{\text{H}}\hat{\hat{\mathbf{q}}}_k^i[n] + b_3^i, \forall n, k, i,$$

$$\widehat{\text{C24a}} : \mathbf{a}_{1,k}^i[n] - \left((\mathbf{a}_{1,k}^i[n])^{j_2}\right)^2 + 2(\mathbf{a}_{1,k}^i[n])^{j_2}\left(\mathbf{a}_{1,k}^i[n] - (\mathbf{a}_{1,k}^i[n])^{j_2}\right)$$
$$\leq 0, \forall n, k, i,$$

$$\widehat{\text{C25a}} : \mathbf{a}_{2,k}^i[n] - \left((\mathbf{a}_{2,k}^i[n])^{j_2}\right)^2 + 2(\mathbf{a}_{2,k}^i[n])^{j_2}\left(\mathbf{a}_{2,k}^i[n] - (\mathbf{a}_{2,k}^i[n])^{j_2}\right)$$
$$\leq 0, \forall n, k, i,$$

where $\mathcal{A} = \{\mathbf{a}_{1,k}^i[n], \mathbf{a}_{2,k}^i[n], \forall n, k, i\}$ and $\hat{\mathcal{Q}} = \{\hat{\mathbf{q}}_k^i[n], \hat{\hat{\mathbf{q}}}_k^i[n], \forall n, k, i\}$. Note that similar to the solution of subproblem 1, the optimization problem in (5.63) is convex formulations, which can be easily solved by CVX [120]. The proposed algorithm is summarized in **Algorithm 5.2**.

5.4.4 Overall Algorithm

The overall algorithm for solving the two subproblems in (5.35) and (5.46) iteratively are summarized in **Algorithm 5.3**. The convergence of the overall proposed algorithm to a stationary point monotonically can be guaranteed due

Algorithm 5.2 Proposed Algorithm for Handling Sub-problem 2 in (5.46)

1: Initialize the convergence tolerance $\epsilon_2 \rightarrow 0$, the maximum number of iterations $I_{2,\max}$, the initial iteration index $j_2 = 0$, the initial variables $\{v_{\mathrm{x}}^{j_2}[n], v_{\mathrm{y}}^{j_2}[n]\}$, and the initial objective value $\hat{P}_{\text{total}}$

2: **repeat** {Main Loop: SCA}

3: Set $j_2 = j_2 + 1$, $\{(u_k^i[n])^{j_2}, v_{\mathrm{x}}^{j_2}[n], v_{\mathrm{y}}^{j_2}[n]\} = \{u_k^i[n], v_{\mathrm{x}}[n], v_{\mathrm{y}}[n]\}$

4: Solving optimization problem in (5.63) to obtain $\{\mathbf{t}[n], \mathbf{v}[n], \nu[n], u_k^i[n]\}$ and $\hat{P}_{\text{total}}$

5: Update $\hat{P}_{\text{total}}^{j_2} = \hat{P}_{\text{total}}$,

6: **until** $j_2 = I_{2,\max}$ or $\frac{|\hat{P}_{\text{total}}^{j_2} - \hat{P}_{\text{total}}^{(j_2-1)}|}{\hat{P}_{\text{total}}^{j_2}} \leq \epsilon_2$

7: Return $\{\mathbf{t}^*[n], \mathbf{v}^*[n]\} = \{\mathbf{t}[n], \mathbf{v}[n]\}$ and $\hat{P}_{\text{total}}^* = \hat{P}_{\text{total}}^{j_2}$

to the compactness of the feasible solution set in (5.16) and the nonincreasing objective value over iterations. Besides, we adopt the solution of subproblem 2 as an input for subproblem 1 over iterations while solving the subproblem in (5.35) and (5.46) iteratively. Besides, the obtained solution can be shown to converge to a suboptimal solution of the optimization problem in (5.16), c.f. [112,123]. Please refer to Appendix B.3 for the proof of the convergence. □

Furthermore, the computational complexity of the proposed suboptimal algorithm is given by [124, 125]

$$\mathcal{O}\Bigg(I_{1,\max}\Bigg(\underbrace{\mathcal{M}_1\mathcal{N}_1^2 \times \sqrt{\mathcal{M}_1}\log\left(\frac{1}{\Delta_1}\right)}_{\text{Subproblem 1}} + \underbrace{\mathcal{M}_2\mathcal{N}_2^2 \times I_{2,\max}\sqrt{\mathcal{M}_2}\log\left(\frac{1}{\Delta_2}\right)}_{\text{Subproblem 2}}\Bigg)\Bigg), \tag{5.64}$$

where $\mathcal{M}_1 = 6NK^2 + 2N + K$, $\mathcal{N}_1 = NK^3 + NK^2 + NK$, $\mathcal{M}_2 = 40NK + 6N + K + 1$, and $\mathcal{N}_2 = 24NK + (100^2 + 200^2)3NK + 7N$ represent the number of inequalities and the number of variables of subproblem 1 and subproblem 2,

Algorithm 5.3 Overall Algorithm for Addressing Problem in (5.16)

1: Initialize the convergence tolerance $\epsilon_3 \rightarrow 0$, the maximum number of iterations $I_{3,\max}$, the initial iteration index $j_3 = 0$, and the initial trajectory $\{\mathbf{t}[n], \mathbf{v}[n]\}$
2: **repeat**
3: Set $j_3 = j_3 + 1$
4: Using **Algorithm 5.1** to obtain a suboptimal result $\tilde{P}_{\text{total}}$, $\{s_k[n], p_k[n]\}$, given the UAV's trajectory and flight velocity $\{\mathbf{t}[n], \mathbf{v}[n]\}$
5: Using **Algorithm 5.2** to obtain a suboptimal result $\hat{P}_{\text{total}}$, $\{\mathbf{t}[n], \mathbf{v}[n]\}$, given the resource allocation $\{s_k[n], p_k[n]\}$
6: Update $\hat{P}^{j_3}_{\text{total}} = \hat{P}_{\text{total}}$
7: **until** $j_3 = I_{3,\max}$ or $\frac{|\hat{P}^{j_3}_{\text{total}} - \hat{P}^{(j_3-1)}_{\text{total}}|}{\hat{P}^{j_3}_{\text{total}}} \leq \epsilon_2$
8: **return** $\{s_k^*[n], p_k^*[n], \mathbf{t}^*[n], \mathbf{v}^*[n]\} = \{s_k[n], p_k[n], \mathbf{t}[n], \mathbf{v}[n]\}$ and $P^*_{\text{total}} = \hat{P}^{j_3}_{\text{total}}$

respectively. Besides, $\Delta_1 > 0$ and $\Delta_2 > 0$ denote the thresholds of convergence tolerance of subproblem 1 and subproblem 2, respectively. Note that we did not take into account the computational complexity of the adopted DNN approach to approximate the outage-guaranteed channel gain when calculating the complexity of the algorithm, as it is computed for once before the execution of the algorithm when the system parameters are determined. Thus, the computational complexity of the proposed suboptimal algorithm is with polynomial time which is suitable for fast implementation [144].

5.5 Numerical Results

In this section, we discuss the system performance of the proposed scheme (PS) based on the following simulation results. The simulation parameters are

Table 5.2: Simulation parameters [1, 5, 6].

Notations	Simulation value	Notations	Simulation value
K	$1 \sim 10$	$\mathbf{t}_0$	$[0; 0; 150]$ m
N	$500 \sim 1{,}000$	$\mathbf{t}_{\mathrm{F}}$	$[500; 500; 150]$ m
σ_k^2	-160 dBm/Hz	$\mathbf{t}_{\min}$	$[0; 0; 100]$ m
β_0	-50 dBW	$\mathbf{t}_{\max}$	$[500; 500; 300]$ m
λ_{C}	0.1 m	$\mathbf{l}_1$	$[300; 150; 0]$ m
M_{R}	100	$\mathbf{l}_2$	$[50; 400; 0]$ m
$\mathbf{l}_{\mathrm{R}}$	$[0; 400; 30]$ m	$\mathbf{l}_3$	$[100; 450; 0]$ m
$V_{\max}$	30 m/s	ε	0.01
V_{acc}	4 m/s^2	α^{AR}	2
τ	0.1 s	α^{RG}	3.6
P_{peak}	36 dBm	α^{AG}	3.6
A_1	0 dB	κ^{RG}	2 dB
A_2	6.43 dB	$\kappa_{\min}$	0 dB
$R_{\min_k}$	$0.5 \sim 5$ bits/s/Hz	$\kappa_{\max}$	30 dB
η	10	$I_{1,\max}$	10
$I_{2,\max}$	5		

summarized in Table 5.2. Generally, we set $K = 3$ for illustration to unveil the assistance brought by the IRS to the UAV communications. In addition, the initial trajectory of the UAV for **Algorithm 5.3** is set as a piecewise linear flight locus at a fixed altitude of 100 meters which the UAV passes by all the GUs in between the starting point and final point with a constant velocity. In order to illustrate the performance gain of the IRS to the UAV communications, we compare the system performance of the PS with different numbers of the IRS elements and some baseline schemes. In particular, we compare the PS with five baseline schemes: (a) *OMA consideration only (OMA)*, where the UAV only serve one GU at each time slot for the OMA scheme and all the other setups remain the same as the PS; (b) *No IRS consideration (NI)*, which removes the IRS from the considered UAV communication system; (c) *Constant flight altitude of the UAV (CFA)*, where the UAV operates at a constant altitude (i.e., 100 meters) and

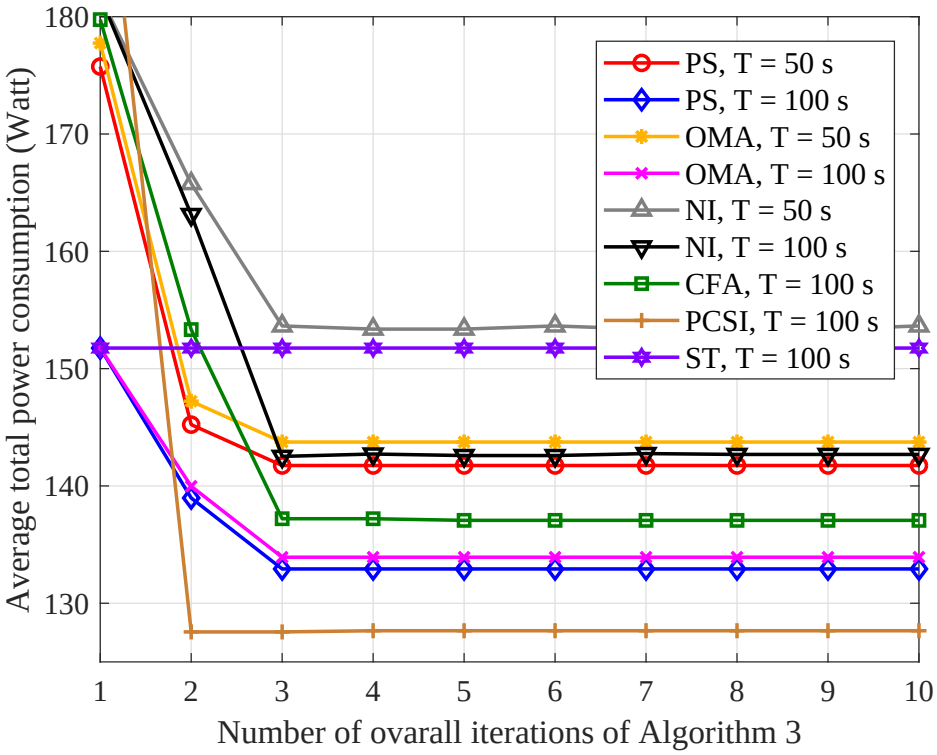

Figure 5.7: Convergence of the PS and baseline schemes for different setups.

only the horizontal trajectory of the UAV is optimized; (d) *Perfect CSI (PCSI)*, where the signal model is based on perfect known CSI and all channels are pure LoS dominated; (e) *Straight trajectory of the UAV (ST)*, where the UAV flies with a straight line trajectory from the initial location to the final location with a constant flight velocity, i.e., 11 m/s. Note that the corresponding resource allocation for NI, CFA, and ST is a subcase of the PS which can be obtained by **Algorithm 5.3** with some straightforward modifications.

5.5.1 Convergence of the Proposed Scheme and Baseline Schemes

Fig. 5.7 illustrates the convergence behavior of the proposed alternating optimization algorithm in **Algorithm 5.3** for minimizing the average total power

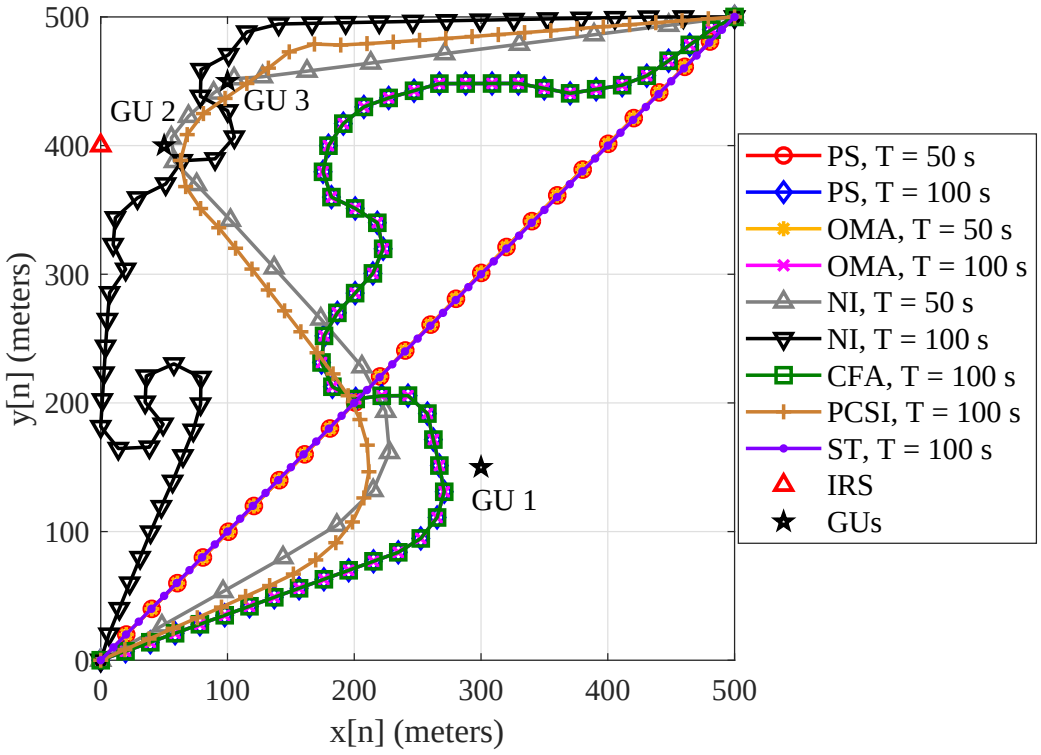

Figure 5.8: The bird's eye view of the locations of the GUs and the IRS as well as the trajectory of the UAV for the PS and baseline schemes with different setups.

consumption. In order to compare the system performance of the PS with baseline schemes, we consider the PS with two different time durations, $T = 50$ s and $T = 100$ s. In other words, there are $N = 500$ and $N = 1,000$ time slots in these settings, respectively. Also, we set the minimum per GU required data rate as $R_{\min_k} = 3$ bits/s/Hz. It can be observed that the system average total power consumption for the PS with different T and M_{R} can rapidly converge to a suboptimal solution within only 5 iterations, which confirms the practicality of the proposed algorithm. On the other hand, similar convergence behavior of the NI scheme, the CFA scheme can be observed as the PS but with worse performance. The average total power consumption of the PCSI scheme converges to the lowest value among all the considered schemes since the PCSI scheme is

the performance upper bound as perfect CSI is available which avoids outages and inefficient flight detour. Detailed discussions comparing the PS and baseline schemes in terms of system performance and their corresponding trajectories will be presented in next sections. In the sequel, the maximum number of iterations of **Algorithm 5.3** of the PS is set as 5 for illustration.

5.5.2 3D Trajectory of the UAV

Fig. 5.8 shows the bird's eye view of the UAV's trajectory obtained by the PS and baseline schemes with different setups. In this figure, we set $R_{\min_k} = 3$ bits/s/Hz. For the PS with a sufficiently long service time duration, i.e., $T = 100$ s, the UAV tends to maintain at a constant horizontal flight speed, i.e., 11 m/s, as indicated by the spaces between two consecutive simulation points, to reduce the total power consumption at the expense of longer flight duration. In contrast, for the case of short service time duration, i.e., $T = 50$ s, the UAV quickly flies over the service area with a relatively high velocity as there is insufficient time for adopting a slow speed or a long detour. In such cases, since reducing the communication distances between the UAV and the desired GUs are not always possible, the PS would also increase the transmit power to satisfy the minimum individual data rate leads to high system power consumption which will be shown in Fig. 5.13.

For comparison, we also plot the UAV's trajectories for baseline schemes in Fig. 5.8. For the OMA scheme, the UAV's horizontal trajectory is similar to the PS for both short and long service time duration, i.e., $T = 50$ s and $T = 100$ s, respectively, as both schemes can efficiently exploit the extra DoF offered by the IRS to optimize the UAV's trajectory. For the NI scheme with a sufficiently long service time duration, i.e., $T = 100$ s, the UAV first flies towards to GU 2

and GU 3 since these two users are close to each other creating a bottleneck in the system performance due to their minimum individual data rate constraints. When the UAV is on the way to GU 2 and GU 3, the UAV would first deviate from the direct path to the centroid formed by GU 2 and GU 3 and fly towards GU 1 for communication such that it can effectively serve GU 1 to satisfy its data rate requirement. Besides, the UAV would spend a sufficient number of time slots on GU 1 circling at the beginning of flight with a large transmit power to satisfy its minimum data rate requirement of GU 1 before approaching GU 2 and GU 3. Thus, the UAV does not require to fly close enough to GU 1 to establish good channel conditions. Moreover, for a shorter service time duration (i.e., $T = 50$ s) of the NI scheme, due to the insufficient number of time slots, the UAV has to fly with an exceedingly high flight velocity, on average 27 m/s, and approach each GU to establish strong channel gain for fulfilling the minimum date rate requirement for each GU. In fact, this trajectory consumes a significantly high flight power due to the longer trajectory and higher flight velocity of the UAV. Also, the UAV's 2D trajectory for the CFA scheme is the same as that for the PS with the same setups, e.g., $T = 100$ s, since the only differences between these schemes is whether to optimize the vertical dimension of the UAV or not. As for the PCSI scheme, with a sufficient service time duration, i.e., $T = 100$ s, the UAV approaches closely to each GU to satisfy the individual minimum data rate requirement with the most power-efficient flight velocity, i.e., 11 m/s with the current setting, to effectively reduce the total system power consumption. On the other hand, the ST scheme shares a similar route as the PS for the case of $T = 50$ s, which is the shortest path between the starting point and the destination. However, the PS consumes much less system power consumption than that of the ST scheme, as will be shown in Fig. 5.14.

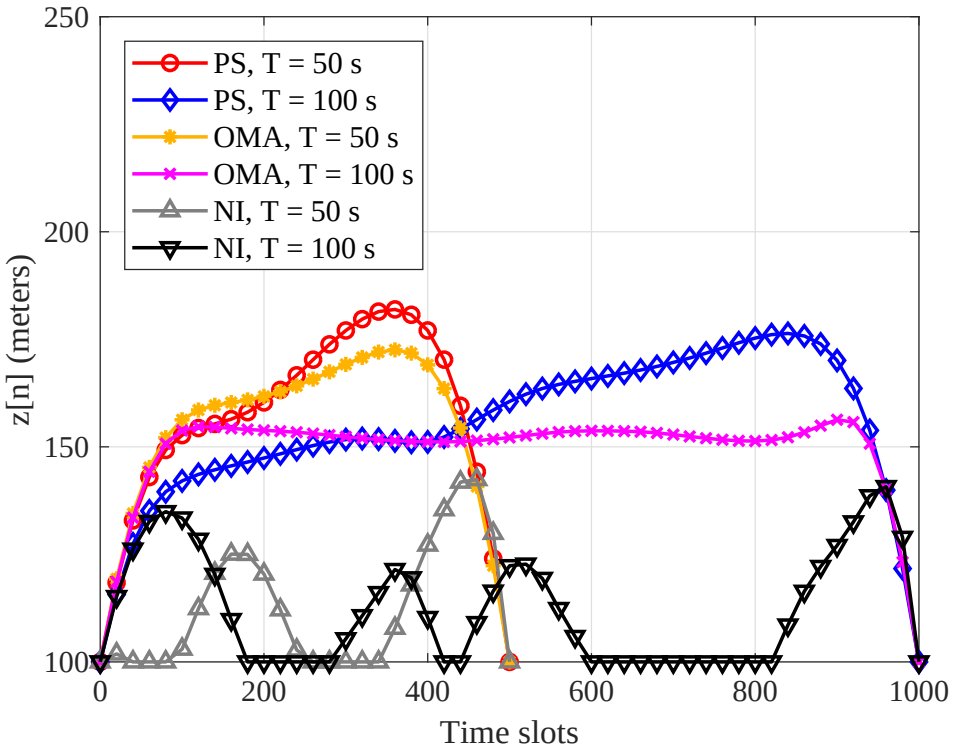

Figure 5.9: The flight altitude of the UAV for the PS and the baseline schemes with different setups.

Fig. 5.9 demonstrates the flight altitude of the UAV's trajectory for the PS and baseline schemes with different setups. Since the UAV for the CFA scheme and the ST scheme have to flight at a constant altitude of 100 m, we do not analyze the performance of these two baseline schemes in this figure. For the PS with the two considered setups, i.e., $T = 50$ s and $T = 100$ s, the UAV prefers a high altitude with an optimized velocity in the journey to fully utilize the higher outage-guaranteed effective channel gain, c.f. Fig. 5.5, since a higher outage-guaranteed effective channel gain can be obtained by adopting a moderately higher flight altitude when the UAV is far away from the GU in terms of horizontal distance. Also, the flight altitude of the UAV adopting NOMA protocol is generally higher than the one adopting OMA. Indeed, a higher altitude

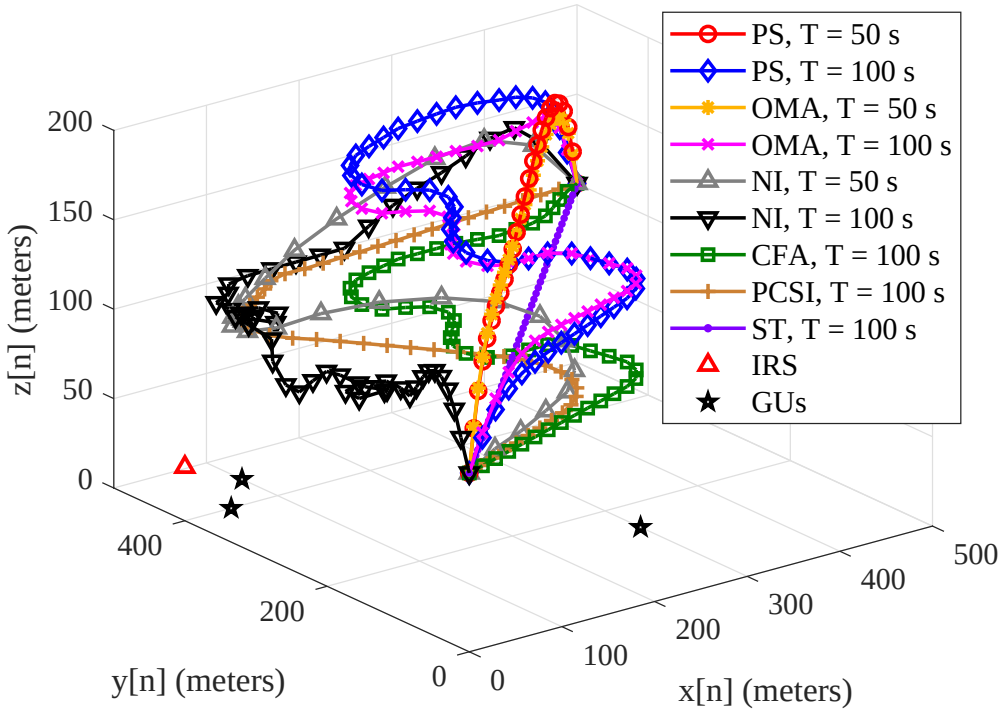

Figure 5.10: The 3D view of the locations of the GUs and the IRS as well as the trajectory of the UAV for the PS and baseline schemes with different setups.

generally provides more freedom of the UAV to promote channel gain disparities of the selected two users for improving the performance of NOMA. On the other hand, as OMA does not have the DoF in serving multiple users at each time instant, flying with a low to moderate altitude is good enough for it to strike a balance between data rate and outage probability. However, for the NI scheme, without the assistance from the IRS, the effective channel gain of the desired GUs is much lower than that of the PS. Indeed, maintaining high-quality channels by reducing the path loss between the UAV and the selected GUs remains the key to satisfy the minimum data rate constraint in the NI scheme. Nevertheless, the UAV of the NI scheme is still willing to adopt a higher altitude occasionally to strike a balance among the total power consumption, outage-guaranteed effective

channel gain, and path loss. In fact, as shown in Fig. 5.9, the parabolic patterns of the UAV's trajectory of the NI scheme appears in those time slots when the UAV is far away from any GUs, since in these areas, the outage-guaranteed effective channel gains are larger when the UAV operates at a higher altitude. In contrast, for the PCSI scheme, the UAV's flight altitude remains at the lowest possible altitude of 100 m. In fact, there is no channel outage event as the CSI is perfect known. Thus, the UAV does not have any incentive to maintain a higher altitude as it would only consume more system energy but leading to a lower data rate. To offer a better visualization of the trajectory of the PS and the baseline scheme, we also plot its 3D trajectory in Fig. 5.10. It can be seen from the optimized 3D trajectory that except the PCSI scheme, to effectively combat channel outage, the UAV should adopt a high flight altitude to reduce the channel uncertainty caused by the altitude-dependent Rician fading, which reducing the communication power.

5.5.3 Outage Probability

Fig. 5.11 demonstrates the outage probability versus the time slots for each GUs. We only take the PS with $T = 100$ s as an example, to calculate the outage probability as stated in constraint C5. The outage probabilities in Fig. 5.11 were averaged over 1,000 random channel realizations by comparing the actual effective channel in (5.18) with the outage-guaranteed effective channel gain in (5.25). Thanks to the proposed DNN approach, the outage probability not only satisfies the required values, but is close to its upper bound value, i.e., $\varepsilon = 0.01$, for any GU and time slots. This illustrates the accuracy of the DNN approach to approximate the outage-guaranteed effective channel gain.

5.5.4 Communication Power Consumption

Fig. 5.12 illustrates the communication power consumption and the achievable data rate versus the time slots for each GUs of the PS and baseline schemes for $T = 100$. As shown in the sub-figures for the communication power and the achievable data rate of the PS, the UAV serves GU 2 and GU 3 over the time slots $n = 420$ and $n = 830$, simultaneously, via NOMA protocol. Note that for those time slots adopting NOMA, the UAV allocates a significantly large portion of the communication power to the weak channel user to satisfy the corresponding minimum individual data rate requirement while a small power is allocated to the user with strong channel condition. This power allocation mechanism aligns with the one in the literature. In contrast, the total communication power consumption for the OMA scheme is much higher than the PS due to the less flexibility of the resource allocation.

5.5.5 Average Total Power Consumption

Fig. 5.13 shows the average power consumption versus the number of GUs for the PS and baseline schemes with different setups. In this simulation, we vary the number of GUs, K, from 1 to 10 to illustrate the impact of the number of GUs on the system performance. We set the locations of these GUs with x-coordinates and y-coordinates as $x_k = [300; 50; 100; 200; 150; 400; 100; 250; 300; 100]$ and $y_k = [150; 400; 450; 100; 350; 400; 250; 250; \ 400; 50]$, respectively. Besides, we assume that the minimum individual data rate is $R_{\min_k} = 3$ bits/s/Hz in this section. It can be observed that the average power consumption of the PS increases with the number of the GUs as the system becomes less flexible in allocating resources when there are more numbers of GUs imposing more stringent constraints. Besides, for the PS with different numbers of IRS elements and time durations,

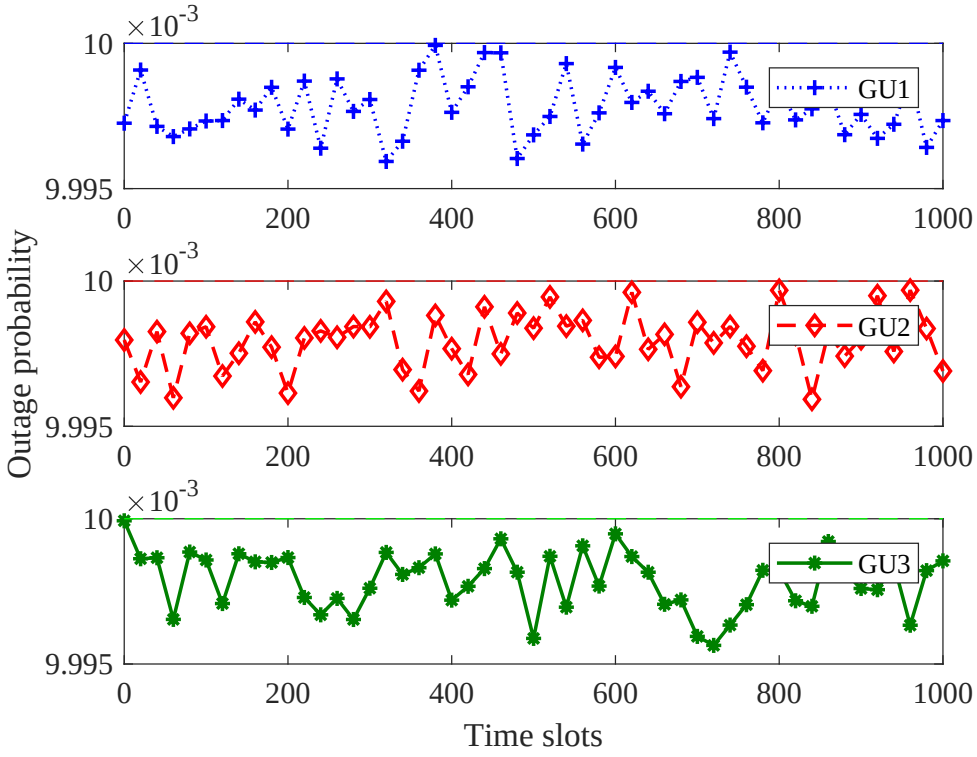

Figure 5.11: The outage probability versus the time slots for each GUs of the PS for $T = 100$ s.

the total power consumption of the system has only a marginal increase when the number of GUs is $K \geq 2$. This can be attributed to the fact that the proposed optimization framework can achieve a better utilizationof the system resources for serving a large number of GUs via jointly optimizing the UAV's 3D trajectory, IRS passive beamforming, and resource allocation. Besides, when $K = 1$, the power consumptions of the PS for different numbers of elements equipped at the IRS are roughly the same since GU 1 is located far away from the IRS. This result illustrates that the performance gain brought by the IRS is sensitive to its distances to the desired GUs. In contrast, although the average power consumption for the NI scheme and CFA scheme have a similar trend as the PS w.r.t. the number of GUs, the former two schemes consume higher power

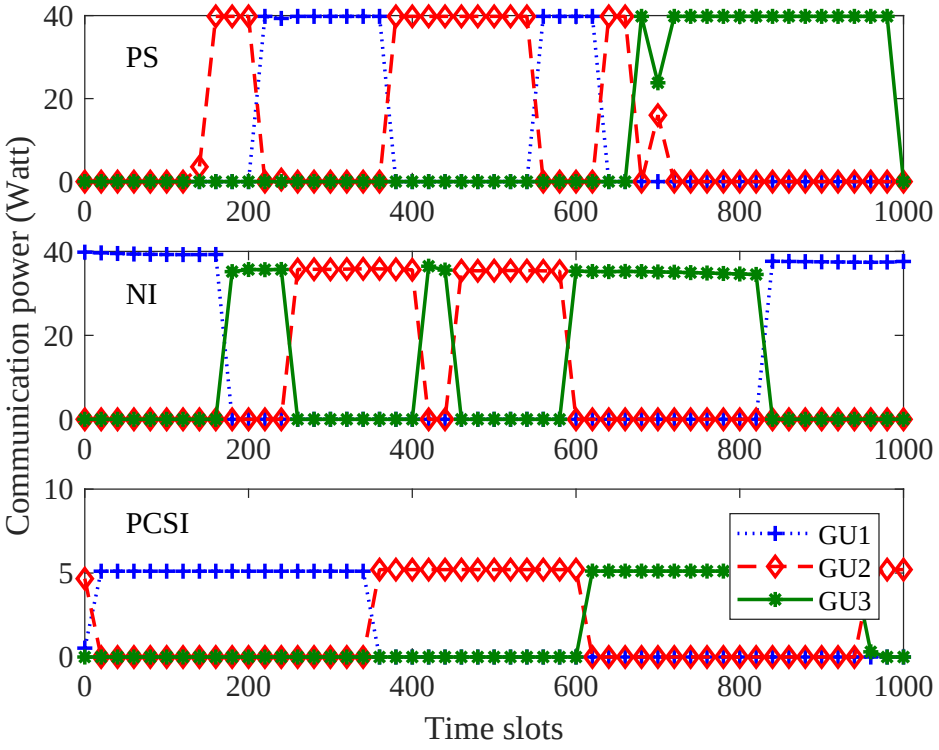

Figure 5.12: The communication power consumption and the achievable data rate versus the time slots for each GUs of the PS and the baseline scheme for $T = 100$.

consumption than that for the PS under the same setting. Indeed, the power consumption differences between these two schemes illustrate the performance gain brought by the IRS and the benefits of optimizing the UAV's flight altitude. Also, similar to the PS, the average total power consumption for the PCSI scheme has a similar increasing slop which demonstrates the superiority of the PS. On the other hand, the performance of the PCSI scheme is still slightly better than that of the PS due to dominated LoS setting and perfect CSI availability in the former.

Fig. 5.14 depicts the average total power consumption of the considered system versus the minimum individual data rate requirement for the PS and baseline schemes. For the PS, the average power consumption slowly increases

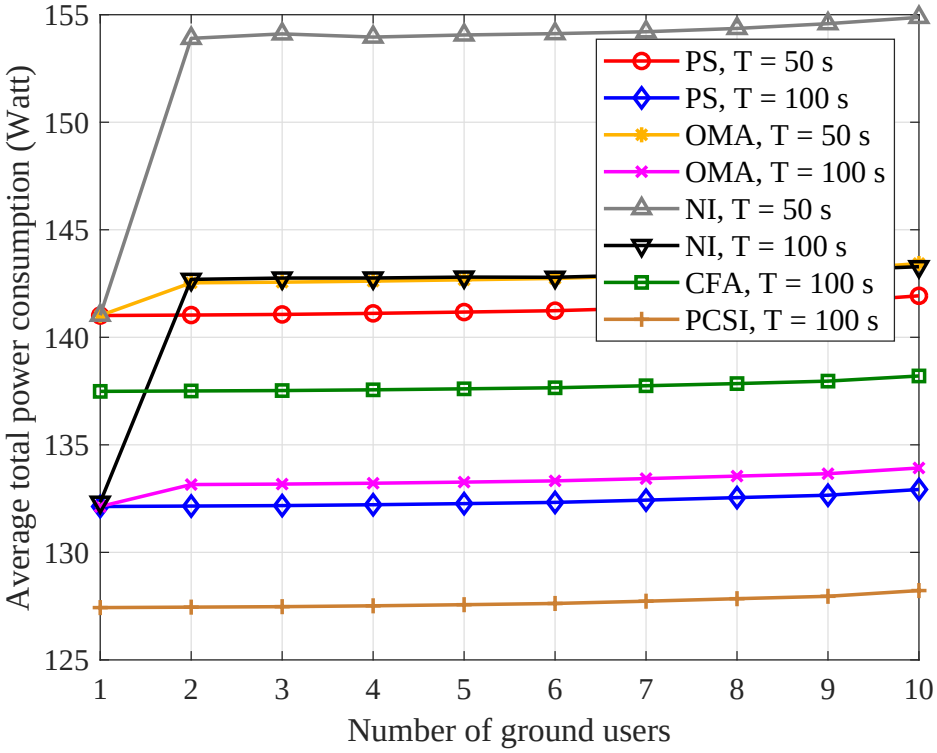

Figure 5.13: The average power consumption versus the number of GUs for the PS and baseline schemes with different setups.

with the minimum individual data rate requirement compared with baseline schemes, since the IRS-assisted system can effectively optimize the system resources to minimize the average power consumption via optimizing the resource allocation and UAV's 3D trajectory. In contrast, the average power consumption of the NI scheme and the CFA scheme scales with the minimum data rate requirement much faster than that of the PS. The reason is that both the NI and CFA systems do not have sufficient DoF to optimize the system resources for the minimization of the total power consumption. In particular, the former is due to lack of the contribution of the large number of elements equipped at the IRS and the latter is due to the fixed UAV's flight height. As for the PCSI scheme, the average power consumption scales slowly with the minimum individual data rate

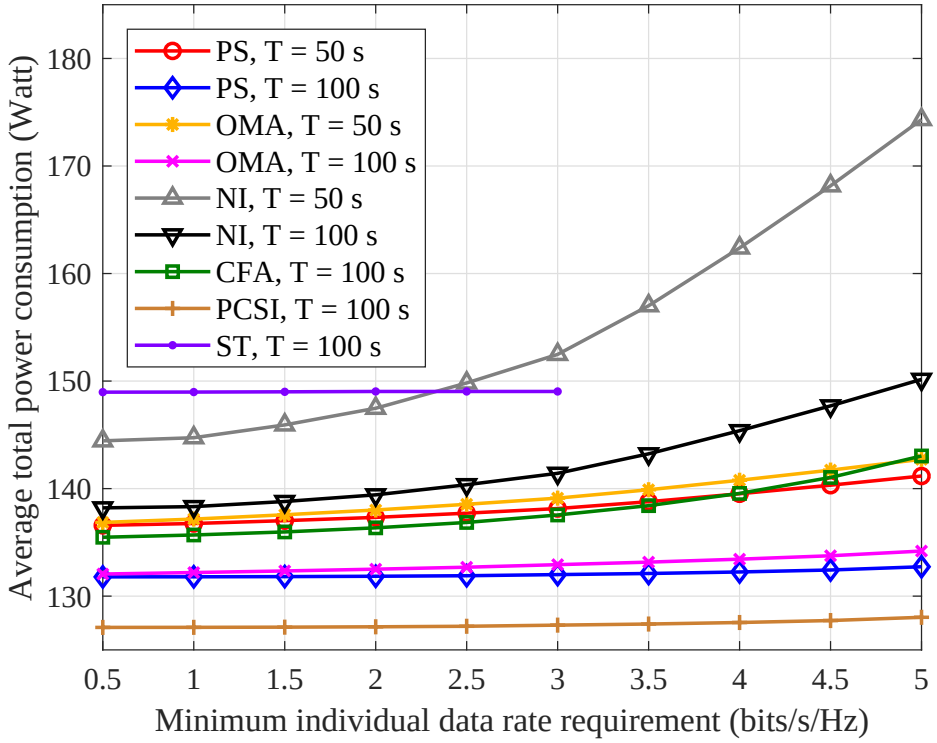

Figure 5.14: The average power consumption versus minimum individual data rate requirement for the PS and baseline schemes with different setups.

requirement since the UAV's trajectory and resource allocation can be efficiently optimized due to the assistance of the IRS, which is similar to the PS. As for the ST scheme, the average power consumption remains almost a constant between $R_{\min} = 0.5$ bits/s/Hz and $R_{\min_k} = 3$ bits/s/Hz. Besides, since there are insufficient DoF and flexibility for optimizing the system resources, an exceedingly stringent minimum data rate requirement, i.e., $R_{\min_k} \geq 3.5$ bits/s/Hz, would lead to an infeasible result, which are not plotted in the figure.

5.6 Summary

In this chapter, we minimized the average total power consumption in an IRS-assisted UAV communication system via jointly optimizing the communication

resource allocation, the 3D trajectory design of the UAV, and the phase shift control of the IRS. The proposed formulation was a non-convex optimization problem taking into account the minimum outage probability and the minimum achievable data rate. To handle the intractability of the outage constraint, we approximated the effective channel function via exploiting the DNN approach to facilitate an outage-guaranteed effective channel gain. A suboptimal solution was achieved by the proposed iterative algorithm based on the alternating optimization method. Numerical results illustrated that the proposed algorithm converges within a small number of iterations and revealed some interesting insights. Particularly, (1) deploying an IRS to assist the UAV communication serves as a key to improve the system performance when the total service time is insufficient; (2) employing the IRS-assisted UAV communication system offers enhanced flexibility in designing the UAV's trajectory; (3) optimizing the 3D trajectory of the UAV is important to improve the system power efficiency; (4) NOMA communications offer higher DoF than that of OMA scheme to minimize the average power consumption via optimizing the UAV's trajectory.

Chapter 6

Thesis Conclusions and Future Works

In this final chapter, we first conclude this thesis and then introduce a future research direction related about our works.

6.1 Conclusions

In this thesis, we have studied and addressed the resource allocation and trajectory design of the UAV in wireless communication systems. We conclude this thesis in the following by summarizing our main contributions.

In Chapter 1, we have presented the motivation, the literature review, the outline, and the main contributions of this thesis. In Chapter 2, we have reviewed some fundamental and related background knowledge of the thesis that are useful in the later chapters.

In Chapter 3, we jointly designed the information UAVs trajectory, the communication resource allocation strategy, and the jamming policy to maximize the system energy efficiency of a secure UAV-orthogonal frequency division multiple access (OFDMA) communication system. The joint design was formulated

as a non-convex optimization problem taking into account the minimum data rate requirement, the maximum tolerable signal-to-interference-plus-noise ratio (SINR) leakage, the minimum safety distance between UAVs, and the imperfect location information of the potential eavesdroppers. An iterative algorithm based on alternating optimization was proposed to achieve a suboptimal solution with low computational complexity.

In Chapter 4, we studied a non-convex power minimization problem for intelligent reflection surface (IRS)-assisted UAV communication systems via jointly optimizing the UAVs trajectory design and resource allocation strategy. We proposed an alternating algorithm to achieve a suboptimal solution efficiently. The proposed algorithm supports the high flexibility of the UAVs trajectory in the communications with the assistance of the IRS.

In Chapter 5, we minimized the average total power consumption in an IRS-assisted UAV communication system via jointly optimizing the communication resource allocation, the three-dimensional (3D) trajectory design of the UAV, and the phase shift control of the IRS. The proposed formulation was a non-convex optimization problem taking into account the minimum outage probability and the minimum achievable data rate. To handle the intractability of the outage constraint, we approximated the effective channel function via exploiting the deep neural network (DNN) approach to facilitate an outage-guaranteed effective channel gain. A suboptimal solution was achieved by the proposed iterative algorithm based on the alternating optimization method. Numerical results illustrated that the proposed algorithm converges within a small number of iterations and revealed some interesting insights.

6.2 Future Works

The explosive growth of traffic demand keeps imposing unprecedentedly challenges for the development of future wireless communication systems, including supporting massive connectivity [145], energy efficiency improvement, ultra-reliable low-latency communications (URLLC) [47], and so on. This thesis has addressed some of these challenges via applying the concept of UAV and IRS as well as improving the system performance with advanced resource allocation design. However, there are still many research issues to be addressed. In the following, we propose a future research direction about the work presented in this thesis.

6.2.1 Online Trajectory Design

In this thesis, the resource allocation and trajectory optimizations were based on the offline design, even for the case of altitude dependent Rician fading with statistical channel state information (CSI). The offline design for UAV communication systems is a reasonable approach when the line-of-sight (LoS) dominates the air-to-ground channel [146, 147]. However, when the small scale fading in the non-line-of-sight (NLoS) path is not negligible and the environment changes over time, adoptive online trajectory design for UAV communication systems is necessary. Since the model-based optimization methods are intractability for online trajectory design, deep Q-learning [148–153] is a feasible solution in this scenario. Thus, optimizing the online trajectory design with imperfect CSI via deep learning should be taken into account for UAV communication systems in future works.

6.2.2 Trajectory Design with Practical Considerations

In this thesis, we assume the availability of perfect hardware such that UAV can fly exactly with the planned route. However, there exists some UAV's positioning errors due to the mechanical precision loss caused by the inaccuracy of mechanical control systems. On the other hand, weather would also impact the UAV's flight, e.g., the wind gust can incur jittering [154]. Therefore, the UAV's position errors due to the weather influence and mechanical precision loss are need to be taken into account for resource allocation and trajectory design on UAV wireless communications. In the future works about UAV communications, we plan to optimize the UAV's 3D trajectory design considering the impact of various practical phenomena.

6.2.3 Orthogonal Time Frequency Space (OTFS)

In this thesis, we assume that OFDM or non-orthogonal multiple access (NOMA) modulations are adopted in UAV wireless communication systems with a well-compensated Doppler effect, which is acceptable for most UAV communication scenarios due to the limited flight velocity of the UAV. However, for some specific scenarios, e.g., a large number of users, stringent quality of service (QoS) requirements, and extremely high flight speed of the UAV, the commonly adopted multiple schemes break down due to their limited system performance. To cope with the scenario of UAV communications when the UAV or the ground terminals have high mobility, the orthogonal time frequency space (OTFS) modulation in the delay-Doppler (DD) domain is introduced in the literatures, i.e., [155–161]. However, the OTFS may introduce higher latency than other modulation since it has to decode information after receiving the whole frame. Therefore, the UAV-OTFS communication system with acceptable latency should be discussed

in future works.

6.2.4 Short-Packet Communications

In this thesis, we assume that a perfect error correctly code with an infinite length is adopted in the considered wireless communication systems. In practice, this can be achieved by applying, e.g., low-density parity-check (LDPC) codes [162, 163]. However, the required infinite code length may introduce exceedingly long delay to the communication systems. As a remedy, various approaches have been proposed in the literature. For example, non-coherent detection was adopted in [164] to reduce the need of sending pilot sequences so as to reduce the end-to-end communication delay. However, the performance of non-coherent detection is usually unsatisfactory. As a result, the notion of short-packet communication was introduced in [47] striking a balance between the communication performance and delay. Besides, the Polar codes [165–167] are proposed to improve system performance for finite-length code communications. Yet, the joint design of trajectory, resource allocation, and codeword length for effective UAV-based communications is challenging as the design problem is highly non-convex. Further research for designing advantage algorithms for obtaining the globally optimal solution of the design problem is needed.

6.2.5 Covert UAV Communications

In this thesis, we studied three works on UAV communications in Chapters 3-5 which can be extended to a more general scenario. For example, as discussed in Chapter 3, optimizing the multiple-antenna information and jammer UAVs trajectory and resource allocation in covert UAV communications [70, 168–170] considering a ground user which located in the uncertain region of the potential

eavesdropper. Besides, as discussed in Chapters 4 and 5, the IRS-assisted UAV communication can be extended to maximizing the secrecy rate of the multiple-IRS UAV communication via optimizing the UAV s trajectory design, the IRSs phase shift, and the resource allocation considering potential eavesdroppers. Also, a new algorithm for obtaining the global optimal solution of the formulated problems is desirable.

Appendix A

Convex Optimization Techniques

In this appendix, we give a brief overview of convex optimization and some adopted basic convex optimization methods for solving different types of linear nonconvex optimization problems.

A.1 Convex Optimization

A.1.1 Standard Form

Without loss of generally, a single-objective convex optimization problem can be written as

$$\begin{aligned} \mathcal{P}_1 : \underset{\mathbf{x}\in\mathcal{S}}{\text{minimize}}\ & f_1(\mathbf{x}) \\ \text{s.t. } & h_1(\mathbf{x}) \leq 0, \\ & g_1(\mathbf{x}) = 0, \end{aligned} \tag{A.1}$$

where $\mathbf{x} \in \mathbb{C}^{n\times n}$ and $\mathcal{S}$ is the feasible solution set of $\mathbf{x}$. Note that $f_1(\mathbf{x}) \in \mathbb{C}^{n\times n} \rightarrow \mathbb{R}$. Functions $h_1(\mathbf{x}) \in \mathbb{C}^{n\times n} \rightarrow \mathbb{R}$ and $g_1(\mathbf{x}) \in \mathbb{C}^{n\times n} \rightarrow \mathbb{R}$ are convex functions with respect to (w.r.t.) $\mathbf{x}$. For example, f_1 satisfies

$$f_1(a\mathbf{x} + b\mathbf{y}) \leq af_1(\mathbf{x}) + bf_1(\mathbf{y}), \tag{A.2}$$

for all $\mathbf{x}, \mathbf{y} \in \mathbb{R}^{n\times n}$ and all $a, b \in \mathbb{R}$ with $a + b = 1$, $a \geq 0$, $b \geq 0$.

A.1.2 Lagrangian

The fundamental of Lagrangian duality is that the weighted constraints in (A.1) are added to the objective function, which is given by

$$L(\mathbf{x}, \lambda, \mu) = f_1(\mathbf{x}) + \lambda h_1(\mathbf{x}) + \mu g_1(\mathbf{x}), \tag{A.3}$$

where $\lambda \geq 0$ and μ represent the Lagrange multipliers corresponding to functions $h_1(\mathbf{x})$ and $g_1(\mathbf{x})$, respectively.

A.1.3 Karush-Kuhn-Tucker (KKT) Conditions

When the functions $f_1(\mathbf{x})$, $h_1(\mathbf{x})$, and $g_1(\mathbf{x})$ of the optimization problem in (A.1) are differentiable w.r.t. $\mathbf{x}$, the vanish gradient at $\mathbf{x}^*$ can be written as

$$\nabla f_1(\mathbf{x}^*) + \lambda^* \nabla h_1(\mathbf{x}^*) + \mu^* \nabla g_1(\mathbf{x}^*) = 0, \tag{A.4}$$

where $\mathbf{x}^*$ and (λ^*, μ^*) are primal and dual optimal points. Thus, the Karush-Kuhn-Tucker (KKT) conditions are

$$h_1(\mathbf{x}^*) \leq 0; \tag{A.5}$$

$$g_1(\mathbf{x}^*) = 0; \tag{A.6}$$

$$\lambda^* \geq 0; \tag{A.7}$$

$$\lambda^* h_1(\mathbf{x}^*) = 0; \tag{A.8}$$

$$\nabla f_1(\mathbf{x}^*) + \lambda^* \nabla h_1(\mathbf{x}^*) + \mu^* \nabla g_1(\mathbf{x}^*) = 0. \tag{A.9}$$

A.2 Difference of Convex Functions

A difference of two convex functions given as:

$$f_2(\mathbf{x}) = h_2(\mathbf{x}) - g_2(\mathbf{x}), \tag{A.10}$$

where $\mathbf{x} \in \mathbb{C}^{n \times n}$. Note that $h_2(\mathbf{x})$ and $g_2(\mathbf{x})$ are continuous monotonic convex functions w.r.t. $\mathbf{x}$. In order to deal with the difference of convex (DC) function as in (A.10), one can obtain the optimal solution via the exhaustive search. Yet, this method is computationally prohibitive. As a compromise approach,

lower computational complexity methods have been proposed to obtain some suboptimal solution. For instance, the successive convex approximation (SCA) can be applied to establish a lower bound of the function $g_2(\mathbf{x})$ in (A.10). Note that to guarantee the convergence of the SCA for $g_2(\mathbf{x})$, for a given $\mathbf{x}^{(\text{iter})}$ in the iter-th iteration, the surrogate objective function $\tilde{g}_2(\mathbf{x}|\mathbf{x}^{(\text{iter})})$ is approximated to $g_2(\mathbf{x})$ taking into account the previous optimization solution $\mathbf{x}^{(\text{iter})}$. The variable $\mathbf{x}^{(\text{iter})}$ converges to a suboptimal point $\mathbf{x}^*$ w.r.t. (A.10) satisfying the first-order optimization conditions if the surrogate objective function $\tilde{g}_2(\mathbf{x}|\mathbf{x}^{(\text{iter})})$ follows

$$\tilde{g}_2(\mathbf{x}|\mathbf{x}^{(\text{iter})}) \leq g_2(\mathbf{x}), \forall \mathbf{x}, \tag{A.11}$$

$$\tilde{g}_2(\mathbf{x}^{(\text{iter})}|\mathbf{x}^{(\text{iter})}) = g_2(\mathbf{x}^{(\text{iter})}), \tag{A.12}$$

$$\nabla_{\mathbf{x}} \tilde{g}_2(\mathbf{x}^{(\text{iter})}|\mathbf{x}^{(\text{iter})}) = \nabla_{\mathbf{x}} g_2(\mathbf{x}^{(\text{iter})}). \tag{A.13}$$

Thus, for given $\mathbf{x}^{(\text{iter})}$ in the iter-th iteration, an upper bound of the DC function (A.10) can be obtained by SCA expansion as

$$g_2(\mathbf{x}) \geq \tilde{g}_2(\mathbf{x}|\mathbf{x}^{(\text{iter})}) = \nabla_{\mathbf{x}} g_2(\mathbf{x}^{(\text{iter})})(\mathbf{x} - \mathbf{x}^{(\text{iter})}), \tag{A.14}$$

$$f_2(\mathbf{x}) \leq \tilde{f}_2(\mathbf{x}|\mathbf{x}^{(\text{iter})}) = h_2(\mathbf{x}) - \tilde{g}_2(\mathbf{x}|\mathbf{x}^{(\text{iter})}) = h_2(\mathbf{x}) - \nabla_{\mathbf{x}} g_2(\mathbf{x}^{(\text{iter})})(\mathbf{x} - \mathbf{x}^{(\text{iter})}). \tag{A.15}$$

Then the suboptimal value $\mathbf{x}^*$ w.r.t. (A.10) is obtained until the convergence.

A.3 Alternating Optimization

For two coupling variables $\mathbf{x}$ and $\mathbf{y}$, a convex objective function is given by

$$\mathcal{P}_2 : \underset{\mathbf{x},\mathbf{y}\in\mathcal{S}}{\text{minimize}}\ f_3(\mathbf{x}, \mathbf{y}), \tag{A.16}$$

where f is a continuous convex function w.r.t. $\mathbf{x}$ or $\mathbf{y}$ and $\mathcal{S}$ is the feasible solution set of $\mathbf{x}$ and $\mathbf{y}$. To overcome the coupling between $\mathbf{x}$ and $\mathbf{y}$, adopting alternating optimization method, the optimization problem in (A.16) can be divided into two subproblems:

$$\mathcal{P}_3 : \underset{\mathbf{x}\in\mathcal{S}}{\text{minimize}}\ f_3(\mathbf{x}|\mathbf{y}), \tag{A.17}$$

$$\mathcal{P}_4 : \underset{\mathbf{y}\in\mathcal{S}}{\text{minimize}}\ f_3(\mathbf{y}|\mathbf{x}), \tag{A.18}$$

and solve them iteratively. Then the optimal value $\mathbf{x}^*$ and $\mathbf{y}^*$ can be obtained until convergence. Please refer to Section B.3 for the proof of the convergence.

A.4 Dinkebach Method

A fractional form objective function is given by

$$\mathcal{P}_5 : \underset{\mathbf{x}\in\mathcal{S}}{\text{minimize}} \ \frac{f_4(\mathbf{x})}{g_4(\mathbf{x})}, \tag{A.19}$$

where $\mathbf{x} \in \mathbb{C}^{n\times n}$ and $\mathcal{S}$ is the feasible solution set of $\mathbf{x}$. Note that $f_4(\mathbf{x})$ and $g_4(\mathbf{x})$ are continuous monotonic convex function and concave function w.r.t. $\mathbf{x}$. By applying the fractional programming theory [19], the objective function of (A.19) can be equivalently transformed into a subtractive form. In particular, the optimal value of γ^* in (A.19) can be achieved if and only if

$$\mathcal{P}_6 : \underset{\mathbf{x}\in\mathcal{S}}{\text{minimize}} \ f_4(\mathbf{x}) - \gamma^* g_4(\mathbf{x}) = f_4(\mathbf{x}^*) - \gamma^* g_4(\mathbf{x}^*) = 0, \tag{A.20}$$

for $f(\mathbf{x}) \geq 0$ and $g(\mathbf{x}) > 0$. Thus, adopting the Dinkelbach method [119], for the iter-th iteration and a given value $\gamma^{(\text{iter})}$, the objective function in (A.20) can be written as:

$$\mathcal{P}_6^{(\text{iter})} : \underset{\mathbf{x}\in\mathcal{S}}{\text{minimize}} \ f_4^{(\text{iter})}(\mathbf{x}) - \gamma^{(\text{iter}-1)} g_4^{(\text{iter})}(\mathbf{x}). \tag{A.21}$$

Then, the value $\gamma^{(\text{iter})}$ should be updated as $\gamma^{(\text{iter})} = \frac{f_4^{(\text{iter})}(\mathbf{x})}{g_4^{(\text{iter})}(\mathbf{x})}$ for each iteration of the Dinkelbach method until convergence. Note that the convergence to the optimal solution of (A.19) is guaranteed if (A.21) is solved optimally in each iteration.

A.5 S-Procedure

Let $\mathbf{F}_i \in \mathbb{S}^{n\times n}$, $\mathbf{g}_i \in \mathbb{R}^{n\times n}$, $c_i \in \mathbb{R}$, the implication

$$\begin{aligned} &\mathbf{x}^{\mathrm{T}}\mathbf{F}_1\mathbf{x} + 2\mathbf{g}_1^{\mathrm{T}}\mathbf{x} + c_1 \leq 0 \\ \Longrightarrow &\mathbf{x}^{\mathrm{T}}\mathbf{F}_2\mathbf{x} + 2\mathbf{g}_2^{\mathrm{T}}\mathbf{x} + c_2 \leq 0 \end{aligned} \tag{A.22}$$

holds if and only if there exists a λ such that

$$\lambda \geq 0, \quad \begin{bmatrix} \mathbf{F}_2 & \mathbf{g}_2 \\ \mathbf{g}_2^{\mathrm{T}} & c_2 \end{bmatrix} \preceq \lambda \begin{bmatrix} \mathbf{F}_1 & \mathbf{g}_1 \\ \mathbf{g}_1^{\mathrm{T}} & c_1 \end{bmatrix}, \tag{A.23}$$

provided there exists a point $\hat{\mathbf{x}}$ with $\hat{\mathbf{x}}^{\mathrm{T}}\mathbf{F}_1\hat{x} + 2\mathbf{g}_1^{\mathrm{T}}\hat{\mathbf{x}} + c_1 < 0$.

Appendix B

Proof of Theories of Chapter 3

B.1 Proof of Theorem 3.1

We follow a similar approach as in [119] to prove Theorem 3.1. First, it can be shown that a solution of the problem in (3.38) is q_1^*:

$$q_1^* = \frac{R(\mathcal{A}^*, \tilde{\mathcal{P}}^*, \tilde{\mathcal{Z}}^*)}{P(\tilde{\mathcal{P}}^*, \mathcal{Z}^*)} \geq \frac{R(\mathcal{A}, \tilde{\mathcal{P}}, \tilde{\mathcal{Z}})}{P(\tilde{\mathcal{P}}, \mathcal{Z})},\ \mathcal{A}, \mathcal{P}, \tilde{\mathcal{P}}, \mathcal{Z}, \tilde{\mathcal{Z}} \in \mathcal{F}. \tag{B.1}$$

Therefore, we have

$$R(\mathcal{A}, \tilde{\mathcal{P}}, \tilde{\mathcal{Z}}) - q_1^* P(\tilde{\mathcal{P}}, \mathcal{Z}) \leq 0,\ \mathcal{A}, \mathcal{P}, \tilde{\mathcal{P}}, \mathcal{Z}, \tilde{\mathcal{Z}} \in \mathcal{F}, \tag{B.2}$$

$$R(\mathcal{A}^*, \tilde{\mathcal{P}}^*, \tilde{\mathcal{Z}}^*) - q_1^* P(\tilde{\mathcal{P}}^*, \mathcal{Z}^*) = 0. \tag{B.3}$$

We can observe that the optimization solution of the problem in (3.2) is q_1^* by comparing (B.2) and (B.3).

Now, the proof of the converse is that a solution, q_1^*, of the problem in (3.2) follows:

$$\begin{aligned} R(\mathcal{A}, \tilde{\mathcal{P}}, \tilde{\mathcal{Z}}) - q_1^* P(\tilde{\mathcal{P}}, \mathcal{Z}) &\leq R(\mathcal{A}^*, \tilde{\mathcal{P}}^*, \tilde{\mathcal{Z}}^*) - q_1^* P(\tilde{\mathcal{P}}^*, \mathcal{Z}^*) \\ &= 0,\ \mathcal{A}, \mathcal{P}, \tilde{\mathcal{P}}, \mathcal{Z}, \tilde{\mathcal{Z}} \in \mathcal{F}. \end{aligned} \tag{B.4}$$

Therefore, we have

$$q_1^* \geq \frac{R(\mathcal{A}, \tilde{\mathcal{P}}, \tilde{\mathcal{Z}})}{P(\tilde{\mathcal{P}}, \mathcal{Z})},\ \mathcal{A}, \mathcal{P}, \tilde{\mathcal{P}}, \mathcal{Z}, \tilde{\mathcal{Z}} \in \mathcal{F}, \tag{B.5}$$

$$q_1^* = \frac{R(\mathcal{A}^*, \tilde{\mathcal{P}}^*, \tilde{\mathcal{Z}}^*)}{P(\tilde{\mathcal{P}}^*, \mathcal{Z}^*)}. \tag{B.6}$$

We can observe that the optimization solution of the problem in (3.38) is q_1^* by comparing (B.5) and (B.6).

B.2 Proof of Theorem 3.2

We follow a similar approach as in [109] to prove Theorem 3.2. First, it can be shown that the optimization problem (3.41) is jointly convex w.r.t. the optimization variables and satisfies the Slater's constraint qualification. We first derive the Lagrangian function of (3.41):

$$\begin{aligned}
&\mathfrak{L}(\boldsymbol{Y}, \boldsymbol{X}, \boldsymbol{V}, \boldsymbol{\mu}, \boldsymbol{\nu}, \boldsymbol{\vartheta}, \mathcal{Z}) \qquad \text{(B.7)}\\
&= \sum_{n=1}^{N} \sum_{i=1}^{N_{\mathrm{F}}} \mathrm{Tr}\big(\mathbf{Z}_i^{\mathrm{J}}[n](\mathbf{Y}_{i,n} - \mathbf{X}_{i,n} - \mathbf{V}_{i,n})\big)\\
&- \sum_{n=1}^{\mathrm{N}} (q_1^{(j_{\mathrm{in}}^{\mathrm{A1}})} + \mu_n + \nu_n \zeta^{\mathrm{J}}) \sum_{i=1}^{N_{\mathrm{F}}} \mathrm{Tr}(\mathbf{Z}_i^{\mathrm{J}}[n])\\
&+ \sum_{n=1}^{N} \sum_{e=1}^{E} \sum_{i=1}^{N_{\mathrm{F}}} \vartheta_{e,i,n} \min_{\|\Delta \mathbf{t}_e^{\mathrm{E}}\| \leq Q_e^{\mathrm{E}}} \mathrm{Tr}(\mathbf{H}_e^{\mathrm{JE}}[n] \mathbf{Z}_i^{\mathrm{J}}[n]) + \Delta,
\end{aligned}$$

where Δ denotes the collection of terms that are not relevant for the proof. Matrices $\mathbf{Y}_{i,n} \succeq \mathbf{0}, \forall i, n$, $\mathbf{X}_{i,n} \succeq \mathbf{0}, \forall i, n$, and $\mathbf{V}_{i,n} \succeq \mathbf{0}, \forall i, n$ are the Lagrange multiplier matrices for the constraint on matrix $\mathbf{Z}_i^{\mathrm{J}}[n]$ in C3b, C18, and C19, respectively. $\boldsymbol{\mu} = \{\mu_n, \forall n\}$, $\boldsymbol{\nu} = \{\nu_n, \forall n\}$, and $\boldsymbol{\vartheta} = \{\vartheta_{e,i,n}, \forall e, i, n\}$ denote the Lagrange multipliers for constraints C4b, C5b, and C7, respectively. Considering (B.7), the KKT conditions related to $\mathbf{Z}_i^{\mathrm{J}^*}[n]$ are given by

$$\mathbf{Y}_{i,n}^*, \mathbf{X}_{i,n}^*, \mathbf{V}_{i,n}^* \succeq \mathbf{0},\ \mu_n^*, \nu_n^*, \vartheta_{e,i,n}^* \geq 0, \tag{B.8}$$

$$\mathbf{Z}_i^{\mathrm{J}^*}[n](\mathbf{Y}_{i,n}^* - \mathbf{X}_{i,n}^* - \mathbf{V}_{i,n}^*) = \mathbf{0}, \tag{B.9}$$

$$\nabla_{\mathbf{Z}} \mathfrak{L} = \mathbf{0}, \tag{B.10}$$

where $\mathbf{Y}^*_{i,n}$, $\mathbf{X}^*_{i,n}$, $\mathbf{V}^*_{i,n}$, μ^*_n, ν^*_n, and $\vartheta^*_{e,i,n}$ are the optimal Lagrange multipliers for the dual problem of (3.41). Besides, (B.9) is the complementary slackness condition and is satisfied when the columns of $\mathbf{Z}^{\mathrm{J}^*}_i[n]$ lie in the null space of $\mathbf{Y}^*_{i,n}-\mathbf{X}^*_{i,n}-\mathbf{V}^*_{i,n}$. To reveal the structure of $\mathbf{Z}^{\mathrm{J}}_i[n]$, we express the KKT condition in (B.10) as

$$\begin{aligned}\mathbf{Y}^*_{i,n}[n] = (q_1^{(j_{\mathrm{in}}^{\mathrm{A1}})} + \mu_n + \nu_n\zeta^{\mathrm{J}})\mathbf{I}_{N_{\mathrm{J}}} + \mathbf{X}^*_{i,n}[n] \\ + \mathbf{V}^*_{i,n}[n] - \sum_{e=1}^{E} \vartheta^*_{e,i,n} \min_{\|\Delta\mathbf{t}^{\mathrm{E}}_e\|\le Q^{\mathrm{E}}_e} \mathbf{H}^{\mathrm{JE}}_e[n],\end{aligned} \tag{B.11}$$

where $\min\limits_{\|\Delta\mathbf{t}^{\mathrm{E}}_e\|\le Q^{\mathrm{E}}_e} \mathbf{H}^{\mathrm{JE}}_e[n]$ is a constant $N_{\mathrm{J}}\times N_{\mathrm{J}}$ matrix since we fix the jammer UAV's trajectory in this system. For notation simplicity, we define $\mathbf{\Xi} = (q_1^{(j_{\mathrm{in}}^{\mathrm{A1}})} + \mu_n + \nu_n\zeta^{\mathrm{J}})\mathbf{I}_{N_{\mathrm{J}}} + \mathbf{X}^*_{i,n}[n] + \mathbf{V}^*_{i,n}[n] \succeq \mathbf{0}$ and $\mathbf{\Omega} = \sum_{e=1}^{E} \vartheta^*_{e,i,n} \min\limits_{\|\Delta\mathbf{t}^{\mathrm{E}}_e\|\le Q^{\mathrm{E}}_e} \mathbf{H}^{\mathrm{JE}}_e[n] \succeq \mathbf{0}$. From (B.8), since matrix $\mathbf{Y}^*_{i,n}[n] = \mathbf{\Xi} - \mathbf{\Omega}$ is positive semi-definite,

$$\lambda^{\max}_{\Xi} \ge \lambda^{\max}_{\Omega} \ge 0, \tag{B.12}$$

must hold, where $\lambda^{\max}_{\Xi}$ and $\lambda^{\max}_{\Omega}$ are the real-valued maximum eigenvalue of matrix $\mathbf{\Xi}$ and $\mathbf{\Omega}$, respectively. Considering the KKT condition related to matrix $\mathbf{Z}^{\mathrm{J}^*}_i[n]$ in (B.9), we can show that if $\lambda^{\max}_{\Xi} > \lambda^{\max}_{\Omega}$, matrix $\mathbf{Y}^*_{i,n}$ will become positive definite and full rank. Besides, the maximum eigenvalue $\lambda^{\max}_{\Xi} > 0$ since $q_1^{(j_{\mathrm{in}}^{\mathrm{A1}})}$ is the energy-efficiency value of the system which is positive. Thus, this would yield the solution $\mathbf{Z}^{\mathrm{J}^*}_i[n] = \mathbf{0}$. On the other hand, if $\lambda^{\max}_{\Xi} = \lambda^{\max}_{\Omega}$, in order to have a bounded optimal dual solution, it follows that the null space of $\mathbf{Y}^*_{i,n}[n]$ is spanned by vector $\mathbf{u}_{\Omega,\max}$, which is the unit-norm eigenvector of Ω associated with eigenvalue $\lambda^{\max}_{\Omega}$. As a result, we obtain the structure of the optimal energy matrix $\mathbf{Z}^{\mathrm{J}^*}_i[n]$ as

$$\mathbf{Z}^{\mathrm{J}^*}_i[n] = \delta\mathbf{u}_{\Omega,\max}\mathbf{u}^{\mathrm{H}}_{\Omega,\max}. \tag{B.13}$$

Therefore, $\mathrm{Rank}(\mathbf{Z}^{\mathrm{J}^*}_i[n]) \le 1$.

B.3 Proof of Convergence of Alternating Optimization

The proposed algorithm contains two nested loops where the outer loop is based on alternating optimization (AO) and the inner loop is based on successive convex approximation (SCA). In the following, we will prove that the proposed algorithm can converge to a stationary point which serves as a suboptimal solution of the formulated problem. In order to simplify the presentation of proof and without loss of generality, we rewrite our proposed optimization problem as following:

$$\begin{aligned} \underset{\mathrm{A,B}}{\text{maximize}}\ & f(\mathrm{A},\mathrm{B}) \\ \text{s.t. } & g(\mathrm{A},\mathrm{B}) \geq 0, \end{aligned} \tag{B.14}$$

where A and B denote two set of optimization variables to be optimized in subproblem 1 and subproblem 2, respectively. $f(\mathrm{A},\mathrm{B})$ and $g(\mathrm{A},\mathrm{B})$ are function with coupled variables A and B. Besides, $f(\mathrm{A},\mathrm{B})$ and $g(\mathrm{A},\mathrm{B})$ are convex functions w.r.t. A given B and B given A, respectively. We first apply AO to resolve the coupling between A and B in (B.14) in this response letter which forms an outer loop. In each outer loop iteration, we need to solve two subproblems as:

$$\begin{aligned} \text{Subproblem 1}\,[\text{given B}]: \ P(\mathrm{A}|\mathrm{B}) = \underset{\mathrm{A}}{\text{maximize}}\ & f(\mathrm{A}|\mathrm{B}) \\ \text{s.t. } & g(\mathrm{A}|\mathrm{B}) \geq 0, \end{aligned} \tag{B.15}$$

$$\begin{aligned} \text{Subproblem 2}\,[\text{given A}]: \ P(\mathrm{B}|\mathrm{A}) = \underset{\mathrm{B}}{\text{maximize}}\ & f(\mathrm{B}|\mathrm{A}) \\ \text{s.t. } & g(\mathrm{B}|\mathrm{A}) \geq 0. \end{aligned} \tag{B.16}$$

To handle subproblem 1, SCA is applied which results in an inner loop. We first discuss the principle of the SCA. In particular, the SCA generates a sequence of convex functions to approximate the non-convex elements. In the iter-th iteration, the objective function and the constraint function are approximated by their lower

bound, $f_{\text{lb}}^{(\text{iter})}(\text{A}|\text{A}^{(\text{iter})},\text{B})$ and $g_{\text{lb}}^{(\text{iter})}(\text{A}|\text{A}^{(\text{iter})},\text{B})$, given by

$$f(\text{A}|\text{B}) \geq f_{\text{lb}}^{(\text{iter})}(\text{A}|\text{A}^{(\text{iter})},\text{B}) = f(\text{A}^{(\text{iter})}|\text{B}) + \nabla_{\text{A}} f(\text{A}^{(\text{iter})}|\text{B})(\text{A}-\text{A}^{(\text{iter})}) \text{ and} \tag{B.17}$$

$$g(\text{A}|\text{B}) \geq g_{\text{lb}}^{(\text{iter})}(\text{A}|\text{A}^{(\text{iter})},\text{B}) = g(\text{A}^{(\text{iter})}|\text{B}) + \nabla_{\text{A}} g(\text{A}^{(\text{iter})}|\text{B})(\text{A}-\text{A}^{(\text{iter})}), \tag{B.18}$$

respectively, for a given feasible solution $\text{A}^{(\text{iter})}$. Note that ∇_{A} denotes the first-order derivative with respect to (w.r.t.) A. Thus, in the iter-th iteration, we solve the following optimization problem

$$\begin{aligned} P_{\text{lb}}^{(\text{iter})}(\text{A}^{(\text{iter})}|\text{B}) = \underset{\text{A}}{\text{maximize}}\ & f_{\text{lb}}^{(\text{iter})}(\text{A}|\text{A}^{(\text{iter})},\text{B}) \\ \text{s.t. }& g_{\text{lb}}^{(\text{iter})}(\text{A}|\text{A}^{(\text{iter})},\text{B}) \geq 0. \end{aligned} \tag{B.19}$$

Denote $\text{A}^{*(\text{iter})}$ be the optimal solution in the iter-th iteration of (B.19) in this response letter. Then, we set $\text{A}^{(\text{iter}+1)} = \text{A}^{*(\text{iter})}$ as the input for the next iteration. The procedure repeats and we have

$$P(\text{A}^{(\text{iter})}|\text{B}) \overset{(a)}{=} P_{\text{lb}}^{(\text{iter})}(\text{A}^{(\text{iter})}|\text{B}) \overset{(b)}{\leq} P_{\text{lb}}^{(\text{iter})}(\text{A}^{j+1}|\text{B}) \overset{(c)}{\leq} P(\text{A}^{j+1}|\text{B}), \tag{B.20}$$

where equality (a) holds due to $f(\text{A}^{(\text{iter})}|\text{B}) = f_{\text{lb}}^{(\text{iter})}(\text{A}|\text{A}^{(\text{iter})},\text{B})$ and $g(\text{A}^{(\text{iter})}|\text{B}) = g_{\text{lb}}^{(\text{iter})}(\text{A}|\text{A}^{(\text{iter})},\text{B})$; inequality (b) holds since $\text{A}^{(\text{iter}+1)}$ is the optimal solution in the (iter + 1)-th iteration for the problem in (B.20) in this response letter; inequality (c) holds because the optimization problem in (B.20) in this response letter provides a lower bound to the performance of subproblem 1 in (B.15) in this response letter due to $f(\text{A}|\text{B}) \geq f_{\text{lb}}^{(\text{iter})}(\text{A}|\text{A}^{(\text{iter})},\text{B})$ and $g(\text{A}|\text{B}) \geq g_{\text{lb}}^{(\text{iter})}(\text{A}|\text{A}^{(\text{iter})},\text{B})$. Since the constraint set and the objective function is compact, the SCA converges to a stationary point. The same proof can be applied for the convergence of applying SCA to subproblem 2.

As for the convergence of AO, we first prove that the objective value is nondecreasing by first solving subproblem 1 via SCA and then use its solution as an input for subproblem 2. In the n-th outer loop iteration, we have

$$P(\text{A}|\text{B}^n) \leq P(\text{A}^{*j}|\text{B}^n) = P(\text{B}^n|\text{A}^{*j}) \leq P(\text{B}^{n+1}|\text{A}^{*j}). \tag{B.21}$$

Similarly, we can prove that the objective value is also nondecreasing when we use

the solution of subproblem 2 as an input for subproblem 1 via AO. As a result, the outer loop, driven by AO, also converges to a stationary point monotonically which completes the proof of the convergence of the overall algorithm.

Appendix C

Proof of Theories of Chapter 4

C.1 Proof of Theorem 4.1

As we aim to minimize the total power consumption, it is desired to maximize the channel gain from the UAV to GU k for satisfying constraint C6. This can be achieved by aligning the phase of the IRS to match with the phase of the channel.

Therefore, the optimal phase control can be obtained by solving

$$\underset{\mathbf{\Phi}}{\text{maximize}} \ |\mu_h\left(\mathbf{\Phi}[n]\right)|^2, \tag{C.1}$$

where $\mu_h\left(\mathbf{\Phi}[n]\right)$ for a given $\mathbf{\Phi}[n]$ can be expressed as

$$\begin{aligned}
&\sqrt{\frac{\beta_0^2}{(d^{\mathrm{AR}}[n])^2 (d_k^{\mathrm{RG}})^2}} \\
&\times \left[1, e^{-j\frac{2\pi\Delta_{\mathrm{R}x}}{\lambda_{\mathrm{c}}}\sin\theta_k^{\mathrm{RG}}\cos\xi_k^{\mathrm{RG}}}, \ldots, e^{-j\frac{2\pi\Delta_{\mathrm{R}x}}{\lambda_{\mathrm{c}}}(M_{\mathrm{R}x}-1)\sin\theta_k^{\mathrm{RG}}\cos\xi_k^{\mathrm{RG}}}\right] \\
&\otimes \left[1, e^{-j\frac{2\pi\Delta_{\mathrm{R}y}}{\lambda_{\mathrm{c}}}\sin\theta_k^{\mathrm{RG}}\sin\xi_k^{\mathrm{RG}}}, \ldots, e^{-j\frac{2\pi\Delta_{\mathrm{R}y}}{\lambda_{\mathrm{c}}}(M_{\mathrm{R}y}-1)\sin\theta_k^{\mathrm{RG}}\sin\xi_k^{\mathrm{RG}}}\right] \mathbf{\Phi}[n] \\
&\times \left[1, e^{-j\frac{2\pi\Delta_{\mathrm{R}x}}{\lambda_{\mathrm{c}}}\sin\theta^{\mathrm{RA}}[n]\cos\xi^{\mathrm{RA}}[n]}, \ldots, e^{-j\frac{2\pi\Delta_{\mathrm{R}x}}{\lambda_{\mathrm{c}}}(M_{\mathrm{R}x}-1)\sin\theta^{\mathrm{RA}}[n]\cos\xi^{\mathrm{RA}}[n]}\right]^{\mathrm{H}} \\
&\otimes \left[1, e^{-j\frac{2\pi\Delta_{\mathrm{R}y}}{\lambda_{\mathrm{c}}}\sin\theta^{\mathrm{RA}}[n]\sin\xi^{\mathrm{RA}}[n]}, \ldots, e^{-j\frac{2\pi\Delta_{\mathrm{R}y}}{\lambda_{\mathrm{c}}}(M_{\mathrm{R}y}-1)\sin\theta^{\mathrm{RA}}[n]\sin\xi^{\mathrm{RA}}[n]}\right]^{\mathrm{H}}.
\end{aligned} \tag{C.2}$$

Note that maximizing the norm of the mean for the effective channel gain is equivalent to align the LoS component of the reflect link with that of the direct link. Therefore, the suboptimal phase control policy of the IRS is obtained as in (4.16).

Appendix D

Proof of Theories of Chapter 5

D.1 Proof of Theorem 5.1

In the formulated problem in (5.16), we can observe that the phase control policy of the IRS, $\mathbf{\Phi}$, only affects the distribution of $C^{\mathrm{I}}_{k,k'}[n]$, $C^{\mathrm{II}}_{k,k'}[n]$, $C^{\mathrm{NSIC}}_{k',k}[n]$, and $C^{\mathrm{II}}_{k,k}[n]$ in constraint C6 − C8, respectively. Thus, for any given optimization variables $\mathcal{S}$, $\mathcal{P}$, $\mathcal{R}$, $\mathcal{T}$, and $\mathcal{V}$, a suboptimal $\mathbf{\Phi}$ can be obtained by maximizing the feasible probability of the GU k exploiting SIC decoding with stage II at C6 in (5.16), e.g.,

$$\underset{\mathbf{\Phi}}{\text{maximize}}\ \Pr\left(s_{k,k'}[n]r_k[n] \leq s_{k,k'}[n]\log_2\left(1+\frac{p_k[n]|h_k[n]|^2}{\sigma_k^2}\right)\right). \tag{D.1}$$

Note that the effective channel follows $h_k[n] \sim \mathcal{CN}\left(\mu_h(\mathbf{\Phi}[n]), \sigma_h^2\right)$, where $\mu_h(\mathbf{\Phi}[n])$ and σ_h^2 denote the mean and variance of the effective channel, respectively, such that $|h_k[n]|^2$ is noncentral chi-squared distributed. Besides, the variance of the effective channel, i.e., σ_h^2, is independent of $\mathbf{\Phi}[n]$ as the introduced phase rotation does not change the distribution of the scattering component in (5.9). Based on the CDF of $|h_k[n]|^2$ in (5.20), problem in (D.1) can be rewritten as the following equivalent form

$$\underset{\mathbf{\Phi}}{\text{minimize}}\ F_{n,k}\left(\frac{\sigma_k^2(2^{r_k[n]}-1)}{p_k[n]},\lambda\right) = 1-Q_\varsigma\left(\sqrt{\lambda},\sqrt{\frac{\sigma_k^2(2^{r_k[n]}-1)}{p_k[n]}}\right), \tag{D.2}$$

where $\lambda = \frac{|\mu_h(\mathbf{\Phi}[n])|^2}{\sigma_h^2}$ and $Q_\varsigma(a,b)$ represent the noncentral parameter and the Marcum Q-function of the noncentral chi-square distribution with 2ς degrees of

freedom (DoF), respectively. Moreover, it can be verified that the derivative of $F_{n,k}(\cdot,\lambda)$ w.r.t. λ is less than 0 and problem (D.2) is equivalent to maximize the noncentral parameter λ of $|h_k[n]|^2$, which is directly proportional to $|\mu_h(\mathbf{\Phi}[n])|^2$. Therefore, the optimal phase control can be obtained by solving

$$\underset{\mathbf{\Phi}}{\text{maximize}} \ |\mu_h\left(\mathbf{\Phi}[n]\right)|^2, \tag{D.3}$$

where $\mu_h\left(\mathbf{\Phi}[n]\right)$ for a given $\mathbf{\Phi}[n]$ can be expressed as

$$\begin{aligned}
&\sqrt{\frac{\beta_0 \kappa_k^{\mathrm{AG}}[n]}{(d_k^{\mathrm{AG}}[n])^{\alpha^{\mathrm{AG}}}(1+\kappa_k^{\mathrm{AG}}[n])}} e^{-j\frac{2\pi d_k^{\mathrm{AG}[n]}}{\lambda_{\mathrm{c}}}} \\
&+ \sqrt{\frac{\beta_0^2 \kappa^{\mathrm{RG}}}{(d^{\mathrm{AR}}[n])^{\alpha^{\mathrm{AR}}}(d_k^{\mathrm{RG}})^{\alpha^{\mathrm{RG}}}(1+\kappa^{\mathrm{RG}})}} e^{-j\frac{2\pi(d_k^{\mathrm{RG}}+d^{\mathrm{AR}}[n])}{\lambda_{\mathrm{c}}}} \\
&\times \left[1, e^{-j\frac{2\pi\Delta_{\mathrm{R}x}}{\lambda_{\mathrm{c}}}\sin\theta_k^{\mathrm{RG}}\cos\xi_k^{\mathrm{RG}}}, \ldots, e^{-j\frac{2\pi\Delta_{\mathrm{R}x}}{\lambda_{\mathrm{c}}}(M_{\mathrm{R}x}-1)\sin\theta_k^{\mathrm{RG}}\cos\xi_k^{\mathrm{RG}}}\right] \\
&\otimes \left[1, e^{-j\frac{2\pi\Delta_{\mathrm{R}y}}{\lambda_{\mathrm{c}}}\sin\theta_k^{\mathrm{RG}}\sin\xi_k^{\mathrm{RG}}}, \ldots, e^{-j\frac{2\pi\Delta_{\mathrm{R}y}}{\lambda_{\mathrm{c}}}(M_{\mathrm{R}y}-1)\sin\theta_k^{\mathrm{RG}}\sin\xi_k^{\mathrm{RG}}}\right] \mathbf{\Phi}[n] \\
&\times \left[1, e^{-j\frac{2\pi\Delta_{\mathrm{R}x}}{\lambda_{\mathrm{c}}}\sin\theta^{\mathrm{RA}}[n]\cos\xi^{\mathrm{RA}}[n]}, \ldots, e^{-j\frac{2\pi\Delta_{\mathrm{R}x}}{\lambda_{\mathrm{c}}}(M_{\mathrm{R}x}-1)\sin\theta^{\mathrm{RA}}[n]\cos\xi^{\mathrm{RA}}[n]}\right]^{\mathrm{H}} \\
&\otimes \left[1, e^{-j\frac{2\pi\Delta_{\mathrm{R}y}}{\lambda_{\mathrm{c}}}\sin\theta^{\mathrm{RA}}[n]\sin\xi^{\mathrm{RA}}[n]}, \ldots, e^{-j\frac{2\pi\Delta_{\mathrm{R}y}}{\lambda_{\mathrm{c}}}(M_{\mathrm{R}y}-1)\sin\theta^{\mathrm{RA}}[n]\sin\xi^{\mathrm{RA}}[n]}\right]^{\mathrm{H}}.
\end{aligned} \tag{D.4}$$

Note that maximizing the norm of the mean for the effective channel gain is equivalent to align the LoS component of the reflect link with that of the direct link. Therefore, the suboptimal phase control policy of the IRS is obtained as in (5.17).

Bibliography

[1] Y. Zeng and R. Zhang, "Energy-efficient UAV communication with trajectory optimization," *IEEE Trans. Wireless Commun.*, vol. 16, no. 6, pp. 3747–3760, Jun. 2017.

[2] H. Lee, S. Eom, J. Park, and I. Lee, "UAV-aided secure communications with cooperative jamming," *IEEE Trans. Veh. Technol.*, vol. 67, no. 10, pp. 9385–9392, Oct. 2018.

[3] Y. Zeng, J. Xu, and R. Zhang, "Energy minimization for wireless communication with rotary-wing UAV," *IEEE Trans. Wireless Commun.*, vol. 18, no. 4, pp. 2329–2345, Apr. 2019.

[4] C. Zhong, J. Yao, and J. Xu, "Secure UAV communication with cooperative jamming and trajectory control," *IEEE Commun. Lett.*, vol. 23, no. 2, pp. 286–289, Feb. 2019.

[5] Q. Wu and R. Zhang, "Intelligent reflecting surface enhanced wireless network via joint active and passive beamforming," *IEEE Trans. Wireless Commun.*, vol. 18, no. 11, pp. 5394–5409, Nov. 2019.

[6] J. Miranda, R. Abrishambaf, T. Gomes, P. Gonalves, J. Cabral, A. Tavares, and J. Monteiro, "Path loss exponent analysis in wireless sensor networks: Experimental evaluation," in *2013 11th IEEE Intern. Conf. Ind. Informat. (INDIN)*, Jul. 2013, pp. 54–58.

[7] Q.-V. Pham, F. Fang, V. N. Ha, M. J. Piran, M. Le, L. B. Le, W.-J. Hwang, and Z. Ding, "A survey of multi-access edge computing in 5G and beyond: Fundamentals, technology integration, and state-of-the-art," *IEEE Access*, vol. 8, pp. 116 974–117 017, Jun. 2020.

[8] L. Zhang, Y.-C. Liang, and D. Niyato, "6G visions: Mobile ultra-broadband, super internet-of-things, and artificial intelligence," *China Commun.*, vol. 16, no. 8, pp. 1–14, Aug. 2019.

[9] H. Yang, A. Alphones, Z. Xiong, D. Niyato, J. Zhao, and K. Wu, "Artificial-intelligence-enabled intelligent 6G networks," *IEEE Network*, vol. 34, no. 6, pp. 272–280, Oct. 2020.

[10] B. Wang, L. Dai, Z. Wang, N. Ge, and S. Zhou, "Spectrum and energy-efficient beamspace MIMO-NOMA for millimeter-wave communications using lens antenna array," *IEEE J. Sel. Areas Commun.*, vol. 35, no. 10, pp. 2370–2382, Oct. 2017.

[11] D. W. K. Ng and R. Schober, "Secure and green SWIPT in distributed antenna networks with limited backhaul capacity," *IEEE Trans. Wireless Commun.*, vol. 14, no. 9, pp. 5082–5097, Sep. 2015.

[12] T. A. Le, Q.-T. Vien, H. X. Nguyen, D. W. K. Ng, and R. Schober, "Robust chance-constrained optimization for power-efficient and secure SWIPT systems," *IEEE Trans. Green Commun. Netw.*, vol. 1, no. 3, pp. 333–346, 2017.

[13] S. Zargari, A. Khalili, Q. Wu, M. R. Mili, and D. W. K. Ng, "Max-min fair energy-efficient beamforming design for intelligent reflecting surface-aided SWIPT systems with non-linear energy harvesting model," *IEEE Trans. Veh. Technol.*, May 2021.

[14] A. El Shafie, D. Niyato, and N. Al-Dhahir, "Enhancing the phy-layer security of MIMO buffer-aided relay networks," *IEEE Wireless Commun. Lett.*, vol. 5, no. 4, pp. 400–403, May 2016.

[15] S. Guruacharya, D. Niyato, M. Bennis, and D. I. Kim, "Dynamic coalition formation for network MIMO in small cell networks," *IEEE Trans. Wireless Commun.*, vol. 12, no. 10, pp. 5360–5372, Sep. 2013.

[16] A. El Shafie, D. Niyato, and N. Al-Dhahir, "Artificial-noise-aided secure MIMO full-duplex relay channels with fixed-power transmissions," *IEEE Commun. Lett.*, vol. 20, no. 8, pp. 1591–1594, Jun. 2016.

[17] J. An, K. Yang, J. Wu, N. Ye, S. Guo, and Z. Liao, "Achieving sustainable ultra-dense heterogeneous networks for 5G," *IEEE Commun. Mag.*, vol. 55, no. 12, pp. 84–90, Dec. 2017.

[18] Z. Wei, L. Zhao, J. Guo, D. W. K. Ng, and J. Yuan, "Multi-beam NOMA for hybrid mmwave systems," *IEEE Trans. Commun.*, vol. 67, no. 2, pp. 1705–1719, Feb. 2019.

[19] D. W. K. Ng, E. S. Lo, and R. Schober, "Energy-efficient resource allocation for secure OFDMA systems," *IEEE Trans. Veh. Technol.*, vol. 61, no. 6, pp. 2572–2585, Jul. 2012.

[20] ——, "Energy-efficient resource allocation in OFDMA systems with large numbers of base station antennas," *IEEE Trans. Wireless Commun.*, vol. 11, no. 9, pp. 3292–3304, Jul. 2012.

[21] Z. Wei, Y. Cai, D. W. Ng, and J. Yuan, "Energy-efficient radio resource management," in *Wiley 5G Ref: The Essential 5G Reference Online*, R. Tafazolli, P. Chatzimisios, and C.-L. Wang, Eds. Wiley Online Library, 2019, pp. 1–23.

[22] D. W. K. Ng, E. S. Lo, and R. Schober, "Energy-efficient resource allocation in multi-cell OFDMA systems with limited backhaul capacity," *IEEE Trans. Wireless Commun.*, vol. 11, no. 10, pp. 3618–3631, Oct. 2012.

[23] Z. Wei, Y. Cai, J. Li, D. W. K. Ng, and J. Yuan, "Energy-efficient resource allocation design for NOMA systems," in *Green Communications for Energy-Efficient Wireless Systems and Networks*, H. A. Suraweera, J. Yang, A. Zappone, and J. Thompson, Eds. London: IET, 2020, ch. 13, pp. 363–399.

[24] C. Liu, J. Wang, X. Liu, and Y.-C. Liang, "Maximum eigenvalue-based goodness-of-fit detection for spectrum sensing in cognitive radio," *IEEE Trans. Veh. Technol.*, vol. 68, no. 8, pp. 7747–7760, Aug. 2019.

[25] C. Liu, H. Li, J. Wang, and M. Jin, "Optimal eigenvalue weighting detection for multi-antenna cognitive radio networks," *IEEE Trans. Wireless Commun.*, vol. 16, no. 4, pp. 2083–2096, Apr. 2017.

[26] C. Liu, H. Li, and M. Jin, "Blind central-symmetry-based feature detection for spatial spectrum sensing," *IEEE Trans. Veh. Technol.*, vol. 65, no. 12, pp. 10 147–10 152, Dec. 2016.

[27] C. Liu, M. Li, and M.-L. Jin, "Blind energy-based detection for spatial spectrum sensing," *IEEE Wireless Commun. Lett.*, vol. 4, no. 1, pp. 98–101, Feb. 2015.

[28] Y. Zeng, Q. Wu, and R. Zhang, "Accessing from the sky: A tutorial on UAV communications for 5G and beyond," *Proceedings of the IEEE*, vol. 107, no. 12, pp. 2327–2375, Dec. 2019.

[29] A. Fotouhi, H. Qiang, M. Ding, M. Hassan, L. G. Giordano, A. Garcia-Rodriguez, and J. Yuan, "Survey on UAV cellular communications: Practical aspects, standardization advancements, regulation, and security challenges," *IEEE Commun. Surveys Tuts.*, vol. 21, no. 4, pp. 3417–3442, Fourthquarter 2019.

[30] L. Gupta, R. Jain, and G. Vaszkun, "Survey of important issues in UAV communication networks," *IEEE Commun. Surveys Tuts.*, vol. 18, no. 2, pp. 1123–1152, Nov. 2015.

[31] Y. Sun, D. Xu, D. W. K. Ng, L. Dai, and R. Schober, "Optimal 3D-trajectory design and resource allocation for solar-powered UAV communication systems," *IEEE Trans. Commun.*, vol. 67, no. 6, pp. 4281–4298, Jun. 2019.

[32] R. Li, Z. Wei, L. Yang, D. W. K. Ng, N. Yang, J. Yuan, and J. An, "Joint trajectory and resource allocation design for UAV communication systems,"

in *2018 IEEE Globe. Commun. Workshops (GC Wkshps)*, Dec. 2018, pp. 1–6.

[33] L. Sboui, H. Ghazzai, Z. Rezki, and M. Alouini, "Achievable rates of UAV-relayed cooperative cognitive radio MIMO systems," *IEEE Access*, vol. 5, pp. 5190–5204, Apr. 2017.

[34] Q. Song and F. Zheng, "Energy efficient multi-antenna UAV-enabled mobile relay," *China Commun.*, vol. 15, no. 5, pp. 41–50, May 2018.

[35] Q. Wang, Z. Chen, W. Mei, and J. Fang, "Improving physical layer security using UAV-enabled mobile relaying," *IEEE Wireless Commun. Lett.*, vol. 6, no. 3, pp. 310–313, Jun. 2017.

[36] X. Jiang, Z. Wu, Z. Yin, Z. Yang, and N. Zhao, "Power consumption minimization of uav relay in NOMA networks," *IEEE Wireless Commun. Lett.*, vol. 9, no. 5, pp. 666–670, May 2020.

[37] E. Koyuncu, "Power-efficient deployment of UAVs as relays," in *IEEE Intern. Workshop on Signal Process. Adv. Wireless Commun. (SPAWC)*, Jun. 2018, pp. 1–5.

[38] C. Zhan, Y. Zeng, and R. Zhang, "Energy-efficient data collection in UAV enabled wireless sensor network," *IEEE Wireless Commun. Lett.*, vol. 7, no. 3, pp. 328–331, Jun. 2018.

[39] I. Jawhar, N. Mohamed, and J. Al-Jaroodi, "Data communication in linear wireless sensor networks using unmanned aerial vehicles," in *International Conference on Unmanned Aircraft Systems (ICUAS)*, May. 2014, pp. 43–51.

[40] C. You and R. Zhang, "3D trajectory optimization in Rician fading for UAV-enabled data harvesting," *IEEE Trans. Wireless Commun.*, vol. 18, no. 6, pp. 3192–3207, Jun. 2019.

[41] Y. Zeng, R. Zhang, and T. J. Lim, "Wireless communications with unmanned aerial vehicles: opportunities and challenges," *IEEE Commun. Mag.*, vol. 54, no. 5, pp. 36–42, May. 2016.

[42] Y. Zeng and R. Zhang, "Energy-efficient UAV communication with trajectory optimization," *IEEE Trans. Wireless Commun.*, vol. 16, no. 6, pp. 3747–3760, Jun. 2017.

[43] G. Zhang, Q. Wu, M. Cui, and R. Zhang, "Securing UAV communications via joint trajectory and power control," *IEEE Trans. Wireless Commun.*, vol. 18, no. 2, pp. 1376–1389, Feb. 2019.

[44] M. Cui, G. Zhang, Q. Wu, and D. W. K. Ng, "Robust trajectory and transmit power design for secure UAV communications," *IEEE Trans. Veh. Technol.*, vol. 67, no. 9, pp. 9042–9046, Sep. 2018.

[45] Y. Cai, Z. Wei, R. Li, D. W. K. Ng, and J. Yuan, "Joint trajectory and resource allocation design for energy-efficient secure UAV communication systems," *IEEE Trans. Commun.*, vol. 68, no. 7, pp. 4536–4553, Mar. 2020.

[46] M. Mozaffari, W. Saad, M. Bennis, Y. Nam, and M. Debbah, "A tutorial on UAVs for wireless networks: Applications, challenges, and open problems," *IEEE Commun. Surveys Tuts.*, vol. 21, no. 3, pp. 2334–2360, Thirdquarter 2019.

[47] Q. Wu, J. Xu, Y. Zeng, D. W. K. Ng, N. Al-Dhahir, R. Schober, and A. L. Swindlehurst, "5G-and-beyond networks with UAVs: From communications to sensing and intelligence," *arXiv preprint arXiv:2010.09317*, Oct. 2020.

[48] X. Yu and Y. Zhang, "Sense and avoid technologies with applications to unmanned aircraft systems: Review and prospects," *Progress in Aerospace Sciences*, vol. 74, pp. 152–166, Apr. 2015.

[49] P. Hügler, F. Roos, M. Schartel, M. Geiger, and C. Waldschmidt, "Radar taking off: New capabilities for UAVs," *IEEE Microwave Magazine*, vol. 19, no. 7, pp. 43–53, Oct. 2018.

[50] H. Essen, W. Johannes, S. Stanko, R. Sommer, A. Wahlen, and J. Wilcke, "High resolution W-band UAV SAR," in *Proc. IEEE Intern. Geosci. Remote Sens. Sympos.* IEEE, Jul. 2012, pp. 5033–5036.

[51] X. Cao, J. Xu, and R. Zhang, "Mobile edge computing for cellular-connected uav: Computation offloading and trajectory optimization," in *Proc. IEEE Intern. Workshop on Signal Process. Advances in Wireless Commun. (SPAWC).* IEEE, Jun. 2018, pp. 1–5.

[52] S. Jeong, O. Simeone, and J. Kang, "Mobile edge computing via a UAV-mounted cloudlet: Optimization of bit allocation and path planning," *IEEE Trans. Veh. Technol.*, vol. 67, no. 3, pp. 2049–2063, May 2017.

[53] Y. Cai, Z. Wei, R. Li, D. W. K. Ng, and J. Yuan, "Energy-efficient resource allocation for secure UAV communication systems," in *2019 IEEE Wireless Commun. Netw. Conf. (WCNC)*, Apr. 2019, pp. 1–8.

[54] M. Mozaffari, W. Saad, M. Bennis, and M. Debbah, "Optimal transport theory for power-efficient deployment of unmanned aerial vehicles," in *2016 IEEE Intern. Conf. Commun. (ICC)*, May 2016, pp. 1–6.

[55] C. You and R. Zhang, "Hybrid offline-online design for UAV-enabled data harvesting in probabilistic LoS channels," *IEEE Transa. Wireless Commun.*, vol. 19, no. 6, pp. 3753–3768, 2020.

[56] A. A. Khuwaja, Y. Chen, N. Zhao, M. Alouini, and P. Dobbins, "A survey of channel modeling for UAV communications," *IEEE Commun. Surveys Tuts.*, vol. 20, no. 4, pp. 2804–2821, Fourthquarter 2018.

[57] L. Xiao, Y. Xu, D. Yang, and Y. Zeng, "Secrecy energy efficiency maximization for UAV-enabled mobile relaying," *IEEE Trans. Green Commun. Netw.*, pp. 1–1, Oct. 2019.

[58] X. Zhou, Q. Wu, S. Yan, F. Shu, and J. Li, "UAV-enabled secure communications: Joint trajectory and transmit power optimization," *IEEE Trans. Veh. Technol.*, vol. 68, no. 4, pp. 4069–4073, Apr. 2019.

[59] A. S. d. Sena, D. Carrillo, F. Fang, P. H. J. Nardelli, D. B. d. Costa, U. S. Dias, Z. Ding, C. B. Papadias, and W. Saad, "What role do intelligent reflecting surfaces play in multi-antenna non-orthogonal multiple access?" *IEEE Wireless Commun.*, vol. 27, no. 5, pp. 24–31, Oct. 2020.

[60] B. Lyu, D. T. Hoang, S. Gong, D. Niyato, and D. I. Kim, "IRS-based wireless jamming attacks: When jammers can attack without power," *IEEE Wireless Commun. Lett.*, vol. 9, no. 10, pp. 1663–1667, Jun. 2020.

[61] H. Han, J. Zhao, D. Niyato, M. Di Renzo, and Q.-V. Pham, "Intelligent reflecting surface aided network: Power control for physical-layer broadcasting," in *Proc. IEEE Intern. Commun. Conf. (ICC)*. IEEE, Jun. 2020, pp. 1–7.

[62] Y. Cai, Z. Wei, S. Hu, D. W. K. Ng, and J. Yuan, "Resource allocation for power-efficient IRS-assisted UAV communications," in *Proc. IEEE Intern. Commun. Conf. Workshops (ICC Workshops)*, Jun. 2020, pp. 1–7.

[63] S. Hu, Z. Wei, Y. Cai, D. W. K. Ng, and J. Yuan, "Sum-rate maximization for multiuser MISO downlink systems with self-sustainable IRS," *arXiv preprint arXiv:2005.11663*, 2020.

[64] S. Hu, Z. Wei, Y. Cai, C. Liu, D. W. K. Ng, and J. Yuan, "Robust and secure sum-rate maximization for multiuser MISO downlink systems with self-sustainable IRS," *arXiv preprint arXiv:2101.10549*, 2021.

[65] C. Liu, X. Liu, Z. Wei, S. Hu, D. W. K. Ng, and J. Yuan, "Deep learning-empowered predictive beamforming for IRS-assisted multi-user communications," *arXiv preprint arXiv:2104.12309*, 2021.

[66] Z. Wei, Y. Cai, Z. Sun, D. W. K. Ng, J. Yuan, M. Zhou, and L. Sun, "Sum-rate maximization for IRS-assisted UAV OFDMA communication systems," *IEEE Trans. Wireless Commun.*, vol. 20, no. 4, pp. 2530–2550, Dec. 2021.

[67] Q. Wu and R. Zhang, "Beamforming optimization for wireless network aided by intelligent reflecting surface with discrete phase shifts," *IEEE Trans. Commun.*, vol. 68, no. 3, pp. 1838–1851, Mar. 2020.

[68] S. Jiao, F. Fang, X. Zhou, and H. Zhang, "Joint beamforming and phase shift design in downlink UAV networks with IRS-assisted NOMA," *J. Commun. Inf. Netw.*, vol. 5, no. 2, pp. 138–149, Jun. 2020.

[69] S. Li, B. Duo, X. Yuan, Y. Liang, and M. Di Renzo, "Reconfigurable intelligent surface assisted UAV communication: Joint trajectory design and passive beamforming," *IEEE Wireless Commun. Lett.*, vol. 9, no. 5, pp. 716–720, May 2020.

[70] L. Wang, K. Wang, C. Pan, W. Xu, and N. Aslam, "Joint trajectory and passive beamforming design for intelligent reflecting surface-aided UAV communications: A deep reinforcement learning approach," *arXiv preprint arXiv:2007.08380*, 2020.

[71] D. W. K. Ng, E. S. Lo, and R. Schober, "Dynamic resource allocation in MIMO-OFDMA systems with full-duplex and hybrid relaying," *IEEE Trans. Commun.*, vol. 60, no. 5, pp. 1291–1304, May 2012.

[72] Q. Wu and R. Zhang, "Common throughput maximization in UAV-enabled OFDMA systems with delay consideration," *IEEE Trans. Commun.*, pp. 1–1, Aug. 2018.

[73] A. A. Nasir, H. D. Tuan, T. Q. Duong, and H. V. Poor, "UAV-enabled communication using NOMA," *IEEE Trans. Commun.*, vol. 67, no. 7, pp. 5126–5138, Mar. 2019.

[74] N. Zhao, X. Pang, Z. Li, Y. Chen, F. Li, Z. Ding, and M.-S. Alouini, "Joint trajectory and precoding optimization for uav-assisted noma networks," *IEEE Trans. Commun.*, vol. 67, no. 5, pp. 3723–3735, Jan. 2019.

[75] P. Monk *et al.*, *Finite element methods for Maxwell's equations*. Oxford University Press, 2003.

[76] A. Goldsmith, *Wireless communications*. Cambridge university press, 2005.

[77] Z. Ding, Z. Yang, P. Fan, and H. Poor, "On the performance of non-orthogonal multiple access in 5G systems with randomly deployed users," *IEEE Signal Process. Lett.*, vol. 21, no. 12, pp. 1501–1505, Dec. 2014.

[78] Z. Wei, L. Yang, D. W. K. Ng, J. Yuan, and L. Hanzo, "On the performance gain of NOMA over OMA in uplink communication systems," *IEEE Trans. Commun.*, vol. 68, no. 1, pp. 536–568, Jan. 2020.

[79] D. Tse and P. Viswanath, *Fundamentals of wireless communication.* Cambridge university press, 2005.

[80] M. M. Azari, H. Sallouha, A. Chiumento, S. Rajendran, E. Vinogradov, and S. Pollin, "Key technologies and system trade-offs for detection and localization of amateur drones," *IEEE Commun. Mag.*, vol. 56, no. 1, pp. 51–57, Jan. 2018.

[81] Z. Hasan, H. Boostanimehr, and V. K. Bhargava, "Green cellular networks: A survey, some research issues and challenges," *IEEE Commun. Surveys Tuts. Mag.*, vol. 13, no. 4, pp. 524–540, Nov. 2011.

[82] V. W. Wong, R. Schober, D. W. K. Ng, and L.-C. Wang, *Key technologies for 5G wireless systems.* Cambridge university press, 2017.

[83] L. Dai, B. Wang, Y. Yuan, S. Han, I. Chih-Lin, and Z. Wang, "Non-orthogonal multiplelarge-scale underlay access for 5G: solutions, challenges, opportunities, and future research trends," *IEEE Commun. Mag.*, vol. 53, no. 9, pp. 74–81, Sep. 2015.

[84] Z. Ding, Y. Liu, J. Choi, Q. Sun, M. Elkashlan, C. L. I, and H. V. Poor, "Application of non-orthogonal multiple access in LTE and 5G networks," *IEEE Commun. Mag.*, vol. 55, no. 2, pp. 185–191, Feb. 2017.

[85] Z. Wei, Y. Jinhong, D. W. K. Ng, M. Elkashlan, and Z. Ding, "A survey of downlink non-orthogonal multiple access for 5G wireless communication networks," *ZTE Commun.*, vol. 14, no. 4, pp. 17–25, Oct. 2016.

[86] F. Fang, H. Zhang, J. Cheng, and V. C. M. Leung, "Energy-efficient resource allocation for downlink non-orthogonal multiple access network," *IEEE Trans. Commun.*, vol. 64, no. 9, pp. 3722–3732, Jul. 2016.

[87] F. Fang, H. Zhang, J. Cheng, S. Roy, and V. C. M. Leung, "Joint user scheduling and power allocation optimization for energy-efficient NOMA systems with imperfect CSI," *IEEE J. Sel. Areas Commun.*, vol. 35, no. 12, pp. 2874–2885, Nov. 2017.

[88] D. W. K. Ng and R. Schober, "Cross-layer scheduling for OFDMA amplify-and-forward relay networks," *IEEE Trans. Veh. Technol.*, vol. 59, no. 3, pp. 1443–1458, Mar. 2010.

[89] Y. Xu, D. Cai, F. Fang, Z. Ding, C. Shen, and G. Zhu, "Outage constrained power efficient design for downlink NOMA systems with partial HARQ," *IEEE Trans. Commun.*, vol. 68, no. 8, pp. 5188–5201, May 2020.

[90] D. Cai, Y. Xu, F. Fang, Z. Ding, and P. Fan, "On the impact of time-correlated fading for downlink NOMA," *IEEE Trans. Commun.*, vol. 67, no. 6, pp. 4491–4504, Mar. 2019.

[91] L. Yang, H. Jiang, Q. Ye, Z. Ding, F. Fang, J. Shi, J. Chen, and X. Xue, "Opportunistic adaptive non-orthogonal multiple access in multiuser wireless systems: Probabilistic user scheduling and performance analysis," *IEEE Trans. Wireless Commun.*, vol. 19, no. 9, pp. 6065–6082, Jun. 2020.

[92] Q. Yang, H.-M. Wang, D. W. K. Ng, and M. H. Lee, "NOMA in downlink SDMA with limited feedback: Performance analysis and optimization," *IEEE J. Sel. Areas Commun.*, vol. 35, no. 10, pp. 2281–2294, Oct. 2017.

[93] Z. Wei, D. W. K. Ng, J. Yuan, and H. M. Wang, "Optimal resource allocation for power-efficient MC-NOMA with imperfect channel state information," *IEEE Trans. Commun.*, vol. 65, no. 9, pp. 3944–3961, Sep. 2017.

[94] T. M. Cover and J. A. Thomas, *Elements of Information Theory.* John Wiley & Sons, Inc., 1991.

[95] D. Tse and P. Viswanath, *Fundamentals of wireless communication.* Cambridge university press, 2005.

[96] J. Ren, Z. Wang, M. Xu, F. Fang, and Z. Ding, "Unsupervised user clustering in non-orthogonal multiple access," in *Pros. IEEE Intern. Conf. on Acoust. Speech and Signal Process. (ICASSP)*, May 2019.

[97] Y. Sun, D. W. K. Ng, J. Zhu, and R. Schober, "Robust and secure resource allocation for full-duplex MISO multicarrier NOMA systems," *IEEE Trans. Commun.*, vol. 66, no. 9, pp. 4119–4137, Sep. 2018.

[98] T. Z. H. Ernest, A. S. Madhukumar, R. P. Sirigina, and A. K. Krishna, "NOMA-aided UAV communications over correlated rician shadowed fading channels," *IEEE Trans. Signal Process.*, vol. 68, pp. 3103–3116, May 2020.

[99] "Study on downlink multiuser supersition transmission (MUST) for LTE (Release 13)," 3GPP TR 36.859, Tech. Rep., Dec. 2015.

[100] DOCOMO and MediaTek. (2017) DOCOMO and MediaTek achieve world's first successful 5G trial using smartphone-sized NOMA chipset-embedded device to increase spectral efficiency. [Online]. Available: https://www.nttdocomo.co.jp/english/info/media_center/pr/2017/1102_02.html

[101] Y. Chen, A. Bayesteh, Y. Wu, B. Ren, S. Kang, S. Sun, Q. Xiong, C. Qian, B. Yu, Z. Ding, S. Wang, S. Han, X. Hou, H. Lin, R. Visoz, and R. Razavi, "Toward the standardization of non-orthogonal multiple access for next

generation wireless networks," *IEEE Commun. Mag.*, vol. 56, no. 3, pp. 19–27, Mar. 2018.

[102] D. W. K. Ng and R. Schober, "Resource allocation and scheduling in multi-cell OFDMA systems with decode-and-forward relaying," *IEEE Trans. Wireless Commun.*, vol. 10, no. 7, pp. 2246–2258, Jul. 2011.

[103] D. W. K. Ng, Y. Wu, and R. Schober, "Power efficient resource allocation for full-duplex radio distributed antenna networks," *IEEE Trans. Wireless Commun.*, vol. 15, no. 4, pp. 2896–2911, Apr. 2016.

[104] Y. Sun, D. W. K. Ng, J. Zhu, and R. Schober, "Multi-objective optimization for robust power efficient and secure full-duplex wireless communication systems," *IEEE Trans. Wireless Commun.*, vol. 15, no. 8, pp. 5511–5526, Aug. 2016.

[105] X. Zhang, D. P. Palomar, and B. Ottersten, "Statistically robust design of linear MIMO transceivers," *IEEE Trans. Signal Process.*, vol. 56, no. 8, pp. 3678–3689, Aug. 2008.

[106] X. Lin, V. Yajnanarayana, S. D. Muruganathan, S. Gao, H. Asplund, H. Maattanen, M. Bergstrom, S. Euler, and Y. . E. Wang, "The sky is not the limit: LTE for unmanned aerial vehicles," *IEEE Commun. Mag.*, vol. 56, no. 4, pp. 204–210, Apr. 2018.

[107] A. Colpaert, E. Vinogradov, and S. Pollin, "Aerial coverage analysis of cellular systems at LTE and mmwave frequencies using 3D city models," *Sensors*, vol. 18, no. 12, p. 4311, Oct. 2018.

[108] C. Liu, W. Yuan, Z. Wei, X. Liu, and D. W. K. Ng, "Location-aware predictive beamforming for UAV communications: A deep learning approach," *IEEE Wireless Commun. Lett.*, vol. 10, no. 3, pp. 668–672, Mar. 2021.

[109] E. Boshkovska, D. W. K. Ng, N. Zlatanov, A. Koelpin, and R. Schober, "Robust resource allocation for MIMO wireless powered communication networks based on a non-linear EH model," *IEEE Trans. Commun.*, vol. 65, no. 5, pp. 1984–1999, May. 2017.

[110] Q. Wu, Y. Zeng, and R. Zhang, "Joint trajectory and communication design for multi-UAV enabled wireless networks," *IEEE Trans. Wireless Commun.*, vol. 17, no. 3, pp. 2109–2121, Mar. 2018.

[111] D. Xu, Y. Sun, D. W. K. Ng, and R. Schober, "Multiuser MISO UAV communications in uncertain environments with no-fly zones: Robust trajectory and resource allocation design," *IEEE Trans. Commun.*, pp. 1–1, Jan. 2020.

[112] J. C. Bezdek and R. J. Hathaway, "Convergence of alternating optimization," *Neural, Parallel & Scientific Comput.*, vol. 11, no. 4, pp. 351–368, Dec. 2003.

[113] J. Lee and S. Leyffer, *Mixed integer nonlinear programming*. Springer Science & Business Media, 2011, vol. 154.

[114] P. P. Bedekar, S. R. Bhide, and V. S. Kale, "Optimum time coordination of overcurrent relays in distribution system using big-M (penalty) method," *WSEAS Trans. Power Syst.*, vol. 4, no. 11, pp. 341–350, 2009.

[115] Q. T. Dinh and M. Diehl, "Local convergence of sequential convex programming for nonconvex optimization," in *Recent Advances in Optimization and its Applications in Engineering*, M. Diehl, F. Glineur, E. Jarlebring, and W. Michiels, Eds. Berlin, Heidelberg: Springer Berlin Heidelberg, 2010, pp. 93–102.

[116] Z. Wei, D. W. K. Ng, J. Yuan, and H. Wang, "Optimal resource allocation for power-efficient MC-NOMA with imperfect channel state information," *IEEE Trans. Commun.*, vol. 65, no. 9, pp. 3944–3961, Sep. 2017.

[117] Y. Sun, D. W. K. Ng, Z. Ding, and R. Schober, "Optimal joint power and subcarrier allocation for full-duplex multicarrier non-orthogonal multiple access systems," *IEEE Trans. Commun.*, vol. 65, no. 3, pp. 1077–1091, Mar. 2017.

[118] A. Ben-Tal, L. El Ghaoui, and A. Nemirovski, *Robust optimization*. Princeton University Press, 2009, vol. 28.

[119] W. Dinkelbach, "On nonlinear fractional programming," *Manag. sci.*, vol. 13, no. 7, pp. 492–498, Mar. 1967.

[120] S. Boyd and L. Vandenberghe, *Convex optimization*. Cambridge university press, Mar. 2004.

[121] J. C. Bezdek and R. J. Hathaway, "Some notes on alternating optimization," in *AFSS International Conference on Fuzzy Systems*. Springer, 2002, pp. 288–300.

[122] Z. Opial, "Weak convergence of the sequence of successive approximations for nonexpansive mappings," *Bulletin Am. Math. Soc.*, vol. 73, no. 4, pp. 591–597, 1967.

[123] N. Vucic, S. Shi, and M. Schubert, "DC programming approach for resource allocation in wireless networks," in *8th International Symposium on Modeling and Optimization in Mobile, Ad Hoc, and Wireless Networks*, May 2010, pp. 380–386.

[124] Y. Nesterov and A. Nemirovskii, *Interior-point polynomial algorithms in convex programming*. Siam, 1994, vol. 13.

[125] I. Pólik and T. Terlaky, "Interior point methods for nonlinear optimization," in *Nonlinear Optimization: Lectures given at the C.I.M.E. Summer School held in Cetraro, Italy, July 1-7, 2007*, G. Di Pillo and F. Schoen, Eds. Berlin, Heidelberg: Springer Berlin Heidelberg, 2010, pp. 215–276.

[126] F. Classen and H. Meyr, "Frequency synchronization algorithms for OFDM systems suitable for communication over frequency selective fading channels," in *Proc. IEEE Veh. Techn. Conf. (VTC)*. IEEE, Jun. 1994, pp. 1655–1659.

[127] M. Di Renzo, K. Ntontin, J. Song, F. H. Danufane, X. Qian, F. Lazarakis, J. De Rosny, D. Phan-Huy, O. Simeone, R. Zhang, M. Debbah, G. Lerosey, M. Fink, S. Tretyakov, and S. Shamai, "Reconfigurable intelligent surfaces vs. relaying: Differences, similarities, and performance comparison," pp. 798–807, Jun. 2020.

[128] Q. Wu and R. Zhang, "Towards smart and reconfigurable environment: Intelligent reflecting surface aided wireless network," *IEEE Commun. Mag.*, vol. 58, no. 1, pp. 106–112, Jan. 2020.

[129] W. Yu and R. Lui, "Dual methods for nonconvex spectrum optimization of multicarrier systems," *IEEE Trans. Commun.*, vol. 54, no. 7, pp. 1310–1322, Jul. 2006.

[130] W. Yuan, N. Wu, A. Zhang, X. Huang, Y. Li, and L. Hanzo, "Iterative receiver design for FTN signaling aided sparse code multiple access," *IEEE Trans. Wireless Commun.*, vol. 19, no. 2, pp. 915–928, Feb. 2020.

[131] M. A. Saeidi, M. J. Emadi, H. Masoumi, M. R. Mili, D. W. K. Ng, and I. Krikidis, "Weighted sum-rate maximization for multi-IRS-assisted full-duplex systems with hardware impairments," *IEEE Trans. Cognitive Commun. Netw.*, Apr. 2021.

[132] Y. Gao, J. Xu, W. Xu, D. W. K. Ng, and M.-S. Alouini, "Distributed IRS with statistical passive beamforming for MISO communications," *IEEE Wireless Commun. Lett.*, vol. 10, no. 2, pp. 221–225, Sep. 2020.

[133] Z. Ding, Z. Yang, P. Fan, and H. V. Poor, "On the performance of non-Orthogonal multiple access in 5g systems with randomly deployed users," *IEEE Signal Process. Lett.*, vol. 21, no. 12, pp. 1501–1505, 2014.

[134] D. Ma, M. Ding, and M. Hassan, "Enhancing cellular communications for UAVs via intelligent reflective surface," in *2020 IEEE Wireless Commun. Netw. Conf. (WCNC)*, May 2020, pp. 1–6.

[135] C. You, B. Zheng, and R. Zhang, "Channel estimation and passive beamforming for intelligent reflecting surface: Discrete phase shift and progressive refinement," *IEEE J. Select. Areas Commun.*, vol. 38, no. 11, pp. 2604–2620, 2020.

[136] A. Ghosh, J. Zhang, J. G. Andrews, and R. Muhamed, *Fundamentals of LTE*. The Prentice Hall communications engineering and emerging technologies series, 2010.

[137] T. Shen and H. Ochiai, "A UAV-aided data collection for wireless powered sensor network over Rician fading channels," in *2019 16th IEEE Annual Consumer Commun. & Networking Conf. (CCNC)*. IEEE, 2019, pp. 1–5.

[138] N. C. Beaulieu and K. T. Hemachandra, "New simple solutions for the bivariate Rician PDF and CDF," in *2010 IEEE Wireless Commun. Netw. Conf.*, Apr. 2010, pp. 1–4.

[139] A. Nuttall, "Some integrals involving the Q_{M} function (corresp.)," *IEEE Trans. Inf. Theory*, vol. 21, no. 1, pp. 95–96, Jan. 1975.

[140] C. Liu, J. Wang, X. Liu, and Y.-C. Liang, "Deep CM-CNN for spectrum sensing in cognitive radio," *IEEE J. Sel. Areas Commun.*, vol. 37, no. 10, pp. 2306–2321, Oct. 2019.

[141] C. Liu, Z. Wei, D. W. K. Ng, J. Yuan, and Y.-C. Liang, "Deep transfer learning for signal detection in ambient backscatter communications," *IEEE Trans. Wireless Commun.*, vol. 20, no. 3, pp. 1624–1638, Mar. 2021.

[142] D. Svozil, V. Kvasnicka, and J. Pospichal, "Introduction to multi-layer feed-forward neural networks," *Chemometrics and intelligent laboratory systems*, vol. 39, no. 1, pp. 43–62, 1997.

[143] C. Liu, X. Liu, D. W. K. Ng, and J. Yuan, "Deep residual learning for channel estimation in intelligent reflecting surface-assisted multi-user communications," *arXiv preprint arXiv: 2009.01423*, 2020.

[144] S. Weiss and R. W. Stewart, "Fast implementation of oversampled modulated filter banks," *Electron. Lett.*, vol. 36, no. 17, pp. 1502–1503, Aug. 2000.

[145] L. Liu and W. Yu, "Massive connectivity with massive MIMO?part II: Achievable rate characterization," *IEEE Trans. Signal Process.*, vol. 66, no. 11, pp. 2947–2959, Mar. 2018.

[146] C. Zhan, H. Hu, X. Sui, Z. Liu, and D. Niyato, "Completion time and energy optimization in the UAV-enabled mobile-edge computing system," *IEEE Internet of Things Journal*, vol. 7, no. 8, pp. 7808–7822, May 2020.

[147] A. Asheralieva and D. Niyato, "Game theory and lyapunov optimization for cloud-based content delivery networks with device-to-device and UAV-enabled caching," *IEEE Trans. Veh. Technol.*, vol. 68, no. 10, pp. 10 094–10 110, Aug. 2019.

[148] J. Xie, C. Liu, Y.-C. Liang, and J. Fang, "Activity pattern aware spectrum sensing: A CNN-based deep learning approach," *IEEE Commun. Lett.*, vol. 23, no. 6, pp. 1025–1028, Jun. 2019.

[149] J. Xie, J. Fang, C. Liu, and L. Yang, "Unsupervised deep spectrum sensing: A variational auto-encoder based approach," *IEEE Trans. Veh. Technol.*, vol. 69, no. 5, pp. 5307–5319, May 2020.

[150] Z. Xiong, Y. Zhang, W. Y. B. Lim, J. Kang, D. Niyato, C. Leung, and C. Miao, "UAV-assisted wireless energy and data transfer with deep reinforcement learning," *IEEE Trans. Cognitive Commun. Netw.*, 2020.

[151] N. Zhao, Y. Cheng, Y. Pei, Y.-C. Liang, and D. Niyato, "Deep reinforcement learning for trajectory design and power allocation in UAV networks," in *Proc. IEEE Intern. Conf. Commun. (ICC)*. IEEE, Jun. 2020, pp. 1–6.

[152] J. Xie, J. Fang, C. Liu, and X. Li, "Deep learning-based spectrum sensing in cognitive radio: A CNN-LSTM approach," *IEEE Commun. Lett.*, vol. 24, no. 10, pp. 2196–2200, Oct. 2020.

[153] M. A. Alsheikh, S. Lin, D. Niyato, and H.-P. Tan, "Machine learning in wireless sensor networks: Algorithms, strategies, and applications," *IEEE Commun. Surveys Tuts.*, vol. 16, no. 4, pp. 1996–2018, Apr. 2014.

[154] W. Yuan, C. Liu, F. Liu, S. Li, and D. W. K. Ng, "Learning-based predictive beamforming for UAV communications with jittering," *IEEE Wireless Commun. Lett.*, vol. 9, no. 11, pp. 1970–1974, Nov. 2020.

[155] Z. Wei, W. Yuan, S. Li, J. Yuan, G. Bharatula, R. Hadani, and L. Hanzo, "Orthogonal time-frequency space modulation: A full-diversity next generation waveform," *arXiv preprint arXiv:2010.03344*, Oct. 2020.

[156] Z. Wei, W. Yuan, S. Li, J. Yuan, and D. W. K. Ng, "Transmitter and receiver window designs for orthogonal time-frequency space modulation," *IEEE Trans. Commun.*, vol. 69, no. 4, pp. 2207–2223, Jan. 2021.

[157] S. Li, J. Yuan, W. Yuan, Z. Wei, B. Bai, and D. W. K. Ng, "Performance analysis of coded OTFS systems over high-mobility channels," *IEEE Trans. Wireless Commun.*, pp. 1–1, Apr. 2021.

[158] Z. Wei, W. Yuan, S. Li, J. Yuan, and D. W. K. Ng, "Off-grid channel estimation with sparse bayesian learning for otfs systems," *arXiv preprint arXiv:2101.05629*, Jan 2021.

[159] S. Li, W. Yuan, Z. Wei, and J. Yuan, "Cross domain iterative detection for orthogonal time frequency space modulation," *arXiv preprint arXiv:2101.03822*, Jan 2021.

[160] W. Yuan, Z. Wei, J. Yuan, and D. W. K. Ng, "A simple variational bayes detector for orthogonal time frequency space (OTFS) modulation," *IEEE Transactions on Vehicular Technology*, vol. 69, no. 7, pp. 7976–7980, Apr. 2020.

[161] S. Li, W. Yuan, Z. Wei, J. Yuan, B. Bai, D. W. K. Ng, and Y. Xie, "Hybrid MAP and PIC detection for OTFS modulation," *IEEE Trans. Veh. Technol.*, pp. 1–1, May 2021.

[162] Y. Liao, L. Yang, J. Yuan, K. Huang, R. Leung, and J. Du, "LDPC code design for delayed bit-interleaved coded modulation," in *Proc. IEEE Inf. Theory Workshop (ITW)*, Aug. 2019, pp. 1–5.

[163] Y. Liao, M. Qiu, and J. Yuan, "Design and analysis of delayed bit-interleaved coded modulation with LDPC codes," *IEEE Trans. Commun.*, vol. 69, no. 6, pp. 3556–3571, Mar. 2021.

[164] V. Jamali, N. Farsad, R. Schober, and A. Goldsmith, "Non-coherent detection for diffusive molecular communication systems," *IEEE Trans. Commun.*, vol. 66, no. 6, pp. 2515–2531, Jan. 2018.

[165] X. Wu, L. Yang, Y. Xie, and J. Yuan, "Partially information coupled polar codes," *IEEE Access*, vol. 6, pp. 63 689–63 702, Sep. 2018.

[166] X. Wu, L. Yang, and J. Yuan, "Information coupled polar codes," in *Proc. IEEE Intern. Sympos. on Inf. Theory (ISIT)*. IEEE, Jun. 2018, pp. 861–865.

[167] M. Qin, J. Guo, A. Bhatia, A. G. i Fàbregas, and P. H. Siegel, "Polar code constructions based on LLR evolution," *IEEE Commun. Lett.*, vol. 21, no. 6, pp. 1221–1224, Jan. 2017.

[168] T.-X. Zheng, H.-M. Wang, D. W. K. Ng, and J. Yuan, "Multi-antenna covert communications in random wireless networks," *IEEE Trans. Wireless Commun.*, vol. 18, no. 3, pp. 1974–1987, Mar. 2019.

[169] X. Zhou, S. Yan, Q. Wu, F. Shu, and D. W. K. Ng, "Intelligent reflecting surface (IRS)-aided covert wireless communications with delay constraint," *IEEE Trans. Wireless Commun.*, Jul. 2021.

[170] C. Wang, Z. Li, J. Shi, and D. W. K. Ng, "Intelligent reflecting surface-assisted multi-antenna covert communications: Joint active and passive beamforming optimization," *IEEE Trans. Commun.*, Feb. 2021.